NMR Spectroscopic Investigations on Asymmetric Aminocatalysis

Dissertation

zur Erlangung des Doktorgrades der Naturwissenschaften

(Dr. rer. nat.)

der Fakultät für Chemie und Pharmazie

der Universität Regensburg

vorgelegt von

Andreas Seegerer

aus Vilseck

im Jahr 2018

Die vorliegende Dissertation beruht auf Arbeiten, die zwischen November 2014 und April 2018 am Arbeitskreis von Frau Professor Dr. Ruth M. Gschwind am Institut für Organische Chemie der Universität Regensburg durchgeführt wurden.

Promotionsgesuch eingereicht:	April 2018
Die Arbeit wurde angeleitet von:	Prof. Dr. Ruth M. Gschwind
Promotionsausschuss:	
Vorsitzender:	Prof. Dr. Alkwin Slenczka
1. Gutachter:	Prof. Dr. Ruth M. Gschwind
2. Gutachter:	Prof. Dr. Werner Kremer
3. Prüfer:	Prof. Dr. Julia Rehbein

NMR Spectroscopic Investigations on Asymmetric Aminocatalysis

Andreas Seegerer

Table of Contents

1 Introduction and Outline

In 2018, asymmetric aminocatalysis represents one of the most important strategies in organocatalysis and hundreds of different enantioselective transformations catalyzed by small chiral amines are known.[1] However, going back around 20 years in history, the field of asymmetric aminocatalysis had, except for a marginal number of publications, not even been discovered.[2] Although the power of small organic molecules, to catalyze organic reactions, has been known for much more than a hundred years,[3] their triumph in asymmetric transformations has been long in coming. Nowadays, the development of the Hajos-Parrish-Eder-Sauer-Wiechert reaction in the early 1970's,[4] enabling the first highly enantioselective transformation catalyzed by L-proline, is regarded as one of the most important milestones in enantioselective organocatalysis. However, back then, "its potential has not been realized […] and remained little more than a laboratory curiosity" (List, B. *Chem. Rev.* **2007**, *107*, 5471).

Finally in 2000, two pioneering publications of List and MacMillan managed to focus the broad interest of the organic chemistry community on asymmetric organocatalysis.[5,6] The introduction of two concepts, describing the activation of aldehydes or ketones by HOMO activation (enamines) and LUMO lowering (iminium ions) and the corresponding conversions with electrophiles or nucleophiles was the start for a great story of success. Beginning with the application of L-proline and its derivatives as secondary amino catalysts, the steady development of new reactions, cascades and catalysts led to a gold rush in organocatalysis.[7] Within a few years, hundreds of publications proved the huge scope of aminocatalysis and helped to establish the field as an important pillar in organocatalysis.[8]

Besides the fast development in terms of reaction design, especially in the beginning of the golden era of asymmetric organocatalysis, detailed mechanistic investigations and studies were scarce. However, insights in reaction pathways and their corresponding kinetics and thermodynamics can be essential to improve yields and enantiomeric excess of reactions. Furthermore, information about the reaction mechanisms is of utmost importance in designing new types of reactions, substrates and catalysts.

Beginning with the first detection of an elusive enamine intermediate in 2010, our working group contributed several important NMR spectroscopic studies about the formation, stability and structure of enamine intermediates during recent years.[9] The goal of this thesis was to use this experience to shed light on additional mechanistic issues in secondary aminocatalysis and to increase the number of options to solve current and future mechanistic questions by the implementation of new NMR spectroscopic tools and techniques.

The first issue analyzed in this thesis, is the remote-stereocontrol in asymmetric dienamine catalysis with Jørgensen-Hayashi type catalysts. The concept of dienamine catalysis represents a vinylogous version of enamine catalysis to enable the catalytic functionalization of α,β-unsaturated aldehydes in their α or γ positions.[10] As in enamine catalysis, a stereoinduction caused by a steric shielding of one site of the intermediates by the catalyst was assumed. However, the elongated distance between the shielding moiety and the active γ position of the dienamine intermediates, and a *Z*/*E* ratio of the second double bond deviating from the *ee* values observed in synthesis, left room for speculations.

Therefore, in chapter 2, an NMR spectroscopic analysis of the structure of the dienamines, derived by the condensation of different aldehydes and catalysts is presented. Furthermore, detailed spectroscopic and computational studies to investigate the formation of the dienamine intermediates are shown and the observed *Z*/*E* ratios regarding the diene subsystem are explained. Based on the shift of the rate determining step of the reaction by the modulation of the acidic additive, for the first time a kinetic preference for conversion of the *Z* dienamine is proven experimentally. In combination with detailed computational analyses, revealing catalyst specific CH-π interactions in the transition states, a delicate interplay between structure, formation and conversion was found to be responsible for a highly effective remote-stereocontrol in dienamine catalysis.

In chapter 3, the focus of the investigations is shifted to the related field of enamine catalysis. Here, in the case of proline catalyzed reactions, a long controversial discussion about the role of iminium ions in the proline catalyzed enamine formation arose already years ago.[11] Due to the lack of a direct experimental access to iminium ion intermediates, their general importance for the formation process of enamines respectively their competition with oxazolidinone intermediates was unclear.

The main problem for the *in situ* detection of the iminium ions by NMR spectroscopy was assumed to be a population below the detection limit of classical NMR experiments.

Therefore, in chapter 3, the chemical exchange saturation transfer (CEST) technique, providing a higher sensitivity, was applied for the first time for the detection of transient reaction intermediates in organocatalysis, proving the missing iminium ion intermediate in a proline catalyzed enamine formation.

In addition to chapter 3, the last two chapters of this thesis are also focused on the development and application of new experimental methods and NMR spectroscopic tools. In general, the steady advancement of existing techniques and the development of new ones are essential to facilitate and to enable the analysis of recent and future mechanistic issues. A great example for this progress in reaction mechanism analysis can be found in the decrypting transition states by light (DTS-hv) method, which was recently developed in our working group.[12] This new method describes an experimental way to investigate the dominant reaction pathway, by a light induced modulation of double bonds, whose configurations are essential for the stereocontrol of a reaction.

Due to the great success in proving the dominant pathways for two Brønsted acid catalyzed reactions of aldimines and ketimines containing one double bond, the idea of a transfer of the DTS-hv method to a more complex system, possessing two double bonds, is described in chapter 4. Based on the example of iminium ion intermediates, derived by the condensation of α,β-unsaturated aldehydes and a Jørgensen-Hayashi catalyst, a detailed theoretical approach of the method is presented. Additionally, first preliminary experimental results applying the DTS-hv method for a [3+3] annulation via iminium ion catalysis are shown and the effect of light on iminium ion intermediates is investigated.

A further example for a new tool in reaction mechanism analysis can be found in chapter 5. Here, an innovative setup for the combination of UV/Vis spectroscopy, NMR spectroscopy, and an *in situ* illumination device is introduced. The fully automated triple combination allows for a simultaneous and time-resolved detection of both diamagnetic and paramagnetic species by merging the specific benefits of the NMR and UV/Vis spectroscopy methods. Therefore, for the first time, this optical fiber based setup enables the acquisition of combined UV/Vis and NMR reaction profiles under the influence of an additional light source, directly inside the magnet. Furthermore, it circumvents all common issues compared to measurements conducted in separated setups, such as deviating concentrations, conditions, light intensities, as well as convection and diffusion. The advantages of the UVNMR-illumination setup are demonstrated on the analysis of a consecutive photoinduced electron transfer (conPET) process[13] and on the isomerization of a photoswitchable spiropyran.

(1) List, B. *Synlett* **2001**, *2001*, 1675; Dalko, P. I.; Moisan, L. *Angew. Chem. Int. Ed.* **2004**, *43*, 5138.; Erkkilä, A.; Majander, I.; Pihko, P. M. *Chem. Rev.* **2007**, *107*, 5416.; Mukherjee, S.; Yang, J. W.; Hoffmann, S.; List, B. *Chem. Rev.* **2007**, *107*, 5471.; Bertelsen, S.; Jørgensen, K. A. *Chem. Soc. Rev.* **2009**, *38*, 2178.

(2) MacMillan, D. W. C. *Nature* **2008**, *455*, 304.

(3) Wöhler, F.; von Liebig, J., *Ann. Pharm.* **1832**, *3*, 249.; von Liebig, J., *Justus Liebigs Ann. Chem.* **1860**, *113*, 246.; Knoevenagel, E., *Ber. Dtsch. Chem. Ges.* **1896**, *29*, 172.; Bredig G.; Fiske, P.S., *Biochem. Z.* **1912**, *46*, 7

(4) Eder, U.; Sauer, G. R.; Wiechert, R., *German patent* **1971**, DE2014757.; Hajos, Z. G.; Parrish, D. R. *German patent* **1971**, DE2102623.; Eder, U.; Sauer, G.; Wiechert, R. *Angew. Chem. Int. Ed.* **1971**, *10*, 496.; Hajos, Z. G.; Parrish, D. R. *J. Org. Chem.* **1974**, *39*, *1615*.

(5) List, B.; Lerner, R. A.; Barbas III, C. F. *J. Am. Chem. Soc.* **2000**, *122*, 2395.

(6) Ahrendt, K. A; Borths, C. J.; MacMillan, D. W. C. *J. Am. Chem. Soc.* **2000**, *122*, 4243.

(7) Melchiorre, P.; Marigo, M.; Carlone, A.; Bartoli, G. *Angew. Chem. Int. Ed.* **2008**, *47*, 6138.

(8) Donslund, B. S.; Johansen, T. K.; Poulsen, P. H.; Halskov, K. S.; Jørgensen, K. A. *Angew. Chem. Int. Ed.* **2015**, *54*, 13860.

(9) Renzi, P.; Hioe, J.; Gschwind, R. M. *Acc. Chem. Res.* **2017**, *50*, 2936.

(10) Marcos, V.; Alemán, J. *Chem. Soc. Rev.* **2016**, *45*, 6812.

(11) Nielsen, M.; Worgull, D.; Zweifel, T.; Gschwend, B.; Bertelsen, S.; Jørgensen, K. A. *Chem. Commun.* **2011**, *47*, 632.; Ashley, M. A.; Hirschi, J. S.; Izzo, J. A.; Vetticatt, M. J. *J. Am. Chem. Soc.* **2016**, *138*, 1756.; Haindl, M. H.; Hioe, J.; Gschwind, R. M. *J. Am. Chem. Soc.* **2015**, *137*, 12835.

(12) Renzi, P.; Hioe, J.; Gschwind, R. M. *J. Am. Chem. Soc.* **2017**, *139*, 6752.

(13) Ghosh, I.; Ghosh, T.; Bardagi, J. I.; Konig, B. *Science* **2014**, *346*, 725.

2 Remote-Stereocontrol in Dienamine Catalysis: *Z*-Dienamine Preferences and Electrophile-Catalyst Interaction Revealed by NMR and Computational Studies

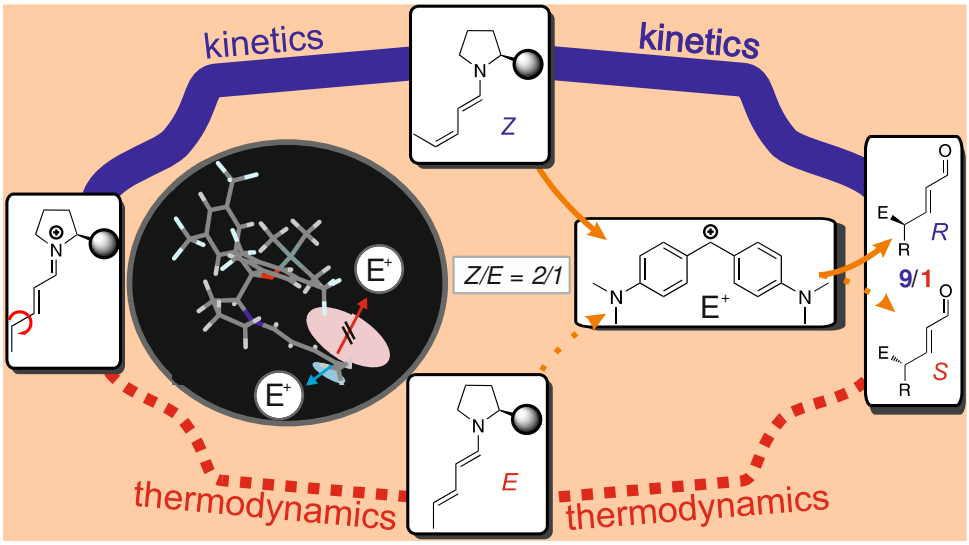

Andreas Seegerer, Johnny Hioe, Michael M. Hammer, Fabio Morana, Patrick J. W. Fuchs and Ruth M. Gschwind.

J. Am. Chem. Soc., **2016**, *138*, 9864–9873

DOI: 10.1021/jacs.6b04008

The majority of the NMR measurements and their analysis presented in this chapter were performed by Andreas Seegerer. All computational studies were done by Dr. Johnny Hioe. Initial NMR experiments about the influence of temperature and acid on this system were performed by Dr. Michael Hammer. Dr. Fabio Morana was responsible for the preparation of all HPLC samples, which were analyzed by Patrick J. W. Fuchs in Leipzig.

2.1 Abstract

Catalysis with remote-stereocontrol provides special challenges in design and comprehension. One famous example is the dienamine catalysis, for which high *ee* values are reported despite insufficient shielding of the second double bond. Especially for dienamines with variable *Z/E*-ratios of the second double bond no correlations to the *ee* values are found. Therefore, the structures, thermodynamics and kinetics of dienamine intermediates in S_N-type reactions are investigated. The NMR studies show that the preferred dienamine conformation provides an effective shielding if large electrophiles are used. Calculations at SCS-MP2/CBS-level of theory and experimental data of the dienamine formation show kinetic preference for the *Z*-isomer of the second double bond and a slow isomerization toward the thermodynamically preferred *E*-isomer. Modulations of the rate determining step by variation of the concentration of the electrophile, allow the conversion of dienamines to be observed. With electrophiles a faster reaction of *Z*- than of *E*-isomers is observed experimentally. Calculations corroborate these results by correlating *ee* values of three catalysts with the kinetics of the electrophilic attack and reveal the significance of CH-π and stacking interactions in the transition states. Thus, for the first time a comprehensive understanding of the remote-stereocontrol in γ-functionalization reactions of dienamines and an explanation to the "*Z/E*-dilemma" are presented. The combination of bulky catalyst subsystems and large electrophiles provides a shielding of one face and causes different reactivities of *E/Z*-dienamines in nucleophilic attacks from the other face. Kinetic preferences for the formation of *Z*-dienamines and their unfavorable thermodynamics support high *ee* values.

2.2 Introduction

Remote-stereocontrol is a noble goal in asymmetric catalysis but a challenge in understanding and design. Prominent examples for the application of this remote-stereocontrol in organocatalysis are found in dienamine,[1–3] trienamine[3,4] and tetraenamine[3,5] transformations. In some of these reactions, very high *ee* values were reported, and for the sterically demanding Diels-Alder type reactions, a plausible reaction mechanism was proposed.[2,6] However, for S_N-type γ-functionalization of dienamines detailed mechanistic studies and experimental insights into the underlying mechanism are, to our knowledge, very limited. This may obviously hamper the further development of the field. The main points under question are the partial shielding of the catalyst moiety and the "*Z/E*-dilemma" of the second double bond in linear aldehydes (see Figure 1) similar to the "*Z/E*-dilemma" known for iminium ion catalysis.[7]

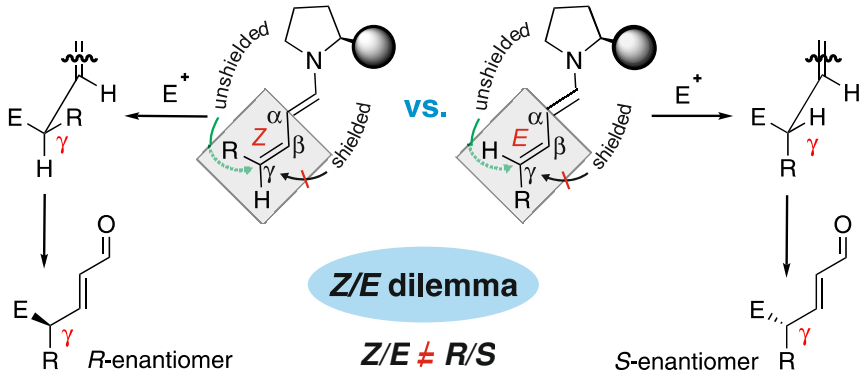

Figure 1. "*Z/E*-dilemma" in dienamine catalysis, i.e., the correlation between the *Z/E*-ratio of the second double bond and the *R/S*-ratio of the products is in dispute.

The dienamine catalysis, which is closely related to the enamine catalysis, has emerged as one of the most promising stereoinducing catalytic models in the α- and γ-functionalization of unsaturated aldehydes.[1,2,8–13] This concept represents a vinylogous version of enamine activation, magnifies the nucleophilic character of the γ-carbon, and enables functionalization reactions of conjugated aldehydes at their α- or γ-position (Figure 2).[2] The first selective γ-functionalization of unsaturated aldehydes with Jørgensen-Hayashi-type catalysts[3,14–16] was presented by Jørgensen *et al.* in 2006.[2] Later, the principle of γ-functionalization of dienamines was extended to S_N1-type reactions with bis[4-(dimethylamino)phenyl]methanol as electrophile source by Christmann *et al.* in 2011.[12] In their study, mixtures of α- and γ-alkylated products were

obtained. For aldehydes, which are disubstituted at the γ-position, the α-alkylated aldehyde was observed as a major product, and in the case of monosubstituted aldehydes the γ:α ratio is inverse. For the γ-alkylation, high to moderate enantioselectivities were achieved (the longer the chain length of the aldehydes, the lower the *ee* values). Later in 2012, Melchiorre *et al.*[11] managed to circumvent these synthetic limitations associated with the geometry control and site selectivity by using α-substituted unsaturated aldehydes. Hence, the formation of α-product is completely suppressed in this case.

In the field of secondary aminocatalysis, especially in the fields of enamine[17–26] and iminium ion activation,[7,27–31] recently some mechanistic insights could be gained in terms of intermediate stabilization, stereoselection modes, and reaction mechanisms. In the first dienamine study[2] already structural properties of the diene system (*E,s-trans,E* and *E,s-trans,Z*, including a *Z/E*-ratio for the second double bond of 2/1) were solved by NMR. For α-substituted dienamines, Melchiorre *et al.* characterized the diene system using NMR analysis and theoretical calculations.[11] In contrast to linear dienamines (*Z/E* = 2/1), α-substituted ones showed exclusively an *E* configuration of the second double bond and both isomers (*E* and *Z*) of the first double bond. This inverted structural preference of the second double bond resulted also in an inversion of the stereocenter at the γ-position of the major product. However, neither in cycloadditions nor in S_N-type reactions, the *Z/E*-ratios fit to the experimental *ee* values, if a classical shielding model is assumed. Therefore, it became even more pressing to rationalize the correlation between the *Z/E*-ratio of the second double bond and the stereochemical outcome.

A potential explanation to this phenomenon is the different stabilization of the transition states toward the two downstream iminium ion intermediates. Indeed, computational studies revealed a kinetically controlled [4+2] Diels-Alder reaction pathway with interactions in the product iminium ion transition state controlling the stereochemical outcome of the reaction.[2,6] In the case of diethyl azodicarboxylate (DEAD) as electrophile, a downstream isomerization of the double bond in the product was proposed to be responsible for the synthetically observed γ-functionalized unsaturated aldehydes.[2,32] For other [4+2] cycloadditions of dienamines, the higher stabilization of the zwitterionic *endo*-iminium intermediate and the corresponding reaction pathway was identified to be responsible for the high stereoselectivity.[6] Furthermore, a computational study of a [5+2] cycloaddition using squaramide-derived bifunctional organocatalysts (providing a preorganization of the electrophile by hydrogen bonds) corroborated the importance of configurational preferences and π-π interactions within the transition states for the diastereomeric ratio.[33] However, for S_N-type reactions of dienamines, it is

still unclear how the stereoselectivity is connected to the *Z/E*-ratio. Furthermore, *in situ* reaction monitoring of dienamine reactions revealing potential time dependences of the *Z/E*-ratios or a faster reaction of *E*- or *Z*-dienamine with electrophiles has not been performed so far.

Therefore, here we present a detailed NMR study of all structural features of dienamines (including the conformation of the catalyst subsystem) validating our computational studies of the dienamine ground states. In addition, theoretical studies of the dienamine reaction pathway were underpinned and compared with experimental kinetic studies of the formation and conversion of various dienamines, which were enabled by intentional shifts of the rate-determining step. With these methods, we gained detailed insights into the stereoselection mode of S_N-type dienamine reactions and could explain the "*Z/E*-dilemma".

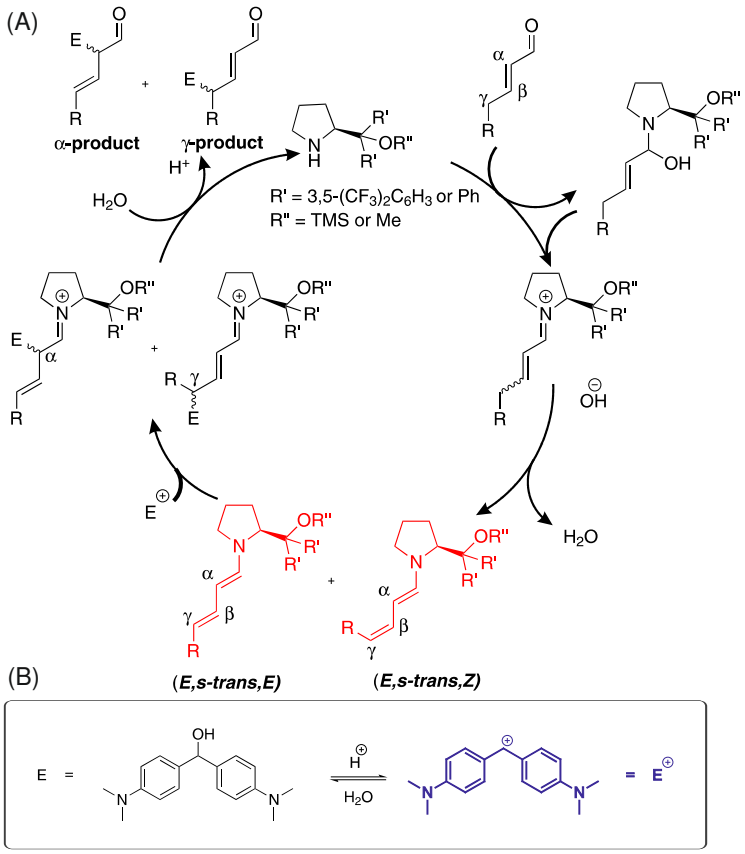

Figure 2. S_N-type dienamine reaction. (A) Proposed catalytic cycle based on previous publications.[2,11,12] (B) Acid-catalyzed equilibrium between the electrophile source E = bis[4-(dimethylamino)phenyl]methanol (Michler's hydrol) and the corresponding electrophile E^+.[34,35]

2.3 Results and Discussion

2.3.1 Model System and Theoretical Levels

To investigate the structural preferences, intermediates, and stereoselection modes in S_N-type dienamine reactions, we selected as model reaction the γ-alkylation of α,β-unsaturated aldehydes with bis[4-(dimethylamino)phenyl]methanol **E** (Figure 2B). As catalysts Jørgensen-Hayashi prolinolethers[15,16,36] **A-C** (Figure 3B) were chosen, since they are known in dienamine catalysis to result in high *ee* values and good yields.[1,2,11,12] In addition, we were experienced in the structural elucidation of intermediates using these catalysts from our enamine studies.[22–26] To reduce the amount of α-substituted product,[12] γ-methyl substituted (4-methyl-2-pentenal **4**) and linear α,β-unsaturated aldehydes ((*E*)-2-pentenal **1**, (*E*)-2-heptenal **2**, (*E*)-2-decenal **3**) with different chain lengths were selected. This leads to a modulation of steric and electronic properties. α-Substituted aldehydes were omitted due to their exclusive *E*-configuration of the second double bond. Therefore, they do not allow an insight into the correlation between *Z/E*-isomerization of the second double bond and its influence on the stereoselectivity.[11] Bis[4-(dimethylamino)phenyl]methanol **E** (Figure 2B), also known as Michler's hydrol, was chosen as electrophile source. It is known to form stabilized carbocations $\mathbf{E^+}$ under acidic conditions (Figure 2B).[34,35] By varying the acidity of the additive, the amount of active electrophile $\mathbf{E^+}$ can be controlled (for UV/Vis-spectra see Supporting Information). In addition, a Diels-Alder pathway is excluded, since the carbocationic species (E^+ see Figure 2B) reacts as an electrophile with nucleophilic reagents such as dienamines.[11,12,35] As the solvent toluene was chosen, because it is the preferred solvent in synthesis for this reaction type.[2,11,12] In this NMR study exclusively dienamines (***E/Z*-1A-C**, ***E/Z*-2C**, ***E/Z*-3C**, **4C)** (*E* and *Z* indicates the configuration of the second double bond, see the Structure of Dienamines section) were detected as intermediates. The iminium ion or aminol species proposed in the catalytic cycle (see Figure 2A) were below the detection limit. High-level quantum chemical calculations (SCS-MP2/CBS; see computational details and Supporting Information) on dienamines were conducted and compared to the experimental data. In addition, the potential influence of iminium ion species on the reactivity and selectivity was investigated by theoretical calculations.

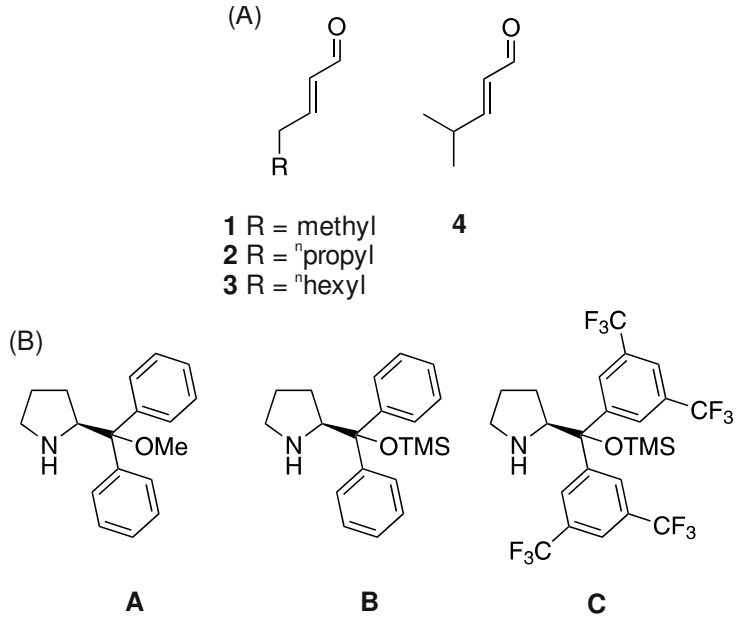

Figure 3. Model systems for structural studies and reaction monitoring. (A) aldehydes **1-4**; (B) Jørgensen-Hayashi type catalysts **A-C**.

2.3.2 Structure of Dienamines

First, the formation and structures of the dienamine species were investigated by NMR analysis with samples of 1 equiv of catalyst and 1 equiv of aldehyde in toluene-d_8 at 180-300 K (Figure 3).

During our investigations, we were able to detect dienamines ***E/Z*-1A-C**, ***E/Z*-2C**, ***E/Z*-3C** and **4C**. The following structural analysis was performed for every dienamine. Generally, all dienamines show the same structural pattern regarding *E/Z*-configuration and conformation of the catalyst subsystem. Therefore, for the sake of clarity in the following discussion, only *trans*-2-pentenal **1** with catalyst **C** is described in detail (for other structural analysis see Supporting Information). For the description of the structural motif of these isomers, first the diene subsystem is discussed and then the structure of the catalyst subsystem.

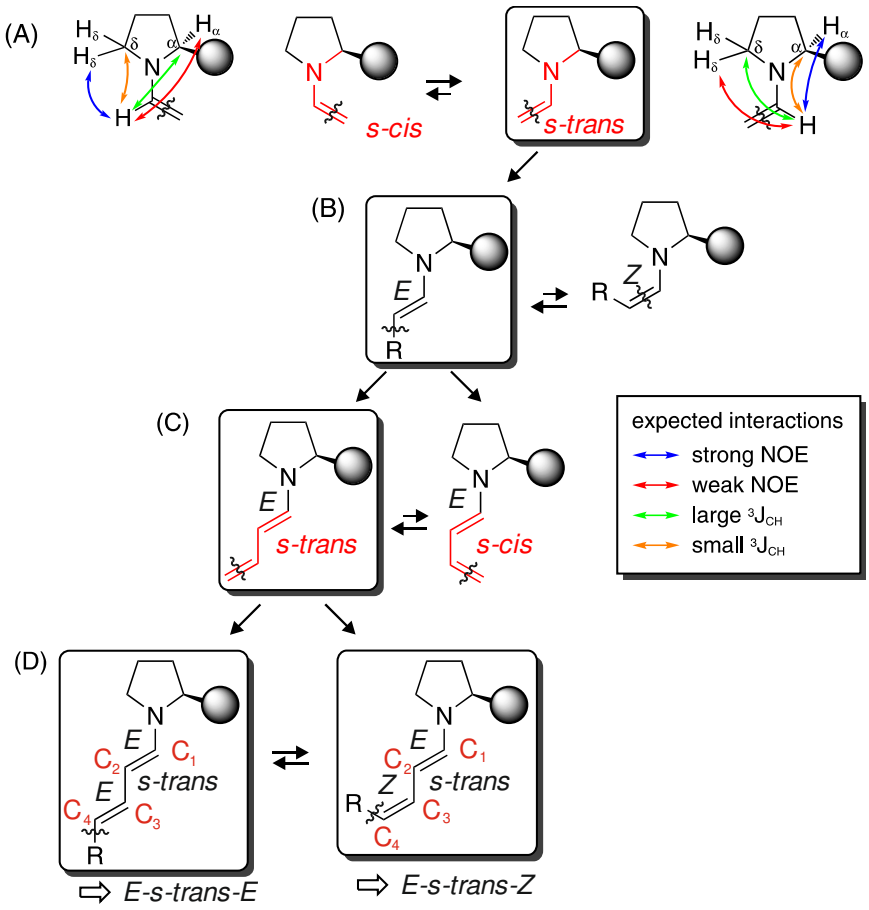

Figure 4. Structural preferences of the diene subsystem. The conformations/ configurations detected by NMR and the corresponding nomenclature are highlighted by boxes. For details, see text.

In the diene subsystem (Figure 4), the first N-C1 single bond can principally adopt two conformations (*s-trans, s-cis).* However, similar to the structural preferences of enamines with catalysts **A-C**,[23] exclusively the *s-trans* conformation is identified in solution for dienamines. This can be confirmed by strong NOE signals between H_1 and H_α, weak interactions between H_1 and $H_{\delta 1,2}$ as well as large $^3J_{CH}$ couplings between H_1 and C_δ (see Supporting Information). The structural preferences of the C_1-C_2 double bond and the C_2-C_3 single bond were determined by $^3J_{HH}$ coupling constant analysis. For the C_1-C_2 double bond, $^3J_{HH}$ coupling constants of 13.2 to 13.5 Hz were found. In agreement with previous NMR studies,[11] theoretical calculations,[2] and our studies of enamines,[22–25] this indicates *E* configured C_1-C_2 double bonds for all dienamine systems under investigation (for $^3J_{HH}$ see Supporting Information). The C_2-C_3 single bond showed smaller $^3J_{HH}$ couplings in the range of 10.3 to 11.3 Hz (see Supporting Information). These values are in good agreement with other literature known examples for *s-trans* diene systems

(10.4-11.2 Hz).[37–39] The first variability within the diene system of the two isomers is related to the configuration of the second double bond between C_3 and C_4 (Figure 4D). Dependent on the length of the alkyl moiety attached to the diene system and on the catalyst applied, *Z/E*-ratios between 0.88 and 2.16 were detected (***Z/E*-1A** = 1.9/1; ***Z/E*-1B** = 2/1; ***Z/E*-1C** =2.16/1; ***Z/E*-2C** = 1.04/1; ***Z/E*-3C**= 0.88/1; for details see Supporting Information).

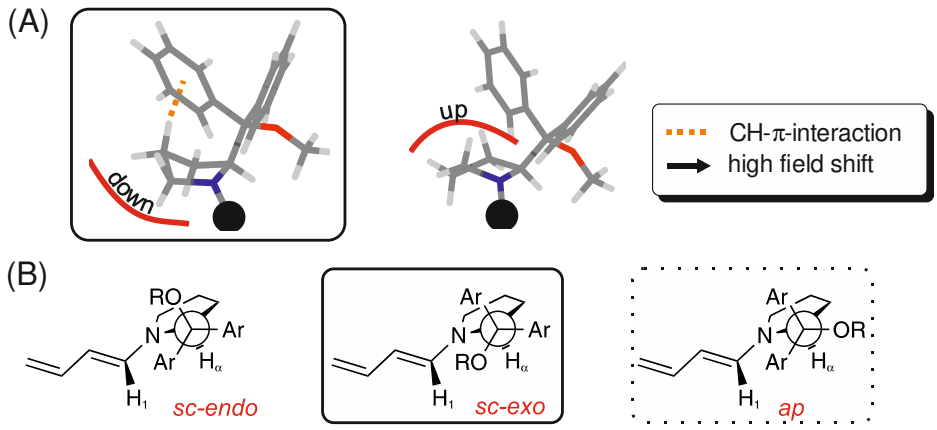

Figure 5. Structural preferences of the catalyst subsystem. The boxes highlight the experimentally found preferences for the puckering of the proline ring as well as for the exocyclic bound moiety of the catalyst. The dashed box indicates a population of *ap* conformer predicted by theoretical calculations.

Next, we investigated the structural and conformational preferences of the catalyst moiety. The exocyclic bond of the catalyst can adopt three conformations, namely *sc-endo*, *sc-exo* and *ap* (see Figure 5B).[23] Using similar structural NMR investigations as previously applied for enamine intermediates with catalysts **A-C**,[23,40] we found the same *down*-puckering of the pyrrolidine ring indicated by an $H_{\gamma 2}$ highfield shift in dienamines in comparison to the free catalyst (see Figure 5A; $\Delta\delta$ ($H_{\gamma 2}$) = -0.54 to -0.79 ppm; for details see Supporting Information). This shift is caused by CH-π-interactions of the aromatic moieties of the catalyst and $H_{\gamma 2}$ in the *sc-exo* or *ap* arrangement. Quantum chemical calculations of the Boltzmann averaged dienamine structures corroborate these experimental data. The Gibbs free energy of *sc-endo* is about 33 kJ/mol above the global minimum at SCS-MP2/CBS level of theory and therefore thermally not populated at our reaction conditions. The NOESY spectra of all investigated dienamine systems showed interactions between H_1 and the protons of the O-protecting group, which is only

plausible in the *sc-exo*-conformation. Theoretical distance calculations for ***E/Z*-1C** showed an NOE-averaged distance of H_1 to H_{OTMS} of 6.00 Å for *ap* and 3.47 Å for *sc-exo*. Using NOESY measurements, the experimental averaged distance between these nuclei was calculated to be 3.80 Å (see Supporting Information for the equation). The detection of this key NOE proves positively the existence of the *sc-exo* conformation. The larger distance is a potential hint for the coexistence of *ap*-conformers, however the experimental error of the NOE in our case does not allow for reliable quantification. The related theoretical calculations predicted almost the same energy for *sc-exo* and *ap* ($\Delta G_{exo\text{-}ap}$ = -0.9 kJ/mol for ***E*-1C**), which is a second indication for the presence of the *ap* conformation in solution.

Subsequently, the shielding of the diene subsystem was investigated by theoretical structure calculations including the experimentally determined preferences discussed above. The calculated 3D models (Figure 6) showed a shielded face of the first double bond within the diene systems (α-position), which hinders an attack of an electrophile comparable to the shielding of the α-position in enamine catalysis.[14] The second double bond (γ-position) is only partially shielded, leading to the problem of remote stereocontrol in dienamines. This partial shielding makes it highly probable that the size of the electrophile influences the effectiveness of the catalyst shielding. Thus, for small electrophiles only poor stereoselectivities are expected. For bulky electrophiles, the partial shielding should be much more effective. Indeed, in dienamine reactions with Michler's hydrol derivatives as electrophiles (bulky electrophiles), high *ee* values were reported for α-substituted enals[11] and our model system *trans*-2-pentenal **1**,[12] whereas to our knowledge, for very small electrophiles high stereoselectivities have not been reported so far. This structural analysis is in agreement with our theoretical calculations of an electrophilic attack from the shielded face in γ-position. The calculated energy barriers (approximately 80 kJ/mol) for an attack in γ-position of both dienamines (***E*-** and ***Z*-1C**) on the carbocationic species $\mathbf{E^+}$ is substantially higher than those of the attack from the unshielded face (44–49 kJ/mol). That means for large electrophiles such as Michler's hydrol, the partially shielded face of dienamine structures is kinetically not accessible even in the γ position (Figure 6).

One consequence of these combined experimental and theoretical investigations is that the reported *ee* value in dienamine catalysis with Michler's hydrol has to originate from a stereodiscrimination between the attack either on *E*-dienamine or *Z*-dienamine from the unshielded face. For our catalyst **C** with *trans*-2-pentenal **1**, a *Z/E*-ratio of 2/1 was found experimentally. This distribution of isomers was already observed before by Jørgensen *et al*.[2] In the case, both *E*- and *Z*-dienamines would react with the electrophile via an

isoenergetic barrier, this *Z/E*-ratio of 2/1 would result in an *ee* value of 33%. However, as shown in our work and also in literature, *ee* values of around 92% are obtained for this reaction (Figure 6).[12] In principle, this deviation between structure related and experimental *ee* values can have two possible causes; first, the experimentally observed *Z/E*-ratio deviates drastically from that active in the catalysis (kinetic versus thermodynamic control) or second, the activation barriers from *E*-dienamine and *Z*-dienamine deviate significantly in their downstream reactions. Of course, also combinations of both reasons are highly probable.

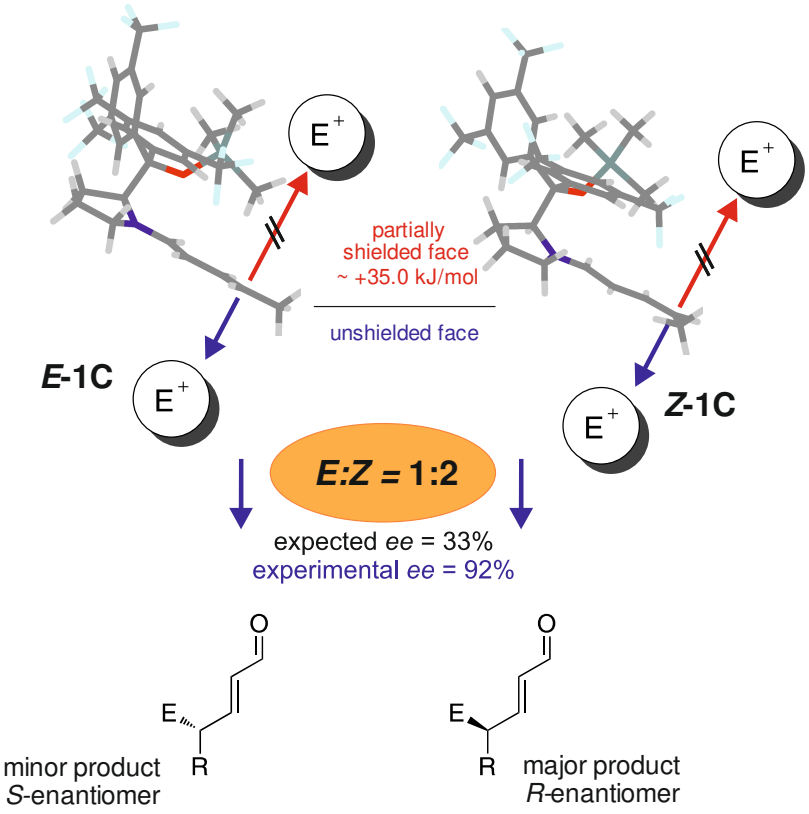

Figure 6. Shielding and remote stereocontrol in dienamines. Top: 3D models of dienamine ***E/Z*-1C** show a partially shielded face from the top side. For bulky electrophiles this partial shielding is sufficient to block electrophilic attacks even in the γ-position (~35 kJ/mol higher energy barriers); Bottom: kinetically preferred attack of both isomers from the unshielded face yielding different enantiomers. Black: expected *ee* value, if both isomers (*E/Z* = 1/2) react with same rate. Blue: experimental *ee* values.

2.3.3 Enantioselectivity and Kinetic Control

To examine the origin of the so far unexplained stereoselection mode of the electrophilic attack in γ-position of dienamines from the unshielded face including also the *Z/E*-ratio, we investigated the kinetics and thermodynamics of dienamine formation and the conversion with Michler's hydrol by NMR and theoretical calculations.[41] First, the formation rates of *Z*-dienamines versus *E*-dienamines were addressed. Under experimental conditions typically used in synthesis, the formation of dienamines is the rate-determining step followed by a fast addition of the electrophile (see discussion below). In these setups, dienamines cannot be detected by NMR. Therefore, our structural investigations of the dienamines were previously performed exclusively without electrophile. A kinetically controlled extremely high *Z/E*-ratio (about 24/1 for an *ee* value of 92%) combined with a subsequent fast isomerization toward the thermodynamic ratio of *Z/E* could therefore easily explain the deviation between the *ee* values obtained in synthesis and the *Z/E*-ratio observed in NMR studies.

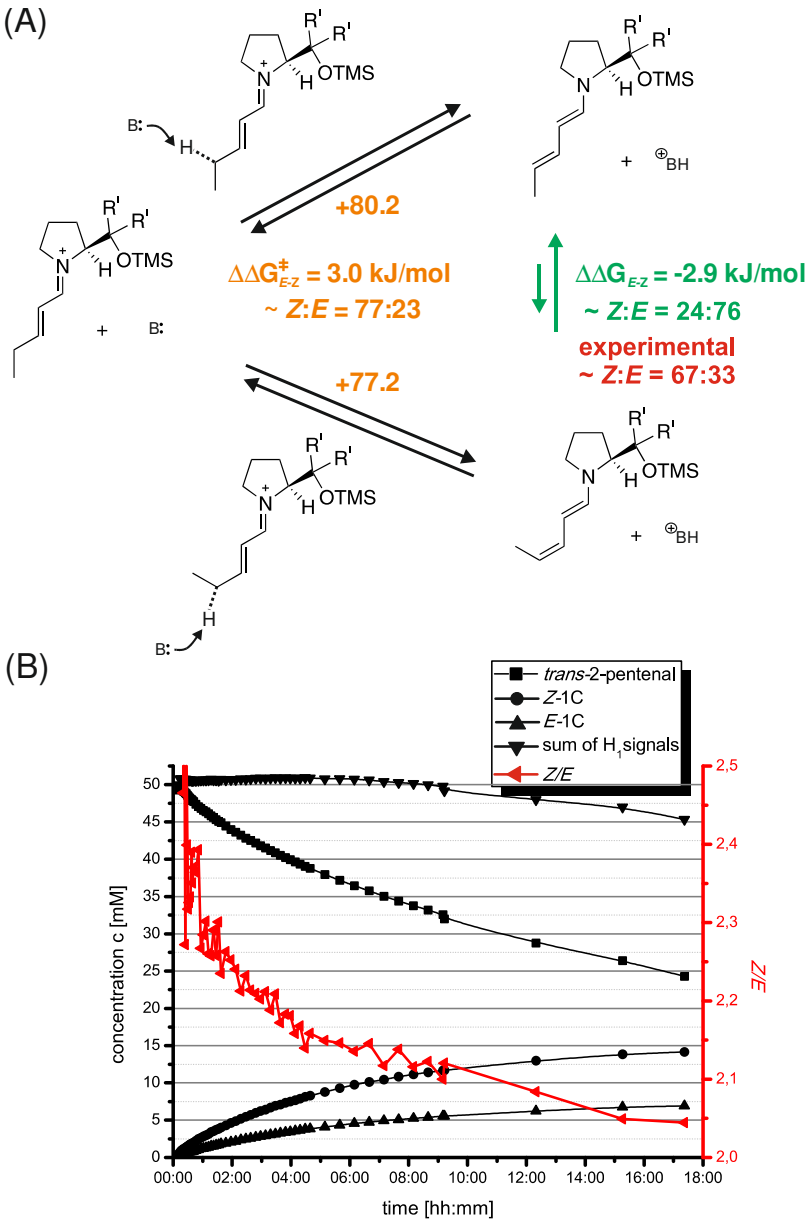

Figure 7. Kinetic control of the *Z*/*E*-ratio of dienamines; (A) Theoretically predicted barriers of dienamine formation from iminium ion precursors agree very well with the experimental values, whereas the thermodynamic distribution of the dienamine ***E*/*Z*-1C** is inverse. All energies are depicted in kJ/mol. (B) NMR reaction profiles of dienamine formation of ***E*/*Z*-1C** revealing a slow but significant change of the *Z*/*E*-ratio support the kinetic preference for *Z* followed by a slow isomerization to *E* (**1** (1 equiv) and **C** (1 equiv) without acid at 300 K in toluene-d_8).

The NMR determined *Z/E*-ratio of the double bond between C_3 and C_4 in all investigated dienamines showed an uncommon high amount of *Z*-isomer (up to a *Z/E*-ratio of 2.16:1 for ***E/Z*-1C**; for the time of determination see Supporting Information). This deviates clearly from previous[2] and our current theoretical calculations of the relative dienamine ground state energies (here with *trans*-2-pentenal **1** as aldehyde), which suggested that the *E*-isomer is marginally more stable than the *Z*-isomer by 0.6 kJ/mol for catalyst **B** to 2.9 kJ/mol for catalyst **C**. The latter (dienamine ***E/Z*-1C**) corresponds to a thermodynamic *Z/E*-ratio of 24:76 (see Figure 7A). This is in good agreement with the work of Jørgensen *et al*. at a lower level of theory (B3LYP/6-31G(d))[2] and indicates a kinetic preference for *Z*-dienamines. Our current calculations showed that the transition state for the deprotonation of iminium ion precursors with a base catalyst model ((*S*)-2-(methoxymethyl)pyrrolidine) leading to *Z*-dienamine is lower by 3 kJ/mol than to *E*-dienamine. A close inspection of the transition-state structures reveals higher steric hindrance in case of the *E*-dienamine as the most probable reason for this energy difference. The lower barrier for the formation of *Z*-dienamine is also predicted when NMe_3 is used as deprotonating agent, which would indicate that the choice of the base is rather insignificant. According to Eyring theory, this energy difference in barrier heights corresponds to a 3.3-fold faster formation of *Z*-dienamine compared to *E*-dienamine, which is similar to the observed ratio of 2/1 for *Z/E* (Figure 7A).

To prove experimentally that the *Z/E*-ratio is kinetically driven and that the *E*-isomer is the thermodynamic product, we investigated the isomerization of the second double bond toward the thermodynamic equilibrium. For this purpose ^{1}H kinetic NMR measurements of the reaction of *trans*-2-pentenal (aldehyde **1**) and catalyst **C** at different temperatures and under the influence of acid were carried out. At 300 K and without acidic additive (Figure 7B) the dienamine formation for ***E/Z*-1C** showed a decrease of *Z/E*-ratio with time (for identical measurements at higher temperatures and/or with acid, accelerated both isomerization and polymerization; see Supporting Information). The final thermodynamic equilibrium was not reached, due to emerging polymerization after around 9 h, visible on the decay of the sum of signal intensities in Figure 7B. Nevertheless, the slow but significant change of the *Z/E*-ratio toward higher amounts of *E* during the initial part of the reaction is in close agreement with the theoretical predictions. The very slow isomerization process lasting for hours in combination with an observed *Z/E*-ratio higher than the theoretically predicted one corroborates a significant kinetic preference of *Z* followed by the isomerization toward *E*, the thermodynamic preference. In addition, both experiment and calculations exclude extremely high

amounts of *Z*- dienamines during the dienamine formation. Thus, an additional factor has to contribute to reach the high *ee* values observed in synthesis.

Therefore, the downstream reactions of the dienamines were investigated next, and further experimental and theoretical investigations of the conversion of the dienamines with the electrophile were performed. The energy barriers (black and red lines) for the conversion to the γ-product (49.6/44.0 kJ/mol) were significantly smaller than for the dienamine (***E*/*Z*-1C**) formation (80.2/77.2 kJ/mol) (Figure 8A). The calculated energy barrier difference translates to several orders of magnitudes in reaction rates, which means the dienamine species is not detectable in solution in the presence of a sufficient amount of electrophile (Figure 8B; using TFA). In an S_N1 reaction (first order by nature), the RDS (rate-determining step) is generally the generation of the carbocation, and therefore its concentration is significantly lower than the nucleophile. As soon as the amount of electrophile equals/exceeds the amount of nucleophile (dienamines), the reaction is dependent on the concentration of both reactants. In the presence of strong acids, the hydrolysis of the hydrol is accelerated, the thermodynamic equilibrium is shifted providing higher concentration of E^+, and the reaction becomes second order. Thus, the reaction cannot be assigned as a classical "S_N1", and the dienamine formation seems to be the RDS. Due to the very fast conversion of dienamines, it is not possible to investigate deviating reaction rates of *Z*- and *E*-dienamines experimentally. Therefore, it was crucial for further experiments to reduce significantly the rate of the electrophilic attack by lowering the concentration of E^+. This has the consequence that now the nucleophile (dienamine) concentration is significantly higher than the electrophile concentration, and the rate-determining step is exclusively the generation of the electrophile (classical S_N1). The pK_a dependency of the generation of the electrophile is schematically represented in Figure 8A by the chemical equilibrium. The amount of active electrophile is varied by using the different acids (see Supporting Information for UV/Vis-spectra). Depending on the acid, the reaction order can be modulated, which leads to a shift of the RDS to the carbocation formation step. This is proven by the simultaneous detection of dienamines and products by NMR (Figure 8C; using AcOH).

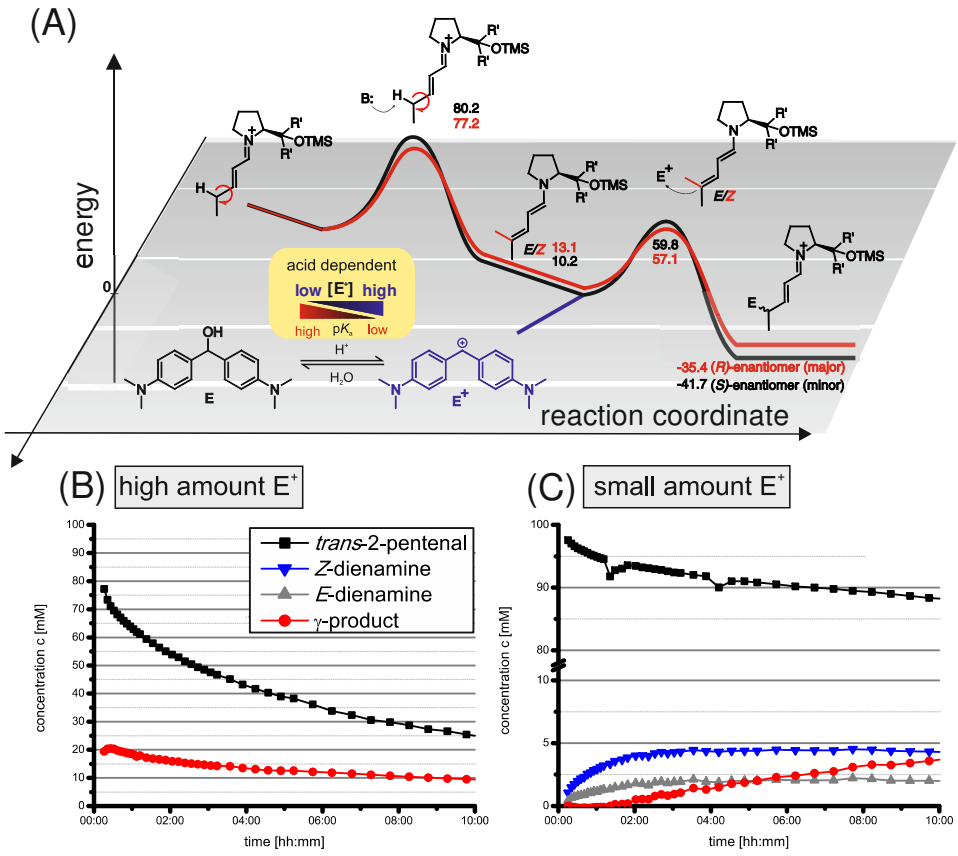

Figure 8. Energy profiles of dienamine reactions and modulation of the RDS by variation of the electrophile concentration. (A) Calculated free energy surfaces (ΔG_{298}) (black ***E*-1C** and red ***Z*-1C** line) at SCS-MP2/CBS level of theory, and schematic acid dependent generation of carbocation E^+. (B and C) The NMR reaction profiles show the shift of the RDS; with TFA, no dienamines are detected (B), whereas with acetic acid, both dienamines are observable (C) (aldehyde **1** (2 equiv), catalyst **C** (0.2 equiv), Michler's hydrol (1 equiv), and TFA or acetic acid (0.1 equiv) at 313 K in toluene-d_8.

An experimental setup with weak acid (AcOH) now allows for the investigation of the relative reactivity of *E*- and *Z*-dienamines with electrophile. In addition to the *Z*/*E*-ratio, the difference in reactivity toward electrophile is proposed as a second factor, which affects the observed *ee* values.

In the case of a kinetically controlled preference of the *Z*-isomer in the electrophilic attack, its amount has to decrease faster than *E*. However, in Figure 8C, both dienamines remain constant after reaching a maximum (4 h). The profile can be explained by the consumption of the free catalyst, which reduced the rate of the dienamines formation. After 4 h the rates of dienamines formation and conversion are comparable leading to a steady state. To prove the kinetic preference of *Z*-dienamines

toward electrophile experimentally, kinetic measurements with higher amount of catalyst (1 equiv) and acetic acid (1 equiv) were performed (Figure 9). The adapted stoichiometric ratio provides two advantages. First, it increases the amount of the dienamines and simplifies the detection. Second and more importantly, both formation and conversion of dienamines are accelerated. After a short offset (4 h), the conversion to the γ-product is faster than the dienamine formation due to the higher concentration of electrophile E^+, which is indicated by the decrease of both dienamines. Despite the faster formation of *Z*-dienamine than *E*-dienamine, the faster conversion of *Z*-dienamine is now observable.[42] This reveals a combination of preferred formation and conversion of *Z*-dienamines as origin of the *ee* values observed in synthesis.

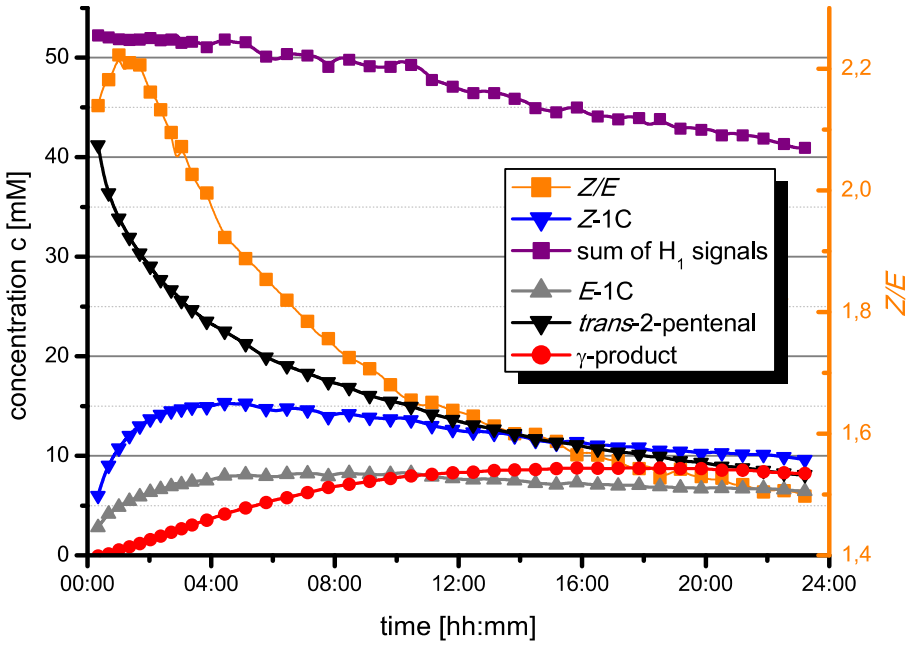

Figure 9. Reaction profile of dienamines ***E/Z-1C***, the resulting *Z/E*-ratio, and simultaneous γ-product formation, showing a faster consumption of *Z*-dienamine. Aldehyde **1** (1 equiv), catalyst **C** (1 equiv), Michler's hydrol (1 equiv), and AcOH (1 equiv) at 313 K in toluene-d_8.

Table 1. Calculated ΔΔG‡ Values [kJ/mol] (Boltzmann averaged) for Dienamine Electrophile Adduct Formation Step for ***E/Z*-1A-C** Translated to Reaction Rate Ratios According to the Eyring Equation and the Resulting Theoretical *ee* Values.[a]

Cat.	Z/E-ratio (approx.)	ΔΔG‡ [kJ/mol]	theor. reaction rate ratio *Z vs E*	theor. *ee*	exptl *ee*
A	2/1	1.89	2.1/1	36%	27%
B	2/1	3.13	3.5/1	56%	48%
C	2/1	5.60	9.5/1	80%	78%

[a] Experimental *ee* values derived from reaction of aldehyde **1** (2 equiv), catalyst **A-C** (0.2 equiv), Michler's hydrol (1 equiv), and acetic acid (0.1 equiv) at 313 K in toluene-d_8 after 24 h.

From these experimental data, the reason for the preferred electrophilic attack on *Z*-compared to *E*-dienamines is unclear. Therefore, further theoretical calculations of the electrophilic attack were conducted. For large electrophiles, the electrophilic attack from the partially shielded face is by far too high in energy (see Figure 6). Considering an exclusive attack from the unshielded side, the *E*-dienamine yields the *S*-enantiomer of the γ-substituted α,β-unsaturated product, whereas the *Z*-dienamine gives the *R*-enantiomer, which is the major product. As we have already shown, the higher population of *Z*-dienamine (~66%) cannot be solely responsible for the variation of the *ee* values, otherwise similar *ee* values across all investigated systems are expected (Table 1). Moreover, the NMR kinetic data shown in Figure 9 indicate a kinetically controlled product conversion preferably from *Z*-dienamine. Indeed, our current predictions showed that the transition state for the electrophile attack on the open face of ***E*-1A-C** is higher than on ***Z*-1A-C (**Boltzmann averaged 1.90-5.60 kJ/mol; for values of ***E/Z*-1C** see Figure 8A).[43]

The theoretical calculations showed that the differences in the free energy barriers (ΔΔG‡) between *Z* and *E* are the results of two effects: the higher thermodynamic stability of *E* compared to *Z* and the differences in dienamine-electrophile interactions in the transition states. Taken together, the calculations of the transition states corroborate the faster formation of the major product from *Z*-dienamine as shown experimentally.

To confirm the kinetic control of the stereoinduction, we determined the *ee* values of *trans*-2-pentenal **1** with Michler's hydrol using three different catalysts (**1** (2 equiv); **A-C** (0.2 equiv); Michler's hydrol (1 equiv); AcOH (0.1 equiv); 313 K in toluene). Despite of similar ***Z/E*-1A-C** ratios of the dienamines, the *ee* values between the catalysts vary strongly, with catalyst **C** being the most enantioselective and **A** the least (Table 1). If the kinetic control is valid, the free energy differences of the transition states for the iminium ion-electrophile adduct formation will correlate with the *ee* values. As shown in Table 1, the highest $\Delta\Delta G^{\ddagger}$ for ***E/Z*-1C** (5.6 kJ/mol) reflects the highest theoretical *ee* value (80%), while the lowest $\Delta\Delta G^{\ddagger}$ for ***E/Z*-1A** (1.90 kJ/mol) reflects the lowest *ee* value (36%). This means these values are in a very good agreement with the experimental *ee* values for the different catalysts.

Next, the kinetic and thermodynamic terms in the product formation step were decomposed to track the origin of the different energy barriers. As previously described, the ***E*-1A-C**-dienamines are thermodynamically slightly more stable than the ***Z*-1A-C** dienamines ($\Delta G_{Z\text{-}E}$(**B**)= 0.6 kJ/mol; $\Delta G_{Z\text{-}E}$(**A**)= 2.5 kJ/mol; $\Delta G_{Z\text{-}E}$(**C**) = 2.9 kJ/mol). Excluding the thermodynamics, the highest pure kinetic effect from the transition states is calculated for catalyst **C** ($\Delta\Delta G^{\ddagger}$-$\Delta G_{Z\text{-}E}$= 5.60 – 2.9 = 2.7 kJ/mol), while the lowest is estimated for catalyst **A** ($\Delta\Delta G^{\ddagger}$-$\Delta G_{Z\text{-}E}$= 1.9 – 2.5 = -0.6 kJ/mol). The positive value for **C** means that the transition state between *E*-dienamine and the electrophile is more unstable than the *Z*-dienamine, and vice versa for **A**. At first glance, the altering stability of the transition states is very puzzling, because both transition states possess the same conformational preference, (*ap*-conformation and *down*-puckering). Hence a precise structure analysis was performed.

From the structure analysis of the transition states, several distinctive interactions could be identified: (1) Stabilizing CH-π interactions between C_5 bound protons of the diene system (e.g. methyl group in ***E/Z*-1A-C**) and one of the aromatic rings of the electrophile (Figure 10A highlighted in yellow), which are present in all transition states of *Z*-dienamines but not in *E*-dienamines. This CH-π interaction seems to be a major factor, which stabilizes the transition state of ***Z*-1A-C**. (2) Stabilizing dispersive interactions (stacking), which extend from the diene system to the pyrrolidine moiety (Figure 10A). (3) Due to the dimension of the electrophile, the shielding group of the catalyst may still interact with the electrophile, either sterically or electrostatically. The magnitude of the stabilization effects is thus modulated by the arrangement between the electrophile and the dienamines. Remarkably, both the transition states of ***E/Z*-1C** exhibit an electrostatic interaction between the *meta*-trifloromethyl group and the aromatic protons of the electrophile (Figure 10B). This has the consequence that the electrophile is rotated in the

direction of the trifluoromethyl substituent. The displacement of the electrophile reduces the stacking interaction between the electrophile and the diene system, particularly in the transition state of ***E*-1C**. In total, the TS ***Z*-1C** showed better electrophile-dienamines interactions (2.7 kJ/mol) than the TS ***E*-1C**.

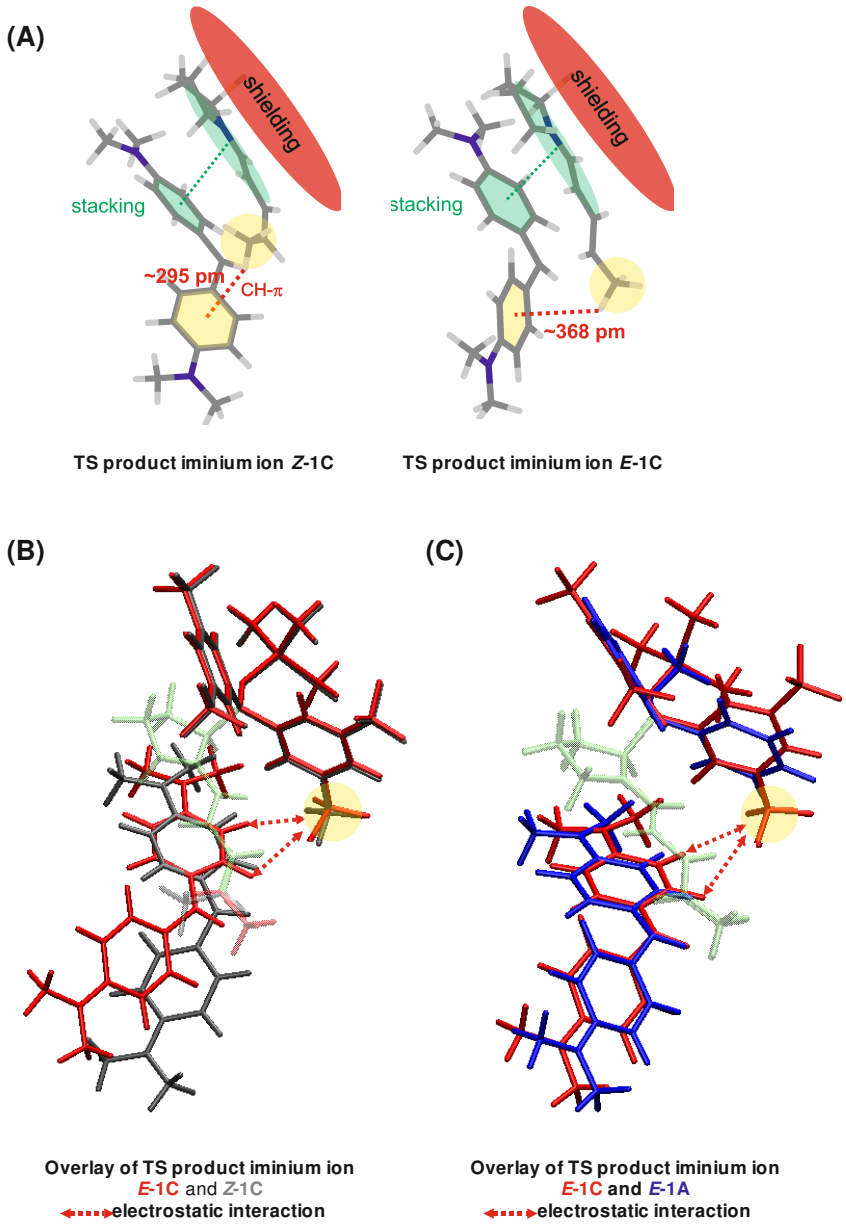

Figure 10. Transition states of iminium ion product formation and their intermolecular interactions: (A) a closer distance shows a stronger CH-π interaction in [E⁺-***Z*-1C**]‡; (B) The alignment of the two dienamines subsystems (green) reveals the different arrangements of the electrophile; (B and C) red dashed arrows show interactions between the CF_3 group and the electrophile; (C) catalyst dependent displacement of E⁺-***E*-1C** compared to E⁺-***E*-1A**.

In contrast, in the transition state of ***E*-1A**, such electrostatic interaction between the electrophile and the shielding moiety of the dienamine does not exist, and the electrophile is not displaced (Figure 10C). Therefore, the magnitude of the stacking interaction is considered to be equal for both ***E/Z*-1A**. In this case ***E*-1A** is becoming marginally more stable than ***Z*-1A** (-0.6 kJ/mol). In summary, the general preference of the conversion of *Z*-dienamines over *E*-dienamines seems to originate from stabilizing CH-π interactions in the transition state between *Z*-dienamine and electrophile. The significant differences of the *ee* values depending on the catalyst applied are caused by structural variations due to interactions between the aryl-substituents of the catalyst and the electrophile (Figure 11).

The main stereocontrol, being the iminium ion product formation, is in principle similar to the stereoselection mode proposed by Jørgensen *et al*. for Diels-Alder type reactions.[2] Interestingly, also the barriers for the γ-functionalization with DEAD are similar. Considering the variability of potential reaction pathways depending on the experimental conditions recently also shown for enamine reactions,[44,45] also the nucleophilic addition to DEAD seems to be possible. In Diels-Alder reactions with DEAD, the transition-state barrier of the product formation is significantly lower than the barrier of the nucleophilic addition.[2] However, in the former reactions a downstream isomerization of the product is necessary.

A recent computational study of [5+2]-cycloaddition reactions using squareamide-derived bifunctional organo-catalysts with structural preorganization revealed similar conformational preferences (pyrrolidine puckering, *E,s-trans*) and similar noncovalent interactions (e.g. π-π stacking) with respect to the formation of the stereocenter at the γ-position of dienamines.[33] Thus, independent of the system, weak dispersion interactions seem to be the key to high stereoselectivities in the dienamine catalysis. However, in our case, high stereoselectivities require additional kinetic preferences to overcome the *Z/E*-dilemma.

2.3.4 Computational Details

Geometry optimization and frequency analysis were performed with Gaussian09 version D.01[46] at DFT level of theory using hybrid metaGGA functional M06-2X-D3/def2-SVP in the gas-phase.[47–49] Subsequently, single point calculations were carried out with ORCA 3.0.3[50] at SCS-RIMP2/CBS level of theory using two points extrapolation procedure (see Supporting Information for details).[51] Solvent correction in toluene was estimated using COSMO-SAC[52–54]as implemented in CRS module of ADF2014[55–57]with COSMO potential generated by Gaussian09 version D.01.

2.4 Conclusion

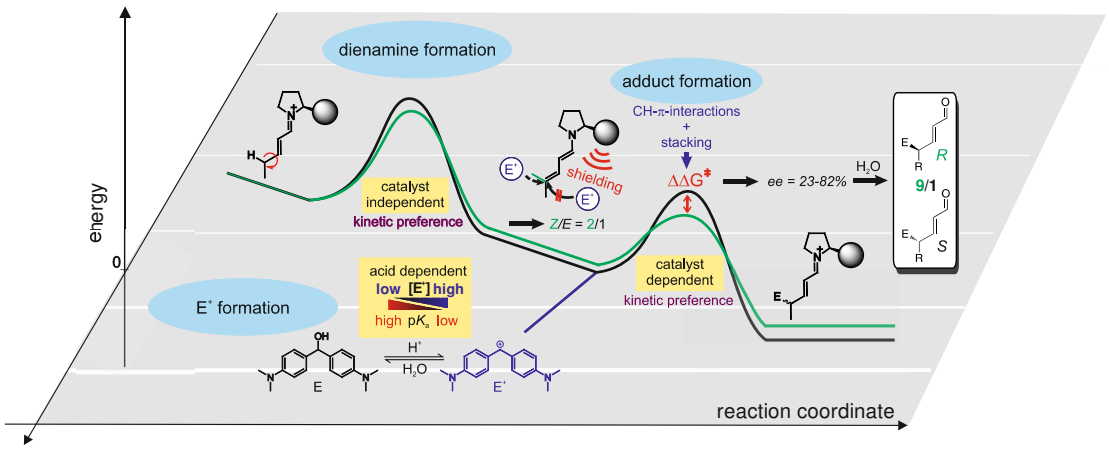

Figure 11. Schematic overview of all investigated reaction features: kinetic preference of *Z*-dienamine formation, effective shielding of the top side and catalyst dependent reaction barriers (ΔΔG‡) for electrophile-adduct formation including a kinetically controlled conversion of *Z*-dienamines and the resulting *ee* values.

To summarize, for the first time the conformational preferences of dienamine intermediates with Jørgensen-Hayashi prolinol ether catalysts were fully characterized by NMR spectroscopy. Similar to enamines, dienamines exhibit in the catalyst moiety *down*-puckering of the pyrrolidine ring and a preference for *sc-exo* conformations. For linear aldehydes, the first double bond is connected via an *s-trans* conformation and is *E* configured. For the second double bond, connected via *s-trans* conformations, the preference for *Z* configurations was confirmed. These structural studies were

underpinned by theoretical calculations of the whole reaction pathway, kinetic NMR studies, and a shift of the rate-determining step by variation of the electrophile concentration. For the first time both the stereoinduction mode of dienamines in S_N-reactions and the "*Z/E*-dilemma of the second double bond" were explained (i.e., the missing clear correlation between the *Z/E* ratio and the *ee* values). In the case of large electrophiles, the partial shielding of the double bond by the catalyst is sufficient to effectively block attacks even in γ-position. As a result, the *ee* values for γ-functionalization has to correlate directly with the reaction profiles of the corresponding *Z*- and *E*-dienamines. Here, three aspects intertwine: the kinetic preference for the formation of *Z*-dienamines, the higher thermodynamic energy level of *Z*-dienamines, and the lower activation barrier for electrophile attacks from *Z*-dienamines. Theoretical studies corroborate for the first time a similar kinetic preference of *Z*-dienamine formation observed in experiments for all catalysts investigated. The main stereodiscrimination is effective in the second step, the electrophile adduct formation. Advantageous CH-π interactions between *Z*-dienamines and the electrophile in the transition state of product iminium ion formation seem to cause faster conversions of *Z*-dienamines in general. Depending on the structure of the catalyst, different interactions between its aryl moieties and the electrophile are observed modulating the stacking between the pyrrolidine/diene and the electrophile. These structural modulations determine the level of the *ee*.

The secret of the highly effective remote stereocontrol in dienamines with *Z/E* variability of the second double bond is thus a delicate interplay of substrate, catalyst, and electrophile structure. Two factors promote high *ee* values: a high *Z/E* dienamine ratio and an effective stereodiscrimination in the product iminium ion formation. From our studies, the *Z/E*-ratio can be enhanced by employing short unsaturated aldehydes. Large electrophiles in combination with bulky interacting catalyst structures support an effective catalyst shielding and high stereodiscrimination for attacks from the unshielded face.

In Diels-Alder as well as S_N-type reactions, the key to high stereoselectivity in the γ-functionalization is the intermolecular interaction in the "product iminium ion transition state". In the case of DEAD as electrophile, an alternative pathway via nucleophilic addition, which is energetically comparable to S_N-type reactions, would allow γ-functionalization without downstream isomerization of the product.

2.5 References

(1) Ramachary, D. B.; Reddy, Y. V. *Eur. J. Org. Chem.* **2012**, *2012*, 865.

(2) Bertelsen, S.; Marigo, M.; Brandes, S.; Dinér, P.; Jørgensen, K. A. *J. Am. Chem. Soc.* **2006**, *128*, 12973.

(3) Donslund, B. S.; Johansen, T. K.; Poulsen, P. H.; Halskov, K. S.; Jørgensen, K. A. *Angew. Chem. Int. Ed.* **2015**, *54*, 13860.

(4) Jia, Z.-J.; Jiang, H.; Li, J.-L.; Gschwend, B.; Li, Q.-Z.; Yin, X.; Grouleff, J.; Chen, Y.-C.; Jørgensen, K. A. *J. Am. Chem. Soc.* **2011**, *133*, 5053.

(5) Zhou, Q.-Q.; Xiao, Y.-C.; Yuan, X.; Chen, Y.-C. *Asian J. Org. Chem.* **2014**, *3*, 545.

(6) Johansen, T. K.; Gómez, C. V.; Bak, J. R.; Davis, R. L.; Jørgensen, K. A. *Chem. Eur. J.* **2013**, *19*, 16518.

(7) Seebach, D.; Gilmour, R.; Grošelj, U.; Deniau, G.; Sparr, C.; Ebert, M.-O.; Beck, A. K.; McCusker, L. B.; Šišak, D.; Uchimaru, T. *Helv. Chim. Acta* **2010**, *93*, 603.

(8) Han, B.; Xiao, Y.-C.; He, Z.-Q.; Chen, Y.-C. *Org. Lett.* **2009**, *11*, 4660.

(9) Jurberg, I. D.; Chatterjee, I.; Tannert, R.; Melchiorre, P. *Chem. Commun.* **2013**, *49*, 4869.

(10) Marqués-López, E.; Herrera, R. P.; Marks, T.; Jacobs, W. C.; Könning, D.; de Figueiredo, R. M.; Christmann, M. *Org. Lett.* **2009**, *11*, 4116.

(11) Silvi, M.; Cassani, C.; Moran, A.; Melchiorre, P. *Helv. Chim. Acta* **2012**, *95*, 1985.

(12) Stiller, J.; Marqués-López, E.; Herrera, R. P.; Fröhlich, R.; Strohmann, C.; Christmann, M. *Org. Lett.* **2011**, *13*, 70.

(13) Talavera, G.; Reyes, E.; Vicario, J. L.; Carrillo, L. *Angew. Chem. Int. Ed.* **2012**, *51*, 4104.

(14) Jensen, K. L.; Dickmeiss, G.; Jiang, H.; Albrecht, Ł.; Jørgensen, K. A. *Acc. Chem. Res.* **2012**, *45*, 248.

(15) Marigo, M.; Wabnitz, T. C.; Fielenbach, D.; Jørgensen, K. A. *Angew. Chem. Int. Ed.* **2005**, *44*, 794.

(16) Hayashi, Y.; Gotoh, H.; Hayashi, T.; Shoji, M. *Angew. Chem. Int. Ed.* **2005**, *44*, 4212.

(17) Mukherjee, S.; Yang, J. W.; Hoffmann, S.; List, B. *Chem. Rev.* **2007**, *107*, 5471.

(18) Bächle, F.; Duschmalé, J.; Ebner, C.; Pfaltz, A.; Wennemers, H. *Angew. Chem. Int. Ed.* **2013**, *52*, 12619.

(19) Burés, J.; Armstrong, A.; Blackmond, D. G. *J. Am. Chem. Soc.* **2011**, *133*, 8822.

(20) Burés, J.; Armstrong, A.; Blackmond, D. G. *Chem. Sci.* **2012**, *3*, 1273.

(21) Duschmalé, J.; Wiest, J.; Wiesner, M.; Wennemers, H. *Chem. Sci.* **2013**, *4*, 1312.

(22) Schmid, M. B.; Zeitler, K.; Gschwind, R. M. *Angew. Chem. Int. Ed.* **2010**, *49*, 4997.

(23) Schmid, M. B.; Zeitler, K.; Gschwind, R. M. *Chem. Sci.* **2011**, *2*, 1793.

(24) Schmid, M. B.; Zeitler, K.; Gschwind, R. M. *Chem. Eur. J.* **2012**, *18*, 3362.

(25) Schmid, M. B.; Zeitler, K.; Gschwind, R. M. *J. Am. Chem. Soc.* **2011**, *133*, 7065.

(26) Schmid, M. B.; Zeitler, K.; Gschwind, R. M. *J. Org. Chem.* **2011**, *76*, 3005.

(27) Lelais, G.; MacMillan, D. W. C. In *Enantioselective Organocatalysis*; Wiley-VCH Verlag GmbH & Co. KGaA: Weinheim, Germany, 2007; Vol. *107*, pp 95–120.

(28) Zimmer, L. E.; Sparr, C.; Gilmour, R. *Angew. Chemie* **2011**, *123*, 12062.

(29) Holland, M. C.; Metternich, J. B.; Mück-Lichtenfeld, C.; Gilmour, R. *Chem. Commun.* **2015**, *51*, 5322.

(30) Holland, M. C.; Metternich, J. B.; Daniliuc, C.; Schweizer, W. B.; Gilmour, R. *Chem. Eur. J.* **2015**, *21*, 10031.

(31) Holland, M. C.; Paul, S.; Schweizer, W. B.; Bergander, K.; Mück-Lichtenfeld, C.; Lakhdar, S.; Mayr, H.; Gilmour, R. *Angew. Chem. Int. Ed.* **2013**, *52*, 7967.

(32) Nielsen, M.; Worgull, D.; Zweifel, T.; Gschwend, B.; Bertelsen, S.; Jørgensen, K. A. *Chem. Commun.* **2011**, *47*, 632.

(33) Roca-López, D.; Uria, U.; Reyes, E.; Carrillo, L.; Jørgensen, K. A.; Vicario, J. L.; Merino, P. *Chem. Eur. J.* **2016**, *22*, 884.

(34) Barker, C. C.; Bridge, M. H.; Stamp, A. *J. Chem. Soc.* **1959**, 3957.

(35) Mayr, H.; Bug, T.; Gotta, M. F.; Hering, N.; Irrgang, B.; Janker, B.; Kempf, B.; Loos, R.; Ofial, A. R.; Remennikov, G.; Schimmel, H. *J. Am. Chem. Soc.* **2001**, *123*, 9500.

(36) Peelen, T. J.; Chi, Y.; Gellman, S. H. *J. Am. Chem. Soc.* **2005**, *127*, 11598.

(37) Moore, R. E.; Pettus, J. A.; Mistysyn, J. *J. Org. Chem.* **1974**, *39*, 2201.

(38) Bothner-By, A. A.; Harris, R. K. *J. Am. Chem. Soc.* **1965**, *87*, 3445.

(39) Goldstein, A. J. H. *J. Mol. Spectrosc.* **1964**, *12*, 76.

(40) Cai, M.; Huang, Y.; Liu, J.; Krishnamoorthi, R. *J. Biomol. NMR* **1995**, *6*, 123.

(41) During our investigations, it was not possible to assign any α-alkylated product for our model system, because of a low signal to noise ratio. However, the stereoselection mode of the α-alkylation product is expected to be identical to the enamine catalysis, and hence not investigated.[14] Interestingly, α,γ-doubly substituted products were detected for the first time (for assignment, see Supporting Information). The kinetic buildup of γ-alkylation products reaches a maximum followed by a decrease due to the formation of the double alkylated product. Despite of best efforts (e.g. variation of acidic additive, catalyst concentration, and temperature) we were not able to influence the ratio of α- and γ-alkylation. The only variation found was an increase of doubly alkylated product by increasing the carbocation concentration.

(42) The initial increase of the *Z/E*-ratio (Figure 9) is most probably an artifact caused by the initially very low concentration of *E*-isomer.

(43) Note that structural analysis revealed that the most stable transition state of the product iminium ion formation exhibits an antiperiplanar arrangement (*ap*-conformation). The *exo*-conformation is marginally higher than the *ap*-conformation (~1 kJ/mol).

(44) Ashley, M. A.; Hirschi, J. S.; Izzo, J. A.; Vetticatt, M. J. *J. Am. Chem. Soc.* **2016**, *138*, 1756.

(45) Haindl, M. H.; Hioe, J.; Gschwind, R. M. *J. Am. Chem. Soc.* **2015**, *137*, 12835.

(46) Frisch, M. J.; Trucks, G. W.; Schlegel, H. B.; Scuseria, G. E.; Robb, M. A.; Cheeseman, J. R.; Scalmani, G.; Barone, V.; Mennucci, B.; Petersson, G. A.; Nakatsuji, H.; Caricato, M.; Li, X.; Hratchian, H. P.; Izmaylov, A. F.; Bloino, J.; Zheng, G.; Sonnenberg, J. L.; Hada M.; Ehara, M.; Toyota, K.; Fukuda, R.; Hasegawa, J.; Ishida, M.; Nakajima, T.; Honda, Y.; Kitao, O.; Nakai, H.; Vreven, T.; Montgomery, Jr., J. A.; Peralta, J. E.; Ogliaro, F.; Bearpark, M.; Heyd, J. J.; Brothers, E.; Kudin, K. N.; Staroverov, V. N.; Kobayashi, R.; Normand, J.; Raghavachari, K.; Rendell, A.; Burant, J. C.; Iyengar, S. S.; Tomasi, J.; Cossi, M.; Rega, N.; Millam, J. M.; Klene, M.; Knox, J. E.; Cross, J. B.; Bakken, V.; Adamo, C.; Jaramillo, J.; Gomperts, R.; Stratmann, R. E.; Yazyev, O.; Austin, A. J.; Cammi, R.; Pomelli, C.; Ochterski, J. W.; Martin, R. L.; Morokuma, K.; Zakrzewski, V. G.; Voth, G. A.; Salvador, P.; Dannenberg, J. J.; Dapprich, S.; Daniels, A. D.; Farkas, Ö.; Foresman, J. B.; Ortiz, J. V.; Cioslowski, J.; Fox, D. J.; *Gaussian 09*, version D.01; Gaussian, Inc.: Wallingford, CT, 2009.

(47) Zhao, Y.; Truhlar, D. G. *Theor. Chem. Acc.* **2008**, *120*, 215.

(48) Weigend, F.; Furche, F.; Ahlrichs, R. *J. Chem. Phys.* **2003**, *119*, 12753.

(49) Grimme, S.; Antony, J.; Ehrlich, S.; Krieg, H. *J. Chem. Phys.* **2010**, *132*, 154104.

(50) Neese, F. *Wiley Interdiscip. Rev. Comput. Mol. Sci.* **2012**, *2*, 73.

(51) Grimme, S. *J. Chem. Phys.* **2003**, *118*, 9095.

(52) Pye, C. C.; Ziegler, T.; van Lenthe, E.; Louwen, J. N. *Can. J. Chem.* **2009**, *87*, 790.

(53) Xiong, R.; Sandler, S. I.; Burnett, R. I. *Ind. Eng. Chem. Res.* **2014**, *53*, 8265.

(54) *COSMO-RS*, SCM Theoretical Chemistry, Vrije Universiteit, Amsterdam, The Netherlands, 2014; http://www.scm.com.

(55) *Amsterdam Density Functional (ADF)*, SCM Theoretical Chemistry, Vrije Universiteit, Amsterdam, The Netherlands, 2014; http://www.scm.com.

(56) Fonseca Guerra, C.; Snijders, J. G.; Te Velde, G.; Baerends, E. J. *Theor. Chem. Acc.* **1998**, *99*, 391.

(57) te Velde, G.; Bickelhaupt, F. M.; Baerends, E. J.; Fonseca Guerra, C.; van Gisbergen, S. J. a.; Snijders, J. G.; Ziegler, T. *J. Comput. Chem.* **2001**, *22*, 931.

2.6 Supporting Information

2.6.1 NMR Measurements

The NMR measurements were performed at 300-313 K on a Bruker Avance III Nanobay 400, a Bruker Avance III 600 (600.25 MHz) and a Bruker Avance III HD 600 (600.13 MHz) with prodigy cryo, phosphorous selective TBIP or fluorine selective TBIF probe. Kinetic data was processed with Bruker Dynamics Center 2. All spectra were processed and evaluated with Bruker Topspin 3.2.

2.6.2 Dienamine Intermediates

All dienamine intermediates were generated and detected *in situ* in a 5 mm standard NMR tube at 298-300 K. For assignment and kinetic measurements a mixture of aldehyde (1 equiv) and catalyst (1 equiv) was dissolved in 0.6 ml toluene-d_8 to give a concentration of 50 mM. All chemicals were purchased from Sigma Aldrich, Acros Organics and TCI Europe and were used as purchased. Only aldehydes **1-4** were purified by distillation before.

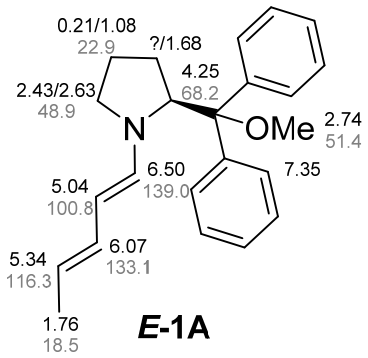

***E*-1A**

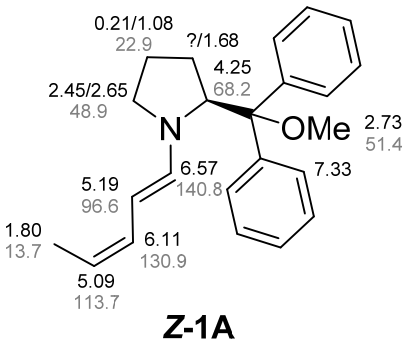

***Z*-1A**

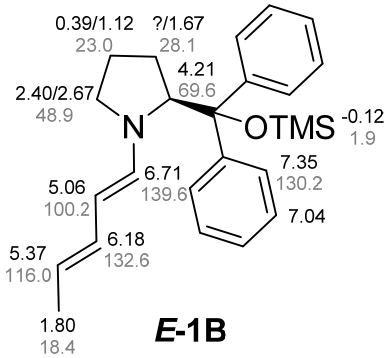

***E*-1B**

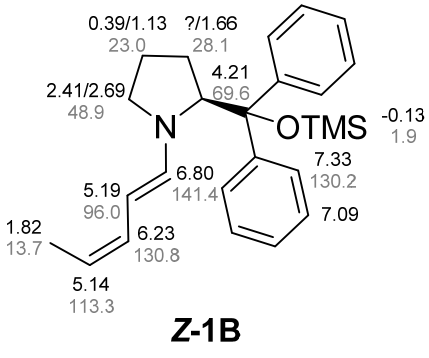

***Z*-1B**

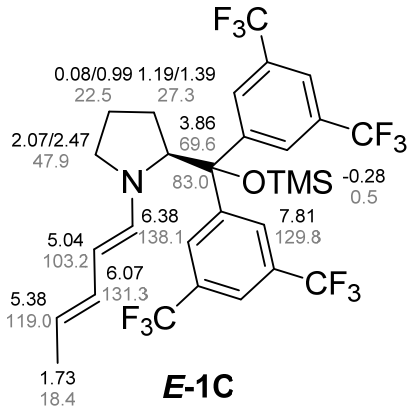

***E*-1C**

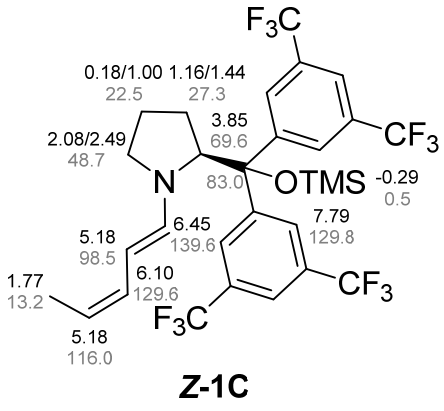

***Z*-1C**

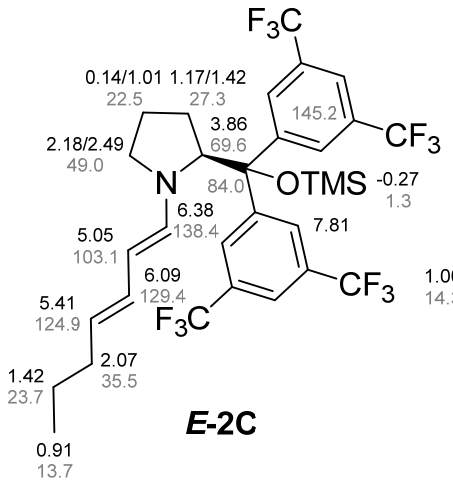

***E*-2C**

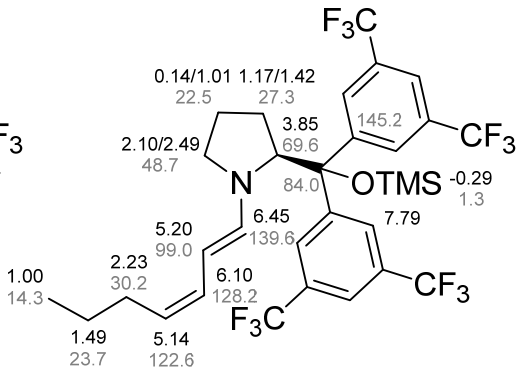

***Z*-2C**

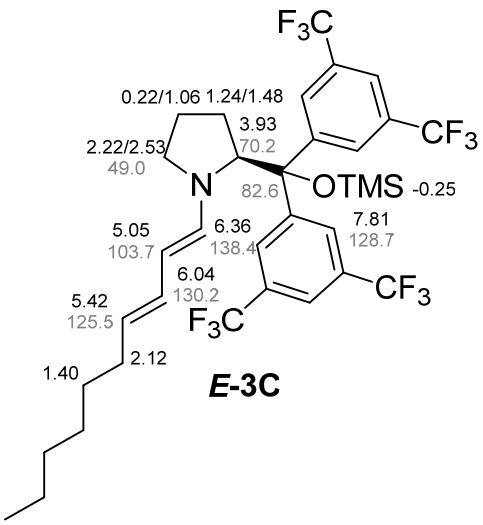

***E*-3C**

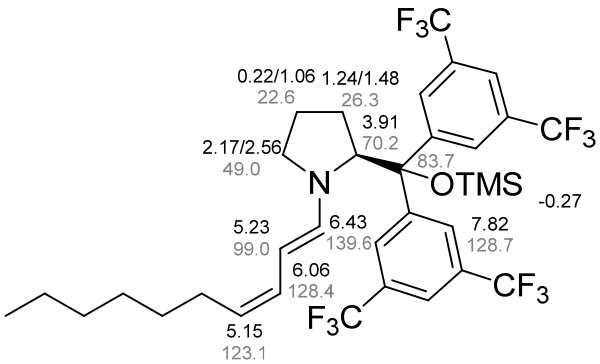

***Z*-3C**

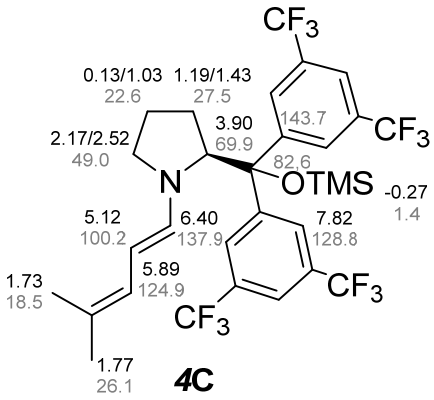

NMR Spectra

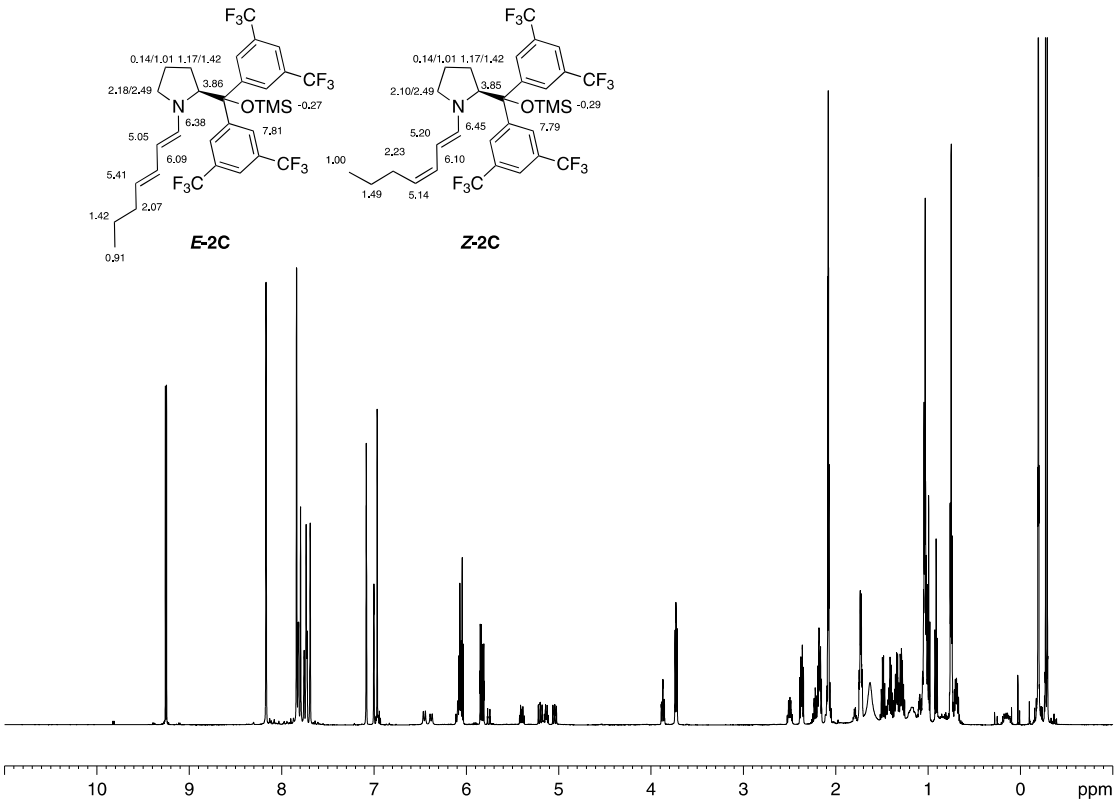

reaction parameters: ^{1}H spectrum (600 MHz) of unpurified ***E-2C*** and ***Z-2C*** yielded by a reaction of *trans-2*-heptenal (1 equiv; 50 mM) and catalyst **C** (1 equiv) in 0.5 ml toluene-d_8 at 300 K.

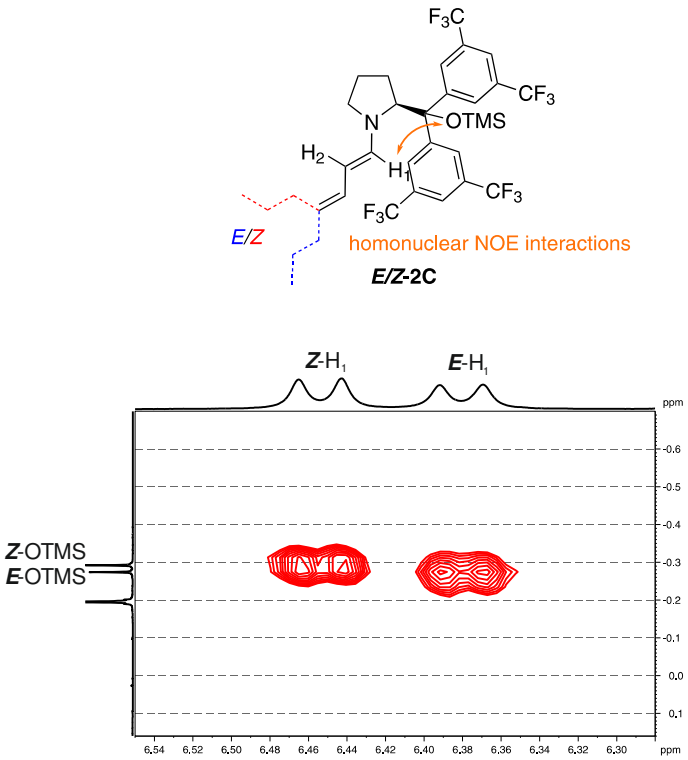

reaction parameters: Segment of $^{1}H^{1}H$-NOESY spectrum (600 MHz) of unpurified ***E-2C*** and ***Z-2C*** at 300 K. Crosspeaks of H_1 protons and the corresponding protons of the OTMS-protecting group for ***E-2C*** and ***Z-2C*** to prove *sc-exo conformation*.

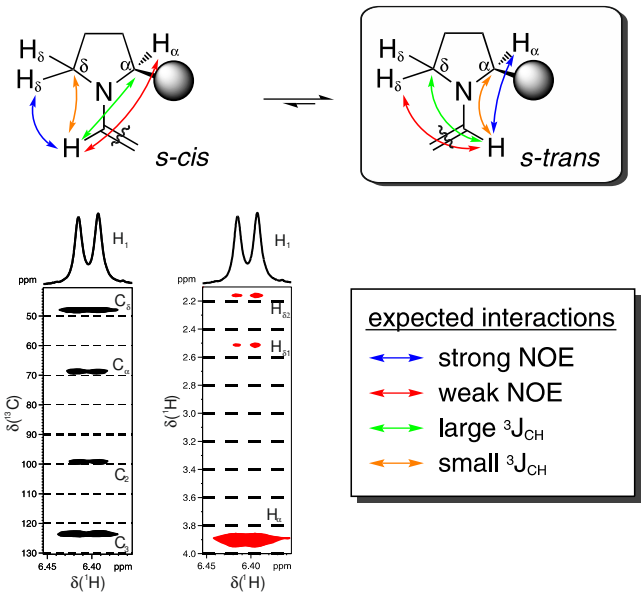

reaction parameters: Segment of NOESY and HMBC spectrum (600 MHz) of unpurified ***4C*** at 298 K. Crosspeaks of H_1 protons and the important pyrrolidine ring protons as well the couplings of H_1 and the important carbon nuclei to prove *s-trans* conformation.

Table 1. Coupling constant analysis of the diene subsystem and the resulting configuration of dienamines. All dienamines were achieved by a reaction of 1 equiv aldehyde and 1 equiv catalyst in toluene-d_8 in a standard NMR tube. For additional reaction parameters see table.

ald.	cat.		$^3J_{H1H2}$ [Hz]	$^3J_{H2H3}$ [Hz]	$^3J_{H3H4}$ [Hz]	configuration	(*Z*/*E* ratio)^{time}
1	A[c]	*E*	13.4	10.4	14.9	*E-s-trans-E*[a]	(1.9/1)^{31h}
		Z	13.2	11.3	10.5	*E-s-trans-Z*[a]	
1	B	*E*	13.4	10.3	14.7	*E-s-trans-E*[a]	(2/1)^{21h}
		Z	13.4	10.7	10.7	*E-s-trans-Z*[a]	
1	C	*E*	13.5	10.6	14.6	*E-s-trans-E*[a]	(2.16/1)^{21h}
		Z	13.5	10.7	10.7	*E-s-trans-Z*[a]	
2	C	*E*	13.3	10.3	14.6	*E-s-trans-E*[a]	(1.04/1)^{11h}
		Z	13.3	11.3	10.6	*E-s-trans-Z*[a]	
3	C	*E*	13.5	10.3	15.0	*E-s-trans-E*[b]	(0.88/1)^{15h}
		Z	13.4	11.3	10.6	*E-s-trans-Z*[b]	
4	C	-	13.3	10.7	-	*E-s-trans*[b]	-

[a]300 K; [b]318 K; [c]2 equiv catalyst

Table 2. Coupling constant analysis of the catalyst subsystem and the resulting puckering of the ring. All dienamines were achieved by a reaction of 1 equiv aldehyde and 1 equiv catalyst in toluene-d_8 in a standard NMR tube. For additional reaction parameters see table.

reference			$^3J_{H\alpha H\beta 2}$ [Hz]	$^3J_{H\delta 2H\gamma 1}$ [Hz]	$^3J_{H\delta 1H\gamma 2}$ [Hz]	$\Delta H_{\gamma 2}$ shift[a] [ppm]	conformation
proline rings in proteins[1,2]			7 – 11	8 – 12	2 – 3	-	*up*
			2 – 3	2 – 3	7 – 12	-	*down*
ald.	cat.		$^3J_{H\alpha H\beta 2}$ [Hz]	$^3J_{H\delta 2H\gamma 1}$ [Hz]	$^3J_{H\delta 1H\gamma 2}$ [Hz]	$\Delta H_{\gamma 2}$ shift[a] [ppm]	conformation
1	A[d]	*E*	overl.	2.18	8.51	-0.68	*down*[b]
		Z	overl.	2.44	8.51	-0.68	*down*[b]
1	B	*E*	overl.	2.80	8.96	-0.79	*down*[b]
		Z	overl.	2.67	8.94	-0.79	*down*[b]
1	C	*E*	2.11	overl.	9.91	-0.60	*down*[b]
		Z	2.21	overl.	10.05	-0.60	*down*[b]
2	C	*E*	2.20	~ 2.4	~ 8-9	-0.54	*down*[b]
		Z	2.25	~ 2.5	~ 8-9	-0.54	*down*[b]
3	C	*E*	2.25	overl.	~ 9	-0.58	*down*[c]
		Z	2.39	overl.	~ 9	-0.55	*down*[c]
4	C	-	2.1	2.3	9.7	-0.55	*down*[c]

[a]compared to free catalyst; [b]300 K; [c]318 K; [d]2 equiv catalyst

Experimental NOE Distance Measurement

The conformational preference of the exocyclic bound moiety of the catalyst was investigated by NOE distance measurements. As an indicator for the three different conformations (*sc-endo, sc-exo* and *ap*) the NOE intensity and the resulting distance (r_{ab}) between H_1 and the protons of the O-protecting group was investigated according to the following equation. The distance between the two pyrrolidine ring protons $H_{\delta1}$ and $H_{\delta2}$ (r_{ref}) was used as a reference. The distance was determined with help of the theoretical calculations of the corresponding dienamines. The NOE intensities between $H_{\delta1}$ and $H_{\delta2}$ (I_{ref}) as well as the intensity between H_1 and H_{OTMS} (I_{ab}) was investigated experimentally with NOESY measurements.

$$\frac{I_{ab}}{I_{ref}} = \frac{r_{ab}^{(-6)}}{r_{ref}^{(-6)}}$$

$$r_{ab}^{(-6)} = \frac{I_{ab}}{I_{ref}} * r_{ref}^{(-6)}$$

Calculation Based NOE Weighted Distance Measurement

The distance information between H_1 and hydrogens of TMS group is relevant for the determination of *sc-exo* conformation. To compare the predicted interatomic distances with the experimental one (NOE based), the distance through space for a nuclei pair *ab* is weighted and averaged according NOE distance dependency (see eq. below). For example in *sc-exo* of dienamine ***E*-1C** the average distance was averaged and calculated over 9 distances between H1 and all of hydrogens in TMS group. The measured distances of nuclei pairs r_{ab} (a in our case is always H_1) were subsequently subjected to the NOE distance dependent factor r^{-6}. Each factorized distance was then divided by the sum of all factorized distances to obtain the weighting factor for each nuclei pair. The distances of every nuclei pair H_1-*b* were then multiplied by the weighting factors. Finally the sum of the weighted distances is the averaged distance, which is to be compared with distance obtained from the experiment.

$$w_{ab} = \frac{r_{ab}^{-6}}{\sum_b r_{ab}^{-6}}$$

$$\bar{r}_{\mathrm{NOE}} = \sum_b w_{ab} r_{ab}$$

Effects of Acids and Temperature on the Polymerization and Isomerization Rate

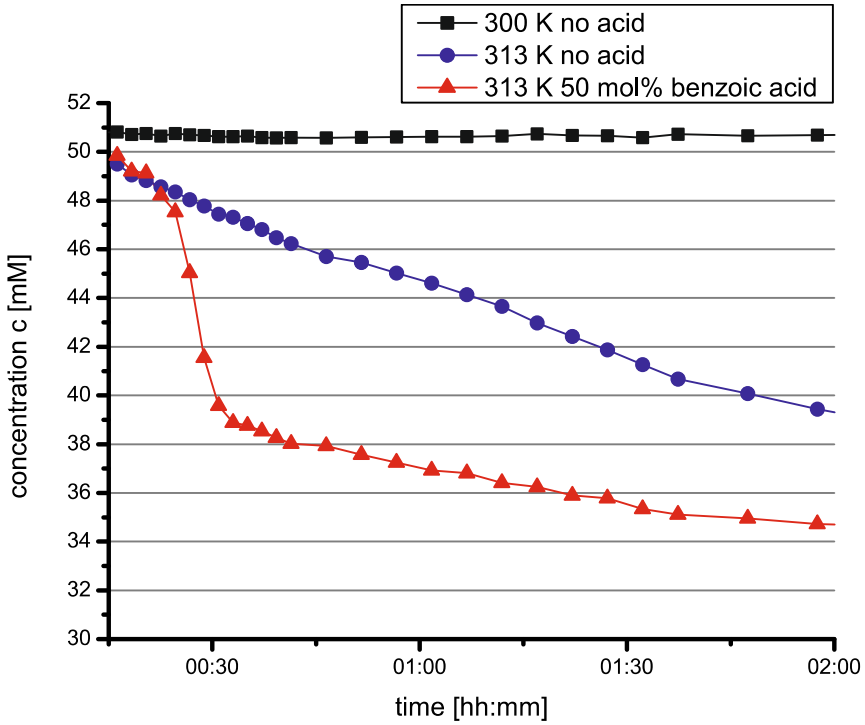

Kinetic profile. Sum of signal intensity of aldehyde **1** (1 equiv) and the deriving species under different conditions with catalyst **C** (1 equiv).

2.6.3 Product Species

The depicted γ-product species are the results of the reaction between the corresponding aldehyde and Michler's hydrol in the presence of a catalyst and an acidic additive (acetic acid, TFA or benzoic acid). For the exact stoichiometry see the captions. The reactions were all carried out by mixing all reagents in toluene-d_8 in a standard 5 mm NMR tube at temperatures of 283-313 K. The assignments were made with NMR measurements of the reaction mixture without purifying the product.

(*E*)-5,5-bis(4-(dimethylamino)phenyl)-4-methylpent-2-enal

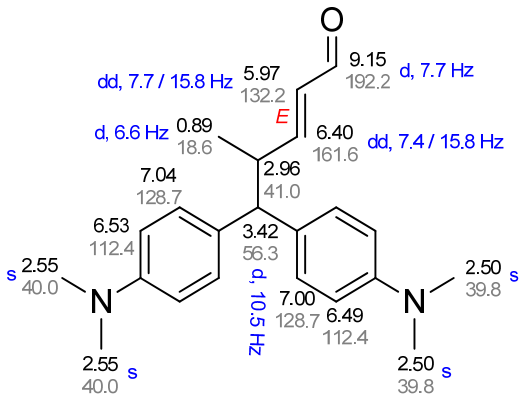

reaction parameters: *trans-2*-pentenal (2 equiv; 100 mM) , catalyst **C** (0.2 equiv), acetic acid (0.1 equiv), Michler's hydol (1 equiv), 313 K, 0.6 ml toluene-d_8, 600 MHz.

(*E*)-4-(bis(4-(dimethylamino)phenyl)methyl)hept-2-enal

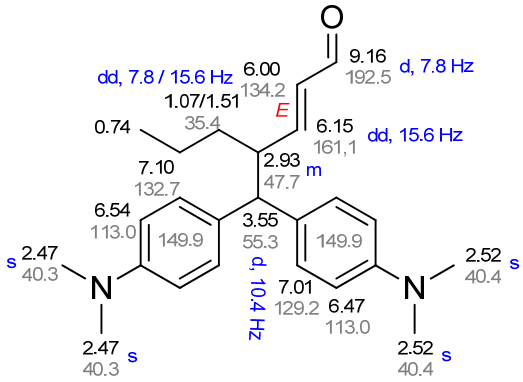

reaction parameters: *trans-2*-heptenal (2 equiv ; 50 mM), catalyst **C** (1 equiv), acetic acid (0.5 equiv), Michler's hydol (1 equiv), 283 K, 1.0 ml toluene-d_8, 600 MHz.

(*E*)-4-(bis(4-(dimethylamino)phenyl)methyl)dec-2-enal

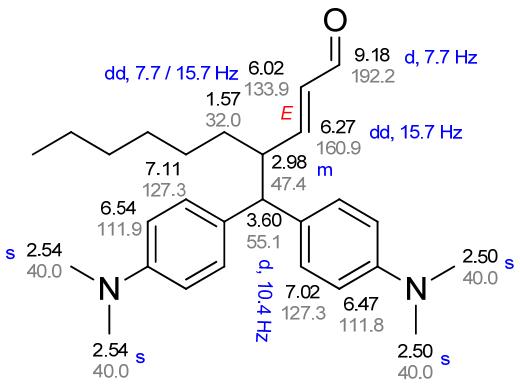

reaction parameters: *trans-2*-decenal (2 equiv), catalyst **C** (0.2 equiv; 50 mM), acetic acid (0.1 equiv), Michler's hydol (1 equiv), 298 K, 0.7 ml toluene-d_8, 600 MHz.

(*E*)-5,5-bis(4-(dimethylamino)phenyl)-4,4-dimethylpent-2-enal

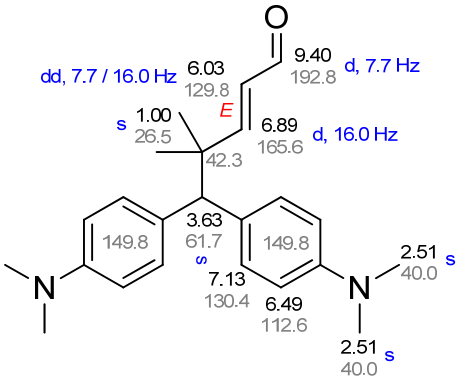

reaction parameters: 4-methyl-*2*-pentenal (2 equiv; 1.6 M), catalyst **C** (0.2 equiv), benzoic acid (0.1 equiv), Michlers hydol (1 equiv), 298 K, 0.250 ml toluene-d_8 for reaction, 0.6 mL toluene-d_8 for measurements, 400 MHz.

α,γ-disubstituted product: (E)-2-(bis(4-(dimethylamino)phenyl)methyl)-5,5-bis(4-(dimethylamino)-phenyl)-4-methylpent-3-enal

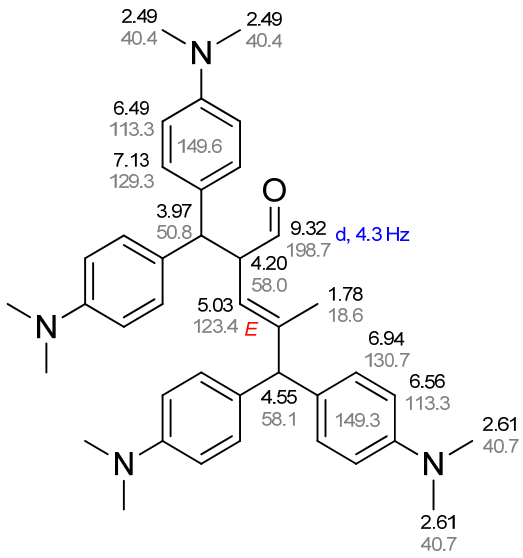

reaction parameters: The α,γ-disubstituted product could be detected in reaction mixtures of *trans-2*-pentenal (1 equiv; 50 mM), catalyst **C** (0.2 equiv), TFA (0.1 equiv) and Michler's hydol (1 equiv) in a 5 mm NMR tube at 300 K in 0.6 ml toluene-d_8 at 600 MHz. However, the detection was also possible, if AcOH was used as well as in reactions with 2 equivalents of *trans-2*-pentenal with TFA at 313 K.

2.6.4 Procedure for the Gamma-Alkylation of *trans*-Pentenal

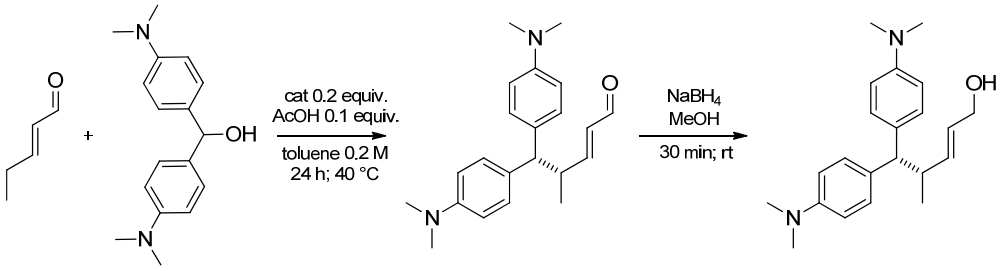

To a solution of the catalyst **A-C** (0.2 equiv, 0.04 mmol) in toluene (1 mL, 0.2 M), *trans*-2-pentenal (2.0 equiv, 0.4 mmol), bis[4-(dimethylamino)phenyl]methanol, (1.0 equiv, 0.2 mmol) and acetic acid (0.1 equiv, 0.02 mmol) were added and the solution was stirred at 40 °C for 24 h. Then the reaction mixture was filtrated through a plastic syringe with a layer of silica inside using Et_2O as eluent. The solvent was evaporated and the crude

product was purified by flash chromatography (SiO_2, pentane/EtOAc 8/2, R_f 0.35) to give a pale yellow oil. The purified aldehyde was dissolved in MeOH (1 mL) and $NaBH_4$ (1.2 equiv on theoretic 100 % yield, 0.24 mmol) was added and the reaction was stirred at rt for 30 minutes. Then, EtOAc (3 mL) and water (1 mL) were added, and the biphasic mixture was strongly stirred for 5 min. The organic phase was collected and the aqueous phase was extracted once with EtOAc (2 ml). The crude alcohol solution was dried over Na_2SO_4, evaporated and purified by preparative TLC (SiO_2, pentane/EtOAc 1/1, R_f 0.30) to afford a colorless oil. The synthesis of the racemic references was carried out using a racemic mixture of catalyst (10 mol% for each enantiomer). Enantiomeric excess was determined by chiral HPLC (column: Lux 5u Cellulose-1 by Phenomenex; solvent: ^{i}PrOH/pentane 1/9; flowrate 0.5 ml/min; temperature: rt; UV 204 nm, τ_{minor} = 23.2 min, τ_{major} = 25.2 min).

(*E*)-5,5-bis(4-(dimethylamino)phenyl)-4-methylpent-2-enal

^{1}H NMR (400 MHz, Tol) δ 9.16 (d, *J* = 7.7 Hz, 2H), 7.07 (4 H), 7.04 (d, 4H), 6.54 (d, *J* = 8.7 Hz, 4H), 6.49 (d, *J* = 8.8 Hz, 4H), 6.39 (dd, *J* = 15.7, 7.4 Hz, 2H), 5.99 (ddd, *J* = 15.7, 7.7, 1.0 Hz, 2H), 3.42 (d, *J* = 10.5 Hz, 2H), 2.96 (dt, *J* = 10.4, 6.5 Hz, 2H), 2.54 (s, 11H), 2.50 (s, 11H), 0.89 (d, *J* = 6.6 Hz, 6H).

^{13}C NMR (100 MHz, Tol) δ 192.9, 162.2, 149.8, 132.9, 132.4, 113.5, 113.4, 56.8, 41.7, 40.7, 40.6, 19.1.

(*E*)-5,5-bis(4-(dimethylamino)phenyl)-4-methylpent-2-en-1-ol

^{1}H NMR (400 MHz, CD_2Cl_2) δ 7.12 – 7.04 (4H), 6.67 – 6.58 (4H), 5.54 (2H), 3.89 (d, *J* = 3.6 Hz, 2H), 3.42 (d, *J* = 10.8 Hz, 1H), 3.02 – 2.94 (m, 1H), 2.86 (s, 6H), 2.85 (s, 6H), 0.94 (d, *J* = 6.6 Hz, 3H).

^{13}C NMR (100 MHz, Tol) δ 137.5, 128.7, 128.7, 128.4, 112.9, 112.7, 63.5, 56.8, 40.7 40.2 19.8. quaternary C atoms are missing.

2.6.5 HPLC Analysis

HPLC traces for the γ-alkylated product of *trans*-2-pentenal ((*E*)-5,5-bis(4-(dimethylamino)phenyl)-4-methylpent-2-enal).

For the general procedure see instructions above.

<u>Catalyst **A**</u> (for incubation time [min] i.e. time before addition of electrophile see traces)

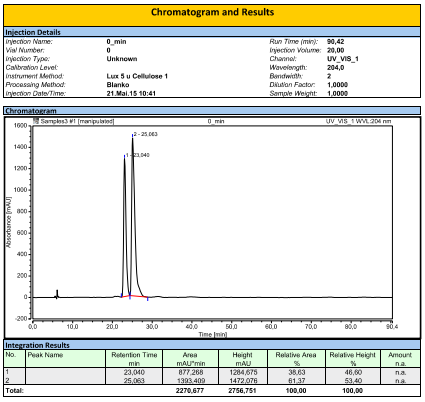

Chromatogram and Results

Injection Details

Injection Name:	0_min	Run Time (min):	90,42
Vial Number:	0	Injection Volume:	20,00
Injection Type:	Unknown	Channel:	UV_VIS_1
Calibration Level:		Wavelength:	204,0
Instrument Method:	Lux 5 u Cellulose 1	Bandwidth:	2
Processing Method:	Blanko	Dilution Factor:	1,0000
Injection Date/Time:	21.Mai.15 10:41	Sample Weight:	1,0000

Chromatogram

Samples3 #1 [manipulated] 0_min UV_VIS_1 WVL:204 nm

Integration Results

No.	Peak Name	Retention Time min	Area mAU*min	Height mAU	Relative Area %	Relative Height %	Amount n.a.
1		23,040	877,268	1284,675	38,63	46,60	n.a.
2		25,063	1393,409	1472,076	61,37	53,40	n.a.
Total:			2270,677	2756,751	100,00	100,00	

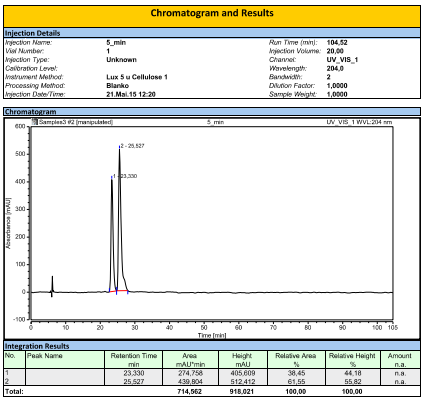

Chromatogram and Results

Injection Details

Injection Name:	5_min	Run Time (min):	104,52
Vial Number:	1	Injection Volume:	20,00
Injection Type:	Unknown	Channel:	UV_VIS_1
Calibration Level:		Wavelength:	204,0
Instrument Method:	Lux 5 u Cellulose 1	Bandwidth:	2
Processing Method:	Blanko	Dilution Factor:	1,0000
Injection Date/Time:	21.Mai.15 12:20	Sample Weight:	1,0000

Chromatogram

Samples3 #2 [manipulated] 5_min UV_VIS_1 WVL:204 nm

Integration Results

No.	Peak Name	Retention Time min	Area mAU*min	Height mAU	Relative Area %	Relative Height %	Amount n.a.
1		23,330	274,758	405,669	38,45	44,18	n.a.
2		25,527	439,804	512,412	61,55	55,82	n.a.
Total:			714,562	918,021	100,00	100,00	

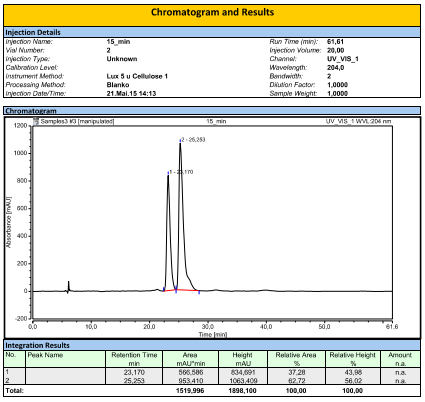

Chromatogram and Results

Injection Details

Injection Name:	15_min	Run Time (min):	61,61
Vial Number:	2	Injection Volume:	20,00
Injection Type:	Unknown	Channel:	UV_VIS_1
Calibration Level:		Wavelength:	204,0
Instrument Method:	Lux 5 u Cellulose 1	Bandwidth:	2
Processing Method:	Blanko	Dilution Factor:	1,0000
Injection Date/Time:	21.Mai.15 14:13	Sample Weight:	1,0000

Chromatogram

Samples3 #3 [manipulated] 15_min UV_VIS_1 WVL:204 nm

Integration Results

No.	Peak Name	Retention Time min	Area mAU*min	Height mAU	Relative Area %	Relative Height %	Amount n.a.
1		23,170	566,586	834,691	37,28	43,98	n.a.
2		25,253	953,410	1063,409	62,72	56,02	n.a.
Total:			1519,996	1898,100	100,00	100,00	

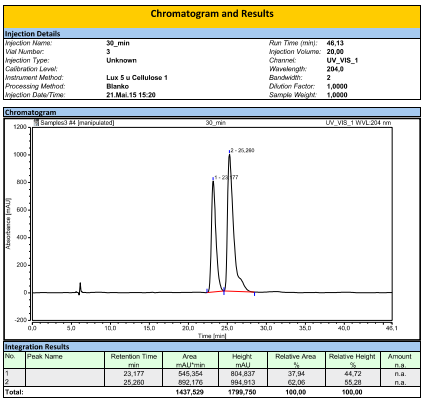

Chromatogram and Results

Injection Details

Injection Name:	30_min	Run Time (min):	46,13
Vial Number:	3	Injection Volume:	20,00
Injection Type:	Unknown	Channel:	UV_VIS_1
Calibration Level:		Wavelength:	204,0
Instrument Method:	Lux 5 u Cellulose 1	Bandwidth:	2
Processing Method:	Blanko	Dilution Factor:	1,0000
Injection Date/Time:	21.Mai.15 15:20	Sample Weight:	1,0000

Chromatogram

Samples3 #4 [manipulated] 30_min UV_VIS_1 WVL:204 nm

Integration Results

No.	Peak Name	Retention Time min	Area mAU*min	Height mAU	Relative Area %	Relative Height %	Amount n.a.
1		23,177	545,354	804,837	37,94	44,72	n.a.
2		25,260	892,176	994,913	62,06	55,28	n.a.
Total:			1437,529	1799,750	100,00	100,00	

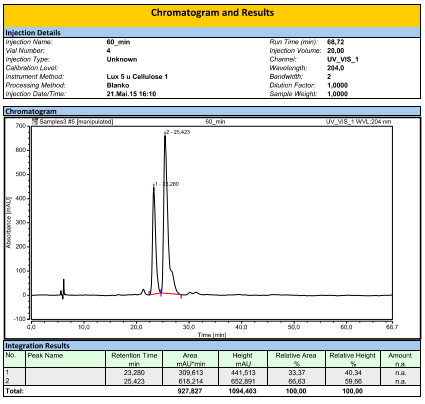

Chromatogram and Results

Injection Details

Injection Name:	60_min	Run Time (min):	68,72
Vial Number:	4	Injection Volume:	20,00
Injection Type:	Unknown	Channel:	UV_VIS_1
Calibration Level:		Wavelength:	204,0
Instrument Method:	Lux 5 u Cellulose 1	Bandwidth:	2
Processing Method:	Blanko	Dilution Factor:	1,0000
Injection Date/Time:	21.Mai.15 16:10	Sample Weight:	1,0000

Chromatogram

Samples3 #5 [manipulated] 60_min UV_VIS_1 WVL:204 nm

Integration Results

No.	Peak Name	Retention Time min	Area mAU*min	Height mAU	Relative Area %	Relative Height %	Amount n.a.
1		23,280	309,613	441,513	33,37	40,34	n.a.
2		25,423	618,214	652,891	66,63	59,66	n.a.
Total:			927,827	1094,403	100,00	100,00	

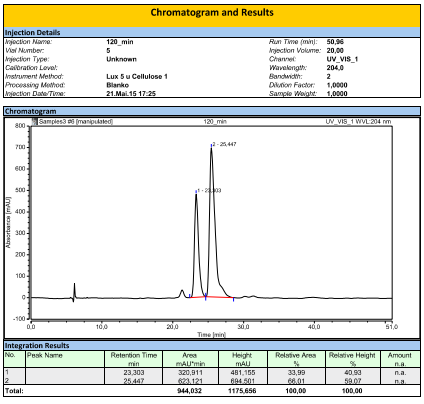

Chromatogram and Results

Injection Details

Injection Name:	120_min	Run Time (min):	50,96
Vial Number:	5	Injection Volume:	20,00
Injection Type:	Unknown	Channel:	UV_VIS_1
Calibration Level:		Wavelength:	204,0
Instrument Method:	Lux 5 u Cellulose 1	Bandwidth:	2
Processing Method:	Blanko	Dilution Factor:	1,0000
Injection Date/Time:	21.Mai.15 17:25	Sample Weight:	1,0000

Chromatogram

Samples3 #6 [manipulated] 120_min UV_VIS_1 WVL:204 nm

Integration Results

No.	Peak Name	Retention Time min	Area mAU*min	Height mAU	Relative Area %	Relative Height %	Amount n.a.
1		23,303	320,911	481,155	33,99	40,93	n.a.
2		25,447	623,121	694,501	66,01	59,07	n.a.
Total:			944,032	1175,656	100,00	100,00	

Catalyst **B** (for incubation time [min] i.e. time before addition of electrophile see traces)

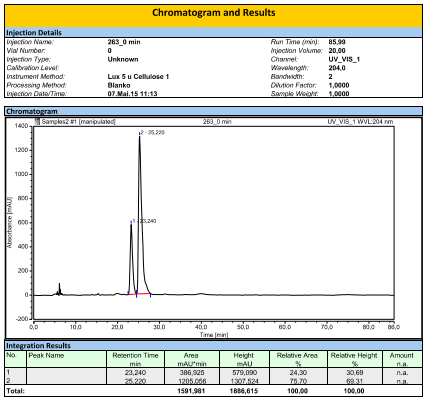

Chromatogram and Results

Injection Details

Injection Name:	263_0 min	Run Time (min):	85,99
Vial Number:	0	Injection Volume:	20,00
Injection Type:	Unknown	Channel:	UV_VIS_1
Calibration Level:		Wavelength:	204,0
Instrument Method:	Lux 5 u Cellulose 1	Bandwidth:	2
Processing Method:	Blanko	Dilution Factor:	1,0000
Injection Date/Time:	07.Mai.15 11:13	Sample Weight:	1,0000

Chromatogram

Samples2 #1 [manipulated] 263_0 min UV_VIS_1 WVL:204 nm

Integration Results

No.	Peak Name	Retention Time min	Area mAU*min	Height mAU	Relative Area %	Relative Height %	Amount n.a.
1		23,240	386,925	579,090	24,30	30,69	n.a.
2		25,220	1205,056	1307,524	75,70	69,31	n.a.
Total:			**1591,981**	**1886,615**	**100,00**	**100,00**	

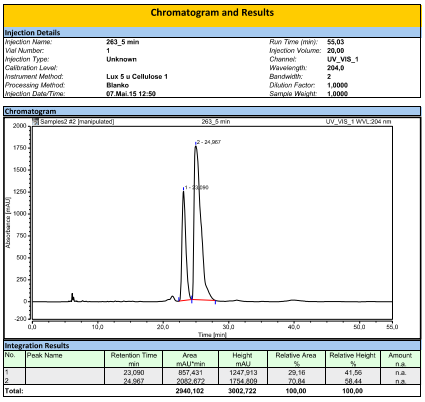

Chromatogram and Results

Injection Details

Injection Name:	263_5 min	Run Time (min):	55,03
Vial Number:	1	Injection Volume:	20,00
Injection Type:	Unknown	Channel:	UV_VIS_1
Calibration Level:		Wavelength:	204,0
Instrument Method:	Lux 5 u Cellulose 1	Bandwidth:	2
Processing Method:	Blanko	Dilution Factor:	1,0000
Injection Date/Time:	07.Mai.15 12:50	Sample Weight:	1,0000

Chromatogram

Samples2 #2 [manipulated] 263_5 min UV_VIS_1 WVL:204 nm

Integration Results

No.	Peak Name	Retention Time min	Area mAU*min	Height mAU	Relative Area %	Relative Height %	Amount n.a.
1		23,090	857,431	1247,913	29,16	41,56	n.a.
2		24,967	2082,672	1754,809	70,84	58,44	n.a.
Total:			**2940,102**	**3002,722**	**100,00**	**100,00**	

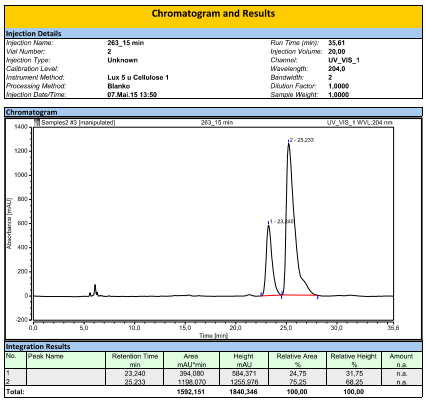

Chromatogram and Results

Injection Details

Injection Name:	263_15 min	Run Time (min):	55,61
Vial Number:	2	Injection Volume:	20,00
Injection Type:	Unknown	Channel:	UV_VIS_1
Calibration Level:		Wavelength:	204,0
Instrument Method:	Lux 5 u Cellulose 1	Bandwidth:	2
Processing Method:	Blanko	Dilution Factor:	1,0000
Injection Date/Time:	07.Mai.15 13:50	Sample Weight:	1,0000

Chromatogram

Samples2 #3 [manipulated] 263_15 min UV_VIS_1 WVL:204 nm

Integration Results

No.	Peak Name	Retention Time min	Area mAU*min	Height mAU	Relative Area %	Relative Height %	Amount n.a.
1		23,240	394,080	584,371	24,75	31,75	n.a.
2		25,233	1198,070	1255,976	75,25	68,25	n.a.
Total:			**1592,151**	**1840,346**	**100,00**	**100,00**	

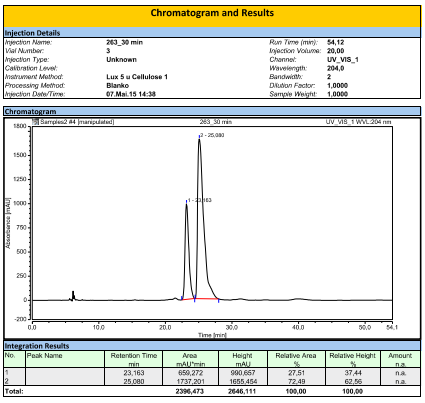

Chromatogram and Results

Injection Details

Injection Name:	263_30 min	Run Time (min):	54,12
Vial Number:	3	Injection Volume:	20,00
Injection Type:	Unknown	Channel:	UV_VIS_1
Calibration Level:		Wavelength:	204,0
Instrument Method:	Lux 5 u Cellulose 1	Bandwidth:	2
Processing Method:	Blanko	Dilution Factor:	1,0000
Injection Date/Time:	07.Mai.15 14:38	Sample Weight:	1,0000

Chromatogram

Samples2 #4 [manipulated] 263_30 min UV_VIS_1 WVL:204 nm

Integration Results

No.	Peak Name	Retention Time min	Area mAU*min	Height mAU	Relative Area %	Relative Height %	Amount n.a.
1		23,163	659,272	990,657	27,51	37,44	n.a.
2		25,080	1737,201	1655,454	72,49	62,56	n.a.
Total:			**2396,473**	**2646,111**	**100,00**	**100,00**	

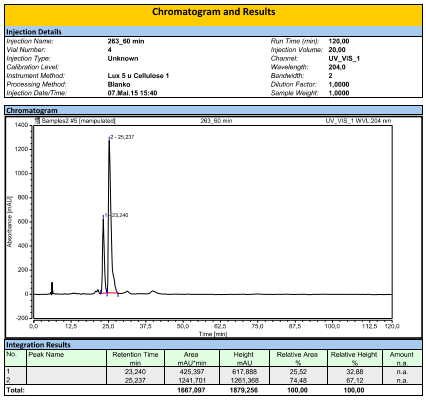

Chromatogram and Results

Injection Details

Injection Name:	263_60 min	Run Time (min):	120,00
Vial Number:	4	Injection Volume:	20,00
Injection Type:	Unknown	Channel:	UV_VIS_1
Calibration Level:		Wavelength:	204,0
Instrument Method:	Lux 5 u Cellulose 1	Bandwidth:	2
Processing Method:	Blanko	Dilution Factor:	1,0000
Injection Date/Time:	07.Mai.15 15:40	Sample Weight:	1,0000

Chromatogram

Samples2 #5 [manipulated] 263_60 min UV_VIS_1 WVL:204 nm

Integration Results

No.	Peak Name	Retention Time min	Area mAU*min	Height mAU	Relative Area %	Relative Height %	Amount n.a.
1		23,240	425,397	617,868	25,52	32,88	n.a.
2		25,237	1241,701	1261,388	74,48	67,12	n.a.
Total:			**1667,097**	**1879,256**	**100,00**	**100,00**	

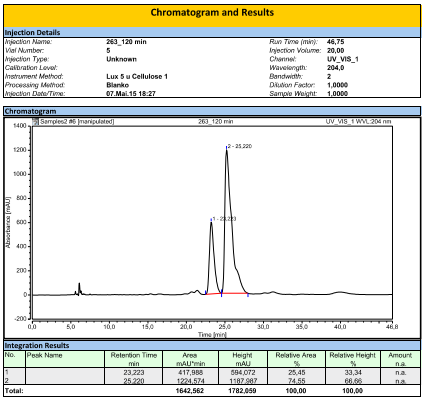

Chromatogram and Results

Injection Details

Injection Name:	263_120 min	Run Time (min):	46,75
Vial Number:	5	Injection Volume:	20,00
Injection Type:	Unknown	Channel:	UV_VIS_1
Calibration Level:		Wavelength:	204,0
Instrument Method:	Lux 5 u Cellulose 1	Bandwidth:	2
Processing Method:	Blanko	Dilution Factor:	1,0000
Injection Date/Time:	07.Mai.15 18:27	Sample Weight:	1,0000

Chromatogram

Samples2 #6 [manipulated] 263_120 min UV_VIS_1 WVL:204 nm

Integration Results

No.	Peak Name	Retention Time min	Area mAU*min	Height mAU	Relative Area %	Relative Height %	Amount n.a.
1		23,223	417,988	594,072	25,45	33,34	n.a.
2		25,220	1224,574	1187,987	74,55	66,66	n.a.
Total:			**1642,562**	**1782,059**	**100,00**	**100,00**	

Catalyst **C** (for incubation time [min] i.e. time before addition of electrophile see traces)

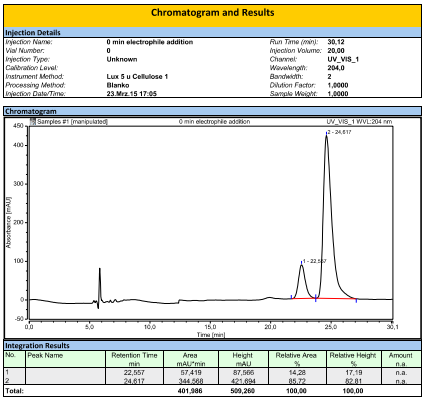

Chromatogram and Results

Injection Details

Injection Name:	**0 min electrophile addition**	*Run Time (min):*	**30,12**
Vial Number:	**0**	*Injection Volume:*	**20,00**
Injection Type:	**Unknown**	*Channel:*	**UV_VIS_1**
Calibration Level:		*Wavelength:*	**204,0**
Instrument Method:	**Lux 5 u Cellulose 1**	*Bandwidth:*	**2**
Processing Method:	**Blanko**	*Dilution Factor:*	**1,0000**
Injection Date/Time:	**23.Mrz.15 17:05**	*Sample Weight:*	**1,0000**

Chromatogram

Integration Results

No.	Peak Name	Retention Time min	Area mAU*min	Height mAU	Relative Area %	Relative Height %	Amount n.a.
1		22,557	57,419	87,566	14,28	17,19	n.a.
2		24,617	344,568	421,694	85,72	82,81	n.a.
Total:			**401,986**	**509,260**	**100,00**	**100,00**	

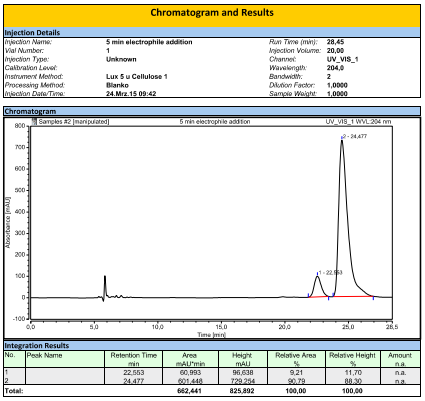

Chromatogram and Results

Injection Details

Injection Name:	**5 min electrophile addition**	*Run Time (min):*	**28,45**
Vial Number:	**1**	*Injection Volume:*	**20,00**
Injection Type:	**Unknown**	*Channel:*	**UV_VIS_1**
Calibration Level:		*Wavelength:*	**204,0**
Instrument Method:	**Lux 5 u Cellulose 1**	*Bandwidth:*	**2**
Processing Method:	**Blanko**	*Dilution Factor:*	**1,0000**
Injection Date/Time:	**24.Mrz.15 09:42**	*Sample Weight:*	**1,0000**

Chromatogram

Integration Results

No.	Peak Name	Retention Time min	Area mAU*min	Height mAU	Relative Area %	Relative Height %	Amount n.a.
1		22,553	60,993	96,638	9,21	11,70	n.a.
2		24,477	601,448	729,254	90,79	88,30	n.a.
Total:			**662,441**	**825,892**	**100,00**	**100,00**	

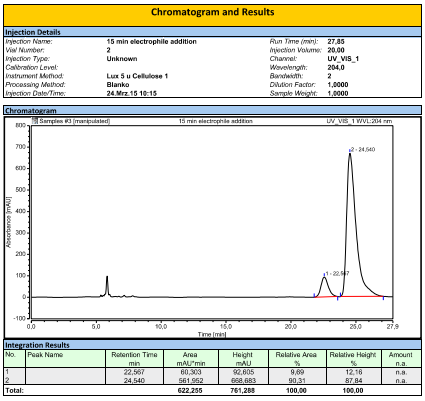

Chromatogram and Results

Injection Details

Injection Name:	**15 min electrophile addition**	*Run Time (min):*	**27,85**
Vial Number:	**2**	*Injection Volume:*	**20,00**
Injection Type:	**Unknown**	*Channel:*	**UV_VIS_1**
Calibration Level:		*Wavelength:*	**204,0**
Instrument Method:	**Lux 5 u Cellulose 1**	*Bandwidth:*	**2**
Processing Method:	**Blanko**	*Dilution Factor:*	**1,0000**
Injection Date/Time:	**24.Mrz.15 10:15**	*Sample Weight:*	**1,0000**

Chromatogram

Integration Results

No.	Peak Name	Retention Time min	Area mAU*min	Height mAU	Relative Area %	Relative Height %	Amount n.a.
1		22,567	60,303	92,605	9,69	12,16	n.a.
2		24,540	561,952	668,683	90,31	87,84	n.a.
Total:			**622,255**	**761,288**	**100,00**	**100,00**	

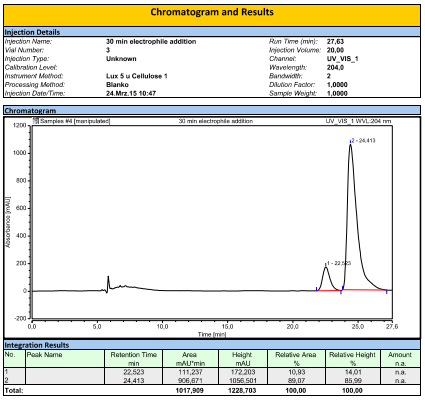

Chromatogram and Results

Injection Details

Injection Name:	**30 min electrophile addition**	*Run Time (min):*	**27,63**
Vial Number:	**3**	*Injection Volume:*	**20,00**
Injection Type:	**Unknown**	*Channel:*	**UV_VIS_1**
Calibration Level:		*Wavelength:*	**204,0**
Instrument Method:	**Lux 5 u Cellulose 1**	*Bandwidth:*	**2**
Processing Method:	**Blanko**	*Dilution Factor:*	**1,0000**
Injection Date/Time:	**24.Mrz.15 10:47**	*Sample Weight:*	**1,0000**

Chromatogram

Integration Results

No.	Peak Name	Retention Time min	Area mAU*min	Height mAU	Relative Area %	Relative Height %	Amount n.a.
1		22,523	111,257	172,203	10,93	14,01	n.a.
2		24,413	906,671	1056,501	89,07	85,99	n.a.
Total:			**1017,909**	**1228,703**	**100,00**	**100,00**	

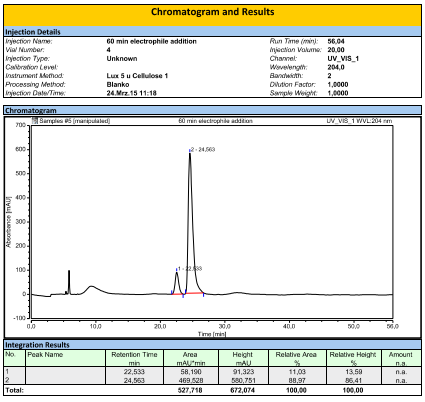

Chromatogram and Results

Injection Details

Injection Name:	**60 min electrophile addition**	*Run Time (min):*	**56,04**
Vial Number:	**4**	*Injection Volume:*	**20,00**
Injection Type:	**Unknown**	*Channel:*	**UV_VIS_1**
Calibration Level:		*Wavelength:*	**204,0**
Instrument Method:	**Lux 5 u Cellulose 1**	*Bandwidth:*	**2**
Processing Method:	**Blanko**	*Dilution Factor:*	**1,0000**
Injection Date/Time:	**24.Mrz.15 11:18**	*Sample Weight:*	**1,0000**

Chromatogram

Integration Results

No.	Peak Name	Retention Time min	Area mAU*min	Height mAU	Relative Area %	Relative Height %	Amount n.a.
1		22,533	58,190	91,323	11,03	13,59	n.a.
2		24,563	469,528	580,751	88,97	86,41	n.a.
Total:			**527,718**	**672,074**	**100,00**	**100,00**	

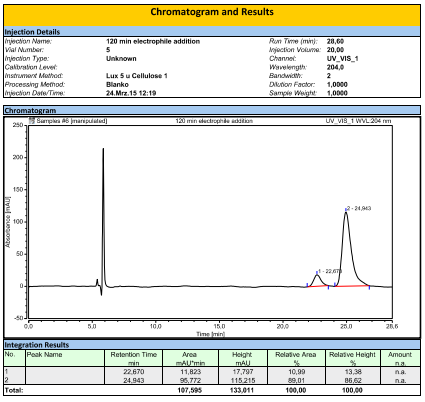

Chromatogram and Results

Injection Details

Injection Name:	**120 min electrophile addition**	*Run Time (min):*	**28,60**
Vial Number:	**5**	*Injection Volume:*	**20,00**
Injection Type:	**Unknown**	*Channel:*	**UV_VIS_1**
Calibration Level:		*Wavelength:*	**204,0**
Instrument Method:	**Lux 5 u Cellulose 1**	*Bandwidth:*	**2**
Processing Method:	**Blanko**	*Dilution Factor:*	**1,0000**
Injection Date/Time:	**24.Mrz.15 12:19**	*Sample Weight:*	**1,0000**

Chromatogram

Integration Results

No.	Peak Name	Retention Time min	Area mAU*min	Height mAU	Relative Area %	Relative Height %	Amount n.a.
1		22,670	11,823	17,797	10,99	13,38	n.a.
2		24,843	95,772	115,215	89,01	86,62	n.a.
Total:			**107,595**	**133,011**	**100,00**	**100,00**	

Table 3. Summary of experimental *ee* values for catalysts **A-C** with the corresponding incubation times (time before electrophile was added). The products was synthesized and purified according to the general procedure above. *Ee* value determination was conducted as indicated above.

Incubation time [min]	Catalyst **A**	Catalyst **B**	Catalyst **C**
0	23	51	71
5	23	42	82
15	25	51	81
30	24	45	78
60	33	49	78
120	32	49	78

To prove the influence of the *Z/E* ratio to the *ee* values of the γ-products, reactions with different incubation times, i.e. the time before adding the electrophile, were made. During the incubation time the *Z/E* ratio was supposed to be changed due to isomerization from *Z*-dienamine to the thermodynamically more stable *E*-dienamie. However, as shown in Table 3, we could not find any correlation between the incubation time and the resulting *ee* values.

2.6.6 UV/Vis Spectra

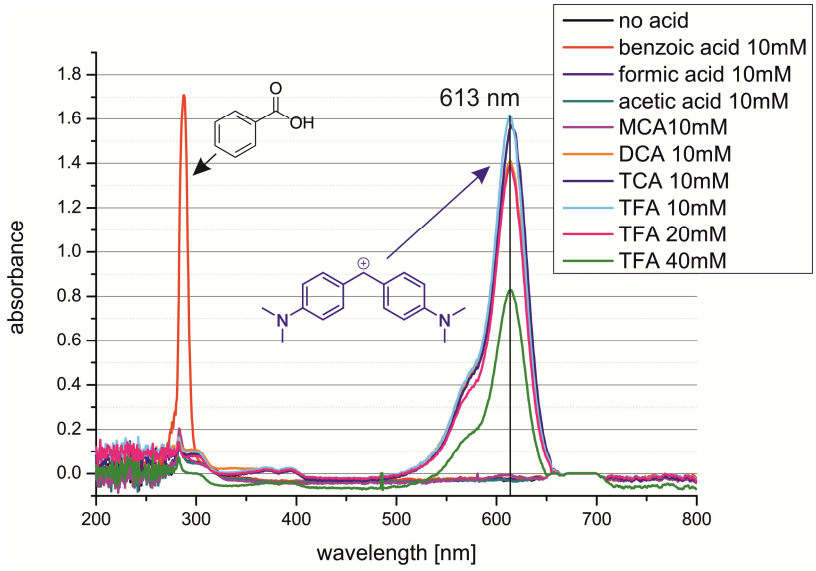

UV/Vis absorbance spectra of Michler's hydrol (15 µM) under the different acids (10 mM) in toluene, indicating a dependence of the amount of the resulting E^+ species and the p*K*a value.

2.6.7 Computational Studies

For details see Appendix (DVD).

2.6.8 References

(1) Schmid, M. B.; Zeitler, K.; Gschwind, R. M. *Chem. Sci.* **2011,** *2*, 1793

(2) Cai, M.; Huang, Y.; Liu, J.; Krishnamoorthi, R. *J. Biomol. NMR* **1995**, *6*, 123.

(3) Grimme, S. Chem. - A Eur. J. 2012, 18, 9955.

3 Chemical Exchange Saturation Transfer in Chemical Reactions: A Mechanistic Tool for NMR Detection and Characterization of Transient Intermediates

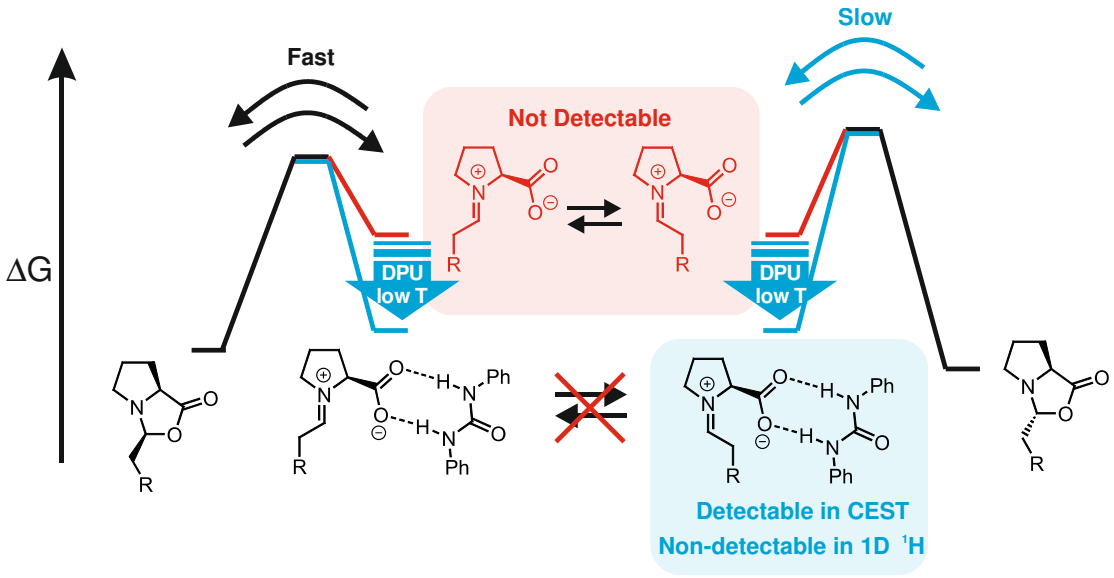

N. Lokesh, **Andreas Seegerer**, Johnny Hioe, and Ruth M. Gschwind*

J. Am. Chem. Soc., **2018**, *140*, 1855–1862

DOI: 10.1021/jacs.7b12343

Initial low temperature and DPU stabilization experiments in DMF-d_7 by NMR spectroscopy leading to the first detection of an iminium ion in this system, as well as the synthesis of deuterated DPU-d_{10} were done by Andreas Seegerer. The implementation and application of the CEST method and the analysis of all experimental exchange rates were performed by N. Lokesh. All computational studies were done by Dr. Johnny Hioe.

3.1 Abstract

The low sensitivity of NMR and transient key intermediates below detection limit are the central problems studying reaction mechanisms by NMR. Sensitivity can be enhanced by hyperpolarization techniques such as dynamic nuclear polarization or the incorporation/interaction of special hyperpolarized molecules. However, all of these techniques require special equipment, are restricted to selective reactions, or undesirably influence the reaction pathways. Here, we apply the chemical exchange saturation transfer (CEST) technique for the first time to NMR detect and characterize previously unobserved transient reaction intermediates in organocatalysis. The higher sensitivity of CEST and chemical equilibria present in the reaction pathway are exploited to access population and kinetics information of low populated intermediates. The potential of the method is demonstrated on the proline-catalyzed enamine formation for unprecedented *in situ* detection of a DPU stabilized zwitterionic iminium species, the elusive key intermediate between enamine and oxazolidinones. The quantitative analysis of CEST data at 250 K revealed the population ratio of [*Z*-iminium]/[*exo*-oxazolidinone] 0.02, relative free energy +8.1 kJ/mol (calculated +7.3 kJ/mol), and free energy barrier of +45.9 kJ/mol ($\Delta G^{\ddagger}_{calc.}$(268 K)= +42.2 kJ/mol) for *Z*-iminium → *exo*-oxazolidinone. The findings underpin the iminium ion participation in enamine formation pathway corroborating our earlier theoretical prediction and help in better understanding. The reliability of CEST is validated using 1D EXSY-build-up techniques at low temperature (213 K). The CEST method thus serves as a new tool for mechanistic investigations in organocatalysis to access key information, such as chemical shifts, populations, and reaction kinetics of intermediates below the standard NMR detection limit.

3.2 Introduction

NMR spectroscopy is a key method to reveal and interpret reaction mechanisms in chemical and catalytic reactions due to its unique potential to provide experimental information about structures, aggregation, and interactions in solution.[1–7] However, the main drawback of NMR spectroscopy is its inherent insensitivity compared to other methods like UV/Vis or mass spectrometry, which often limits its applicability. For the mechanistic investigation of chemical reactions by NMR, this drawback is especially serious, since in most reactions the intermediates, which are key to the reaction mechanism, are low populated, short lived, and most often below the detection limit. Failure in observing such key intermediates (missing evidence) often leads to ambiguity in understanding the reaction pathway. The theoretical calculations can assist in predicting possible mechanistic pathways, however, the experimental detection of more active intermediates and its kinetic data during the reaction is essential to pinpoint the most plausible pathway.

One notable example is the proline or proline derivative-mediated enamine catalysis, which evolved as a versatile tool in a broad scope of enantioselective transformations of carbonyl compounds.[8–10] However, for almost a decade, an *in situ* detection of the central enamine intermediate in proline-catalyzed aldol reaction was lacking, leading to controversial discussions about its formation,[11–18] stabilization,[4,19] and the subsequent transformation pathways. In the earlier stage, Seebach and Eschenmoser suggested that the observed oxazolidinone exists in equilibrium with the enamines (Figure 1).[14] In 2010 our group was able to NMR detect and characterize the *in situ* generated enamine intermediate through solvent/additive-induced stabilization.[4,16,19,20] The observed chemical exchange between oxazolidinone and enamine and the missing evidence for iminium ion were strongly indicative for an enamine formation via oxazolidinone (referred as oxazolidinone pathway, Figure 1).[14] Further, this was also supported by recent kinetic isotope effect measurements for a L-proline catalyzed α-amination of 3-phenyl-propionalaldehyde.[21] In contrast, List and Houk proposed an enamine formation via zwitterionic iminium ion intermediates (referred as iminium pathway, Figure 1),[9,12,17,18] supported by DFT-calculations.[11] The recent kinetic studies in our working group[15] revealed that enamine formation rate and barrier conform to the calculated pathway via iminium intermediate. Furthermore, the barriers of the ring opening step from oxazolidinone toward the iminium intermediate are generally much lower than the proton

abstraction to form enamine and *exo* ↔ *endo* interconversion via double bond rotation (Figure 1).[15]

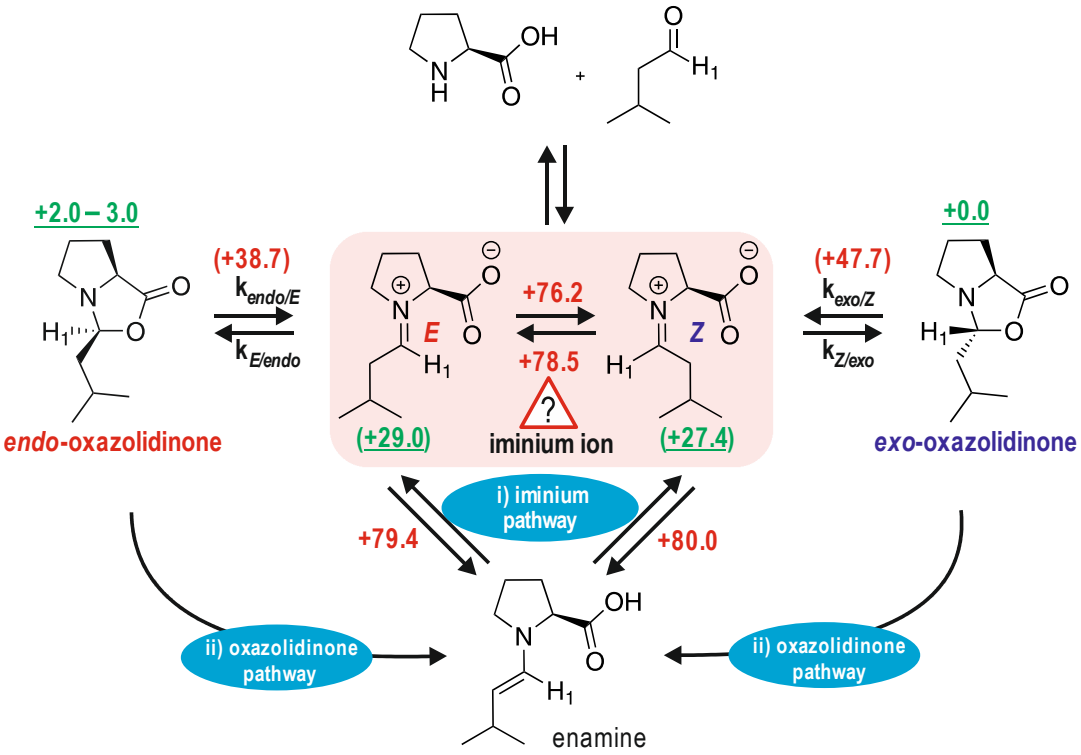

Figure 1. Formation of enamine, the central iminium ion intermediates are elusive. i) iminium pathway: formation of enamine by deprotonation of an iminium ion; ii) oxazolidinone pathway: direct formation of enamine by deprotonation of a oxazolidinone intermediate. The energy values shown are obtained from theoretical calculations (with parentheses) and experiments (without parentheses).[15] **Green** (underlined): relative free energy to *exo*-oxazolidinone in DMSO at 300 K. **Red**: free energy barrier predicted by theory and measured from EXSY-experiment in DMSO at 300 K.[15] All calculations were performed without any external base.

Despite the quantitative agreement to the kinetic data, the existence of such unstable zwitterionic intermediates remains intriguing. Recent higher level theoretical calculation showed that the *E*/*Z*-iminium intermediates are indeed located about 27-30 kJ/mol higher than the corresponding *endo*/*exo*-oxazolidinone even in high polar medium.[15] According to Boltzmann distribution, this corresponds to a population of 0.03% relative to oxazolidinones (µM amount in reaction condition), which is unlikely to be detected by conventional NMR. To prove the possible participation of iminium ions in this L-proline catalyzed reaction, it necessitates more sensitive NMR techniques and/or stabilization methods to increase its amount.

Hyper polarization techniques such as dissolution DNP[22–24], PHIP[25–27], SABRE[25–27], CIDNP/photo CIDNP[28–31] are used to enhance the sensitivity of the NMR signals. However, despite successful detection of low concentrated nuclei,[32] the hyperpolarization techniques lack generality due to additional requirements, such as radicals and microwave in DNP, para hydrogen in PHIP and SABRE, and radical pair presence in CIDNP or photo-CIDNP, which are suitable only to specific reactions or reaction conditions and often alters the chemical pathways. Furthermore, use of cryo-probes can enhance sensitivity, however these are incompatible at low temperatures, which are most often necessary for intermediates stabilization.[1,3]

In this regard, the chemical exchange saturation transfer (CEST) technique has attracted immense interest. The method provides more than 10 fold sensitivity enhancement,[33,34] which is moderate compared to hyperpolarization techniques, but more importantly it does not influence the reaction system as it does not require external agents, such as radicals, para hydrogen etc. For CEST the only requirements are the existence of a chemical exchange in the slow exchange regime on the NMR time scale ($k \leq |\Delta v|$) and one of the chemical exchange species being visible in conventional NMR experiments.[35] CEST can then detect a low populated conformer or species below the conventional NMR detection limit. This is achieved by saturation transfer of selectively saturated nuclei from low populated site to major populated site via chemical/conformational exchange. During the saturation process, more numbers of saturated nuclei from a low populated site accumulate at major populated site resulting in a decrease in intensity of major populated nuclei peak, which is more amplified than direct detection of low populated nuclei.[35] The CEST method does not require any pre knowledge of chemical shift information, as the method involves a stepwise systematic scanning of the chemical shift regions by selective saturation. The decrease in intensity as a function of saturation offset (chemical shift) provides information about relative population, structure, and rate of exchange of saturated molecule via Bloch–McConnell equations.[36–38] However, CEST also shows decrease in intensity due to NOE interactions as well, which often complicates the study. Few methods were reported which eliminate NOE interactions.[39,40] In addition, various CEST modules were developed, such as, proton detected, heteronuclear detected, and multiple quantum-based methods to avoid overlapping, cover a broad range of exchange rates, and accelerate the experiment.[41–45]

Initial application of CEST was shown in MRI as an alternative contrast imaging technique.[46–48] In this, the exchangeable protons in exogenous/endogenous compounds are selectively saturated and are detected indirectly through an intensity decrease in the water signal due to saturation transfer, which gives enhanced sensitivity even for low concentrated molecules.[33,34] Recently, the signal amplification obtained in CEST is exploited for very compelling application in detecting invisible conformations of biomolecules, such as proteins and nucleic acids, which were never detected in conventional NMR experiments before.[43,45,49] Despite the broad application of the CEST technique for the study of protein conformations and its high potential to reveal invisible states, to the best of our knowledge, the method has never been employed in reaction intermediate studies of chemical or catalytic reactions so far.

Here, we present for the first time CEST application for detection and characterization of low populated transient reaction intermediates in chemical and catalytic reactions, which are not visible in conventional NMR experiments. The advantage of signal amplification obtained in CEST and present chemical equilibrium in reaction pathway are explored, to prove for the first time *in situ* existence of iminium ion intermediates in enamine catalysis, which are key intermediates in the enamine formation pathway. Furthermore, the population of the invisible intermediate, its thermal stability, and free energy barrier for ring opening and closing are obtained through quantitative analysis of CEST profiles. At low temperature, the reliability of the CEST data about energies and exchange rates is validated by 1D EXSY and computational studies. The detection of such thermodynamically unstable intermediates underpins the formation pathway via iminium ion.

3.3 Results and Discussion

In the following it is described how even a complicated multisite equilibrium in a reaction can be prepared/adapted to the successful application of CEST. For this, mainly three points have to be addressed i) absolute population of the elusive intermediate ii) slow exchange, and iii) reduction of multisite equilibria. Without additives, slow exchange and two site equilibria can be reached at low temperatures, but the population is still too low (see *CEST without Stabilizing Agent*). Upon addition of an additive, its effect on the chemical shifts and the intermediate structures is analyzed (see *DPU as Stabilizing Agent at 300 K*). Applying additive and low temperature, all three requirements for CEST are fulfilled, and theoretical calculations show that the additive does not significantly alter the kinetics of the investigated part of the reaction (see *DPU as Stabilizing Agent at Low Temperature*) allowing its application to detect the elusive iminium intermediate (see *Detection of Z-Iminium via CEST*). The reduction of multisite equilibrium to two site equilibrium allows for the quantitative determination of thermodynamic and kinetic parameters by CEST (see *Population and Kinetics via CEST Profile*). Finally, at very low temperatures, the CEST results were validated by classical 1D EXSY rate measurements, further the benefits of CEST are highlighted over EXSY (see *Validation of CEST Method*).

Model system. To successfully illustrate the potential of CEST for detection and characterization of elusive iminium intermediates, an appropriate model system has to be chosen, which allows simultaneous detection of oxazolidinone diastereomers and enamine intermediates in the reaction by conventional NMR and shows slow chemical exchanges between the intermediates. Based on our earlier experience, the L-proline-catalyzed homo aldol condensation of 3-methylbutanal fulfills these requirements (Figure 1).[4,15,50] In addition, the formed intermediates, that is, *endo*/*exo*-oxazolidinones, enamines, and the substrates, give the best signal separation in NMR for proton H_1 (Figure 2). The proton H_1 of the elusive iminium ion is expected to be found well-separated at around 9 ppm based on our theoretical calculations and earlier reports.[51,52] Thus, in CEST selective saturation around 9 ppm should cause an intensity decrease for the H_1 signal of the oxazolidinones and/or enamines if they are in slow exchange with the elusive iminium intermediates (Figure 1).

CEST without Stabilizing Agent. The recorded 1D ^{1}H NMR spectrum for the reaction shows well-separated signals of the H_1 proton for all three detectable intermediates, enamine, *exo*- and *endo*-oxazolidinone (see highlighted signals in Figure 2A). As expected, the stable oxazolidinone intermediates are observed in 1D ^{1}H NMR (Figure 2), but due to the higher energy, the iminium ion intermediates were not observed. The approximate population of intermediates formed in the investigated reaction are 4 mM, 1.8 mM and 0.7 mM respectively, for *exo*-, *endo*-oxazolidinone and enamine. According to our previous calculation in DMSO, the oxazolidinone is 27-30 kJ/mol more stable than the iminium intermediates,[15] which refers to a population of iminium ions <0.03% or equivalently 1.2 µM in the reaction. This is clearly below the threshold of conventional NMR spectroscopy. However, even CEST measurements with much higher sensitivity (more than 10 fold) at 300 K do not show any decrease of intensities for the H_1-protons of oxazolidinones/enamines on saturating around 9 ppm.

The thermal instability of the iminium intermediates seems to be one of the problems to be solved. Additionally, the calculated activation energy for the ring opening process is low (in DMSO at 300 K, *exo* → *Z* = 47.7 kJ/mol; *endo* → *E* = 38.7 kJ/mol; Figure 1), therefore we expect fast exchange. A common strategy to circumvent both issues is by reducing the temperature to stabilize the charge separated species (i.e., in this case the zwitterionic iminium ions, by increasing the dielectric constant of the medium) and to slow down exchange. Therefore, DMF is used in the investigation, since it is highly polar similar to DMSO, and also allows measurement at low temperature up to 213 K.

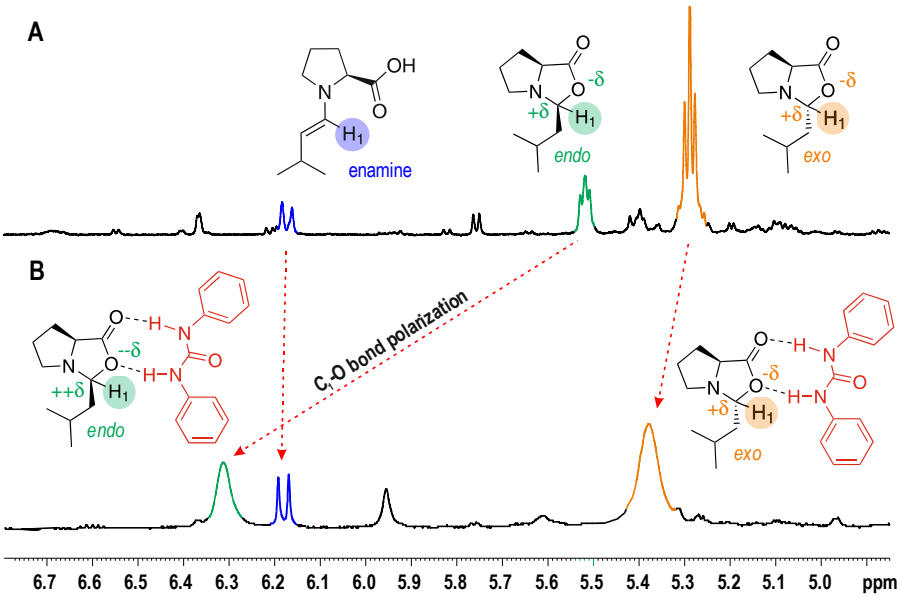

Figure 2. 1D ^{1}H NMR spectra of the reaction mixture of L-proline and 3-methylbutanal in DMF-d_7 at 300 K without (A) and with DPU (B).

However, the low-temperature 1D ^{1}H NMR, 1D EXSY, and CEST experiments down to 215 K did not give any evidence for iminium ion intermediates even though the system is expected to be in the slow exchange regime (see Figure S1 in Supporting Information for spectra without DPU). This implies that the stabilization of charge separated species by increasing dielectric constant is not sufficient to alter the thermal population for the detection even in CEST.

DPU as Stabilizing Agent at 300 K. Therefore, next the iminium population was increased by an additive. It was shown in literature that addition of thiourea derivatives could possibly stabilize proline iminium ion species.[53] As also shown in earlier[19,50] and current studies in DMSO/DMF, a significant downfield shift of H_1 *endo*-oxazolidinone proton ($\Delta\delta$ = 0.8 ppm) upon the addition of 1 equiv of DPU (N,N'-diphenyl urea) to the investigated reaction mixture was observed (Figure 2B). In contrast, only a slight shift for *exo*-oxazolidinone ($\Delta\delta$ = 0.1 ppm), and nearly no shift for the enamine peak is observed.[19,50] For these observations, there are several possible roots, which could induce the shift at 300 K when DPU is added. The first obvious one is the deshielding of H_1 by the aromatic moiety of the DPU, which might be different for *endo*- and *exo*-oxazolidinone. However, from our detailed structural analysis, no particular effect is expected since the aromatic ring is remotely located relative to H_1 of both oxazolidinones (see Supporting Information).

The second possible reason is due to the formation of significant iminium species along with the oxazolidinones, which could be in fast exchange with each other leading to downfield averaged peak for H_1.[50] In that case, the peak location is determined by the population percentage of the two exchanging molecules, that is, *endo* ↔ *E* and *exo* ↔ *Z* (considering negligible exchange between *exo* and *endo*). However, EXSY measurement at 300 K revealed similar interconversion rates for *endo* → *exo* (+72.5 kJ/mol) and *exo* → *endo* (+72.9 kJ/mol) (Figure 3). This indicates a thermodynamic equivalency between *E*- and *Z*-iminium. Furthermore, the population analysis of *endo* and *exo* (peak integration) showed a relatively higher free energy for *endo*-oxazolidinone (2.0 kJ/mol), which puts *E*-iminium energetically nearer to the *endo*-oxazolidinone. Hence, one might tend to expect the more pronounced shift observed for H_1 of *endo*-oxazolidinone. Nevertheless, as it will be indicated later by CEST, at 300 K the population of the *E*/*Z*-iminium is expected to be very low ([*Z*-iminium]/[*exo*] < 2% or $\Delta G_{Z\text{-}exo}$(300 K) > 9.5 kJ/mol; *E*-iminium/[*endo*] < 5% or $\Delta G_{E\text{-}endo}$(300 K) > 7.5 kJ/mol). Given an expected H_1 shift of the iminium species located at ~9 ppm,[51,52] such low iminium population cannot contribute significantly to the observed average shift

(maximum Δδ = 0.18 ppm shift in case of 5% *E*-iminium population and 95% *endo*-oxazolidinone).

A third possible explanation is provided by the charge and structural analysis of oxazolidinones. Detailed structural analysis revealed that the C_1-O bond is elongated by the complexation with DPU, however, more pronounced in *endo*-oxazolidinone than in *exo*-oxazolidinone (see Supporting Information; H_1 is attached to C_1). Consequently, the developed charge polarization along the C_1-O bond in oxazolidinones causes the deshielding effect for H_1 (stronger in *endo*, Figure 2B, Supporting Information). Therefore, contrary to the general expectation, the major effect observed at 300 K is not due to the population of iminium ion in the system, but rather due to the increased polarization of the C_1-O bond.

At this point, the observed H_1 chemical shift change only indicates a significant interaction between oxazolidinone and DPU. However, the detection and detailed characterization of iminium ions, as well as the kinetics of its formation are not accessible due to low iminium ion population and too fast exchange at 300 K.

DPU as Stabilizing Agent at Low Temperature. Therefore, the reaction mixture was cooled again to minimize the chemical exchange between the intermediates and to stabilize the iminium ion. On decreasing the temperature until 250 K, a continued downfield shift and broadening for the H_1-signal of *endo*-oxazolidinone is observed (Figure 3A and 3B). This significant shift is attributed to both C_1-O polarization and interconversion between *endo* ↔ *E*-iminium ion. However, at low temperature, downfield shift is expected mainly due to increased population of zwitterionic *E*-iminium ion. Below 250 K, the peak completely diminishes due to broadening (Figure 3A), and we were unable to reach the slow exchange regime for the application of CEST (detailed estimation for the population of *E*-iminium ion and *endo*-oxazolidinone through classical peak analysis is shown in the Supporting Information). On the other hand, a slight upfield shift (Figure 3B) and line broadening on down to 280 K (Figure 3A, coalescence point) is observed for H_1 signal of *exo*-oxazolidinone, indicating a possible *exo*-oxazolidinone ↔ *Z*-iminium exchange shift to the slow exchange regime. On further decreasing the temperature (< 280 K), the broadened peak becomes narrower (Figure 3A). This narrower-broader-narrower profile confirms slow exchange regime for *exo*-oxazolidinone ↔ *Z*-iminium, which is a prerequisite for the application of CEST.

The quantum chemical calculations showed that the *E*/*Z*-iminium intermediates are massively stabilized by the presence of DPU due to the H-bond formation (ΔG_{268} *Z*-iminium vs *exo* = +7.2 kJ/mol and ΔG_{268} *E*-iminium vs *endo* = +2.8 kJ/mol, Figure 3C).

Moreover, the calculated free energy difference between *E*- and *Z*- iminium at 268 K amounts to 1.6 kJ/mol in favor of *E*-iminium. Surprisingly, the ring opening barriers were not affected significantly by the complexation with the additive ($\Delta G^{\ddagger}_{268}$ = +35.8 kJ/mol for *endo* → *E* and +49.5 kJ/mol for *exo* → *Z,* Figure 3C; see Figure 1 for barriers without DPU). At low temperature (T ≤ 250 K), apart from the exchange between iminium and oxazolidinone, no exchange is possible between *endo*/*exo* ↔ enamine and *exo* ↔ *endo or Z* ↔ *E* (1D ^{1}H EXSY showed no exchange peak, Figure 4B) due to the high barrier for deprotonation and double bond rotation (Figure 3C: Measured $\Delta G^{\ddagger}_{300}$ *exo* ↔ *endo* and *exo*/*endo* ↔ enamine; $\Delta G^{\ddagger}_{T}$ is quasiconstant over temperature 215 to 300 K). Thus, we expect that the reduced thermal energy permits only the ring opening process to occur during T_1 time scale (Figure 3C), the remaining exchange pathways are by far slow or nil and do not interfere with CEST application. Thus, the application of low temperature simplifies the complex multisite exchange system of the enamine catalysis into two site slow exchange equilibrium on CEST experimental timescale (T_1 time scale), which allows a straightforward and reliable extraction of kinetic and thermodynamic information on iminium ion from CEST.

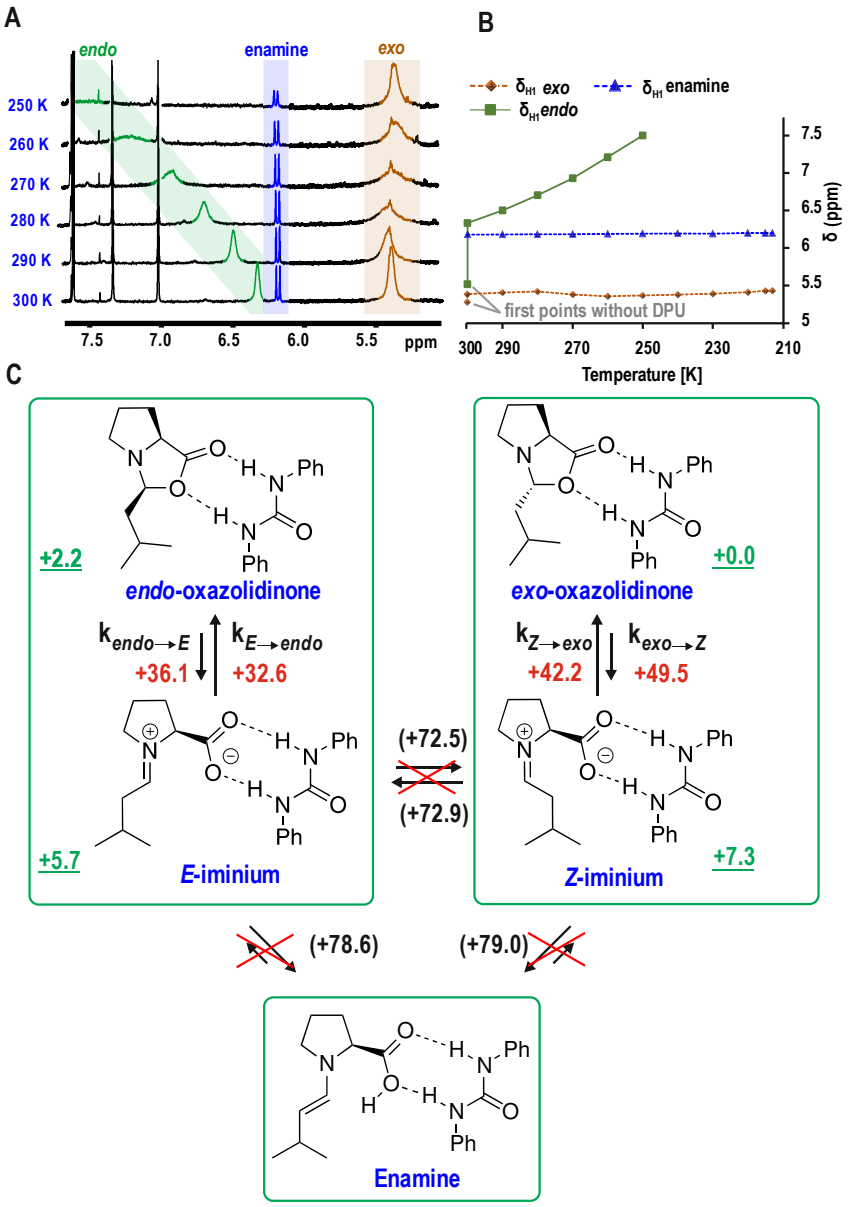

Figure 3. Temperature dependent stacked ^{1}H 1D spectra (A) with decrease in temperature H_1 of *endo*-oxazolidinone peak shows line broadening and downfield shift, and H_1 of *exo*-oxazolidinone shows narrower-broader-narrower profile indicating shift of *exo* ↔ *Z* exchange to slow exchange regime. Temperature-dependent plot of H_1 peak shift of *exo*- and *endo*-oxazolidinone and enamine in presence of DPU (the first points at 300 K are without DPU) (B). At low temperature, no chemical exchange occurs between *exo*- and *endo*-oxazolidinone via iminium (T < 250 K) as well as oxazolidinones and the enamine (T < 270 K). Numbers (kJ/mol) indicated in black with parenthesis: experimental free energy barrier from EXSY at 300 K; red: calculated free energy barrier at 268 K; green (underlined): calculated relative Gibbs free energy at 268 K (C).

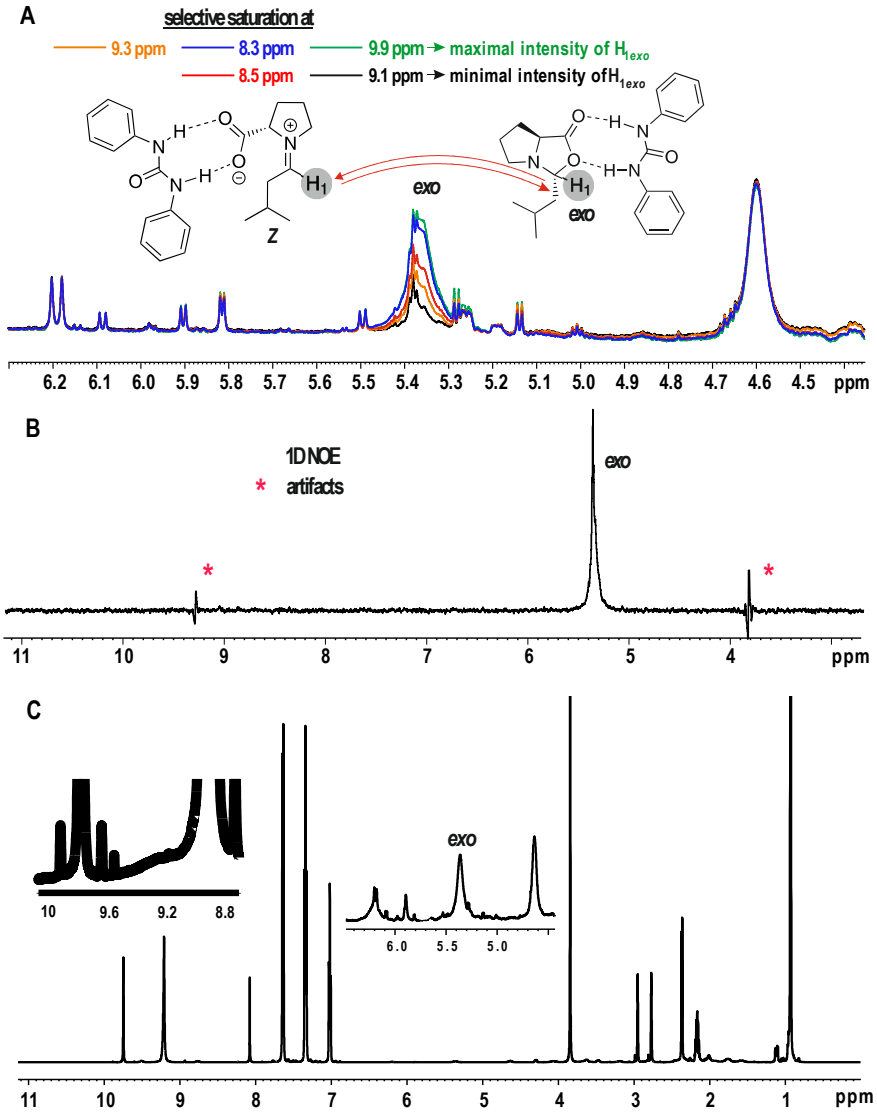

Figure 4. CEST (A), 1D ^{1}H EXSY with mixing time 450 ms (B), 1D ^{1}H NMR (C) spectra at 250 K. CEST shows decrease in intensity of *exo*-oxazolidinone due to saturation transfer from iminium, confirming the presence of iminium ions. EXSY shows no observation of iminium ion. Inset shows scaled *exo*-oxazolidinone intermediate peak from 1D ^{1}H spectrum (C).

Detection of *Z*-Iminium via CEST. After successfully preparing the system for complying the prerequisites, slow exchange regime and two site equilibrium, the system is examined for iminium detection by CEST. The temperature was cooled stepwise, each step down by 10 K. At each temperature, the 1D CEST experiments were recorded as described above, while selectively saturating around 9 ppm and monitoring the intensity of the oxazolidinone peaks. Above 250 K, no reduction was observed, but at 250 K, the measured CEST experiment showed a decrease in intensity for the *exo*-oxazolidinone

peak (Figure 4A). The decrease in intensity is pronounced as selective saturation approaches 9.12 ppm. At 9.12 ppm a maximum drop in intensity was observed, which lessens as the selective saturation moves away from 9.12 ppm. This indicates the presence of a transient iminium ion intermediate at 9.12 ppm, which chemically exchanges with *exo*-oxazolidinone. As discussed above, the high energy barrier between *exo*- and *endo*-oxazolidinone (Figure 3C: $\Delta G^{\ddagger}_{300}$ *exo* → *endo* = +72.9 kJ/mol; *endo* → *exo* = +72.5 kJ/mol) completely excludes interconversion between *exo*- and *endo*-oxazolidinone via C=N double bond rotation at T ≤ 250 K, which is evidenced by the EXSY showing no exchange between the two diastereomers (Figure 4B). Since the intensity decrease is only observed for H_1-*exo*-oxazolidinone, it implies the detected iminium ion is *Z*-configured (Figure 3C).

Thus, CEST enables the first detection of an iminium ion intermediate in this enamine formation. In contrast, the selective 1D ^{1}H EXSY for the same reaction mixture at the same conditions does not show any exchange peak at 9.12 ppm on selective excitation of the *exo*-oxazolidinone peak (Figure 4B). Due to the low population of the iminium ion under these conditions, the sensitivity of EXSY or other conventional NMR methods is insufficient to detect the transient intermediates. The iminium ion observation only in CEST clearly highlights its potential in detection of transient reaction intermediates. Importantly it does not require any additional hyperpolarizing sources and hence gives information about intermediates without influencing the chemical systems. Additionally, the method is also possible in case of high spectral complexity (Figure 4C).

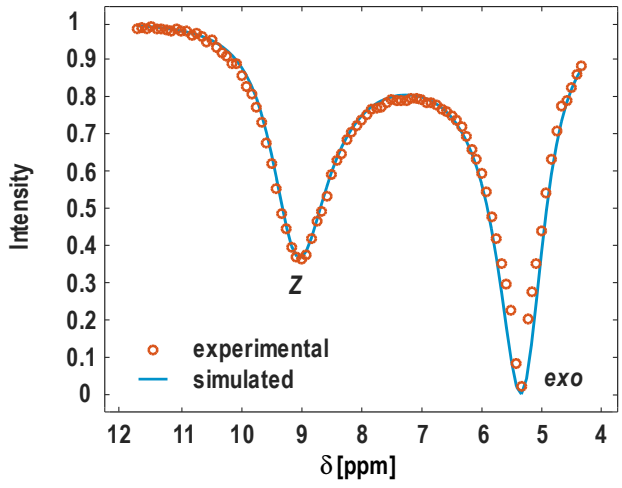

Figure 5. CEST profile at 250 K; intensity variation of H_1 *exo* peak on stepwise selective saturation over chemical shift. The major dip at 5.4 ppm is due to saturation of the H_1 *exo* peak itself and minor peak is due to saturation transfer from *Z*-iminium ion.

Population and Kinetics via CEST Profile. In the subsequent step, a complete CEST profile, that is, a plot of intensity change of *exo*-oxazolidinone peak vs chemical shift of selective saturation was generated to determine the population of the *Z*-iminium ion and to measure the rate of ring opening/ring closing (Figure 5, circles). To access encoded information, exchange rates and population ratio [*Z*]/[*exo*], a two site exchange CEST profile (Figure 5, blue curve) was simulated by using Bloch–McConnell equations,[36–38] which correlates concentration of exchange species, longitudinal relaxation rates, and exchange rate constants (Supporting information).

Table 1. Relative Populations and Rate Constants Measured from CEST and 1D EXSY

		CEST		1D EXSY
temperature (K)	[*Z*]/[*exo*]	$k_{z/exo}$ (s^{-1})	$k_{exo/z}$ (s^{-1})	$k_{exo\,/\,z}$ (s^{-1})
250 K	0.02	1300 ± 50	26 ±2	n.a.
213 K	0.08	50 ± 3	4 ± 1	2.15 ± 1

Subsequently, the simulated data were fitted to the experimental data (Figure 5) with a multiparameter optimization. The parameters concentration of *exo*-oxazolidinone (M_{exo} = 1) and the longitudinal relaxation times of oxazolidinone (T_{1exo}) and *Z*-iminium ion (T_{1z}) are fixed, while varying the concentration of *Z*-iminium ion (M_{imi}) and the rate of ring closing ($k_{Z\rightarrow exo}$). The longitudinal relaxation time (T_{1exo} = 1.8 s) of *exo*-oxazolidinone was obtained by an inversion recovery experiment while saturating the iminium ion resonance at 9.12 ppm. The same T_1 value was assumed for the corresponding *Z*-iminium ion as well. The solutions of Bloch-McConnell equations and data fitting procedure are followed as mentioned in earlier reports[37,54] and discussed in the Supporting Information. The obtained rates of exchange $k_{Z\rightarrow exo}$, $k_{exo\rightarrow Z}$ and the population of *Z*-iminium ion are reported in Table 1. We could obtain a ring closing rate constant of $k_{Z\rightarrow exo} \approx 1300\ s^{-1}$ and a ring opening rate constant $k_{exo\rightarrow Z} \approx 26\ s^{-1}$ at 250 K. The relative population collected from CEST is *Z*/*exo* ≈ 0.02, which corresponds to +8.1 kJ/mol free energy difference in favor for *exo*. The free energy barriers at 250 K calculated for ring closing and ring opening from the rates by using Eyring equation are +45.9 and +54 kJ/mol, respectively. The energies obtained are in good agreement with our theoretical data ($\Delta G^{\ddagger}_{268}$ = +42.2 kJ/mol *Z* → *exo* and +49.5 kJ/mol for *exo* → *Z*). This quantitative information of iminium ions fills the missed blanks in enamine reaction pathway, assisting in better understanding.

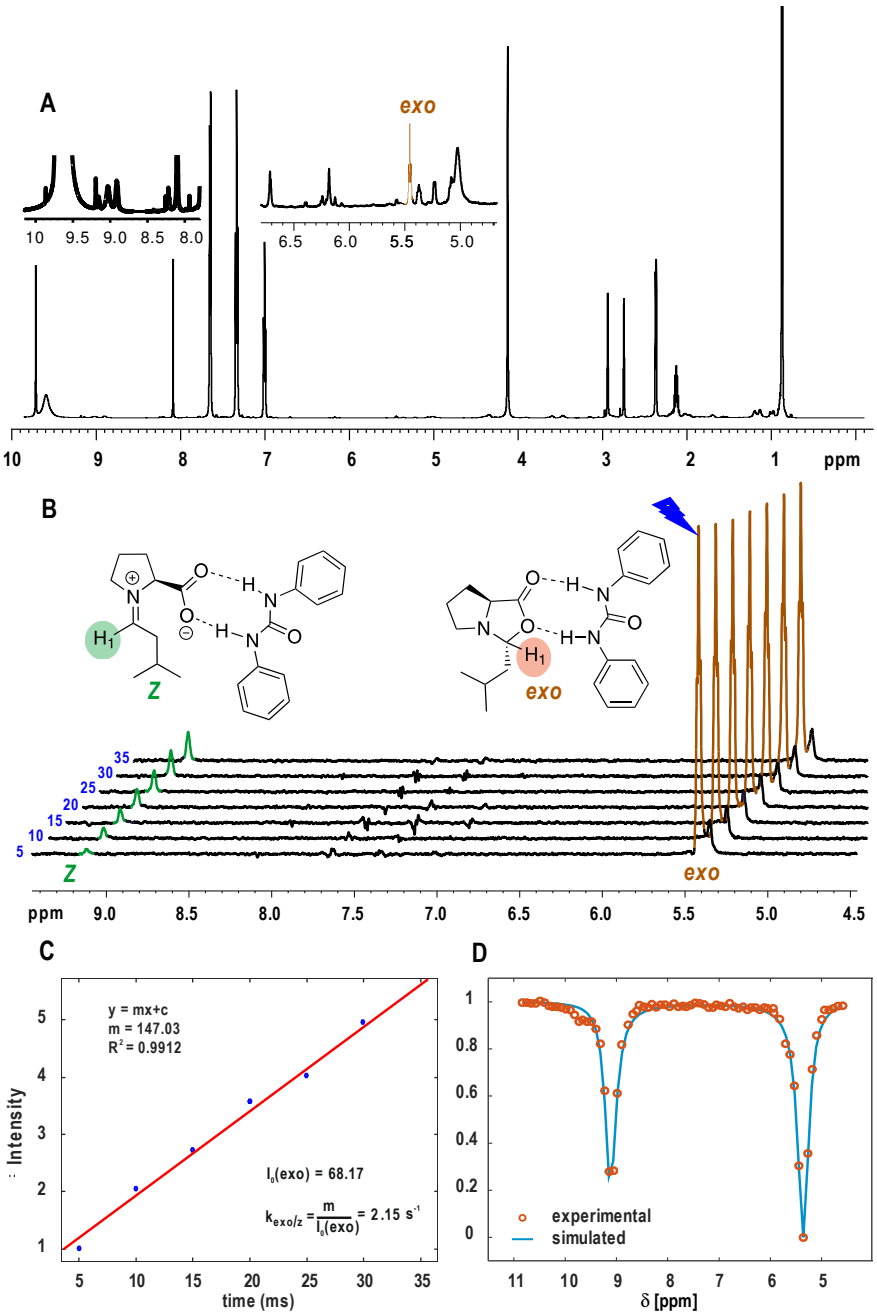

Figure 6. Normal 1D ^{1}H spectrum, show two scaled regions around 5.5 ppm and 9 ppm at 213 K (A). 1D 1H EXSY stacked spectra with different mixing time, in ms increments (B). Linear plot of intensity of iminium peak obtained from 1D EXSY vs mixing time for measurement of exchange rate (C). CEST experimental (circles) and simulated (curve) spectra at 213 K (D).

Validation of CEST Method. The CEST measurements and its profile indicated that the population of the *Z*-iminium is still by far too low to be detected by conventional NMR (80 µM). The traditional way to increase the population and minimize the transiency of the charge separated intermediate is to increase the dielectricity of the solvent by decreasing the measurement temperature. Indeed, at 213 K, we could observe a 4-fold enhancement of the iminium intermediate population by CEST (0.32 mM). The enhancement allows us also to detect the iminium species by conventional NMR (Figure 6A). Additionally, at this temperature we detected an exchange peak at 9.12 ppm in the conventional 1D EXSY experiment by the selective excitation of the H_1 *exo*-oxazolidinone peak (5.4 ppm; Figure 6B).

This gives us the opportunity to compare both CEST and 1D EXSY data for exchange rate measurements. Therefore, a series of 1D EXSY experiments were recorded with different mixing times (5-35 ms in 5 ms increment), the obtained spectra are shown in Figure 6B. To determine the rate constant from the EXSY data, a plot of intensity of the *Z*-iminium peak vs mixing time is generated (Figure 6B-C). It is known that in the initial linear buildup, the slope directly gives the rate of exchange from *exo*-oxazolidinone to *Z*-iminium ion.[15] From the rate and the initial *exo*-oxazolidinone concentration (I_0(*exo*)), the rate constant for ring opening, $k_{exo/Z} \approx 2.15\ s^{-1}$ is obtained (Figure 6C). The initial intensity (I_0(*exo*)) is obtained by back calculation from the spectra.

For comparison, CEST experiments were recorded at 213 K for the same mixture. The plotted CEST spectra are shown in Figure 6D. Again the rate constant and population of *Z*-iminium are extracted by comparing with simulated spectra from the Bloch-McConnell equations; the shown circles are experimental data and the curve represents a simulated profile. For simulating the CEST profile a relaxation time T_1=0.8 s was used for both *exo*-oxazolidinone and *Z*-iminium ion, which was obtained from inversion recovery experiment for *exo*-oxazolidinone peak while on saturating at 9.12 ppm. The obtained rate constants and population are compared and are tabulated in Table 1. At 213 K, the obtained rate constants from 1D EXSY and CEST for ring opening are $k_{exo \rightarrow Z} \approx 2.15\ s^{-1}$ and 4 s^{-1} respectively. The values obtained from both methods are of the same magnitude and hence it validates CEST [within experimental error 5-7%]. The reduced exchange rate at 213 K results in narrower line width for CEST profile (Figure 6D) compared to linewidths in CEST profile at 250 K (higher exchange rates; Figure 5).

Even at 213 K, CEST shows comparatively a stronger amplified signal for *Z*-iminium ion than in the 1D EXSY spectra. In addition CEST provides information about the concentration of *Z*-iminium ion and both rate constants of ring closing ($k_{Z \rightarrow exo}$) and ring

opening ($k_{exo \rightarrow Z}$). In this case the obtained relative concentration of *Z*-iminium is [*Z*]/[*exo*] ≈ 0.08, rate constant for ring closing is ≈ 50 s^{-1}, and rate constant for ring opening is ≈ 4 s^{-1}. The corresponding activation barrier obtained for ring closing and ring opening are 44.1 and 49.1 kJ/mol, respectively. On the other hand 1D EXSY only gives the rate constant of ring opening ($k_{exo \rightarrow Z}$). A difficulty in the integration of ^1H peak of *Z*-iminium ion in 1D ^1H due to low intensity and overlap of other peaks (Figure 6A) restricts the extraction of population and rate constant $k_{Z \rightarrow exo}$. Furthermore, extraction of rate constants from 1D EXSY needs a series of experiments with varied mixing time and it needs to satisfy linear relationship, which takes more time and is a serious problem particularly for low concentrated nuclei. This more often violates linearity relationship between intensity buildup and mixing time.

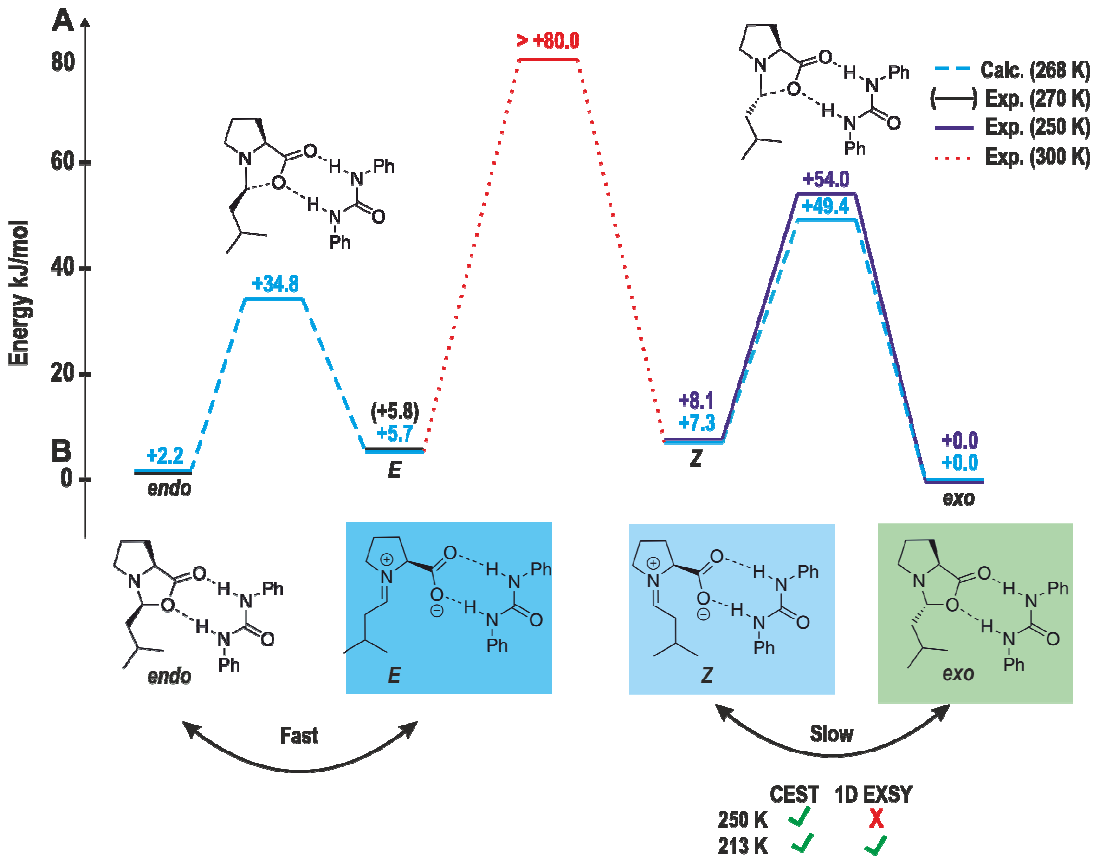

Figure 7. Compared thermal energies and free energies barrier obtained from experimental and theoretical calculations for *endo*-, *exo*-oxazolidinone, *E* and *Z*-iminium. For the *exo* ↔ *endo* exchange, the barrier was taken from the data at 300 K. The relative energy of *endo* to *exo* could not be obtained at 250 K, but assumed as the similar to the theoretical value at 268 K (Blue with dashed lines).

In summary, the experimental results gained by the application of CEST in combination with 1D EXSY and high-level theoretical calculations provide detailed free energy landscape of *E*, *Z*-iminium ions, *endo* as well as *exo*-oxazolidinone in enamine formation pathway (Figure 7). The unprecedented detection of the *Z*-iminium ion intermediate, accessed free energies, and free energy barriers between *E* ↔ *endo* (calculated) and *Z* ↔ *exo* (experimental and calculated) verify our earlier theoretical calculations supporting the iminium pathway in the present system.

Computational Details.

The geometry of all intermediates and transition states were optimized at TPSS-D3/def2-SVP level of theory in continuum (CPCM) of DMF. The dielectric constant of the solvent (DMF) was modified to mimic low temperature condition of the NMR measurement ($\varepsilon_{268\text{-}215K}$ = 42.99-55.08). Nevertheless, the relative energy of the intermediates does not change significantly (<1 kJ/mol) upon variation of dielectric constants. However, at low temperature theoretical calculations fail to predict correct populations of iminium ions due to difficulties to simulate the effect of dielectricity changes of polar solvents (DMF).

Subsequently thermochemical analysis was performed to identify unambiguously the minima (zero imaginary vibrational mode) and maxima (exactly one imaginary vibrational mode). Single points calculations at DLPNO-CCSD(T)/CBS level of theory were added above the optimized geometry (for the extrapolation procedure see Supporting Information).[55,56] The software used for optimization, frequency analysis, and NMR shifts calculation was Gaussian09 D.01.[57] For the single points ORCA 3.0.3 was employed.[58] NBO6.0 was used for charge analysis.[59]

3.4 Conclusion

The study illustrates the high potential of the CEST method as a mechanistic tool to detect low populated intermediates (inaccessible to classical NMR methods), enabling new insights into the reaction pathway. In addition to the enhanced sensitivity, CEST provides thermodynamic and kinetic data of these intermediates in terms of population and exchange rates. The obtained detailed information about mechanistic steps between the intermediates assists in experimental validation of theoretically proposed mechanistic pathways. In the present mechanistic study of enamine formation, the CEST elucidates a possible mechanistic pathway by detecting and characterizing the previously missed *in situ* iminium ions. The obtained population and energy barriers pinpointed the iminium pathways and corroborated earlier theoretical predictions. Thus, CEST together with computational studies offer a better approach to probe missing intermediates in the reaction to pinpoint the possible mechanistic pathway.

In general, most of the chemical or catalytic reactions possess equilibria, which can be explored for application of CEST in mechanistic investigations. Further, the method can be combined with other sensitivity enhancement methods, like dissolution DNP, PHIP or use of cryo probes, which can multiple the sensitivity to access ultra-low (nano molar) concentrated intermediates.

3.5 References

(1) Greindl, J.; Hioe, J.; Sorgenfrei, N.; Morana, F.; Gschwind, R. M. *J. Am. Chem. Soc.* **2016**, *138*, 15965.

(2) Seegerer, A.; Hioe, J.; Hammer, M. M.; Morana, F.; Fuchs, P. J. W.; Gschwind, R. M. *J. Am. Chem. Soc.* **2016**, *138*, 9864.

(3) Sorgenfrei, N.; Hioe, J.; Greindl, J.; Rothermel, K.; Morana, F.; Lokesh, N.; Gschwind, R. M. *J. Am. Chem. Soc.* **2016**, *138*, 16345.

(4) Schmid, M. B.; Zeitler, K.; Gschwind, R. M. *Angew. Chem. Int. Ed.* **2010**, *49*, 4997.

(5) Frihed, T. G.; Bols, M.; Pedersen, C. M. *Chem. Rev.* **2015**, *115*, 4963.

(6) Zhang, L.; Ren, Y.; Yue, B.; He, H. *Chem. Commun.* **2012**, *48*, 2370.

(7) Lodewyk, M. W.; Siebert, M. R.; Tantillo, D. J. *Chem. Rev.* **2012**, *112*, 1839.

(8) Marigo, M.; Jørgensen, K. A. In *Enantioselective Organocatalysis*; Wiley-VCH Verlag GmbH & Co. KGaA: Weinheim: Germany, 2007; pp 56–76.

(9) List, B. *Synlett* **2001**, *2001*, 1675.

(10) Mukherjee, S.; Yang, J. W.; Hoffmann, S.; List, B. *Chem. Rev.* **2007**, *107*, 5471.

(11) Sharma, A. K.; Sunoj, R. B. *Angew. Chem. Int. Ed.* **2010**, *49*, 6373.

(12) List, B.; Lerner, R. A.; Barbas III, C. F. *J. Am. Chem. Soc.* **2000**, *122*, 2395.

(13) Bahmanyar, S.; Houk, K. N.; Martin, H. J.; List, B. *J. Am. Chem. Soc.* **2003**, *125*, 2475.

(14) Seebach, D.; Beck, A. K.; Badine, D. M.; Limbach, M.; Eschenmoser, A.; Treasurywala, A. M.; Hobi, R. *Helv. Chim. Acta* **2007**, *90*, 425.

(15) Haindl, M. H.; Hioe, J.; Gschwind, R. M. *J. Am. Chem. Soc.* **2015**, *137*, 12835.

(16) Schmid, M. B.; Zeitler, K.; Gschwind, R. M. *J. Am. Chem. Soc.* **2011**, *133*, 7065.

(17) List, B.; Hoang, L.; Martin, H. J. *Proc. Natl. Acad. Sci.* **2004**, *101*, 5839.

(18) List, B. *Acc. Chem. Res.* **2004**, *37*, 548.

(19) Schmid, M. B.; Zeitler, K.; Gschwind, R. M. *Chem. Eur. J.* **2012**, *18*, 3362.

(20) Schmid, M. B.; Zeitler, K.; Gschwind, R. M. *Chem. Sci.* **2011**, *2*, 1793.

(21) Ashley, M. A.; Hirschi, J. S.; Izzo, J. A.; Vetticatt, M. J. *J. Am. Chem. Soc.* **2016**, *138*, 1756.

(22) Gajan, D.; Bornet, A.; Vuichoud, B.; Milani, J.; Melzi, R.; van Kalkeren, H. A.; Veyre, L.; Thieuleux, C.; Conley, M. P.; Gruning, W. R.; Schwarzwalder, M.; Lesage, A.; Copere, C.; Bodenhausen, G.; Emsley, L.; Jannin, S. *Proc. Natl. Acad. Sci.* **2014**, *111*, 14693.

(23) Bornet, A.; Maucourt, M.; Deborde, C.; Jacob, D.; Milani, J.; Vuichoud, B.; Ji, X.; Dumez, J. N.; Moing, A.; Bodenhausen, G.; Jannin, S.; Giraudeau, P. *Anal. Chem.* **2016**, *88*, 6179.

(24) Chen, C.; Shih, W.; Hilty, C. *J. Am. Chem. Soc.* **2015**, *137*, 6965.

(25) Duckett, S. B.; Mewis, R. E. *Acc. Chem. Res.* **2012**, *45*, 1247.

(26) Barskiy, D. A.; Shchepin, R. V.; Coffey, A. M.; Theis, T.; Warren, W. S.; Goodson, B. M.; Chekmenev, E. Y. *J. Am. Chem. Soc.* **2016**, *138*, 8080.

(27) Eshuis, N.; Hermkens, N.; Van Weerdenburg, B. J. A.; Feiters, M. C.; Rutjes, F. P. J. T.; Wijmenga, S. S.; Tessari, M. *J. Am. Chem. Soc.* **2014**, *136*, 2695.

(28) Lee, J. H.; Sekhar, A.; Cavagnero, S. *J. Am. Chem. Soc.* **2011**, *133*, 8062.

(29) Eisenreich, W.; Joshi, M.; Weber, S.; Bacher, A.; Fischer, M. *J. Am. Chem. Soc.* **2008**, *130*, 13544.

(30) Roth, H. D.; Manion Schilling, M. L. *J. Am. Chem. Soc.* **1980**, *102*, 4303.

(31) Morris, J. I.; Morrison, R. C.; Smith, D. W.; Garst, J. F. *J. Am. Chem. Soc.* **1972**, *94*, 2406.

(32) Kiryutin, A. S.; Sauer, G.; Yurkovskaya, A. V.; Limbach, H.-H.; Ivanov, K. L.; Buntkowsky, G. *J. Phys. Chem. C* **2017**, *121*, 9879.

(33) Guivel-Scharen, V.; Sinnwell, T.; Wolff, S. D.; Balaban, R. S. *J. Magn. Reson.* **1998**, *133*, 36.

(34) Ward, K.; Aletras, A.; Balaban, R. *J. Magn. Reson.* **2000**, *143*, 79.

(35) Liu, G.; Song, X.; Chan, K. W. Y.; Mcmahon, M. T. *NMR Biomed.* **2013**, *26*, 810.

(36) McMahon, M. T.; Gilad, A. A.; Zhou, J.; Sun, P. Z.; Bulte, J. W. M.; van Zijl, P. C. M. *Magn. Reson. Med.* **2006**, *55*, 836.

(37) Woessner, D. E.; Zhang, S.; Merritt, M. E.; Sherry, A. D. *Magn. Reson. Med.* **2005**, *53*, 790.

(38) Zaiss, M.; Bachert, P. *Phys. Med. Biol.* **2013**, *58*, R221.

(39) Yuwen, T.; Sekhar, A.; Kay, L. E. *Angew. Chem. Int. Ed.* **2017**, *56*, 6122.

(40) Lee, J.-S.; Regatte, R. R.; Jerschow, A. *J. Magn. Reson.* **2012**, *215*, 56.

(41) Xu, X.; Lee, J. S.; Jerschow, A. *Angew. Chem. Int. Ed.* **2013**, *52*, 8281.

(42) Döpfert, J.; Witte, C.; Schröder, L. *J. Magn. Reson.* **2013**, *237*, 34.

(43) Zhao, B.; Hansen, A. L.; Zhang, Q. *J. Am. Chem. Soc.* **2014**, *136*, 20.

(44) Ling, W.; Eliav, U.; Navon, G.; Jerschow, A. *J Magn Reson* **2009**, *194*, 29.

(45) Long, D.; Delaglio, F.; Sekhar, A.; Kay, L. E. *Angew. Chem. Int. Ed.* **2015**, *54*, 10507.

(46) Thorarinsdottir, A. E.; Du, K.; Collins, J. H. P.; Harris, T. D.*J. Am. Chem. Soc.* **2017**, 139, 15836.

(47) Ling, W.; Regatte, R. R.; Navon, G.; Jerschow, A. *Proc. Natl. Acad. Sci. U. S. A.* **2008**, *105*, 2266.

(48) Cai, K.; Haris, M.; Singh, A.; Kogan, F.; Greenberg, J. H.; Hariharan, H.; Detre, J. A.; Reddy, R. *Nat. Med.* **2012**, *18*, 302.

(49) Vallurupalli, P.; Bouvignies, G.; Kay, L. E. *J. Am. Chem. Soc.* **2012**, *134*, 8148.

(50) Schmid, M. B. Ph. D. Thesis, University of Regensburg Regensburg-Germany, 2011.

(51) Lakhdar, S.; Tokuyasu, T.; Mayr, H. *Angew. Chem. Int. Ed.* **2008**, *47*, 8723.

(52) Grošelj, U.; Beck, A.; Schweizer, W. B.; Seebach, D. *Helv. Chim. Acta* **2014**, *97*, 751.

(53) El-Hamdouni, N.; Companyó, X.; Rios, R.; Moyano, A. *Chem. Eur. J.* **2010**, *16*, 1142.

(54) Zaiss, M.; Zu, Z.; Xu, J.; Schuenke, P.; Gochberg, D. F.; Gore, J. C.; Ladd, M. E.; Bachert, P. *NMR Biomed.* **2015**, *28*, 217.

(55) Riplinger, C.; Neese, F. *J. Chem. Phys.* **2013**, *138*, 34106.

(56) Riplinger, C.; Sandhoefer, B.; Hansen, A.; Neese, F. *J. Chem. Phys.* **2013**, *139*, 134101.

(57) Frisch, M. J.; Trucks, G. W.; Schlegel, H. B.; Scuseria, G. E.; Robb, M. A.; Cheeseman, J. R.; Scalmani, G.; Barone, V.; Mennucci, B.; Petersson, G. A.; Nakatsuji, H.; Caricato, M.; Li, X.; Hratchian, H. P.; Izmaylov, A. F.; Bloino, J.; Zheng, G.; Sonnenberg, J. L.; Hada M.; Ehara, M.; Toyota, K.; Fukuda, R.; Hasegawa, J.; Ishida, M.; Nakajima, T.; Honda, Y.; Kitao, O.; Nakai, H.; Vreven, T.; Montgomery, Jr., J. A.; Peralta, J. E.; Ogliaro, F.; Bearpark, M.; Heyd, J. J.; Brothers, E.; Kudin, K. N.; Staroverov, V. N.; Kobayashi, R.; Normand, J.; Raghavachari, K.; Rendell, A.; Burant, J. C.; Iyengar, S. S.; Tomasi, J.; Cossi, M.; Rega, N.; Millam, J. M.; Klene, M.; Knox, J. E.; Cross, J. B.; Bakken, V.; Adamo, C.; Jaramillo, J.; Gomperts, R.; Stratmann, R. E.; Yazyev, O.; Austin, A. J.; Cammi, R.; Pomelli, C.; Ochterski, J. W.; Martin, R. L.; Morokuma, K.; Zakrzewski, V. G.; Voth, G. A.; Salvador, P.; Dannenberg, J. J.; Dapprich, S.; Daniels, A. D.; Farkas, Ö.; Foresman, J. B.; Ortiz, J. V.; Cioslowski, J.; Fox, D. J.; *Gaussian 09* (Gaussian, Inc.: Wallingford, CT, USA **2009**).

(58) Neese, F. *Wiley Interdiscip. Rev. Comput. Mol. Sci.* **2012**, *2*, 73.

(59) Glendening, E. D.; Badenhoop, J. K.; Reed, A. E.; Carpenter, J. E.; Bohmann, J. A.; Morales, C. M.; Landis, C. R.; Weinhold, F. NBO 6.0., Theoretical Chemistry Institute, University of Wisconsin: Madison, WI, 2013.

3.6 Supporting Information

3.6.1 General Information

The chemicals for this study were purchased from Sigma Aldrich and Deutero and were used without further purification. DPU-d_{10} was synthesized according to the following procedure. All NMR experiments were performed at 213-300 K on a Bruker Avance III Nanobay 400 and a Bruker Avance III 600 (600.25 MHz) with a fluorine selective TBIF probe or a phosphorous selective TBIP probe. All spectra were processed and evaluated with Bruker Topspin 3.2.

3.6.2 Synthesis of DPU-d_{10}

In a flame dried Schlenk flask, under argon atmosphere triphosgene (0.1 equiv, 617.3 mg, 2.1 mmol) was dissolved in THF (20 ml) and was cooled to 0 °C. A mixture of aniline-d_5 ($C_5D_5NH_2$; 1.0 equiv, 2.15 g, 21.9 mmol) and NEt_3 (1.5 equiv, 4.5 ml, 32.5 mmol) in THF (20 ml) was added drop wise. After stirring the reaction mixture for 30 minutes at 0 °C, it was allowed to warm up to room temperature. After 1 h white precipitate was formed. The solution was washed with an aqueous $NaHCO_3$ solution (sat.) and the organic phase was separated. The aqueous phase was washed with EtOAc. The combined organic phases were dried over Na_2SO_4, filtered and the solvent was removed under reduced pressure. The crude product was washed with Et_2O and dried under vacuum to give the white product (1.1 g, 78%). Due to the partial incomplete deuteration of the aromatic protons, small signals for the aromatic protons could be detected. The amine protons showed higher signal intensities.

^{1}**H-NMR** (400MHz, DMSO-d_6) [ppm]: 6.96 (s, H_{arom}), 7.27 (s, H_{arom}), 7.44 (s, H_{arom}), 8.66 (s, 2H, NH)

^{13}**C-NMR** (100MHz, DMSO-d_6) [ppm]: 117.7 (C_{arom}), 127.9 (C_{arom}), 128.2 (C_{arom}), 139.5 (C_{arom}), 152.4 (C=O)

3.6.3 Sample Preparation

All samples in this study were prepared by dissolving L-proline (1 equiv; 50 or 100 mM), 3-methylbutanal (1 equiv) and diphenylurea (DPU) in 0.6 ml DMF-d_7 in a 5 mm standard NMR tube. If not otherwise indicated 1 equiv of DPU or DPU-d_{10} was used.

3.6.4 NMR Spectroscopic Investigations in the Absence of DPU at 300-215 K

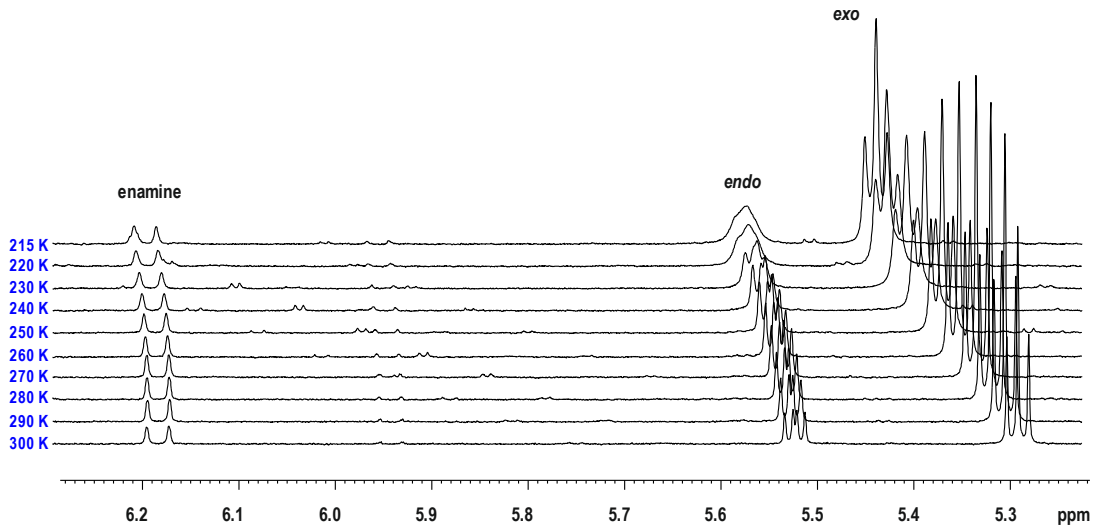

Figure S1. Stacked part of the 1D ^{1}H spectra of the reaction mixture of L-proline (1 equiv) and 3-methylbutanal (1 equiv) in DMF-d_7 at 300-215 K, showing H_1 proton chemical shift of intermediates *exo-, endo*-oxazolidinone and enamine.

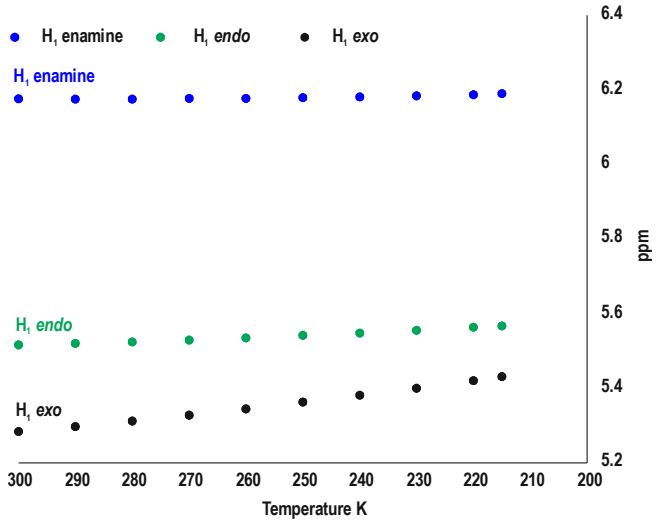

Figure S2. Plot of temperature dependent shift for H_1 protons of *endo*-, *exo*-oxazolidinone and enamine in a reaction mixture of L-proline (1 equiv) and 3-methylbutanal (1 equiv) in DMF-d_7 at 300-215 K. In the absence of DPU the shift is not significant.

3.6.5 NMR Spectroscopic Investigations in the Presence of DPU

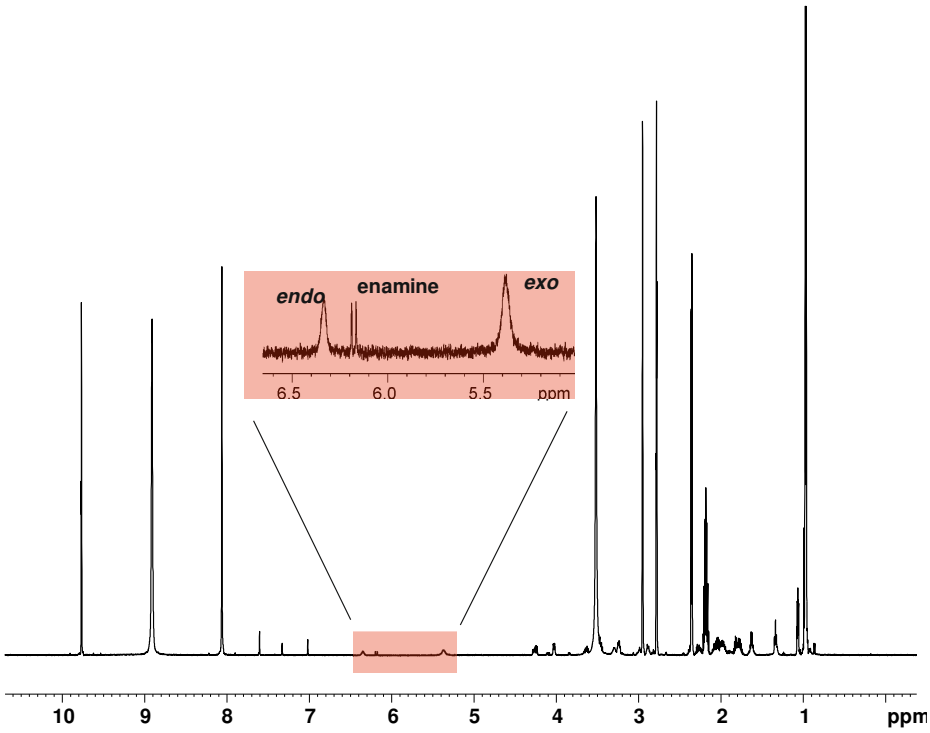

Figure S3. 1D ^{1}H spectrum of the reaction mixture of L-proline (1 equiv) and 3-methylbutanal (1 equiv) in DMF-d_7 at 300 K in presence of DPU-d_{10} (1 equiv). The highlighted region shows the corresponding H_1 protons of all detectable intermediates, *exo*-, *endo*-oxazolidinone and enamine.

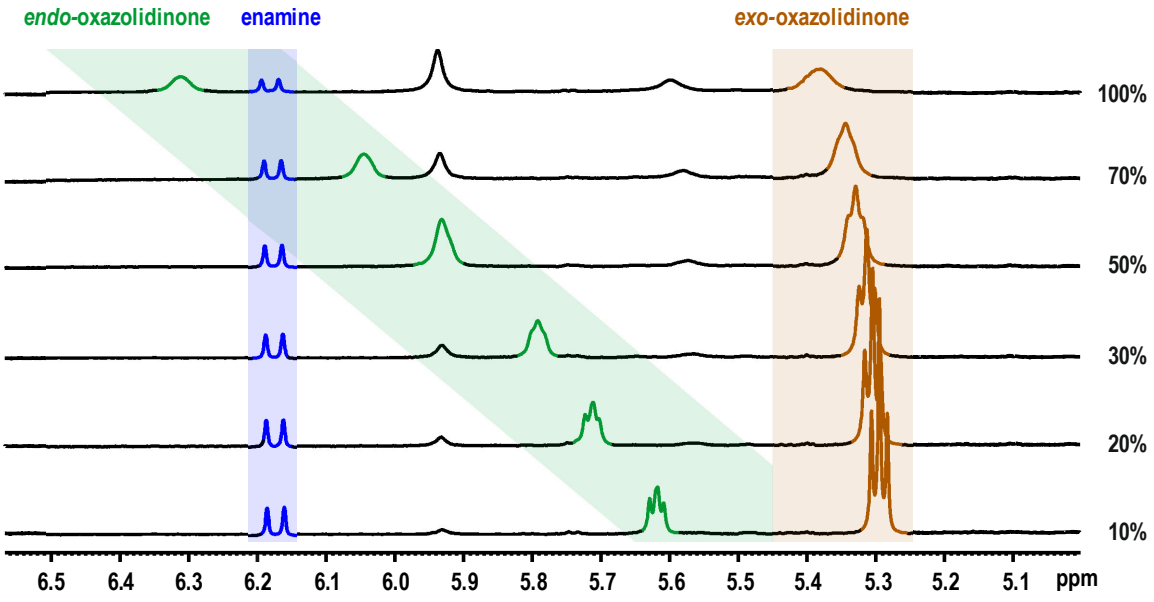

Figure S4. DPU concentration-dependent shift for the H_1 protons of *endo*-, *exo*-oxazolidinone and enamine in a reaction mixture of L-proline (1 equiv), 3-methylbutanal (1 equiv) and the indicated amount of DPU (10-100%; 100% = 1 equiv) in DMF-d_7 at 300 K.

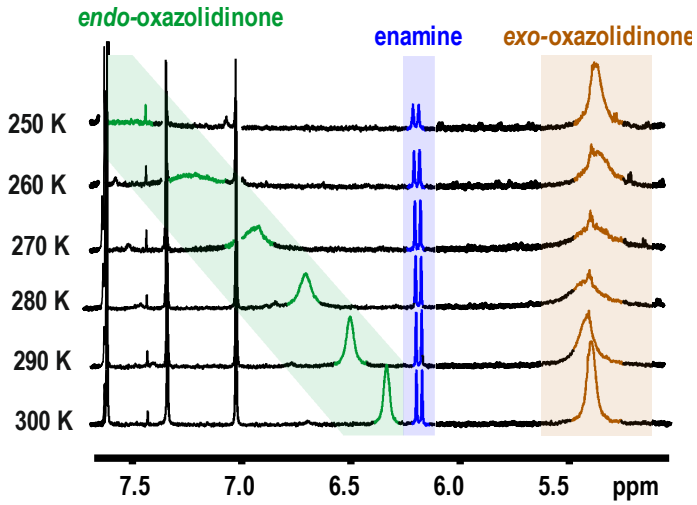

Figure S5. Temperature dependent shift for the H_1 protons of *endo*-, *exo*-oxazolidinone and enamine in a reaction mixture of L-proline (1 equiv), 3-methylbutanal (1 equiv) and DPU (1 equiv) in DMF-d_7 at 300-250 K. The continued line broadening and downfield shift for H_1 of *endo* indicates fast exchange regime for *endo*-oxazolidinone ↔ *E*-Iminium. The narrower-broader-narrower profile for H_1 of *exo* shows shifting from fast exchange to slow exchange regime for *exo*-oxazolidinone ↔ *Z*-Iminium.

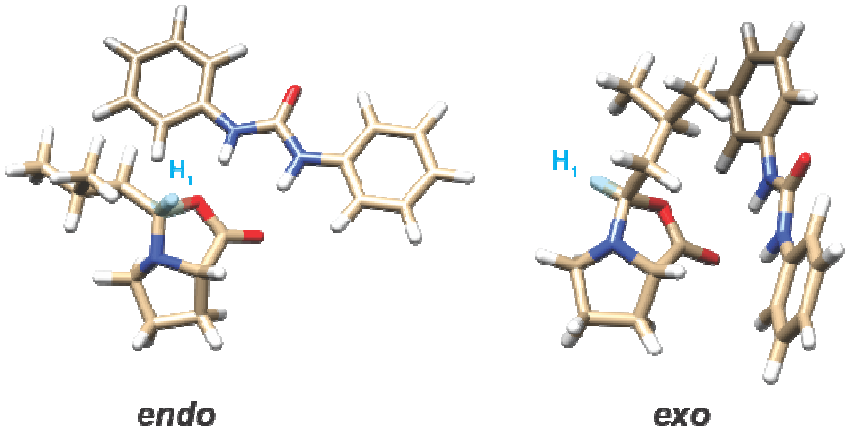

Figure S6. Most stable calculated structures of *endo*- and *exo*-oxazolidinone in complexation with DPU. The calculations did not reveal any deshielding effect of the aryl moieties of the DPU on the H_1 protons of *endo*- or *exo*-oxazolidinone. However the calculations (see Charge and Bond Length Analysis) showed a C_1-O bond elongation causing a shift of H_1. The shift of H_1 is more pronounced in *endo*-oxazolidinone.

3.6.6 Charge and Bond Length Analysis

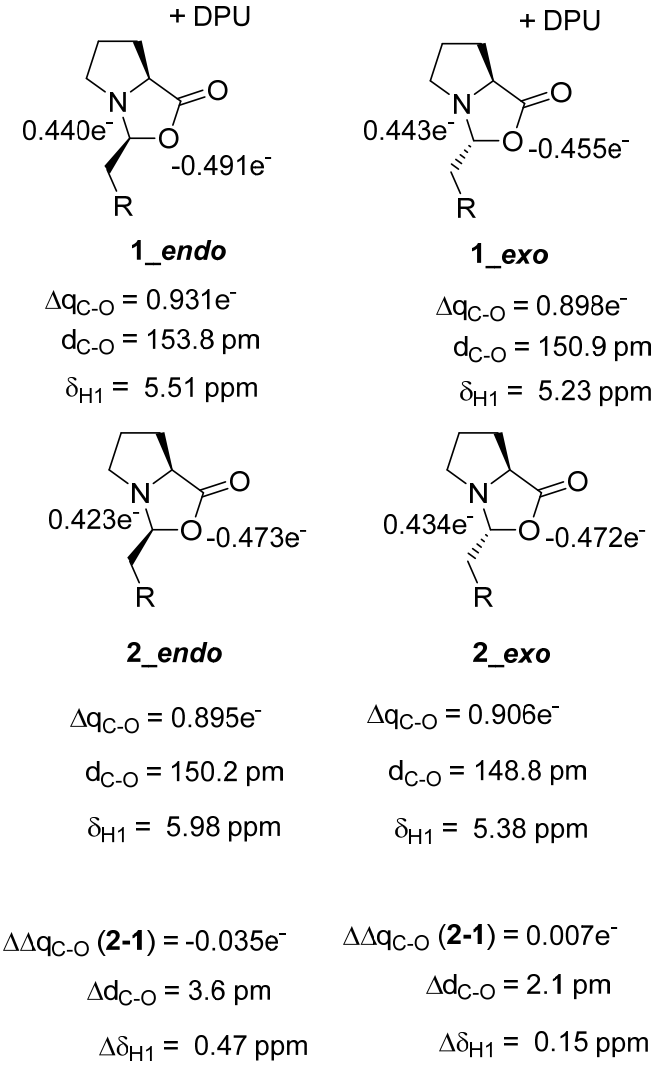

Figure S7. Calculated NBO charges for *exo*- and *endo*-oxazolidinone along the C_1-O bond with and without DPU. The resulting bond elongation is translated to change in chemical shift for the H_1 protons, explaining the stronger shift in case of H_1 of *endo*-oxazolidinone (see manuscript).

3.6.7 Effect of Temperature on *E*-Iminium Population in Presence of DPU

Possible reasons for the shift of the H_1 signal of *endo*-oxazolidinone at 300 K in presence of DPU, shown above (Figure S4), were discussed in detail in the manuscript. Decrease in temperature enhanced *E*-iminium ion population causing continued downfield shift for H_1 of *endo*-oxazolidinone peak. For *Z*-iminium ion and *exo*-oxazolidinone quantitative data regarding exchange rates and thermal population were obtained directly from CEST (see manuscript). Unlike the *Z*-iminium ion, it is not possible to analyze the kinetic and thermodynamics by CEST due to the fast exchange ($k \geq \Delta v$) between *E*-iminium ion and *endo*-oxazolidinone. At 300 K, the EXSY measurements (data shown below) showed similar exchange rates for interconversion between *exo* ↔ *endo*, indicating equivalent thermal stability for *E*- and *Z*-iminium ion. The CEST measurement showed that *Z*-iminium ion is located +8.1 kJ/mol above the *exo*-oxazolidinone at 250 K, and is expected to be even higher at room temperature. Due to the similar thermal stability of *E*/*Z*-iminium, the *E*-iminium ion is located at least +6.1 kJ/mol above the *endo*-oxazolidinone (considering the ΔG_{300} of 2.0 kJ/mol between *exo* and *endo*). This means, the population effect of iminium species at 300 K is negligible.

The decrease of temperature results a continuous shift for the *endo* peak, which allows us to extract the population of *E*-iminium ion. However, the downfield due to the C_1-O bond polarization must be discounted for all measurements at all temperature. The obtained relative population plots are shown below.

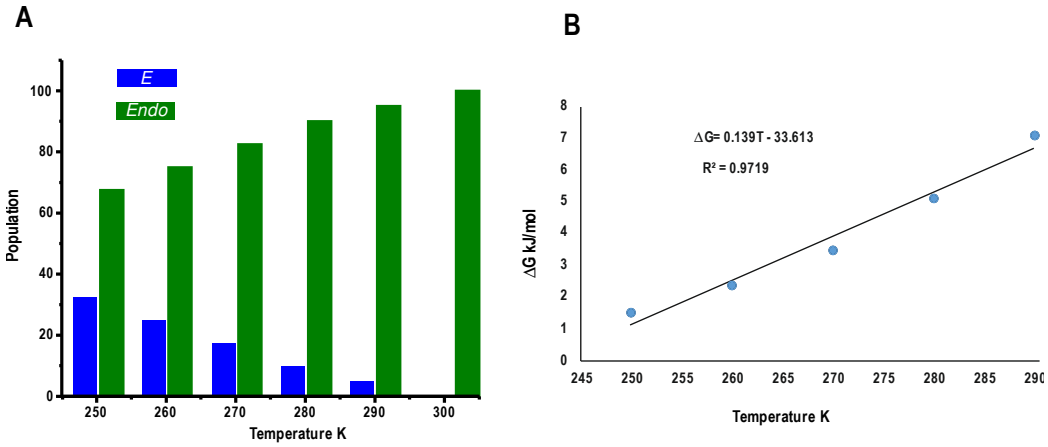

Figure S8. Plot of [*E*-iminium]/[*endo*-oxazolidinone] population dependency on temperature (A); Variation of difference in free energy between *endo*-oxazolidinone and *E*-iminium structure with temperature, the – ΔS suggest more ordered structure for *E*-iminium:DPU than *endo*-oxazolidinone:DPU (B). For these measurements 1 equiv of DPU was used.

Upon decreasing temperature to 250 K, the energy gap diminishes, and the interconversion process enters toward slow exchange regime (broadening of signals). Furthermore, the plot $\Delta G_{E/endo}$ vs temperature yields a negative ΔS (-139 J/(mol*K)), which implicates a more ordered state of *E*-iminium relative to *endo*-oxazolidinone in presence of DPU. This is rather surprising because it is usually assumed that the oxazolidinone is more rigid than the iminium. The more ordered state at *E*-iminium side would mean that DPU associates stronger with the zwitterionic species than the neutral oxazolidinone.

3.6.8 1D ^{1}H EXSY Studies to Obtain Rate Constants and Free Energy Barriers

A series of 1D ^{1}H EXSY experiments were measured by exciting ^{1}H protons of *exo*-, *endo*-oxazolidinone and enamine for different mixing times. The plot of intensity versus mixing time directly provides rate exchange from the slope, which can be used to extract rate constant and hence the free energy barrier.

<u>*exo*-oxazolidinone → *endo*-oxazolidinone</u>

The Intensity I_0 (*exo*) is the relative intensity of ^{1}H proton of *exo*-oxazolidinone at 0 s.

By Eyring equation $k = \frac{k_B T}{h} e^{\frac{-\Delta G^{\ddagger}}{RT}}$ T = 300 K

For k = 1.26 s^{-1}, the free energy barrier for *exo* → *endo* is $\Delta G^{\ddagger}$ = 72.9 kJ/mol

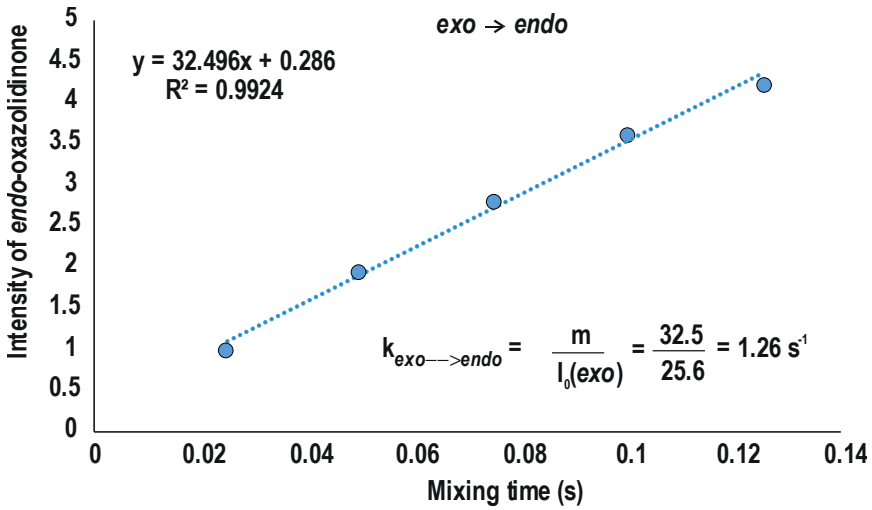

Figure S9. 1D selective EXSY build-up curve for *exo* → *endo* exchange. The dashed line represents the initial slope, which is used for rate approximation.

***endo*-oxazolidinone → *exo*-oxazolidinone**

The Intensity I_0 (*endo*) is the relative intensity of ^{1}H proton of *endo*-oxazolidinone at 0 s.

By Eyring equation, $k = \frac{k_B T}{h} e^{\frac{-\Delta G^{\ddagger}}{RT}}$ T = 300 K

For rate constant k = 1.5 s^{-1}, the free energy barrier for *endo* → *exo* is $\Delta G^{\ddagger}$ = 72.5 kJ/mol. The values suggest similar thermal stability for *E*- and *Z*-iminium, since C=N rotation is the rate measurement step.

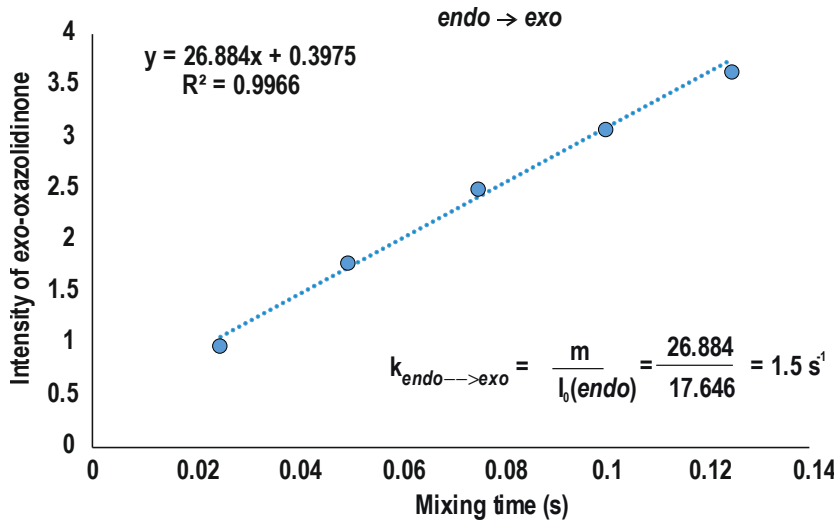

Figure S10. 1D selective EXSY build-up curve for *endo* → *exo* exchange. The dashed line represents the initial slope, which is used for rate approximation.

<u>*exo*-oxazolidinone → enamine</u>

The Intensity I_0 (enamine) is the relative intensity of ^1H proton of enamine at 0 s.

By Eyring equation $k = \frac{k_B T}{h} e^{\frac{-\Delta G^{\ddagger}}{RT}}$ T = 300 K

For rate constant k = 0.113 s^{-1}, the free energy barrier for *exo* → enamine is $\Delta G^{\ddagger}$ = 79 kJ/mol

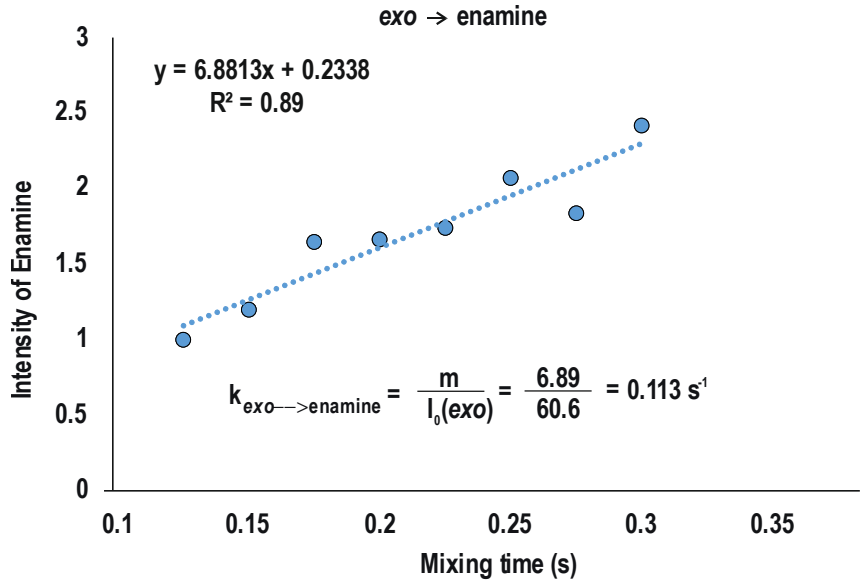

Figure S11. 1D selective EXSY build-up curve for *exo* → enamine exchange. The dashed line represents the initial slope, which is used for rate approximation.

<u>*endo*-oxazolidinone → enamine</u>

Due to near frequency separation between H_1 of *endo* and enamine, the quantitative EXSY data was not possible. In *endo*/*exo*-oxazolidinone to enamine conversion, the rate determining step is conversion from *E*/*Z*-iminium to enamine. At 300 K, the thermal stability of *E*- and *Z*-iminium are similar, assuming similar free energy barrier for both *E* → enamine and *Z* → enamine. The derived *endo* → enamine free energy barrier is 78.6 kJ/mol.

3.6.9 ^{1}H CEST Pulse Sequence

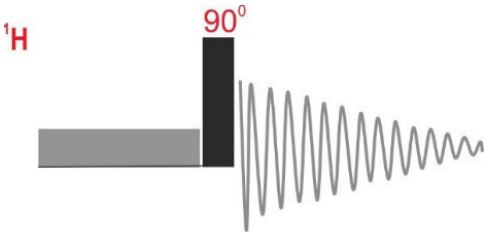

Figure S12. CEST pulse sequence

The CEST pulse sequence, applied for the measurements, consists of an initial continuous saturation pulse, followed by a 90^0 pulse. In all our experiments the saturation is applied for 0.75 s with B_1 ≈ 45 Hz RF strength. Acquisition time Aq = 1 s, and an interscan delay time d1 of 3 s is used.

The saturation offset was scanned with incremental steps of 50 Hz, from up field to down field, while monitoring H_1 peak intensity of *exo*-oxazolidinone. The data, this is, the intensity of marked H_1 peak in *exo*-oxazolidinone vs saturation offset (CEST profile) was plotted for further analysis

3.6.10 Possible Intermediate Probes to Detect Iminium Ion in the System

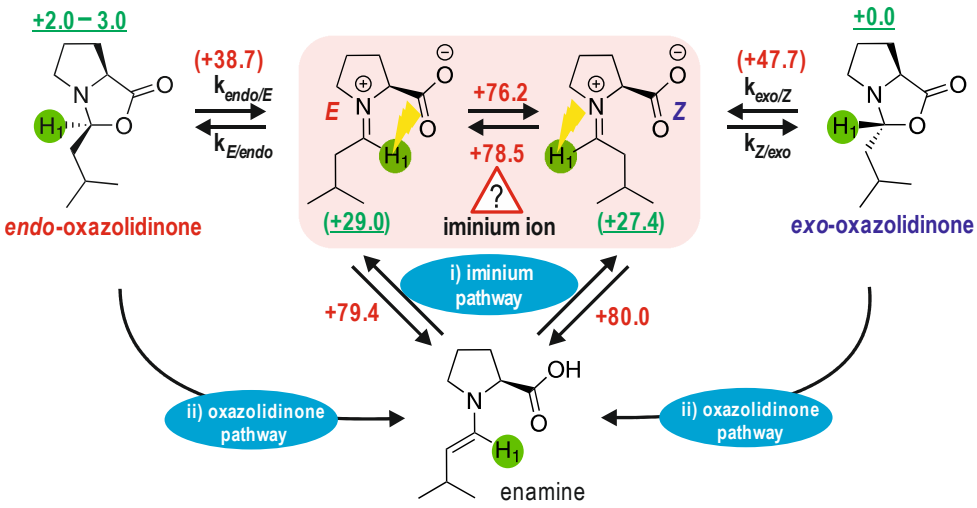

Figure S13. Possible equilibria between the intermediates in the reaction system

In principle it is possible to observe the decreased intensity by CEST on saturation of H_1 proton of iminium ion (≈ 9 ppm) in all three intermediates *exo*-, *endo*-oxazolidinone and enamine. Since all these three intermediates exchanges with iminium ion as shown in Figure S13. However at room temperature due to very less concentration of iminium ion even in presence of DPU, it could not be detected by CEST. On decrease in temperature to stabilize the iminium ion, the exchange of iminium ion with enamine freezes and iminium ion exchange happens only with oxazolidinones. Therefore at low temperature the saturation effect on iminium ion can be observed only in oxazolidinone. Further it was observed that at 250 K, the slow exchange regime is achieved only for *exo* ↔ *Z*-iminium ion, which is a prerequisite in the CEST experiment.

3.6.11 Bloch-McConnell Equations for Two Site Exchange

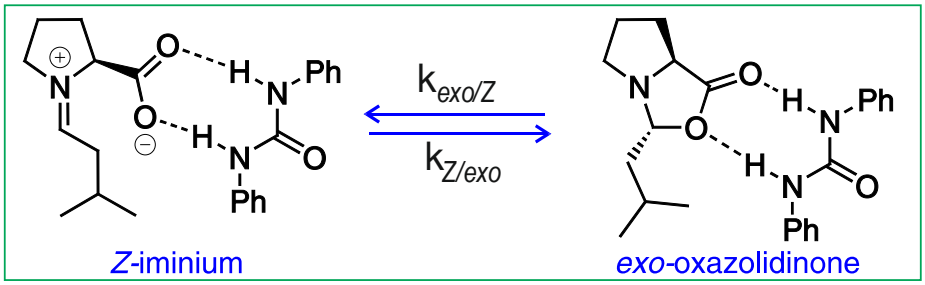

Figure S14. Two site exchange equilibrium between *Z*-iminium ion and *exo*-oxazolidinone.

For our two site exchange system, here between *exo*-oxazolidinone and *Z*-iminium ion, the equations are:

$$\frac{dM_x^{exo}}{dt} = -\Omega_{exo}M_y^{exo} - R_2^{exo}M_x^{exo} - k_{exo\to Z}M_x^{exo} + k_{Z\to exo}M_x^{im} \quad [1]$$

$$\frac{dM_x^{im}}{dt} = -\Omega_{im}M_y^{im} - R_2^{im}M_x^{im} - k_{Z\to exo}M_x^{im} + k_{exo\to Z}M_x^{exo} \quad [2]$$

$$\frac{dM_y^{exo}}{dt} = -\Omega_{exo}M_x^{exo} - R_2^{exo}M_y^{exo} - k_{exo\to Z}^{exo}M_y^{exo} + k_{Z\to exo}M_y^{im} - \omega_1 M_Z^{exo} \quad [3]$$

$$\frac{dM_y^{im}}{dt} = -\Omega_{im}M_x^{im} - R_2^{im}M_y^{exo} - k_{Z\to exo}^{im}M_y^{im} + k_{exo\to Z}M_y^{exo} - \omega_1 M_Z^{exo} \quad [4]$$

$$\frac{dM_z^{exo}}{dt} = -R_1^{exo}(M_z^{exo} - M_0^{exo}) - k_{exo\to Z}M_z^{exo} + k_{Z\to exo}M_z^{im} + \omega_1 M_y^{exo} \quad [5]$$

$$\frac{dM_z^{im}}{dt} = -R_1^{im}(M_z^{im} - M_0^{im}) - k_{Z\to exo}M_z^{im} + k_{exo\to Z}M_z^{exo} + \omega_1 M_y^{im} \quad [6]$$

Here,

$M_{x,y,z}^{exo}$ and $M_{x,y,z}^{exo}$ are magnetization of *exo*-oxazolidinone and iminium ion;

$k_{Z\to exo}$ and $k_{exo\to Z}$ are rate constants;

Ω_{im} = offset frequency of iminium proton (H_1);

Ω_{exo} = offset frequency of *exo*-oxazolidinone proton (H_1);

$$R_2^{exo} = \frac{1}{T_{2exo}} \qquad R_2^{im} = \frac{1}{T_{2im}} \qquad R_1^{exo} = \frac{1}{T_{1exo}} \qquad R_1^{im} = \frac{1}{T_{1im}}$$

T_{2exo} and T_{2im} are spin-spin relaxation times for H_1 proton of *exo*-oxazolidinone and iminium ion.

T_{1exo} and T_{1im} are spin-lattice relaxation times for H_1 proton of exo-oxazolidinone and iminium ion.

3.6.12 CEST Spectra (Profile) Simulation Details

CEST spectra are simulated using numerical solutions of above Bloch-McConnell equations. Simulations are carried out in MATLAB as described in earlier reports.[1-3] The used initial input parameters are M_{0exo}, M_{0im}, ω_1, T_{1exo}, T_{1imi} and $k_{Z/exo}$.

Here,

M_{0exo}, is initial magnetization of *exo*-oxazolidinone at equilibrium;

M_{0imi}, is initial magnetization of *Z*-Iminium ion at equilibrium;

ω_1 is strength of RF saturation in Hz ;

T_{1exo} and T_{1imi} are longitudinal relaxations of chosen proton in *exo*-oxazolidinone and *Z*-iminium ion respectively;

$k_{Z/exo}$ is rate of ring closing from *Z*-iminium to *exo*-oxazolidinone.

In all simulated spectra, we used M_{0exo} = 1 and ω_1= 45 Hz. The T_{1exo} values are experimentally obtained by inversion recovery experiment while saturating at 9.12 ppm. M_{0imi} and $k_{z/exo}$ are varied to match simulation spectra with that of experimental data via multi parameter optimization.

Case 1 (250 K):

M_0(*exo*) = 1, ω_1 = 45 Hz and T_{1exo} = T_{1im} = 1.8 s are fixed.

Case 2 (213 K):

M_0(*exo*) = 1, ω_1 = 45 Hz and T_{1exo} = T_{1im} = 0.8 s are fixed.

3.6.13 Details of Theoretical Calculations

Extrapolation procedure

The total energy at DLPNO-CCSD(T)/CBS level of theory were extrapolated according to the extrapolation formula [7-10].

$$E_{SCF}^{X} = E_{SCF}^{\infty} + Ae^{-a\sqrt{X}} \quad [7]$$

$$E_{corr,MP2}^{\infty} = \frac{X^{\beta}E_{corr,MP2}^{X} - (X-1)^{\beta}E_{corr,MP2}^{X-1}}{X^{\beta}-(X-1)^{\beta}} \quad [8]$$

$$E_{MP2}^{\infty} = E_{SCF}^{\infty} + E_{corr,MP2}^{\infty} \quad [9]$$

$$E_{CCSD(T)}^{\infty} = E_{CCSD(T)}^{def2-TZVPP} + E_{MP2}^{\infty} - E_{MP2}^{def2-TZVPP} \quad [10]$$

Table 1. ΔG268 CCSD(T)/CBS (Boltzmann averaged) + ΔG_{solv} (CPCM) in a.u.

	Ground States	Transition States (Ring Opening)
exo-oxazolidinone	-1282.024904	-1282.006070
endo-oxazolidinone	-1282.023829	-1282.010202
Z-iminium ion	-1282.022150	
E-iminium ion	-1282.022783	

Geometry of stationary points (most stable conformations)

See Appendix (DVD).

3.6.14 References

(1) McMahon, M. T.; Gilad, A. A.; Zhou, J.; Sun, P. Z.; Bulte, J. W. M.; van Zijl, P. C. M. *Magn. Reson. Med.* **2006**, *55*, 836.
(2) Woessner, D. E.; Zhang, S.; Merritt, M. E.; Sherry, A. D. *Magn. Reson. Med.* **2005**, *53*, 790.
(3) Zhou J.; van Zijl P. C. M. *Prog. Nucl. Magn. Reson. Spectrosc.* **2006**, *48,* 109.

4 Decrypting Transition States by Light: Chances, Possibilities and Limitations. A Preliminary Study in Iminium Ion Catalysis

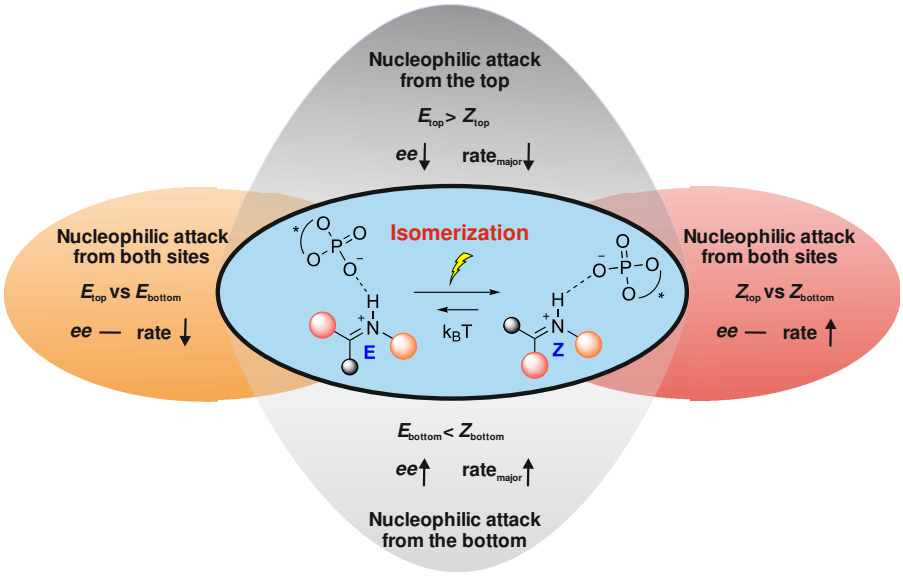

The theoretical approach for the application of the DTS-hv method in secondary aminocatalysis, presented in this chapter was elaborated by Andreas Seegerer. Dr. Polyssena Renzi preformed all experiments to determine the yield and the enantiomeric excess of the reactions and did the corresponding assignments by NMR spectroscopy. Trifluoroacetaldehyde phenylhydrazone was synthesized by Andreas Seegerer and Dr. Polyssena Renzi. The synthesis of the iminium perchlorate salt was done by Willibald Stockerl, who further conducted the first isomerization experiments for the perchlorate iminium ion salt and did the assignment for the three iminium ion isomers shown in the Experimental Part. All other NMR spectroscopic investigations in this chapter (Figure 5, 6) as well as the experimental results in the Additional Findings section were done by Andreas Seegerer.

4.1 Basic Concept of DTS-hv

Since the beginning of the millennium, the broad field of asymmetric organocatalysis became indispensable in the world of modern chemistry.[1–6] Although, the first asymmetric transformations with the natural amino acid L-proline as a catalyst were presented in the early 1970's,[5,7–9] it took almost 30 years until its breakthrough.[1] Based on the pioneering work of List, Barbas, MacMillan, and coworkers in the year 2000,[10,11] enantioselective organocatalysis emerged as a third pillar in the field of asymmetric catalysis, next to enzymes and transition-metal complexes.[6] After almost two decades of steady progress, the number of publications showing a variety of different catalysts and reaction types is unimaginably high.[1–6,12] However, especially in the beginning of the golden era of organocatalysis, detailed studies about the corresponding reaction mechanisms were rather limited.[13] Later, more detailed investigations,[5,12,14–28] like the first detection of elusive enamine intermediates in our group,[13,29] revealed the complexity of such mechanistic studies. Most of the time, the analysis of reaction mechanisms is very time consuming and require various combinations of different analytical and spectroscopic tools and techniques. Despite great progress in the experimental analysis of reaction mechanisms during the last years, computational studies are often the method of choice, since they enable a fast prediction of energetic profiles of reactions and provide information about their transition states,[30] which are not accessible by standard spectroscopic methods.

Recently, our group presented an innovative approach to investigate experimentally the active pathways of an asymmetric organocatalytic reaction, corroborating detailed computational analyses of transition states.[31] The decrypting transition states by light (DTS-hv) method is based on the analysis of specific fingerprint patterns, which are directly connected with the transition states of a reaction. These fingerprint patterns represent characteristic variations in the enantioselectivity and/or rate of a reaction. According to the DTS-hv method, a change in *ee* values and reaction rates can be induced by targeted photoisomerization of a double bond within a reactant, if the configuration of this double bond is decisive for the stereoinduction in the transition state. Therefore, a change in *ee* values and reaction rates is directly correlated to the isomerization process, which can be used as a mechanistic tool to differentiate between different possible pathways of the reaction (Figure 1).[31]

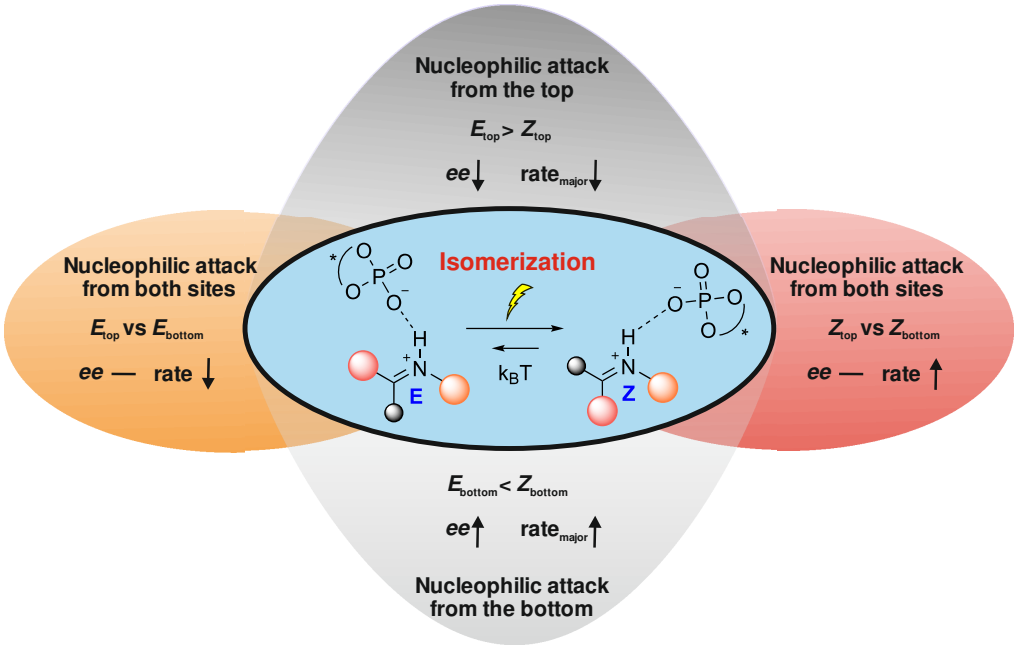

Figure 1. Schematic presentation of the DTS-hv method describing four different fingerprint patterns (i.e. change in the *ee* value and rate of a reaction) for a Brønsted acid catalyzed reaction of aldimines/ketimines including a light induced isomerization from *E*→*Z*. I) *E* pathway dominant: Competition of E_{top} vs E_{bottom}, i.e. isomerization *E*→Z: rate ↓, Δ*ee* = 0. II) *Z* pathway dominant: Competition of Z_{top} vs Z_{bottom}, i.e. isomerization *E*→Z: rate ↑, Δ*ee* = 0. III) Nucleophilic attack from the top site. E_{top} and Z_{top} competing. E_{top} dominant (gives major enantiomer); *E*→Z: *ee* ↓, rate$_{major}$ ↓. IV) Nucleophilic attack from the bottom site. E_{bottom} and Z_{bottom} competing. Z_{bottom} dominant (gives major enantiomer); *E*→Z: *ee* ↑, rate$_{major}$ ↑.[31]

The power of this new method was demonstrated for the first time on an asymmetric Brønsted acid ((*R*)-TRIP; (*R*)-3,3′-bis(2,4,6-triisopropylphenyl)-1,1′-binaphthyl-2,2′-diyl hydrogen phosphate) catalyzed transfer hydrogenation of ketimines (Scheme 1A) with Hantzsch ester (diethyl 4-dihydro-2,6-dimethyl-3,5-pyridinedicarboxylate) under the influence of a 365 nm light source.[32] A second example of a nucleophilic addition of acetylacetone to *N*-boc protected aldimines (Scheme 1B) validated the DTS-hv method.[31] In both reactions the configuration of the double bond within the ketimine/aldimine is supposed to be crucial for their enantioselective transformations (Figure 1)[31]. Based on earlier computational studies,[33–35] a dominant *Z* pathway (*E* vs *Z)* in the hydrogenation of ketimines and a dominant *E* pathway for the nucleophilic attack to aldimines was predicted. However, a fast experimental access to the underlying mechanisms was missing.

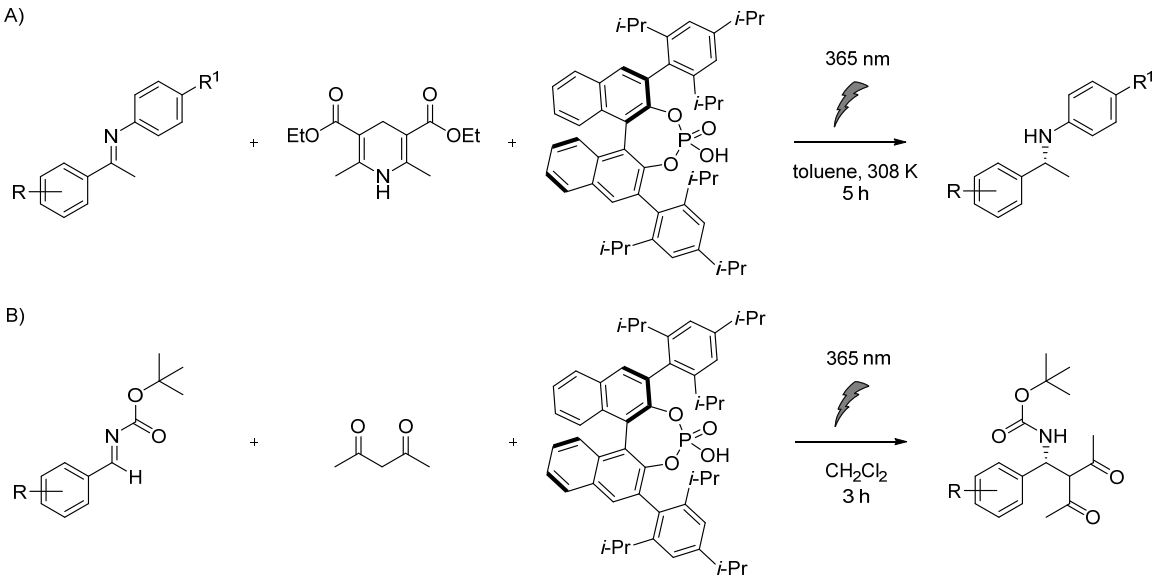

Scheme 1. Overview of reactions used by Renzi *et al*. to show the potential of the DTS-hv method in Brønsted acid catalysis.[31] A) Enantioselective reduction of ketimines to the corresponding amine, catalyzed by (*R*)-TRIP under the influence of light (365 nm). B) Enantioselective nucleophilic addition of acetylacetone to different aldimines under the influence of (*R*)-TRIP and light (365 nm).

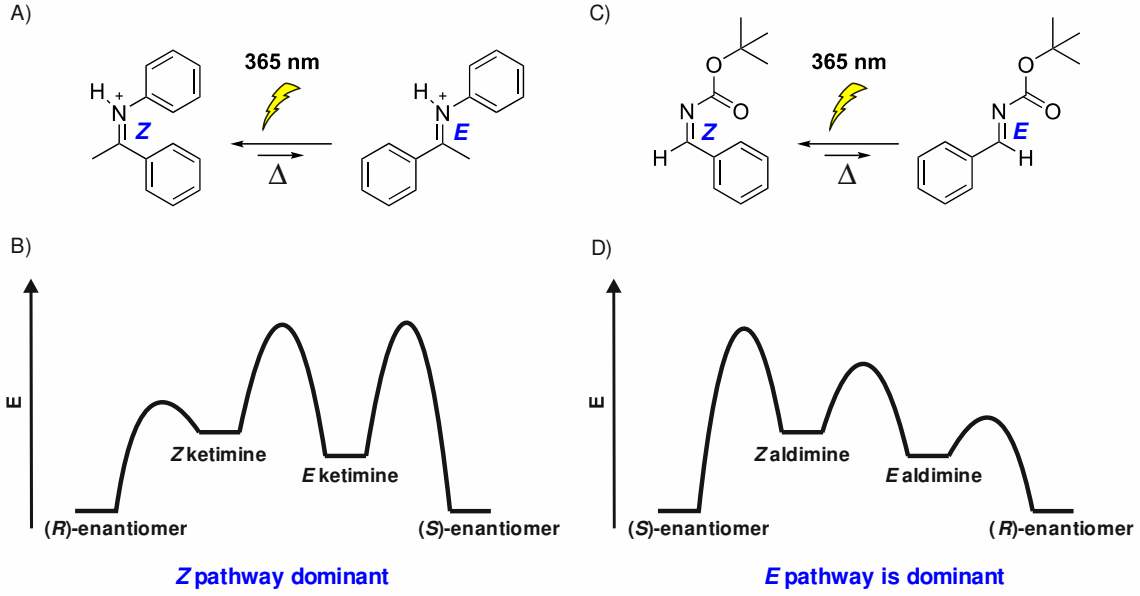

Figure 2. A) Isomerization of *E* ketimine to *Z* ketimine with light (365 nm). B) Schematic energy profile with a dominant *Z* pathway yielding the (*R*)-enantiomer of the product. The *E* pathway is not contributing C) Isomerization of *E* aldimine to *Z* aldimine with light (365 nm). D) Schematic energy profile with a dominant *E* pathway yielding the (*R*)-enantiomer of the product. The *Z* pathway is not contributing.

Therefore, to investigate and to prove the preferred pathways for both reactions (Scheme 1) experimentally by DTS-hv, the reactions were executed under the influence of continuous illumination (365 nm). Here, for both reactions the prerequisites for the DTS-hv method were fulfilled. This means: i) the double bond within the aldimine/ketimine can be isomerized by light (365 nm) without significant photodegradation ($E_{ketimine} \rightarrow Z_{ketimine}$, $E_{aldimine} \rightarrow Z_{aldimine}$, Figure 2A,C); ii) the rate of the isomerization is lower or comparable to the rate of the enantioselective step (Figure 2B,D); and iii) no change of the reaction mechanism is caused by light (i.e. no background reaction).[31]

In the case of the hydrogenation of ketimines (Scheme 1A), a rise in the yield, which was correlated with the increased rate was observable when the reaction was executed under continuous illumination (365 nm). Additionally, no change in the *ee* value of the product was detected. Due to the photoisomerization from $E_{ketimine} \rightarrow Z_{ketimine}$, shown by *in situ* illumination NMR, this specific fingerprint pattern ($\Delta ee = 0$; rate ↑) positively confirmed, that only the *Z* pathway is active under these conditions (Figure 1).[31] This result is partially in agreement with theoretical calculations proposed by Goodman *et al.*[35] The unchanged *ee* value proves the competition of two *Z* pathways for the nucleophilic attack (top and bottom), being responsible for the enantioselectivity of the reaction (Figure 1, II).

In contrast, in the case of the nucleophilic addition of acetylacetone to the aldimines (Scheme 1B), a reduction of the product formation rate was caused by the isomerization of the double bond from *E* to *Z* with light (365 nm, Figure 2C). However, also in this reaction no change in *ee* was observable ($\Delta ee = 0$; rate ↓). Applying the DTS-hv method to decrypt this specific fingerprint pattern, it was confirmed that the reaction exclusively follows the *E* pathway (Figure 1, I). However, also here two competitive *E* pathways (top, bottom) are decisive for the enantiomeric excess. Therefore, no effect on the *ee* values could be found.[31]

To summarize, the DTS-hv method represents a new mechanistic tool to prove active reaction pathways involved in organocatalytic transformations by the analysis of characteristic fingerprint patterns. These fingerprint patterns are generated via a light induced photoisomerization of double bonds, if their configurations are decisive for the stereoselectivity of the reactions. Due to the fact, that many reactive compounds in asymmetric transformations possess double bonds, which might be isomerizable by light, a broad scope of the DTS-hv method is expected.

4.2 DTS-hv – A Theoretical Approach For More Complex Systems

The previously described examples for transfer hydrogenation reactions of aldimines and ketimines under the influence of a Brønsted acid catalyst (section 4.1) demonstrated the high potential of the DTS-hv method for the investigation of active reaction pathways. The isomerization of the double bond by light was found to be a useful tool for the experimental verification of transition states, if the corresponding prerequisites of the method are fulfilled.[31] However, in contrast to the aldimines and ketimines, analyzed in this first study, many organic compounds posses more extended conjugated double bond systems. Therefore, a transfer of the DTS-hv method to systems containing two or more double bonds would be highly desirable. To examine the applicability and the benefit of the DTS-hv method also for more complex systems with different competing isomers (e.g. *E* vs *Z*) and more than one double bond, a theoretical approach, discussing all possible fingerprint patterns for a diene system, is presented. Furthermore, based on this theoretical discussion, prospective applications of the DTS-hv method in synthesis are revealed and first experimental results are analyzed.

4.2.1 Application of DTS-hv in Asymmetric Aminocatalysis

As a model system, to prove the applicability of the DTS-hv method for a more complex organocatalytic transformation (in terms of configurational variety), the field of secondary aminocatalysis with Jørgensen-Hayashi prolinol ether catalysts **A**, **B** and α,β unsaturated aldehydes was chosen due to several reasons. First of all, the key intermediates derived by a condensation of the catalysts and aldehydes, namely iminium ions and dienamines (Scheme 2), posses a conjugated diene moiety.[36,37]

Based on various results of other groups[38–40] and confirmed by our own studies,[41,42] a steric shielding of one active site is given (Scheme 2) for both types of intermediates. Therefore, an influence of the configuration of the diene subsystem on the *ee* value of reactions is highly likely, which represents a decisive criterion for a successful application of the DTS-hv method. In the case of iminium ion catalysis the competition between the major *E*,*E* and the minor *Z*,*E* isomer, regarding the C=N double bond of the diene system, is assumed to influence the stereoselectivity.[12,39] In contrast, in dienamine catalysis the configuration of the second C=C double bond (*E*,*E* vs *E*,*Z*) was found to influence the enantioselectivity (chapter 2). This means, in contrast to the examples shown before (section 4.1), that the enantioselectivity of the reaction is controlled by a competition of different isomers of the intermediate (*E* vs *Z*) and not by the direction of the attack (e.g. Z_{top} vs Z_{bottom}).

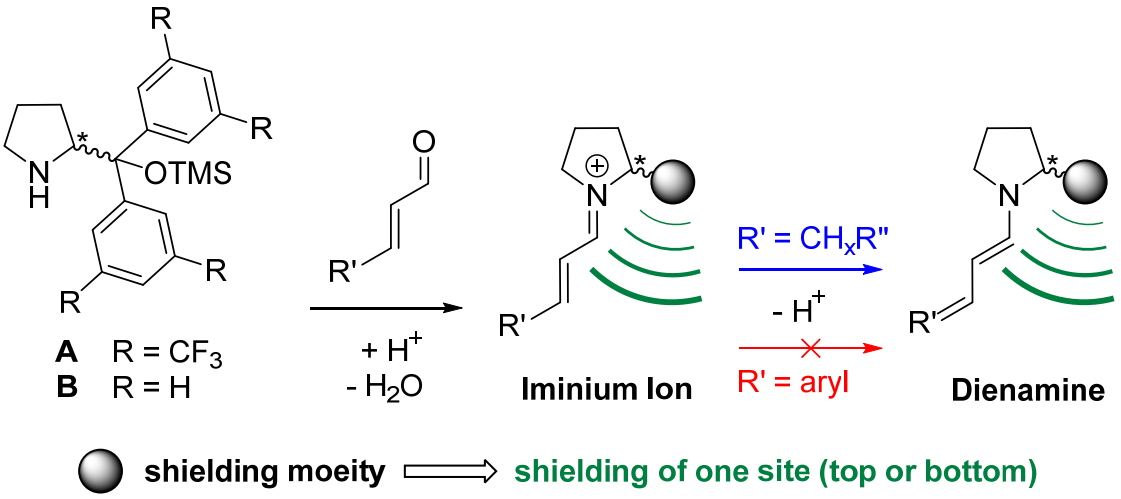

Scheme 2. Formation of dienamine and iminium ion intermediates with Jørgensen-Hayashi type catalysts **A, B**. The enantioselectivity is caused by a steric shielding of one site of the intermediates by the shielding moiety of the catalyst.[38–40,42]

Furthermore, next to the selective shielding of one active site of the diene subsystem, which reduced significantly the number of possible fingerprint patterns of the DTS-hv method, it was recently shown, that Jørgensen-Hayashi type catalysts are also valuable catalysts in photochemical organocatalytic applications.[43–46] Therefore, the required photo stability for a mechanistic investigation of a reaction under the influence of light can be assumed.

Due to some examples in nature for the photoinduced isomerization of double bonds in iminium ions[47–49] e.g. in rhodopsin, the iminium ion catalysis was chosen as a starting point to apply the DTS-hv method in secondary aminocatalysis with Jørgensen-Haysashi type catalysts.

4.2.2 DTS-hv Fingerprint Patterns in Iminium Ion Catalysis

In this first study, for the sake of clarity, exclusively iminium ion intermediates, derived by a condensation of Jørgensen-Hayashi type catalysts and α,β unsaturated aldehydes were investigated (Figure 3). Based on their outstanding relevance in synthesis,[36] only nucleophilic additions in the β position of the iminium ions are discussed. Furthermore, only the configuration of the diene subsystem was taken into account to analyze the influence of the iminium ion structure on the *ee* value and the reaction rates. For the catalyst subsystem a steric shielding of one site (Scheme 2) and an identical structure for all iminium ion intermediates is assumed.[38]

In the diene subsystem of iminium ion intermediates (Figure 3), the configuration of the two double bonds and the single bond (respectively the concentration of the

corresponding isomers) is supposed to significantly influence the enantioselectivity of a nucleophilic addition, if similar reaction rates in the product formation for the different isomers or a slow isomerization between the isomers is given (prerequisite of DTS-hv[31]). Assuming two possible configurations/conformations for every bond, this means, *trans* (*E*) or *cis* (*Z*) for the double bonds and *s-trans* and *s-cis* for the single bond, 8 possible combinations have to be considered. However, based on earlier reports[12,38,39] and our own experience in dienamine catalysis,[42] the conformation of the single bond is expected to be exclusively *s-trans*. This reduces the number of possible scenarios influencing the stereoinduction to four.

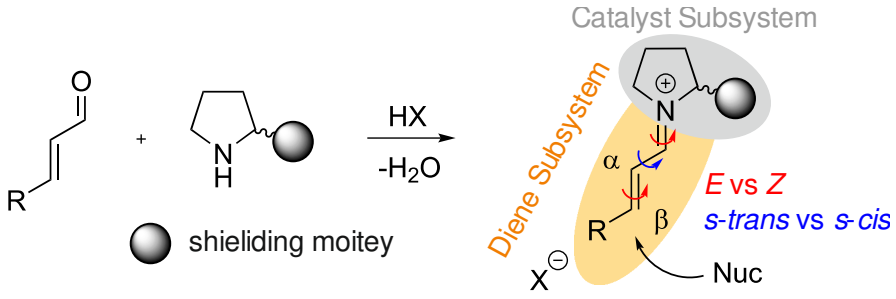

Figure 3. Reaction of an α,β-unsaturated aldehydes (R = alkyl, aryl) and a prolinol ether type catalyst under the influence of acid HX. For the discussion, the structure of the resulting iminium ion intermediate is divided in a diene and catalyst subsystem. The catalyst subsystem is assumed to be fixed for all iminium ion intermediates under investigation. The diene subsystem contains two isomerizable double bonds and one single bond (*E* vs *Z* for the double bonds; *s-trans* vs *s-cis* for the single bond.)

Throughout the following study, the first character in the description of the pathways always represents the configuration of the N=C double bond. For the sake of clarity, a complete shielding by the catalyst moiety is assumed for one site of the iminium ion. Therefore, the enantiomeric excess observed in a reaction, has to be based on the competition between isomers, which are yielding different enantiomers (*E*,*E* and *Z*,*Z* vs *E*,*Z* and *Z*,*E*; Scheme 3,4). Enantiopure reactions with only one active pathway (*ee* = 100%) are excluded. Furthermore, according to the prerequisites of the DTS-hv method,[13] a slower thermal backisomerization compared to the reaction with the nucleophile is supposed for all described fingerprint patterns.

Based on earlier reports, the *E*,*E* iminium ion is expected to be the most stable and highest populated isomer in a thermodynamic equilibrium,[38,39,50] therefore it is used as a starting point for the discussion of all possible fingerprint patterns in iminium ion catalysis. Due to the variety of the fingerprint patterns, two different scenarios are discussed separately. In Scheme 3, the *E*,*E* and respectively the *Z*,*Z* isomer yield the

major enantiomer of the reaction (Scenario 1). In contrast, in Scheme 4 the *Z*,*E* and *E*,*Z* isomers describe the active pathways to form the major enantiomer (Scenario 2).

Scenario 1:

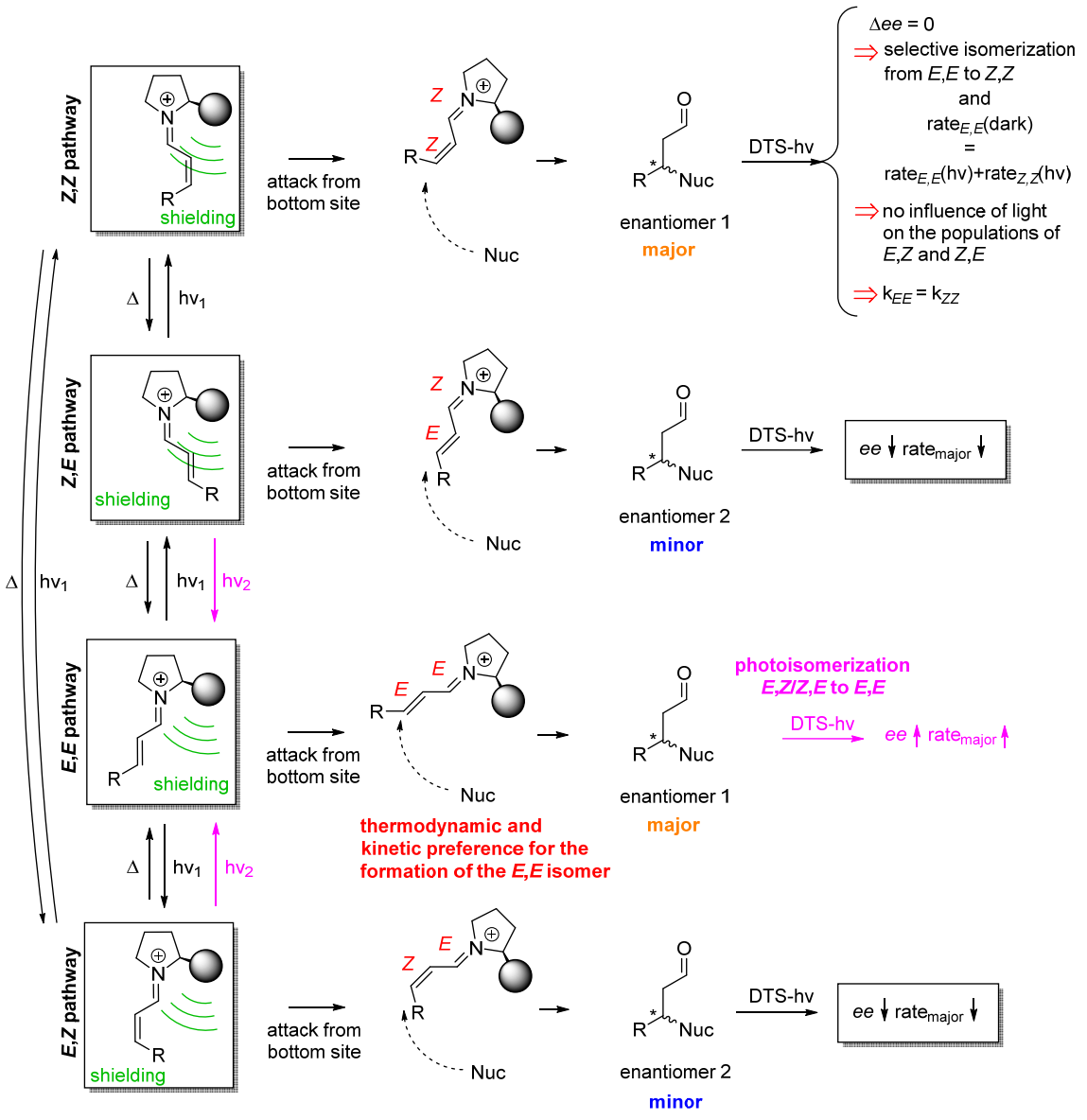

Scheme 3. Description of all possible pathways for a nucleophilic addition to an iminium ion intermediate under the influence of light (Scenario 1). A steric shielding of the top site of the diene subsystem is assumed due to the shielding moiety of the catalyst.

Starting with the *E*,*E* pathway, which yields the major enantiomer of the product, an irradiation with light can cause an isomerization of one double bond (*E*,*Z*;*Z*,*E*) or both double bonds (*Z*,*Z*). If the iminium ion is able to absorb light with a specific wavelength, the gained energy (hv_1) can be used to cross the rotational barrier of the double bond, and the equilibrium is shifted towards another isomer.

1) Isomerization to *E*,*Z*/*Z*,*E*

In the case of an isomerization of one double bond within the diene subsystem (*E*,*E*→*E*,*Z*; *E*,*E*→*Z*,*E)*, the rate for the formation of the major enantiomer is decreased. In contrast, the rate for the formation of the minor enantiomer is increased due to a higher concentration of *E*,*Z* or *Z*,*E.* As a consequence the *ee* value of the product is decreased. A significant population of the *E*,*Z* or *Z*,*E* isomers by light could even cause an inversion of the stereocenter, which would be a great new tool in synthetic applications.

If there is no information, which double bonds within the diene subsystem is selectively isomerized, no differentiation between the *E*,*Z* and *Z*,*E* pathway can be made, since both pathways yield the same enantiomer. In this case, further investigations about the dominant pathway are required.

2) Isomerization to *Z*,*Z*

For the sake of completeness, the isomerization to *Z*,*Z* is mentioned here, however is assumed to be highly unlikely. Therefore it is excluded in the later discussion (section 4.3).

If the irradiation with light (hv) causes a selective isomerization of *E,E* to *Z*,*Z* without influencing the population of the *E*,*Z* and *Z*,*E* isomers, no change in the *ee* value of the product would be detectable ($\Delta ee = 0$). Requirement for this is that the sum of the rates for the *E,E* and *Z*,*Z* pathways under influence of light equal the rate of product formation along the *E*,*E* pathway in absence of light ($rate_{E,E}(dark) = rate_{E,E}(hv) + rate_{Z,Z}(hv)$; see equations (1)-(8)). Deviating rates and also different rate constants k ($k_{E,E}$ vs $k_{Z,Z}$) would cause a change in the *ee* value, due to the competition with the unchanged *E*,*Z and Z*,*E* pathways (equations (9)-(13)).

Without light:

$$rate_{E,E}(dark) = k_{E,E}[E,E]_{dark}*[Nuc] \quad (1)$$

$$rate_{Z,Z}(dark) = k_{Z,Z}[Z,Z]_{dark}*[Nuc] = 0 \quad (2)$$

$$rate_{E,Z}(dark) = k_{E,Z}[E,Z]_{dark}*[Nuc] = rate_{E,Z}(hv) \quad (3)$$

$$rate_{Z,E}(dark) = k_{Z,E}[Z,E]_{dark}*[Nuc] = rate_{Z,E}(hv) \quad (4)$$

$$ee_{dark} = rate_{E,E}(dark) - rate_{E,Z}(dark) – rate_{Z,E}(dark) \quad (5)$$

With light:

$$ee_{hv} = rate_{E,E}(hv) + rate_{Z,Z}(hv) - rate_{Z,E}(dark) - rate_{E,Z}(dark) \quad (6)$$

$$ee_{dark} = ee_{hv} \rightarrow \Delta ee = 0 \quad (7)$$

$$rate_{E,E}(dark) - rate_{E,Z}(dark) - rate_{Z,E}(dark) = rate_{E,E}(hv) + rate_{Z,Z}(hv) - rate_{Z,E}(dark) - rate_{E,Z}(dark)$$

$$\rightarrow rate_{E,E}(dark) = rate_{E,E}(hv) + rate_{Z,Z}(hv) \quad (8)$$

$$k_{E,E}[E,E]_{dark}*[Nuc] = k_{E,E}[E,E]_{hv}*[Nuc] + k_{Z,Z}[Z,Z]_{hv}*[Nuc] \quad (9)$$

$$[E,E]_{hv} = [E,E]_{dark} - [Z,Z]_{hv} \quad (10)$$

$$k_{E,E}[E,E]_{dark}*[Nuc] = k_{E,E}([E,E]_{dark} - [Z,Z]_{hv})*[Nuc] + k_{Z,Z}[Z,Z]_{hv}*[Nuc] \quad (11)$$

$$k_{E,E}[Z,Z]_{hv}*[Nuc] = k_{Z,Z}[Z,Z]_{hv}*[Nuc] \quad (12)$$

$$\rightarrow k_{E,E} = k_{Z,Z} \quad (13)$$

In other cases, in which the populations of the *E*,*Z* and *Z*,*E* isomers are also affected by light, a change in the *ee* value is caused. A higher population of *E*,*Z* and *Z*,*E* would cause a decrease in the *ee* value (see prior paragraph), whereas a lower concentration (*E*,*Z*/*Z*,*E*→*Z*,*Z*) would allow for an increased *ee* value of the product.

3) Photoisomerization *E*,*Z*/*Z*,*E*→*E*,*E*

In addition to the latter described scenario increasing the *ee* value of the product, the idea of a photoisomerization from *E*,*Z* and *Z*,*E* to *E*,*E* with a different wavelength (hv_2) is introduced. If a significant shift of the absorption maxima of the *E*,*Z* and/or *Z*,*E* isomers compared to the *E*,*E* isomer is caused by the configurational change, light with a different wavelength might be used to isomerize selectively *E*,*Z*/*Z*,*E*→*E*,*E*. The increased concentration of the *E*,*E* isomer would raise the rate of the major enantiomer formation and respectively the *ee* value of the product. Therefore, higher *ee* values could be reached in synthesis applying the strategy of a selective photoisomerization of *E*,*Z*/*Z*,*E*→*E*,*E*.

Scenario 2:

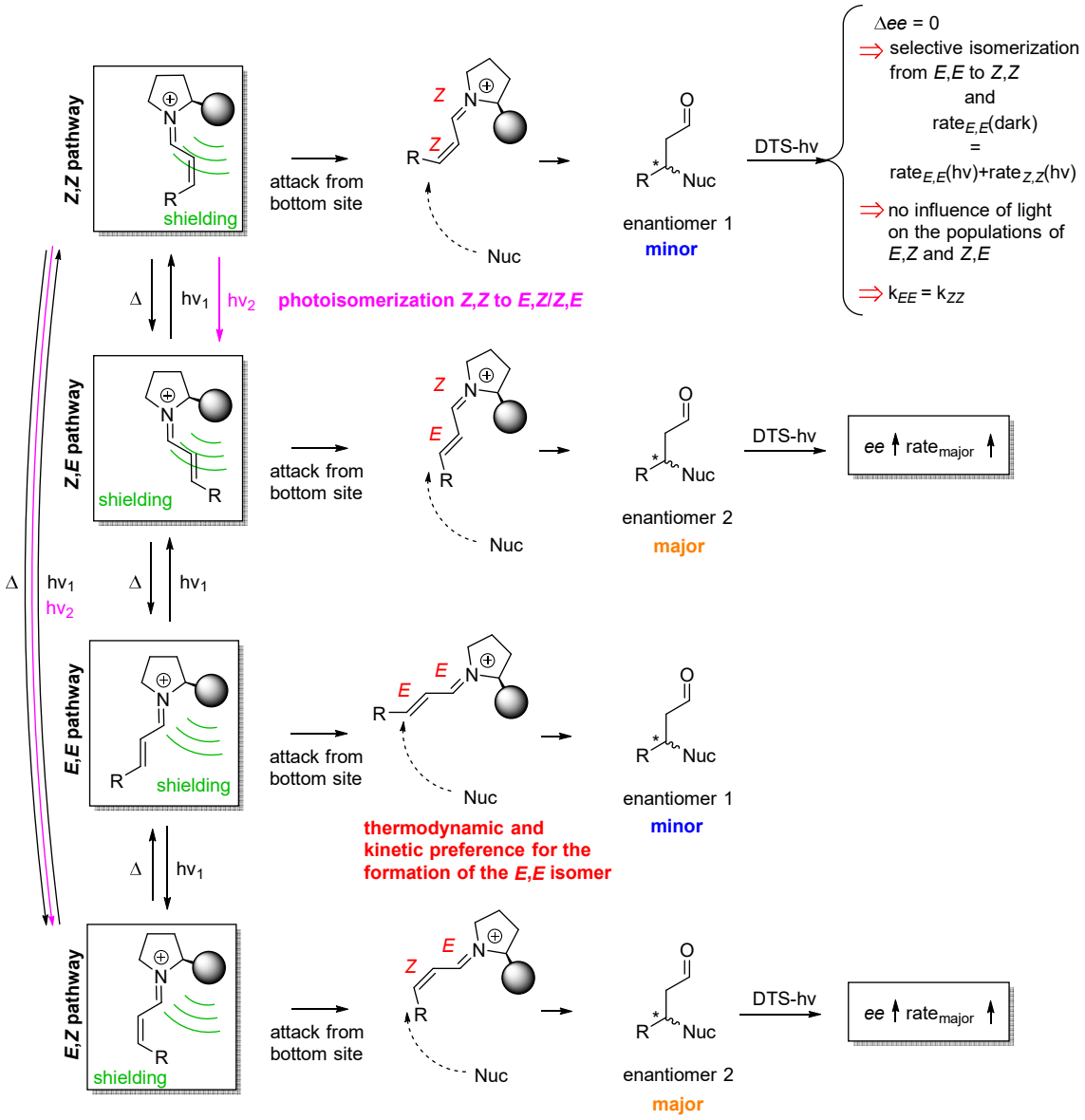

Scheme 4. Description of all possible pathways for a nucleophilic addition to an iminium intermediate under the influence of light (Scenario 2). A steric shielding of the top site of the diene subsystem is assumed due to the shielding moiety of the catalyst.

In contrast to Scenario 1, now the *E*,*E* isomer yields the minor enantiomer of the reaction. However, also here, it is regarded as the most stable and highest populated isomer in the thermodynamic equilibrium. The *E*,*Z* or *Z*,*E* pathway is supposed to be the dominant pathway; both lead to the major enantiomer (Scheme 4). Therefore, the rate for the *E*,*E* pathway has to be lower than the rate for thermal isomerization (*E*,*E*→*E*,*Z*/*Z*,*E*).

1) Isomerization to *E*,*Z*/*Z*,*E*

The isomerization of one double bond within the diene subsystem of the *E*,*E* isomer (*E*,*E*→*E*,*Z*; *E*,*E*→*Z*,*E)* causes an increase in the *ee* value of the product, since the concentration of the isomers (*E*,*Z*/*Z*,*E*), yielding the major enantiomer, is now higher. Based on the higher concentration also their rate for the product formation is increased.

2) Isomerization to *Z*,*Z*

Analogous to Scenario 1, i.e. a selective isomerization of *E,E* to *Z*,*Z* without influencing the population of *E*,*Z* and *Z*,*E* isomers causes no change in the *ee* value of the product, if the overall rate for the formation of the minor enantiomer is not influenced ($rate_{E,E}$(dark) = $rate_{E,E}$(hv) + $rate_{Z,Z}$(hv)).

In all other cases, in which also the populations of the *E*,*Z* and *Z*,*E* isomers are affected, a change in the *ee* value is caused. A higher population of *E*,*Z* and *Z*,*E* would cause an increase in the *ee* value, whereas a lower concentration (*E*,*Z*/*Z*,*E*→*Z,Z*) would lead to a reduction of the enantiomeric excess.

3) Photoisomerization *Z*,*Z*→ *E*,*Z*/*Z*,*E*

Also in Scenario 2, a photoisomerization from *Z*,*Z* to *E*,*Z*/*Z*,*E* would be feasible, if the absorbance maxima of the *Z*,*Z* isomer and the *E*,*Z*/*Z*,*E* isomer would differ significantly. The irradiation with light of a different wavelength (hv_2) might increase the concentration of the *E*,*Z*/*Z*,*E* isomers, respectively the *ee* value of the product.

Based on this theoretical approach, we assume that the irradiation with light according to the DTS-hv method could even allow for reactions or pathways, which are not accessible under normal reaction conditions. This means, in the case of a reactive isomer, which is not populated without light and a stable unreactive isomer, an irradiation with light could cause an isomerization of a double bond within the intermediates to make a new reaction pathway feasible, which enables the transformation of the intermediate.

4.3 Experimental Application of DTS-hv

To prove the theoretical approach for the applicability of the DTS-hv method in iminium ion catalysis, described in the last sections, a first experimental study was conducted. The initial results are presented and a short outlook for further investigations is given.

4.3.1 Model Reaction

As a model reaction for our investigations, a formal [3+3] annulations of α,β unsaturated aldehydes **1** with trifluoroacetaldehyde phenylhydrazone **2** (in the following text called hydrazone) was chosen randomly.[51] For this reaction, Rueping and coworkers reported an enantioselective conversion of α,β-unsaturated aldehydes **1** to cyclic dihydropyridazins **7**, catalyzed by a Jørgensen-Hayashi type prolinol ether **A** (Scheme 5). Via a nucleophilic attack of the hydrazone **2** to the β position of an iminium ion intermediate **3**, the formation of an enamine **4** and the consecutive transformation to a saturated aldehyde intermediate **5**, under regeneration of the catalyst **A** was proposed. By the attack of the lone pair of the nitrogen to the carbonyl group of the aldehyde **5**, a six-membered cyclic alcohol **6**, which was experimentally proven, is generated. The final product **7** is formed by the elimination of water under acidic conditions.[51]

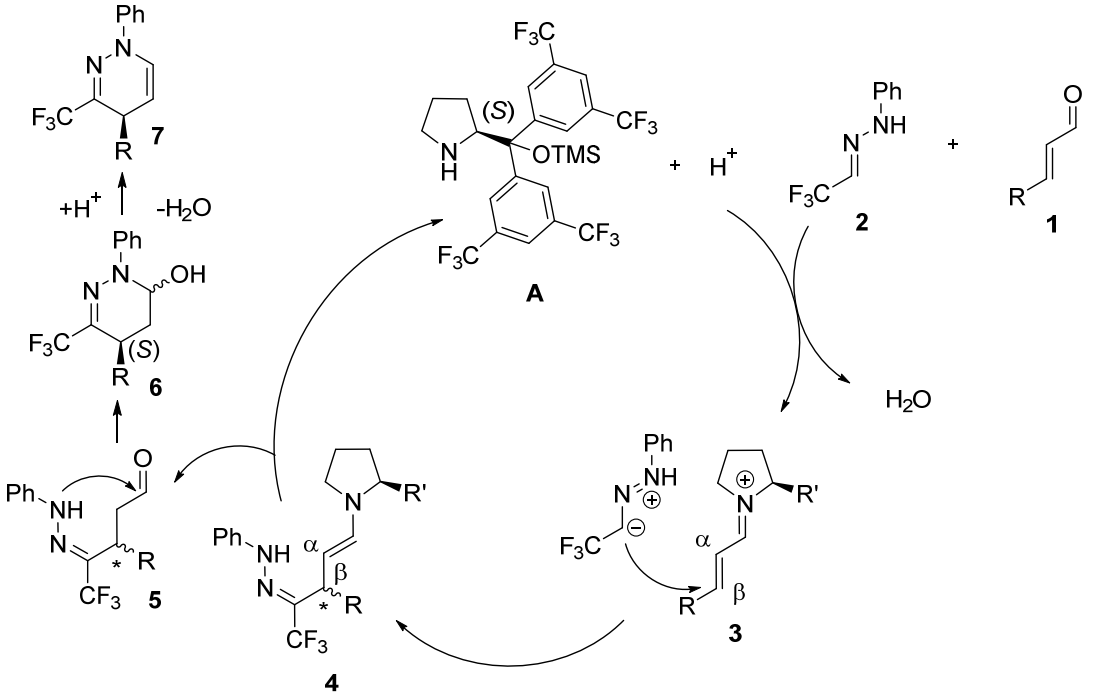

Scheme 5. Proposed catalytic cycle of a [3+3] annulations of α,β unsaturated aldehydes **1** with hydrazone **2**, catalyzed by (*S*)-2-(bis(3,5-bis(trifluoromethyl)phenyl)-((trimethylsilyl)oxy)methyl)pyrrolidine **A**.[51]

For the sake of clarity, for this system some assumptions for the application of the DTS-hv method were made: i) according to the results of Rueping and coworkers, the *E*,*E* pathway is expected to yield the (*S*)-configured product (major enantiomer in synthesis), if the (*S*)-enantiomer of the catalyst is used.[51] Therefore, Scenario 1 (see section 4.2.2) is used for the following discussion. ii) the isomerization of both double bonds from *E*,*E* to the *Z*,*Z* configured iminium ion is excluded, since this pathway also yields the (*S*)-enantiomer. iii) based on previous studies, the conformation of the single bond within the diene subsystem of the iminium ion is *s-trans* in all iminium ion intermediates.[12,38,39] iv) the bulky shielding moiety of the catalyst only allows for an attack of the nucleophile to one site of the iminium ion intermediate (shielding).

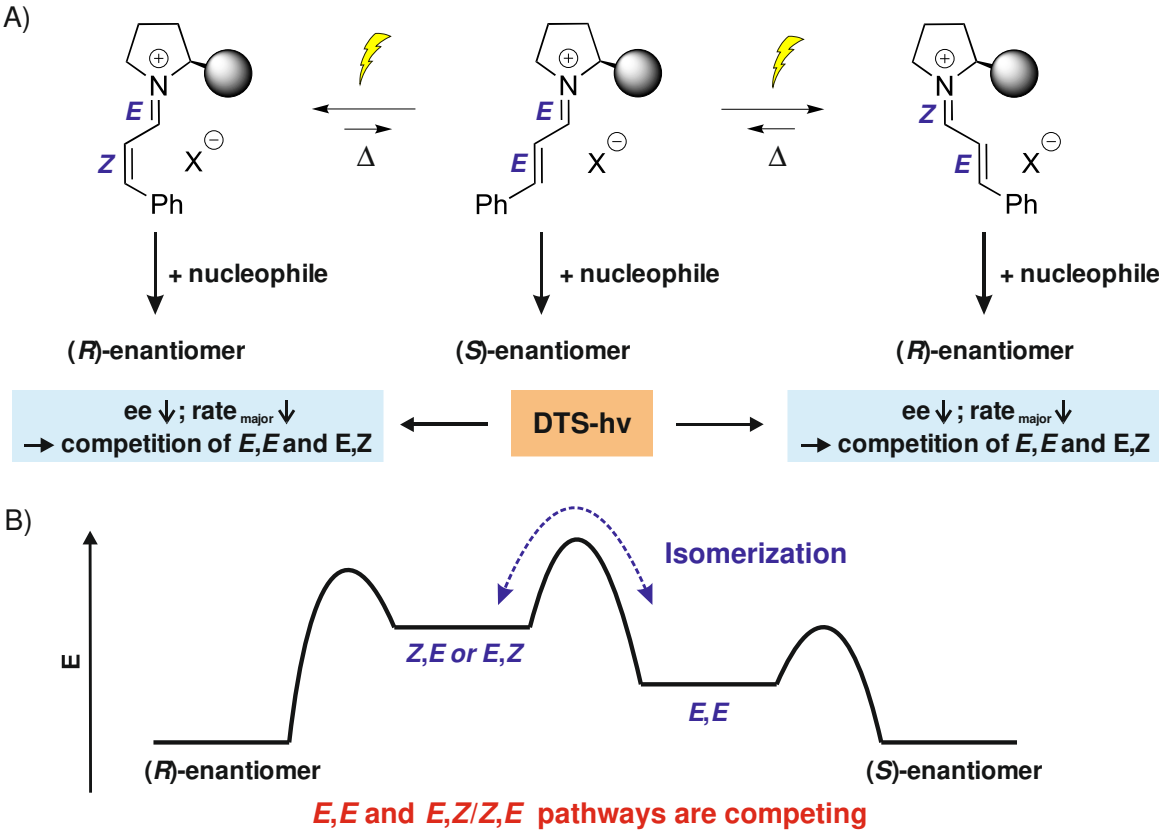

Figure 4. A) Possible reaction pathways for a nucleophilic addition to iminium ions depending on the configuration of their diene subsystem, which can be modulated by light. The corresponding fingerprint patterns according to the DTS-hv method for the different pathways are shown in the colored boxes. B) Schematic energy profile, for the competition of the *E*,*E* and *E*,*Z*/*Z*,*E* pathways (Scenario 1). The barriers for the nucleophilic addition to iminium ions are lower or comparable to the barrier for the isomerization process.

Taking these assumptions into account, according to Scenario 1, an irradiation of the reaction with light should change the rate of the major product formation as well as the *ee* value (ee ↓; $rate_{major}$ ↓). Prerequisite for this observation would be an isomerization of one double bond within the conjugated diene subsystem of the iminium ion (Figure 4A). In Figure 4B the resulting energy profile for the competition between the *E*,*E* and *E*,*Z* or *Z*,*E* pathway is shown. The barriers for the competing pathways have to be similar, so both can be active. Additionally, the rate of the thermal backisomerization (*E*,*Z* → *E*,*E* or *Z*,*E* → *E*,*E*) has to be equal or lower than the rate for the nucleophilic attack, otherwise no effect on the enantiomeric excess of the product is possible.

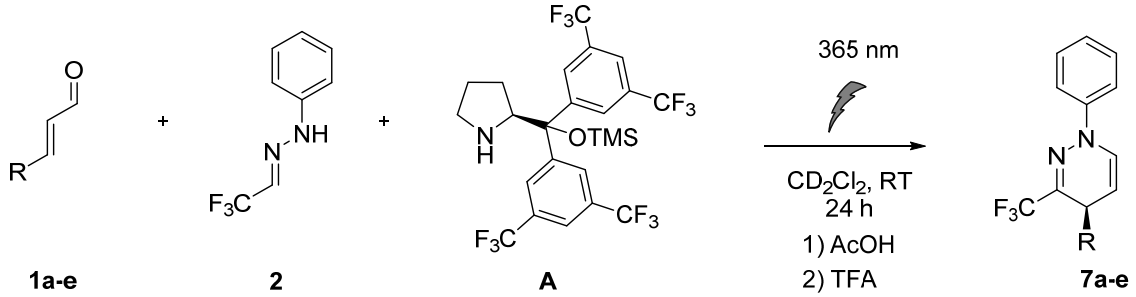

Scheme 6. Reaction of aldehyde **1a-e** (2 equiv), hydrazone **2** (1 equiv) and catalyst **A** (0.2 equiv) in dichloromethane under the influence of acetic acid (1 equiv) and light (365 nm). After 24 h, trifluoroacetic acid (TFA; 0.2 equiv) is added to yield product **7**.

Table 1. Comparison between the experimental results of the reaction (Scheme 6) obtained in the dark and under the influence of light.

Substrate	λ [nm]	*ee* [%]	$yield^{isolated}$ [%]
1a; R = CH_3	-	64	73
	365	32	8
1b; R = CH_2CH_3	-	84	34
	365	72	28
1c; R = Ph	-	73	98
	365	44	48
1d; R = *p*-OMe-C_6H_4	-	74	45
	365	46	30
1e; R = *p*-Br-C_6H_4	-	81	76
	365	70	55

To investigate the active pathway and to prove the validity of the DTS-hv method (Scenario 1), the reaction of aldehyde **1a-e**, hydrazone **2** and catalyst **A** was conducted under the influence of acetic acid with and without light (365 nm) (Scheme 6). As shown in Table 1, a decrease in *ee* and in yield was found experimentally for all aldehydes under illumination. These results positively confirm the influence of light on the reaction outcome. However, no information, if this change in enantioselectivity is caused by an isomerization of a double bond (*E*,*E* → *E*,*Z* and/or *Z*,*E*) can be gained. Therefore, more detailed investigations about the influence of light on the diene subsystem of the iminium ion intermediates were required. For this purpose, NMR spectroscopy was the method of choice since it enables a fast quantitative analysis of the ratio between the different isomers in solution. Additionally, by the application of our LED based illumination device, the influence of light can be investigated in real time inside the NMR spectrometer.[52]

4.3.2 NMR Spectroscopic Investigations

As a model system for the NMR spectroscopic investigations, the reaction of cinnamaldehyde **1c**, catalyst **A**, and hydrazone **2** was chosen. Due to the lack of a proton in γ position of the diene subsystem of the corresponding iminium ion, the formation of dienamines is suppressed (Scheme 2), which simplifies the spectroscopic investigations. Furthermore, several examples in literature showed, that cinnamaldehyde is readily forming stable iminium ions with secondary amines,[38,39,50] enabling the investigation of isolated iminium ion salts under the influence of light.

Under reaction conditions, i.e. in the presence of acetic acid (Scheme 6), no iminium ion intermediates could be detected by NMR. However, a consecutive formation of aldehyde intermediate **5** and two diastereomers of the cyclic intermediate **6** could be proven, supporting the proposed reaction mechanism by Rueping (for the assignments see the Experimental Part).[51] To convert the cyclic intermediates into the final product by an elimination of water, the addition of a stronger acid like trifluoroacetic acid (pK_a = -0.25 (H_2O) vs 4.76 (H_2O) for acetic acid)[53] was required. Alternatively, the acidity of silica gel can be exploited to form the product during the purification procedure via column chromatography.

Possible reasons, why the iminium ions are not detectable under these reaction conditions, might be either a very low population below the detection limit or a fast conversion to the product or both. However, a former study of Hayashi *et al.* proved that no iminium ions derived by a condensation of cinnamaldehyde and a Jørgensen-Hayashi type catalyst are detectable under the influence of acetic acid.[50] Even in the absence of a

nucleophile, the stabilization of the iminium ion by the acetate counterion seems to be insufficient. Therefore, a population below the detection limit is assumed under these conditions. To increase the population of the iminium ion intermediates, the reaction was conducted in the presence of trifluoroacetic acid instead of acetic acid.[50] Based on the report of Rueping, a change to TFA accelerates the reaction and slightly lowers the *ee* value of the product most probably due to an additional acid catalyzed product formation.[51] Under the influence of TFA (Figure 5A), the detection of two iminium ion isomers (*E*,*E* and *Z*,*E)* by NMR spectroscopy was enabled, whereby a clear preference for the formation of the *E*,*E* iminium could be found (Figure 5B, t = 0 h). This preference is in line with former studies about cinnamaldehyde derived iminium ions.[38,39] To investigate the conversion of the iminium ion intermediates with the nucleophile, hydrazone **2** was added to the reaction mixture after a sufficient amount of iminium ion was formed *in situ* (Figure 5B).

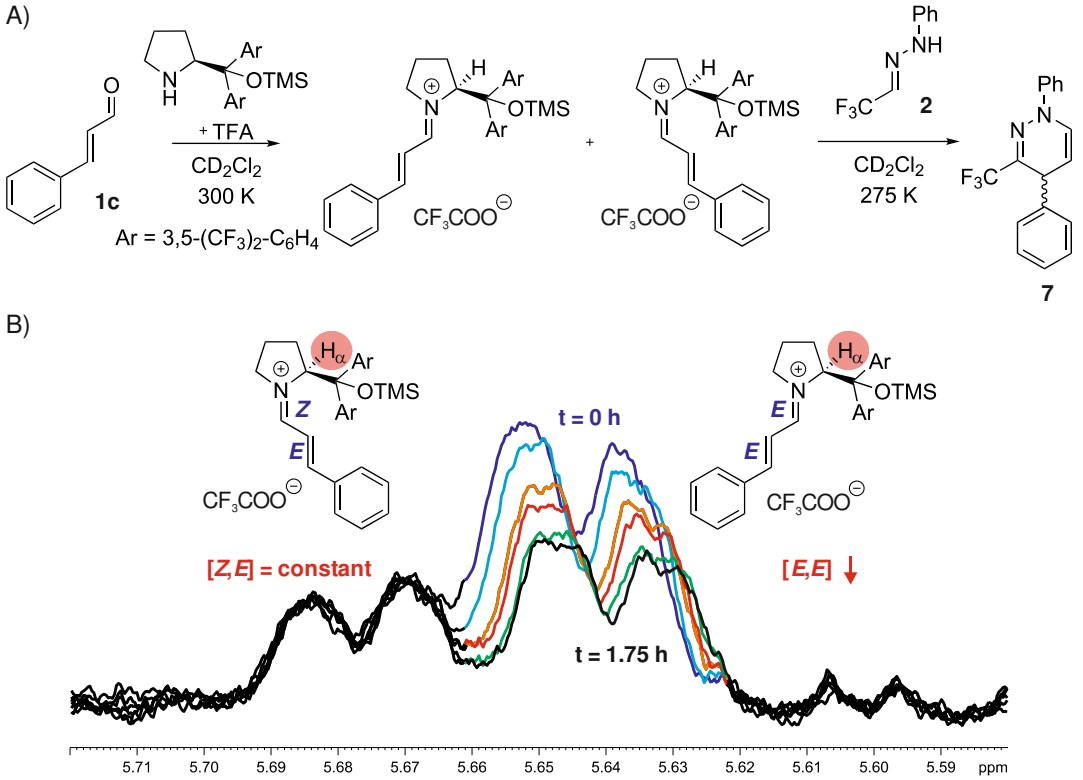

Figure 5. A) Formation of iminium ion intermediates (*E*,*Z* and *Z*,*E*), derived by equimolar (50 mM) reaction of cinnamaldehyde **1c**, catalyst **A** and TFA in CD_2Cl_2 at 300 K. Conversion of the iminium ion to the product by the addition of hydrazone **2**. B) Stacked ^1H spectra at 275 K showing the decrease of the H_α signal intensity selectively for the *E*,*E* isomer over time, after the addition of nucleophile **2** (1 equiv). The change in the concentration of the *Z*,*E* isomer is negligible, proving a strong preference for the conversion of the *E*,*E* isomer, respectively the formation of the (*S*)-enantiomer.

As shown in Figure 5, after the addition of hydrazone **2**, a selective decrease in the intensity of the H_α signal of the *E*,*E* isomer could be proven by NMR. Simultaneously, intermediates **5**, **6** and the product **7** are formed (data not shown, for assignment see the Experimental Part). The constant concentration of the *Z*,*E* isomer (Figure 5) can be explained either by a significant lower rate for the *Z*,*E* pathway or by a continuous regeneration of the *Z*,*E* iminium ion, if the rates for the formation and its conversion are equal (steady state). Based on the clear preference for the (*S*)-enantiomer of the product in synthesis, which is formed via the *E*,*E* or *Z*,*Z* pathway, a very low rate for the *Z*,*E* pathway is assumed. Therefore, this result proves experimentally the preference for the *E,E* pathway over the *Z*,*E* pathway.

As a consequence, we propose a competition of the *E*,*E* and *E*,*Z* pathways to be responsible for the change in the enantiomeric excess for the reactions conducted under the influence of light. Unfortunately, *in situ* illumination studies with light of a 365 nm LED inside the NMR spectrometer did not reveal any evidence for the presence of the *E*,*Z* iminium ion intermediate. The detection is supposed to be hindered either by a fast thermal backisomerization (*E*,*Z*→*E*,*E*) or by a very low population below the threshold under these conditions. To exclude a rapid backisomerization, additional experiments at low temperatures (210 K) were conducted to reduce its rate, however even under these modified conditions no *E*,*Z* isomer could be detected. Hence, either the thermal backisomerization is still too fast or more likely, the decreased temperature caused a shift of the equilibrium even more towards the thermally preferred *E*,*E* isomer. To analyze the effect of light (365 nm) on iminium ions in more detail, a stable iminium ion perchlorate salt, derived by the reaction of cinnamaldehyde, catalyst **A** and perchloric acid, was synthesized and isolated.[50]

In the absence of light, only the *E*,*E* and *Z*,*E* iminium ion isomers could be detected by NMR spectroscopy (Figure 6A, t = 0 min; ratio *Z*,*E*/*E*,*Z*/*E*,*E* = 6/0/94). First *in situ* illumination experiments inside the NMR spectrometer with a 365 nm LED showed an isomerization of both double bonds within the diene subsystem at 300 K (*E*,*E*→*Z*,*E* and *E*,*E*→*E*,*Z*) (Figure 6A, t = 45 min; ratio *Z*,*E*/*E*,*Z*/*E*,*E* = 13/21/66)). During the steady decrease of the signal intensity of the H_α proton of the *E*,*E* signal, a slight increase of the *Z*,*E* signal and a more pronounced formation of the *E*,*Z* isomer could be detected.

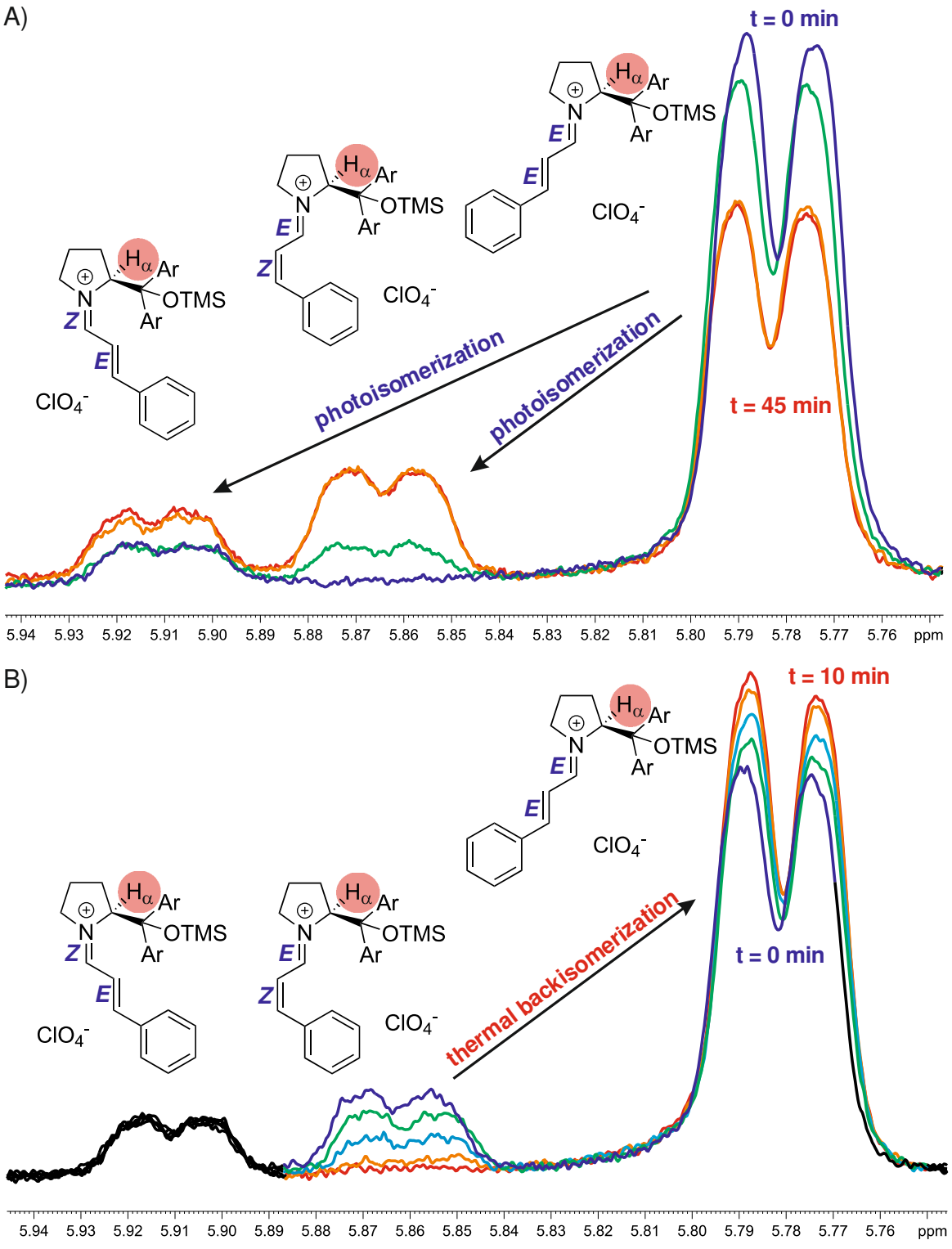

Figure 6. A) Stacked 1D ^{1}H spectra, to show the light (365 nm) induced isomerization of an iminium ion perchlorate salt based on the change in signal intensities of the H_{α} signals over time (CD_2Cl_2; 300 K). An isomerization form *E*,*E* to *E*,*Z* and *Z*,*E* could be proven experimentally. However, a clear preference for the isomerization to *E*,*Z* could be found. B) Stacked 1D ^{1}H spectra for the selective thermal backisomerization exclusively from *E*,*Z*→*E*,*E* over ≈ 10 min.

Furthermore, a fast decrease of the concentration of the *E*,*Z* isomer by thermal backisomerization was observable, when the light was turned off. In contrast the amount of the *Z*,*E* isomer remained unchanged (Figure 6B). After the light (365 nm) was switched off after ~ 19 h, the *Z*,*E*/*E*,*Z*/*E*,*E* ratio changed within 10 minutes from 10/16/74 to 10/-/90, proving the isomerization from *E*,*Z*→*E*,*E* (Figure 6B). It has to mentioned, that a slight deviation in the ratios during the illumination was found (t = 45 min; ratio *Z*,*E*/*E*,*Z*/*E*,*E* = 13/21/66 vs t ~ 19 h; *Z*,*E*/*E*,*Z*/*E*,*E* = 10/16/74. This deviation is most probably caused by a slight photodegradation of the iminium ion species, since the H_α signal intensity of all iminium ion species is marginally decreasing.

To investigate the reactivity of the different isomers, hydrazone **2** was added to the isomerized solution at low temperature to freeze the equilibrium and to slow down the reaction. However, even at room temperature no reaction of the iminium ions with hydrazone **2** could be detected by NMR spectroscopy. Nevertheless, due to the strong preference for the formation of the *E*,*Z* isomer during the illumination with 365 nm (Figure 6) and the very low reactivity of the *Z*,*E* isomer (Figure 5), we assume a reaction of the *E*,*Z* isomer to be responsible for the change in the *ee* values (Table 1). If indeed, a competition between the *E,E* and *E,Z* isomer instead of the *Z*,*E* isomer, as it is preferably assumed in synthesis would be decisive for the *ee* value of this reaction, a new potential for transformations via iminium ion catalysis might be revealed.

It has to be stated, that the presented results are just preliminary and further investigations are necessary. However, this was beyond the scope of this thesis. First of all, the presence of the *E*,*Z* isomer in absence of light has to be proven. Here, probably the application of the CEST technique (chapter 3) or the usage of cryo-probes might be the key to detect populations below the detection limit of the measurements, which were conducted so far. Furthermore, reactions with stronger nucleophiles, according to the Mayr scales,[54–56] has to be investigated to validate the reactivity of the *E*,*Z* isomer and variations in the concentration of the nucleophile have to be tested, to exclude a steady state for the formation and conversion of the *Z*,*E* isomer under these conditions.

4.4 Conclusion

To summarize, in this chapter, the applicability of the DTS-hv method in a more complex organocatalytic reaction was presented and investigated for the first time. On the example of an iminium ion catalyzed [3+3] annulation of α,β-unsaturated aldehydes with hydrazones, all possible fingerprint patterns regarding the diene subsystem of the key intermediates were discussed according to the DTS-hv method. Furthermore, the resulting scenarios, describing the change in the *ee* value and yield of a reaction under the influence of light, were used to predict new possible application of light induced isomerization in synthesis.

In agreement with the DTS-hv method, first experimental results proved an influence of light on the enantiomeric excess and yield of the reaction. By additional NMR spectroscopic investigations in absence of light, a strong preference for the conversion of the *E*,*E* iminium ion isomer could be shown. The constant concentration of the corresponding *Z*,*E* isomer in the presence of the hydrazone nucleophile indicated an inferior role in the reaction. Further *in situ* isomerization experiments of an isolated iminium ion perchlorate salt inside the NMR spectrometer enabled a detection of the corresponding *E*,*Z* isomer. Based on the low reactivity of the *Z*,*E* isomer in presence of the nucleophile, the formation and conversion of the *E*,*Z* isomer under the influence of light is assumed to be responsible for the change in the *ee* value of the reaction. If this competition between the *E*,*E* and the *E*,*Z* iminium ion isomer could be proven to decisive for the *ee* value instead of the reaction of the *Z*,*E* isomer, a totally new aspect in iminium ion catalysis would be revealed. Normally, to the best of our knowledge, an exclusive competition between the two isomers, differing in the configuration around the C=N double bond, is assumed in synthesis. Unfortunately, so far an experimental prove for this theory is missing, however further studies, including different catalysts and nucleophiles, and using improved spectroscopic techniques, are in progress in our working group. Nevertheless, we are convinced that the DTS-hv method can develop as a versatile tool in enantioselective aminocatalysis.

4.5 Experimental Part

General Information

The chemicals for this study were purchased from Sigma Aldrich and Deutero. The aldehydes were purified by distillation before usage; all other chemicals were used without further purification. The deuterated dichloromethane-d_2, used in the NMR studies, was dried by refluxing over CaH_2. All NMR experiments were performed at 300 K (if not otherwise indicated) on a Bruker Avance III Nanobay 400 and a Bruker Avance III 600 (600.25 MHz) with a fluorine selective TBIF probe. All spectra were processed and evaluated with Bruker Topspin 3.2 and Bruker Topspin 4.0.

Synthesis of Hydrazone 2

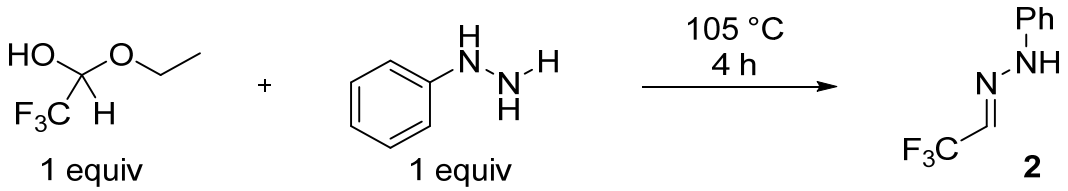

In a 25 ml round bottom flask, equipped with a drying tube with $CaCl_2$, 1-ethoxy-2,2,2-trifluoroethan-1-ol (1.31 ml, 1 equiv) and phenylhydrazine (1 ml, 1 equiv) were heated for 4 h to 105 °C without any additional solvent. After cooling, the resulting yellow solid was washed with ice cold n-pentane to yield the desired hydrazone **2** (40%).[57]

^{1}H-NMR (400 MHz, $CDCl_3$): δ= 6.95 (q, 1H), 6.98 (t, 1H), 7.08 (d, 2H), 7.30 (pt, 2H), 7.94 (bs, 1H).

General Procedure

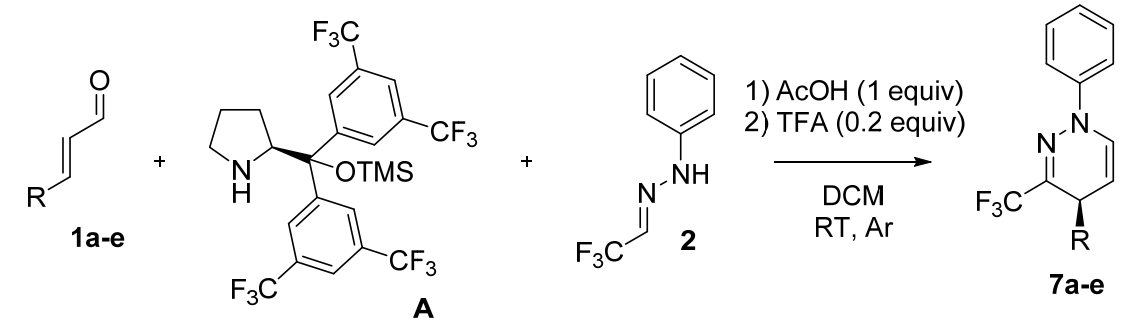

In a pre-dried Schlenk tube equipped with a magnetic stirring-bar, 20 mol% of catalyst **A** (0.032 mmol) and trifluoromethylacetaldehyde hydrazone **2** (1 equiv, 0.16 mmol) were dissolved in 1.25 mL DCM, before 2 equiv of aldehyde **1a-e** (0.32 mmol) were added. The solution was stirred at room temperature and under irradiation with a 365 nm LED lamp (the control reaction was run without illumination). After 10 minutes, 1 equiv of acetic acid (0.16 mmol) was added to the reaction. After 24 h, TFA (0.2 equiv; 0.032 mmol) was added to the reaction and then it was stirred at room temperature overnight. The crude reaction mixture was purified by column chromatography over silica gel (petroleum ether/DCM 10/1).

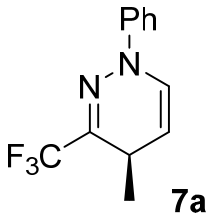

7a

The product **7a** was synthesized and isolated according to the general procedure. The *ee* was determined by CSP-HPLC, CHIRAPAK IB column, eluant *n*-hexane/*i*-propanol 99.7/0.3, flow 0.6 mL/min, retention times: τ_1= 7.56 min, τ_2= 7.97 min, column compartment temperature 20°C, λ= 254 nm.

^{1}H-NMR (400 MHz, $CDCl_3$): δ= 1.18 (d, 3H, J= 6.8 Hz), 3.23-3.33 (m, 1H), 5.05-5.10 (dd, 1H), 6.76 (d, 1H, J= 7.6 Hz), 7.05-7.14 (m, 1H), 7.31-7.39 (m, 4H).

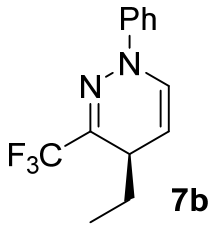

7b

The product **7b** was synthesized and isolated according to the general procedure. The *ee* was determined by CSP-HPLC, CHIRALPAK IB column, eluant *n*-hexane/*i*-propanol 99.7/0.3, flow 0.6 mL/min, retention times: τ_1= 7.14 min, τ_2= 7.40 min, column compartment temperature 20°C, λ= 254 nm.

^{1}H-NMR (400 MHz, $CDCl_3$): δ= 0.92 (t, 3H, J= 7.44 Hz), 1.43-1.63 (m, 2H), 3.25-3.31 (m, 1H), 5.0-5.07 (dd, 1H), 6.82 (d, 1H, J= 7.64), 7.06-7.12 (m, 1H), 7.32-7.39 (m, 4H).

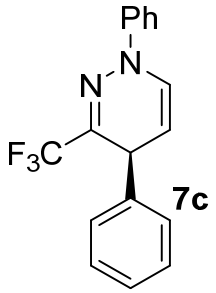

7c

The product **7c** was synthesized and isolated according to the general procedure. The *ee* was determined by CSP-HPLC, CHIRALCEL OD-H column, eluant *n*-hexane/*i*-propanol 95/5, flow 1 mL/min, retention times: τ_1= 6.73 min, τ_2= 8.22 min, column compartment temperature 20°C, λ= 254 nm.

^{1}H-NMR (400 MHz, $CDCl_3$): δ= 4.42 (d, 1H, J= 5.32 Hz), 5.21-5.26 (m, 1H), 6.92 (d, 1H, J= 7.8 Hz), 7.10-7.18 (m, 1H), 7.21-7.46 (m, 9H).

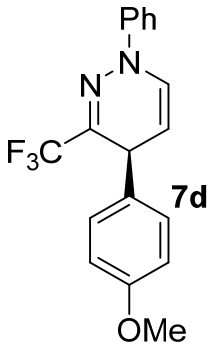

7d

The product **7d** was synthesized and isolated according to the general procedure. The *ee* was determined by CSP-HPLC, CHIRALCEL OD-H column, eluant *n*-hexane/*i*-propanol 95/5, flow 1 mL/min, retention times: τ_1= 6.69 min, τ_2= 8.92 min, column compartment temperature 20°C, λ= 254 nm.

^{1}H-NMR (400 MHz, $CDCl_3$): δ= 3.79 (s, 3H), 4.35 (d, 1H; J= 5.31 Hz), 5.17-5.25 (m, 1H), 6.82-6.88 (m, 2H), 6.89-6.93 (m, 1H), 7.08-7.18 (m, 1H), 7.36-7.42 (m, 4H).

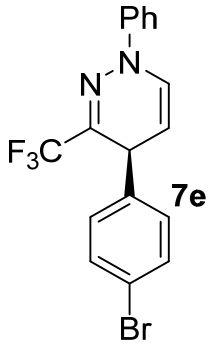

7e

The product **7e** was synthesized and isolated according to the general procedure. The *ee* was determined by CSP-HPLC, CHIRALCEL OD-H column, eluant *n*-hexane/*i*-propanol 95/5, flow 1 mL/min, retention times: τ_1= 5.30 min, τ_2= 6.80 min, column compartment temperature 20°C, λ= 254 nm.

^{1}H-NMR (400 MHz, $CDCl_3$): δ= 4.41 (d, 1H; J= 5.31 Hz), 5.17-5.25 (m, 1H), 6.94 (d, 1H; J= 7.8 Hz), 7.08-7.21 (m, 3H), 7.39-7.51 (m, 6H).

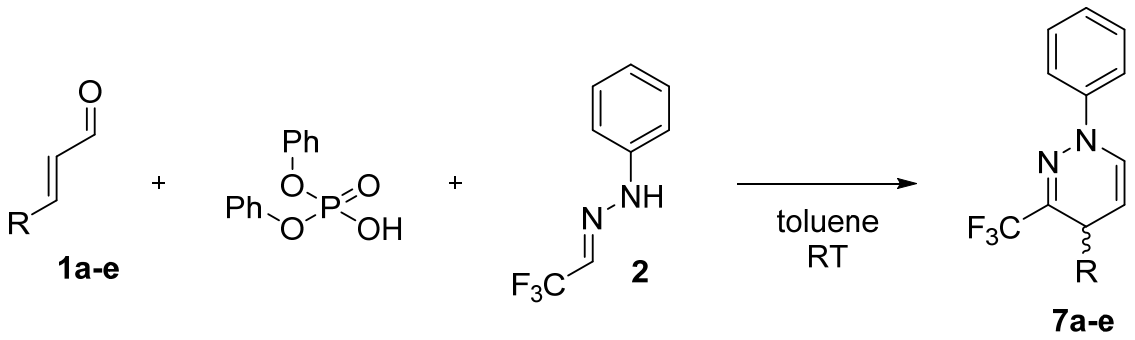

1.5 equiv 0.2 equiv 1 equiv

To synthesize the racemic mixtures of product **7a-e**, hydrazone **2** (0.27 mmol, 1 equiv), aldehyde **1a-e** (0.4 mmol, 1.5 equiv) and diphenylphosphate (0.054 mmol, 0.2 equiv) were dissolved in 1 ml toluene. After the reaction, the product was isolated by column chromatography (petroleum ether/DCM 10/1).

Assignment of Intermediates Under Reaction Conditions with AcOH

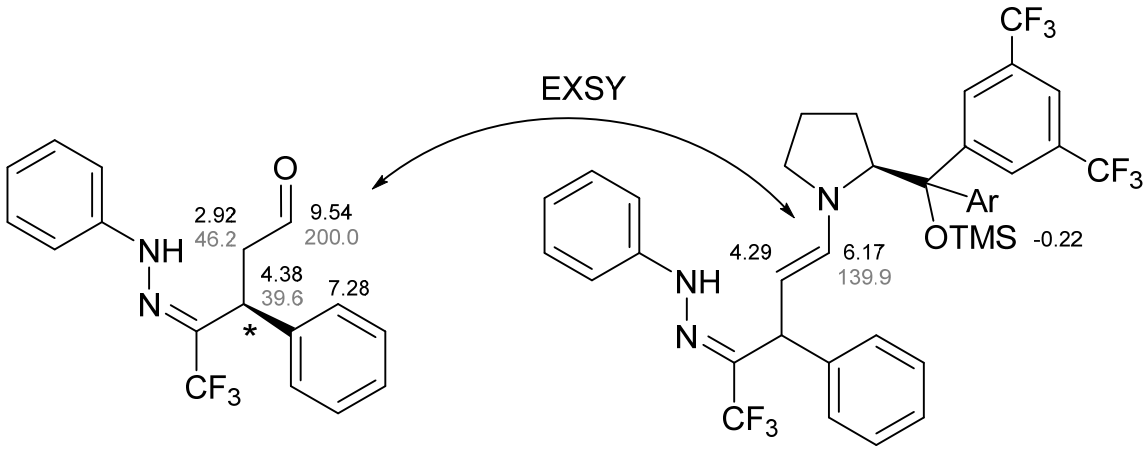

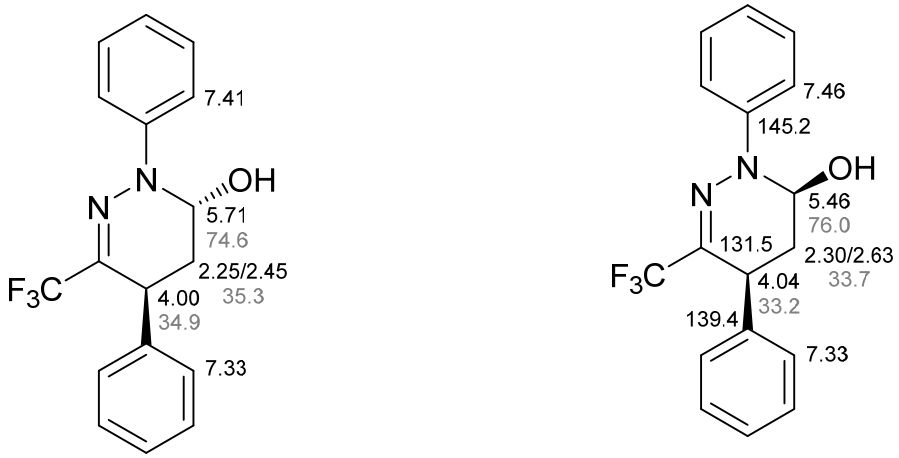

Sample Preparation

In a predried Schlenk tube, under Argon atmosphere, 20 mol% of catalyst **A** (0.026 mmol) and trifluoromethylacetaldehyde hydrazone **2** (1 equiv, 0.13 mmol) were dissolved in 1.00 mL DCM-d_2. The solution was cooled to -10 °C, before cinnamaldehyde **1c** (0.26 mmol) and 10 minutes later acetic acid (0.13 mmol) was added. The solution was stirred for 4 d at -10 °C. For the assignment of the intermediates by NMR spectroscopy, the solution was transferred to a standard NMR tube and a standard set of spectra (COSY, NOESY, HSQC, and HMBC) was recorded. Due to signal overlap most of the time, only the analysis of the central spin system was enabled. Therefore, no detailed information about the exact structures is available. However, based on the proposed pathway by Rueping, theses intermediates seem to be highly likely.[51]

Assignment of Intermediates Under Reaction Conditions with TFA

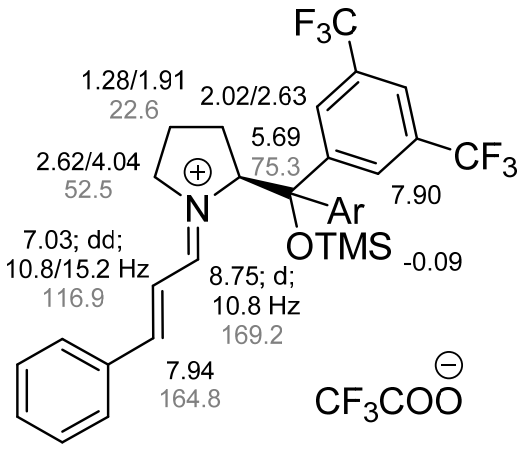

***E*,*E* isomer**

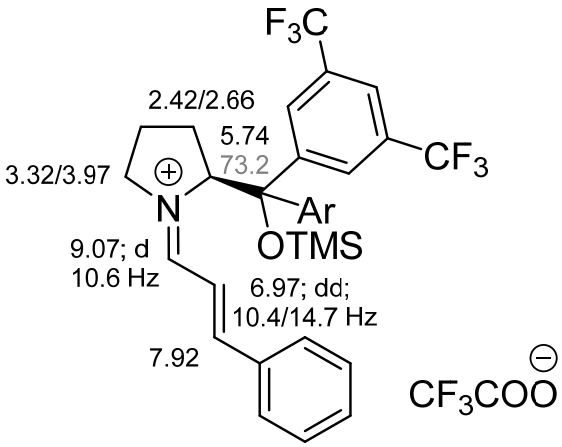

***Z*,*E* isomer**

Ar = 3,5-$(CF_3)_2$-C_6H_3

Sample Preparation

For the NMR spectroscopic investigations of the iminium ion intermediates, equimolar solutions of catalyst **A**, cinnamaldehyde **1c**, and TFA were prepared, to increase the amount of iminium ion intermediates. Therefore, catalyst **A** (1 equiv, 0,025 mmol) cinnamaldehyde **1c** (1 equiv, 0,025 mmol), and TFA (1 equiv, 0,025 mmol) were dissolved in 0.5 mL DCM-d_2 inside a 5 mm NMR tube. The measurements for the assignment were executed at 300 K.

Assignment of Iminium Perchlorate Isomers

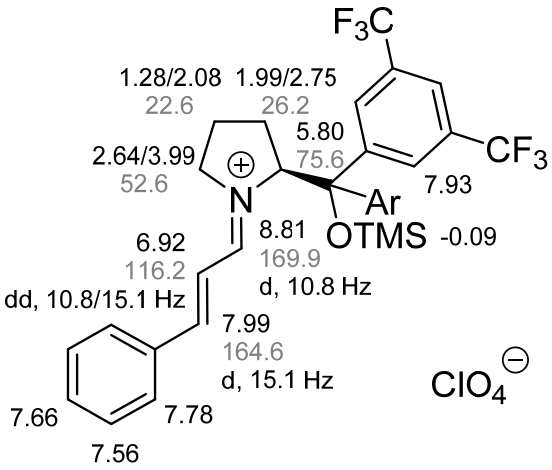

***E*,*E* isomer**

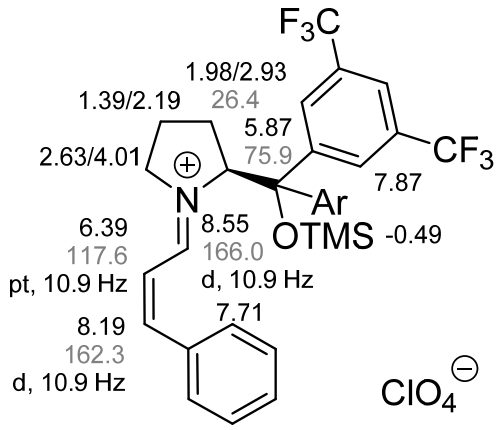

***E*,*Z* isomer**

Ar = 3,5-$(CF_3)_2$-C_6H_3

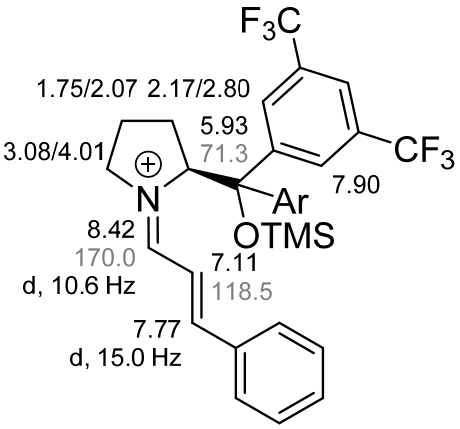

***Z*,*E* isomer** $ClO_4^{\ominus}$

Sample Preparation

To investigate the structure of iminium ion intermediates, as well as their behavior under the influence of light (365 nm) a stable iminium ion perchlorate salt was synthesized according to a literature known procedure.[50] For the NMR spectroscopic investigations, a solution (25 mM) of iminium ion perchlorate in DCM-d_2 (0.5 ml; dry) was illuminated *in situ* within the NMR spectrometer with a 365 nm LED. By irradiation, an isomerization to the *E*,*Z* isomer was induced. The resulting assignments of the three isomers are shown above. The chemical shifts, indicated for the *E*,*E* and *Z*,*E* isomer are in agreement with earlier reports.[38,39,50]

4.6 Additional Findings

4.6.1 6π-Electrocyclizations

Another approach to synthesize 1,4-dihydropyrodazines **7** was also presented by Rueping and coworkers in 2013.[58] Here, instead of the Jørgensen-Hayashi-type catalyst **A** (see above), an asymmetric sterically demanding Brønsted acid catalyst **C** was used. In the proposed reaction mechanism a condensation of hydrazone **2** and α,β-unsaturated aldehydes **1b-d** is suggested to yield a cationic iminium intermediate **8** with a conjugated 6 π electron system. Together with the asymmetric phosphate of the catalyst, the cationic intermediate forms a chiral ion pair. After a thermally allowed 6π-disrotatory electrocyclization a 6-membered ring is formed, which gives the desired product after the elimination of the protonated catalyst. (Scheme 7)

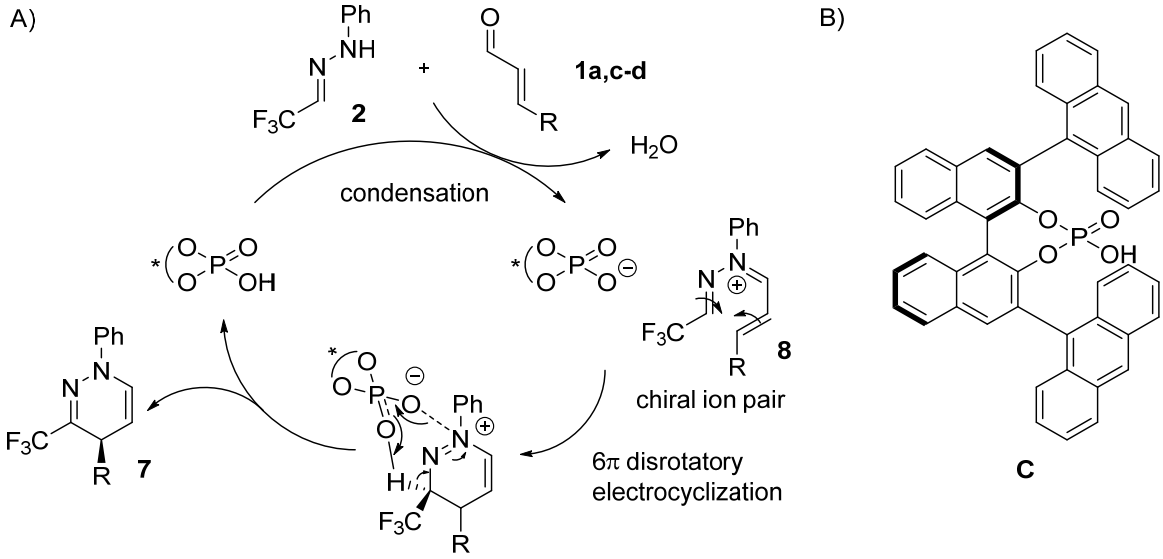

Scheme 7. A) Proposed catalytic cycle by Rueping *et. al.*[58] B) Brønsted acid catalyst **C** ((*R*)-3,3′-Bis(9-anthracenyl)-1,1′-binaphthyl-2,2′-diyl hydrogenphosphate).

In order to investigate the influence of light on this reaction and to analyze the dominant pathway by NMR applying the DTS-hv method, the reaction (Scheme 8) was conducted under continuous illumination with different wavelength (365 nm, 455 nm). The reaction without additional illumination acts as a reference.

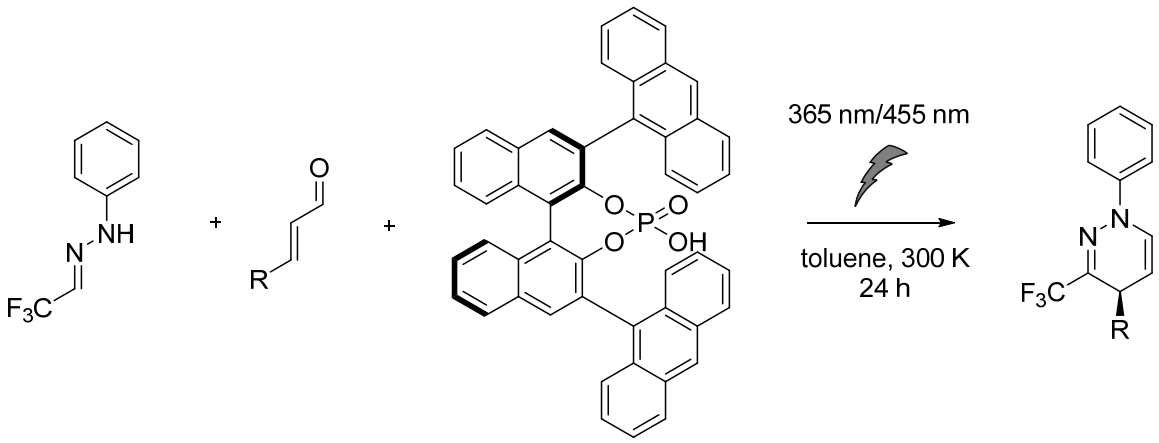

Scheme 8. Reaction of hydrazone **2** (1 equiv) with different α,β-unsaturated aldehydes **1b**-**d** (R = Me, Ph, *p*-OMe-C_6H_4; 1.5 equiv) under the influence of catalyst **C** (0.08 equiv) and light (365 nm, 455 nm) in toluene at 300 K (24 h).

As shown in Table 2, depending on the substituents R of the unsaturated aldehydes **1b-d**, strong variations in the *ee* values of the products could be found. In the case of the linear *trans*-pent-2-enal **1b** (R = CH_2CH_3), the change in *ee* is not that significant, therefore a deviation independent of the presence of light is assumed. In contrast, in the case of the aromatic substituents (R = Ph, *p*-OMe-C_6H_4), a strong influence of light was observable. In both cases the *ee* values were decreased significantly or even inverted, as shown for **1d** (R = *p*-OMe-C_6H_4). The intensity of this effect increased with a decreasing wavelength of the light applied for illumination (365 nm > 455 nm). Furthermore, the yields of all reactions dropped significantly when changing the light source from 455 nm to 365 nm.

Tabel 2. Reaction of hydrazone **2** (1 equiv) with different α,β-unsaturated aldehydes **1b**-**d** (R = CH_2CH_3, Ph, *p*-OMe-C_6H_4; 2 equiv) under the influence of catalyst **C** (0.08 equiv) and light (365 nm, 455 nm) in toluene at 300 K (24 h). n.d. = not determined

Substrate	λ [nm]	*ee* [%]	yield^{isolated} [%]
	-	58	74
1b; R = CH_2CH_3	455	60	n.d.
	365	47	3
	-	41	21
1c; R = Ph	455	19	4
	365	-	0
	-	55	n.d.
1d; R = *p*-OMe-C_6H_4	455	-23	18
	365	-33	4

The reason for this significant decrease/inversion of the *ee* values can most likely be found in the underlying reaction mechanism. As proposed by Rueping, the reaction is a 6π electrocyclization reaction driven by thermal energy.[58] This means according to the Woodward-Hoffmann rules a disrotatory cyclization in the HOMO orbital of the conjugated 6π electron system of the intermediate (chiral ion pair, Scheme 7) is allowed.[59]

Now, using additional light (365 nm, 455 nm) in this reaction, an excitation of an electron to a higher orbital might be possible, if the molecule/intermediate is able to absorb the light of a certain wavelength. Having a single occupied molecular orbital present, now according to the Woodward-Hoffmann rules a conrotatory σ bond formation, yielding the other enantiomer, would be allowed (Figure 7).[59] Therefore, in the case of **1c**, **1d** (R = Ph, *p*-OMe-C_6H_4) a change in the reaction mechanism is assumed.

This means one important prerequisite of the DTS-hv method is not given and hence the method is not applicable for this reaction.

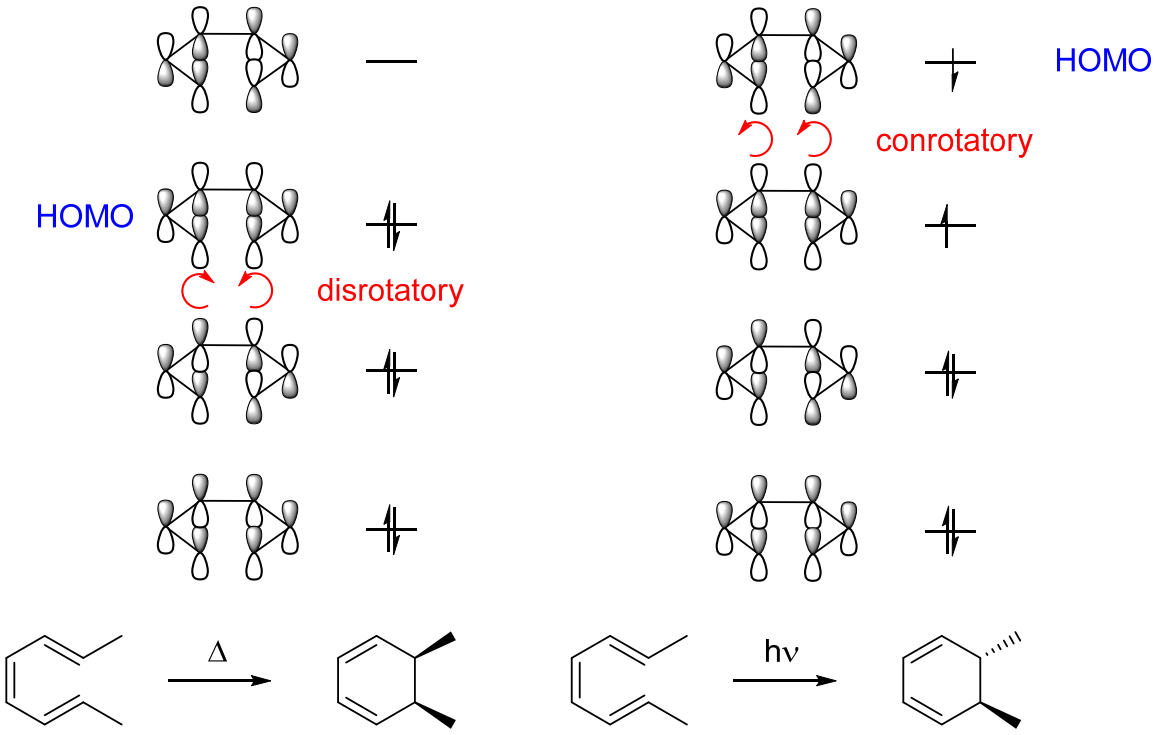

Figure 7. Schematic representation of the Woodward-Hoffmann rules for a 6π electrocyclization reaction of a triene. In the case of a thermal driven reaction, the σ bond is formed disrotatory (*left*). In the presence of light, one electron is excited to a higher orbital, which now allows a conrotatory σ bond formation (*right*).[59]

Another important aspect to mention here is the observed decrease in yield when additional light was applied. A comparison of three ^{1}H NMR reaction profiles (Figure 8-10) of a reaction of *trans*-pent-2-enal **1b** and hydrazone **2** under the influence of catalyst **C** and light with different irradiation wavelengths (365/455 nm) was made. The reaction profile, recorded in the absence of light (Figure 8), was used as a reference. The other reaction profiles revealed an acceleration of the reaction under irradiation, most prominent in the reaction with 365 nm (Figure 9). Furthermore, in the case of 365 nm, a fast decrease of the product signal after around 1.5 h was observable, indicating the product being destroyed by light (365 nm). Irradiation of the isolated product with light (365 nm) confirmed this observation (data not shown). Although the reaction profile (455 nm, Figure 10) does not show a decrease in the intensity of the product signal for the reaction with *trans*-pent-2-enal **1b** after 14 h, a decrease of the yield for the other aldehydes **1c,d** (R = Ph, *p*-OMe-C_6H_4) is expected based on the experimental results (Table 2).

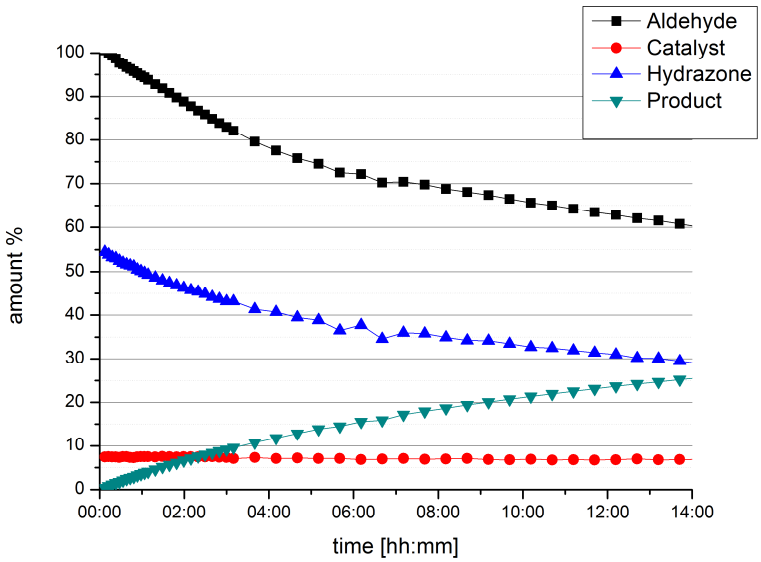

Figure 8. ^{1}H NMR reaction profile in absence of light. Reaction of hydrazone **2** (1 equiv, 0.044 mmol), aldehydes **1b** (R = CH_2CH_3; 1.5 equiv), catalyst **C** (0.08 equiv) in 0.5 ml toluene-d_8 at 300 K

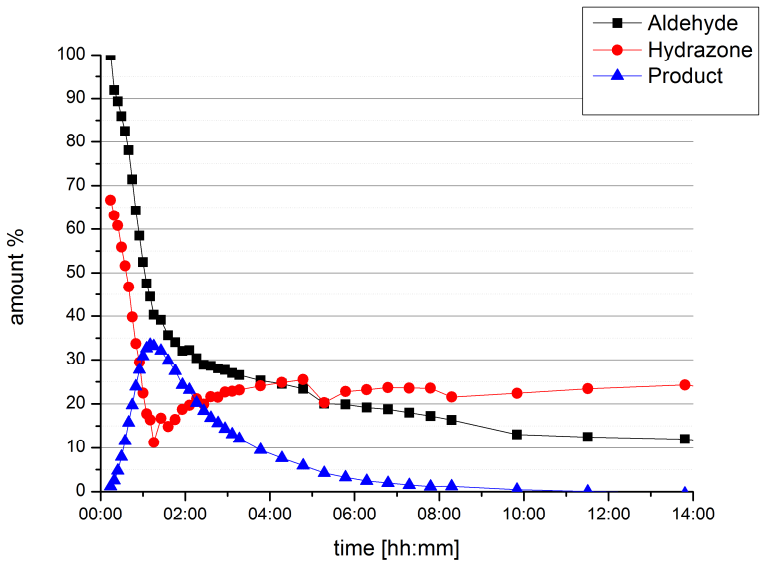

Figure 9. ^{1}H NMR reaction profile under the influence of light (365 nm). Reaction of hydrazone **2** (1 equiv, 0.044 mmol), aldehydes **1a** (R = CH_2CH_3; 1.5 equiv), catalyst **C** (0.08 equiv) in 0.5 ml toluene-d_8 at 300 K

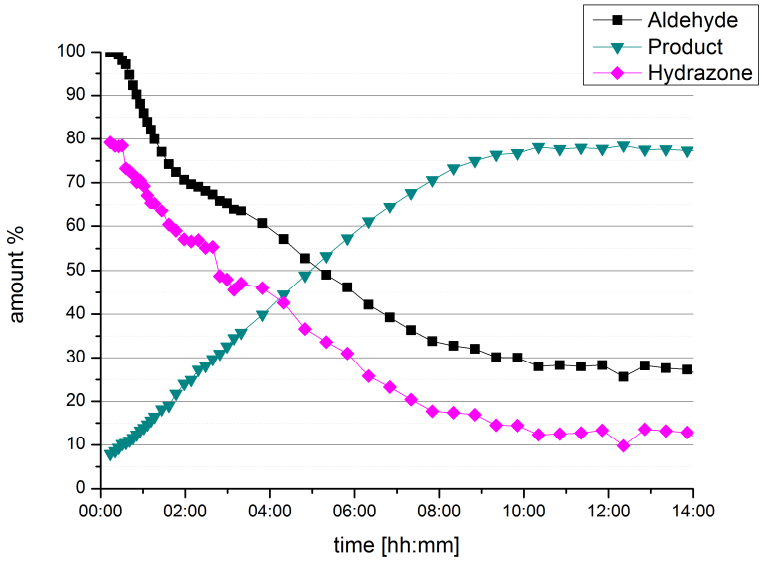

Figure 10. ^{1}H NMR reaction profile under the influence of light (455 nm). Reaction of hydrazone **2** (1 equiv, 0.044 mmol), aldehydes **1a** (R = CH_2CH_3; 1.5 equiv), catalyst **C** (0.08 equiv) in 0.5 ml toluene-d_8 at 300 K

In summary, the data shown in this study about Brønsted acid catalyzed electrocyclizations revealed some important prerequisites if reactions are going to be investigated and analyzed by the DTS-hv method: i) Make sure, that the reaction mechanism is not changed, when light is present. Also a light-induced background reaction in the absence of a catalyst has to be excluded. ii) Make sure, your product is not labile under the influence of light, otherwise the indicative change in yield, proposed by the DTS-hv method, cannot be used to analyze the dominant reaction pathway.

4.6.2 Experimental Part

In a predried Schlenk tube, hydrazone **2** (88.5 mM, 1equiv) and catalyst **C** (0.08 equiv) were dissolved in 3 ml toluene p.a. Aldehyde (**1b**-**d**; 1.5 equiv) was added and the solution was stirred for 24 h, at room temperature in absence or presence of light (365 nm or 455 nm; see Table 2). After 24 h the solvent was removed and the corresponding product was isolated by column chromatography (petroleum ether/DCM = 10/1).

For the assignments of the products **7b**-**d** by NMR spectroscopy as well as for the HPLC analysis see section 4.5.

4.7 References

(1) MacMillan, D. W. C. *Nature* **2008**, *455*, 304.

(2) Bertelsen, S.; Jørgensen, K. A. *Chem. Soc. Rev.* **2009**, *38*, 2178.

(3) Melchiorre, P.; Marigo, M.; Carlone, A.; Bartoli, G. *Angew. Chem. Int. Ed.* **2008**, *47*, 6138.

(4) Dalko, P. I.; Moisan, L. *Angew. Chem. Int. Ed.* **2004**, *43*, 5138.

(5) Mukherjee, S.; Yang, J. W.; Hoffmann, S.; List, B. *Chem. Rev.* **2007**, *107*, 5471.

(6) Donslund, B. S.; Johansen, T. K.; Poulsen, P. H.; Halskov, K. S.; Jørgensen, K. A. *Angew. Chem. Int. Ed.* **2015**, *54*, 13860.

(7) Eder, U.; Sauer, G. R.; Wiechart, R. **1971**, German Patent DE2014757.

(8) Hajos, Z. G.; Parrish, D. R. **1971**, German Patent DE2102623.

(9) Hajos, Z. G.; Parrish, D. R. *J. Org. Chem.* **1974**, *39*, 1615.

(10) List, B.; Lerner, R. A.; Barbas III, C. F. *J. Am. Chem. Soc.* **2000**, *122*, 2395.

(11) Ahrendt, K. a; Borths, C. J.; MacMillan, D. W. C. *J. Am. Chem. Soc.* **2000**, *122*, 4243.

(12) Nielsen, M.; Worgull, D.; Zweifel, T.; Gschwend, B.; Bertelsen, S.; Jørgensen, K. A. *Chem. Commun.* **2011**, *47*, 632.

(13) Renzi, P.; Hioe, J.; Gschwind, R. M. *Acc. Chem. Res.* **2017**, *50*, 2936.

(14) Ashley, M. A.; Hirschi, J. S.; Izzo, J. A.; Vetticatt, M. J. *J. Am. Chem. Soc.* **2016**, *138*, 1756.

(15) Holland, M. C.; Metternich, J. B.; Mück-Lichtenfeld, C.; Gilmour, R. *Chem. Commun.* **2015**, *51*, 5322.

(16) Holland, M. C.; Paul, S.; Schweizer, W. B.; Bergander, K.; Mück-Lichtenfeld, C.; Lakhdar, S.; Mayr, H.; Gilmour, R. *Angew. Chem. Int. Ed.* **2013**, *52*, 7967.

(17) Bächle, F.; Duschmalé, J.; Ebner, C.; Pfaltz, A.; Wennemers, H. *Angew. Chem. Int. Ed.* **2013**, *52*, 12619.

(18) Burés, J.; Armstrong, A.; Blackmond, D. G. *Chem. Sci.* **2012**, *3*, 1273.

(19) Burés, J.; Armstrong, A.; Blackmond, D. G. *J. Am. Chem. Soc.* **2011**, *133*, 8822.

(20) Zimmer, L. E.; Sparr, C.; Gilmour, R. *Angew. Chem.* **2011**, *123*, 12062.

(21) Sharma, A. K.; Sunoj, R. B. *Angew. Chem. Int. Ed.* **2010**, *122*, 6517.

(22) Lelais, G.; MacMillan, D. W. C. In *Enantioselective Organocatalysis*; Wiley-VCH Verlag GmbH & Co. KGaA: Weinheim, Germany, 2007; Vol. *107*, pp 95–120.

(23) Seebach, D.; Beck, A. K.; Badine, D. M.; Limbach, M.; Eschenmoser, A.; Treasurywala, A. M.; Hobi, R.; Prikoszovich, W.; Linder, B. *Helv. Chim. Acta* **2007**, *90*, 425.

(24) List, B. *Acc. Chem. Res.* **2004**, *37*, 548.

(25) List, B.; Hoang, L.; Martin, H. J. *Proc. Natl. Acad. Sci.* **2004**, *101*, 5839.

(26) Bahmanyar, S.; Houk, K. N.; Martin, H. J.; List, B. *J. Am. Chem. Soc.* **2003**, *125*, 2475.

(27) Erkkilä, A.; Pihko, P. M. *Eur. J. Org. Chem.* **2007**, 4205.

(28) Nozière, B.; Córdova, A. *J. Phys. Chem. A* **2008**, *112*, 2827.

(29) Schmid, M. B.; Zeitler, K.; Gschwind, R. M. *Angew. Chem. Int. Ed.* **2010**, *49*, 4997.

(30) Seebach, D.; Groselj, U.; Badine, M. D.; Schweizer, B. W.; Beck, A. K. *Helv. Chim. Acta* **2008**, *91*, 1999.

(31) Renzi, P.; Hioe, J.; Gschwind, R. M. *J. Am. Chem. Soc.* **2017**, *139*, 6752.

(32) This type of reaction was independently developed by List and Rueping in 2005. However in their reports the reactions were conducted in the absence of light: Rueping, M.; Sugiono, E.; Azap, C.; Theissmann, T.; Bolte, M. *Org. Lett.* **2005**, *7*, 3781.; Hoffmann, S.; Seayad, A. M.; List, B. *Angew. Chem. Int. Ed.* **2005**, *44*, 7424.

(33) Reid, J. P.; Simón, L.; Goodman, J. M. *Acc. Chem. Res.* **2016**, *49*, 1029.

(34) Simón, L.; Goodman, J. M. *J. Org. Chem.* **2011**, *76*, 1775.

(35) Simón, L.; Goodman, J. M. *J. Am. Chem. Soc.* **2008**, *130*, 8741.

(36) Erkkilä, A.; Majander, I.; Pihko, P. M. *Chem. Rev.* **2007**, *107*, 5416.

(37) Marcos, V.; Alemán, J. *Chem. Soc. Rev.* **2016**, *45*, 6812.

(38) Grošelj, U.; Seebach, D.; Badine, D. M.; Schweizer, W. B.; Beck, A. K.; Krossing, I.; Klose, P.; Hayashi, Y.; Uchimaru, T. *Helv. Chim. Acta* **2009**, *92*, 1225.

(39) Seebach, D.; Gilmour, R.; Grošelj, U.; Deniau, G.; Sparr, C.; Ebert, M.-O.; Beck, A. K.; McCusker, L. B.; Šišak, D.; Uchimaru, T. *Helv. Chim. Acta* **2010**, *93*, 603.

(40) Bertelsen, S.; Marigo, M.; Brandes, S.; Dinér, P.; Jørgensen, K. A. *J. Am. Chem. Soc.* **2006**, *128*, 12973.

(41) Schmid, M. B.; Zeitler, K.; Gschwind, R. M. *Chem. Sci.* **2011**, *2*, 1793.

(42) Seegerer, A.; Hioe, J.; Hammer, M. M.; Morana, F.; Fuchs, P. J. W.; Gschwind, R. M. *J. Am. Chem. Soc.* **2016**, *138*, 9864.

(43) Silvi, M.; Verrier, C.; Rey, Y. P.; Buzzetti, L.; Melchiorre, P. *Nat. Chem.* **2017**, *9*, 868.

(44) Silvi, M.; Arceo, E.; Jurberg, I. D.; Cassani, C.; Melchiorre, P. *J. Am. Chem. Soc.* **2015**, *137*, 6120.

(45) Bahamonde, A.; Melchiorre, P. *J. Am. Chem. Soc.* **2016**, *138*, 8019.

(46) Arceo, E.; Jurberg, I. D.; Álvarez-Fernández, A.; Melchiorre, P. *Nat. Chem.* **2013**, *5*, 750.

(47) Berbasova, T.; Santos, E. M.; Nosrati, M.; Vasileiou, C.; Geiger, J. H.; Borhan, B. *ChemBioChem* **2016**, *17*, 407.

(48) Ernst, O. P.; Lodowski, D. T.; Elstner, M.; Hegemann, P.; Brown, L. S.; Kandori, H. *Chem. Rev.* **2014**, *114*, 126.

(49) Mariano, P. S. *Tetrahedron* **1983**, *39*, 3845.

(50) Gotoh, H.; Uchimaru, T.; Hayashi, Y. *Chem. - A Eur. J.* **2015**, *21*, 12337.

(51) Volla, C. M. R.; Das, A.; Atodiresei, I.; Rueping, M. *Chem. Commun.* **2014**, *50*, 7889.

(52) Feldmeier, C.; Bartling, H.; Riedle, E.; Gschwind, R. M. *J. Magn. Reson.* **2013**, *232*, 39.

(53) Evans, D. A. pKa Table http://evans.rc.fas.harvard.edu/pdf/evans_pKa_table.pdf (accessed Sep 17, 2014).

(54) Mayr, H.; Bug, T.; Gotta, M. F.; Hering, N.; Irrgang, B.; Janker, B.; Kempf, B.; Loos, R.; Ofial, A. R.; Remennikov, G.; et al. *J. Am. Chem. Soc.* **2001**, *123*, 9500.

(55) Mayr, H.; Ofial, A. R. *Pure Appl. Chem.* **2005**, *77*, 1807.

(56) Mayr, H. Reactivity Scales for Organocatalytic Reactions http://www.cup.lmu.de/oc/mayr/ReactScalesPoster OrgCatOrgMetCarbanions.pdf (accessed Apr 24, 2018).

(57) Carroccia, L.; Fioravanti, S.; Pellacani, L.; Tardella, P. *Synthesis* **2010**, 4096.

(58) Das, A.; Volla, C. M. R.; Atodiresei, I.; Bettray, W.; Rueping, M. *Angew. Chem. Int. Ed.* **2013**, *52*, 8008.

(59) Woodward, R. B.; Hoffmann, R. *J. Am. Chem. Soc.* **1965**, *87*, 395.

5 Combined *in situ* Illumination-NMR-UV/Vis Spectroscopy: A New Mechanistic Tool in Photochemistry

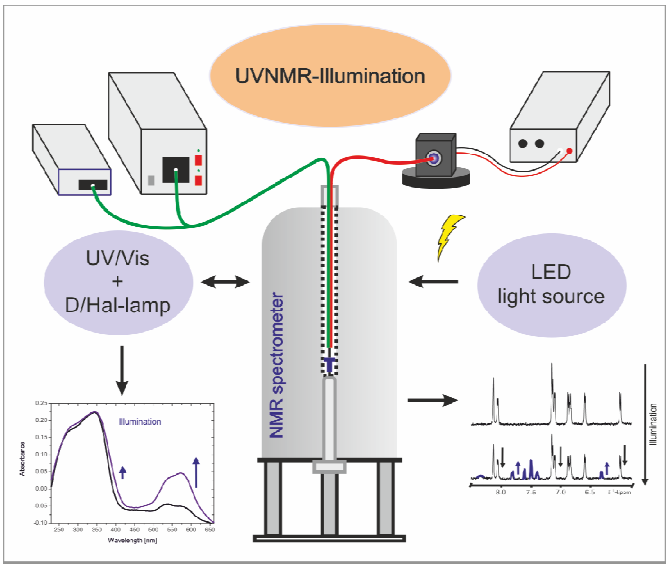

Andreas Seegerer, Philipp Nitschke, and Ruth M. Gschwind*

Angew. Chem. Int. Ed. **2018**

DOI: 10.1002/anie.201801250R1

The UVNMR-illumination setup was developed and realized by Andreas Seegerer. Together with Philipp Nitschke the setup was further improved and full automation was implemented. Philipp Nitschke recorded and analyzed the combined UVNMR reaction profiles and performed all NMR experiments except those for the assignments of the spiropyran species.

5.1 Abstract

Synthetic applications in photochemistry are booming. Despite great progress in the development of new reactions, mechanistic investigations are still challenging. Therefore, we present a fully automated *in situ* combination of NMR spectroscopy, UV/Vis spectroscopy, and illumination to allow simultaneous and time-resolved detection of paramagnetic and diamagnetic species. This optical fiber-based setup enables the first acquisition of combined UV/Vis and NMR spectra in photocatalysis, as demonstrated on a conPET process. Furthermore, the broad applicability of combined UVNMR spectroscopy for light-induced processes is demonstrated on a structural and quantitative analysis of a photoswitch, including rate modulation and stabilization of transient species by temperature variation. Owing to the flexibility regarding the NMR hardware, temperature, and light sources, we expect wide-ranging applications of this setup in various research fields.

5.2 Introduction

Photocatalysis is one of the booming fields in organic synthesis and experienced a nearly exponential increase in publications of synthetic strategies and applications during the last decades.[1] Despite the high impact of new light-induced transformations on synthesis, detailed insights into photocatalytic mechanisms are still a real challenge. In photochemistry, ultrafast UV/Vis spectroscopy is so far the most commonly used method for detailed mechanistic studies, owing to its capability to detect the initial photoexcited states.[2] We and also other groups have recently shown that NMR spectroscopy can provide essential mechanistic information on photochemical and photocatalytic processes, despite its insensitivity and poor time resolution,[3] by providing quantitative reaction profiles of reactants, products, and intermediates. Complementary to ultrafast UV/Vis, mechanistic features downstream from the initial photoexcitation, such as single- versus two-electron transfer processes,[3b] proton transfer pathways, or multiple concurrent reaction mechanisms, can be elucidated by NMR spectroscopy.[3a] Furthermore, owing to its high resolution spectra, NMR spectroscopy provides detailed structural information about intermolecular interactions[4] and aggregation, revealing key information of activation or deactivation of substrates or catalysts in photocatalysis.[5]

However, besides the limited time resolution, NMR spectroscopy faces the additional challenge that single electron transfer (SET) processes, which are typical for photocatalysis, cause an interplay of paramagnetic and diamagnetic species. Often, the lifetime of these paramagnetic radical intermediates is so short that they do not even affect the NMR spectra of the diamagnetic species. The information on these transient radicals can often be accessed only by photo-chemically induced dynamic nuclear polarization (photo-CIDNP) through their diamagnetic recombination and disproportionation products.[3b,6] In contrast, stable long-lived radicals can impose severe challenges to NMR spectroscopy. While in the case of several inorganic complexes or proteins paramagnetic NMR can be successfully applied,[7] it is usually not possible to detect paramagnetic states of small organic molecules, such as those used as photocatalysts in photochemistry. Furthermore, for stable radical states of photocatalysts, chemical exchange often leads to severe line broadening even for the diamagnetic states.[3b]

Because consecutive photoinduced electron transfer (conPET) processes[8] (Figure 1) recently emerged as a hot topic to address the activation of strong bonds and higher redox potentials, detailed mechanistic investigations are highly demanded in the photocatalysis community. In conPET processes, long-lived radical anions (usually elusive to NMR spectroscopy) are the central key intermediates generated by PET utilizing a sacrificial electron donor **D**. A second photoexcitation of this radical anion leads to a photoexcited state with reduction potentials up to -2.4 V.[8,9] This provides an elegant way to increase the scope for metal-free photoredox catalysis under mild conditions using commercially available organic photocatalysts.

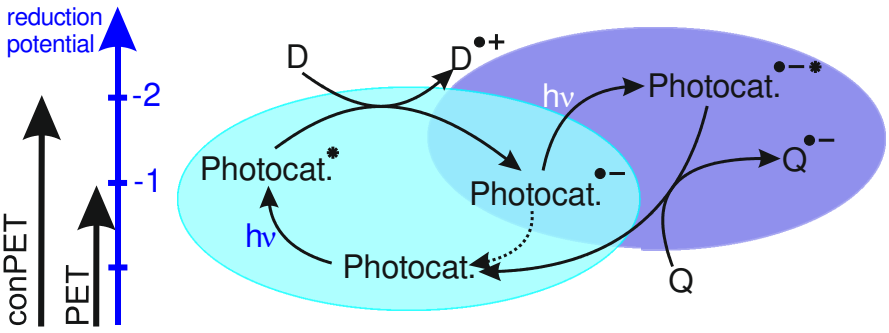

Figure 1. Schematic of a consecutive photoinduced electron transfer (conPET) process.[8c] D = sacrificial electron donor, Q = quenching substrate.

To extend the scope of high-resolution NMR spectroscopic investigations in photocatalysis with stable radicals, a combined NMR and UV/Vis spectroscopic tool would be ideal.[10] However, reaction profiles of photocatalytic processes featuring longer reaction times of up to several hours or even days impose severe challenges for separated setups. While also separated setups can match experimental conditions such as temperature and concentration, an exact match of light absorption/intensity, which depend on the geometry and positioning of light source and reaction vessel as well as parameters such as convection/diffusion properties, is best realized by using an *in situ* combination.

In addition to photocatalysis, a combined *in situ* setup of UV/Vis, NMR, and illumination would show a broad applicability in the field of photoswitches and molecular machines.[11] Herein, such a setup provides direct, quantitative correlations between absorbance and structure of switching states and can be used to track full conversion cycles.[12]

For static equilibria, Tolstoy *et al.* introduced an *in situ* combination of UV/Vis and high-resolution solution NMR spectroscopy (UVNMR) in 2009 to achieve absolute comparability of both methods.[13] However, this setup cannot be applied for dynamic, light-induced (photo) chemical processes because of the hampered diffusion caused by a reflector between bulk solution for NMR spectroscopy and an aliquot for UV/Vis spectroscopy. Furthermore, an additional light source for illumination is missing and the NMR probe has to be drilled to guide optical fibers to the tip of the NMR tube.

Therefore, in this paper we describe a fully automated triple combination of *in situ* illumination and UV/Vis and NMR spectroscopy. The potential of this setup is demonstrated by acquisition of combined UVNMR reaction profiles of a light-induced conPET process and a photoswitchable spiropyran.

5.3 Results and Discussion

Our new optical fiber-based UVNMR-illumination setup combines a UV/Vis-reflection dip probe (Avantes) with our *in situ* LED-illumination device[14] inside an NMR spectrometer (see Figure 2A). The optical fiber for illumination (with a sandblasted tip) and the reflection dip probe for UV/Vis measurements are placed together inside a coaxial quartz glass insert within an amberized NMR tube. The optical fiber for illumination and the reflection dip probe (Figure 2B) were used for guiding the light of the LED-illumination device and the deuterium-halogen (D-Hal)-lamp directly into the NMR tube and to detect the reflected light. A PTFE insert inside the NMR tube acts as reflector (Figure 2B).

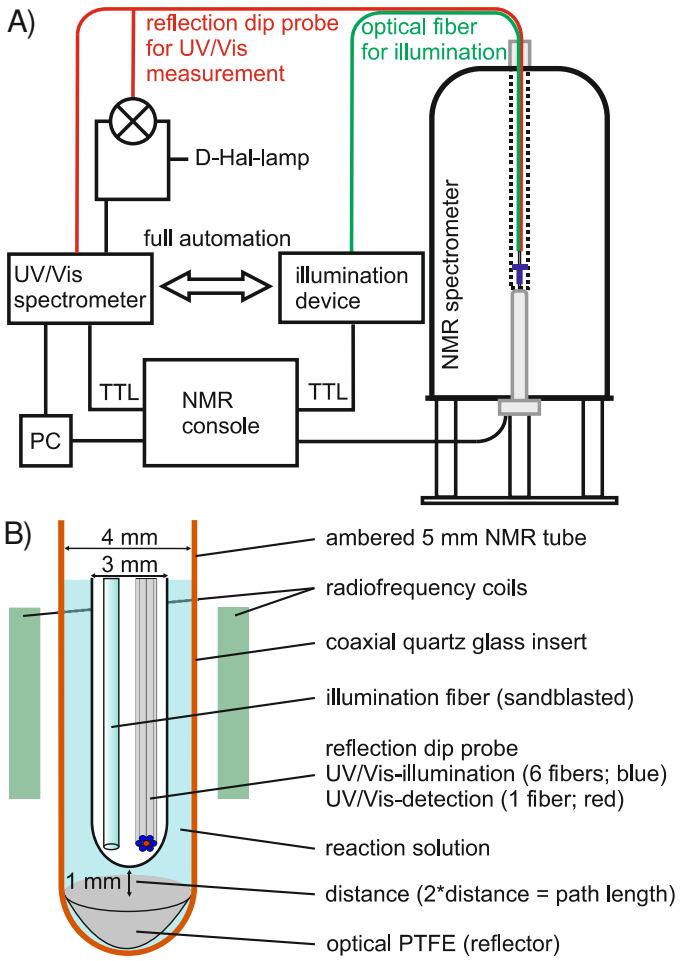

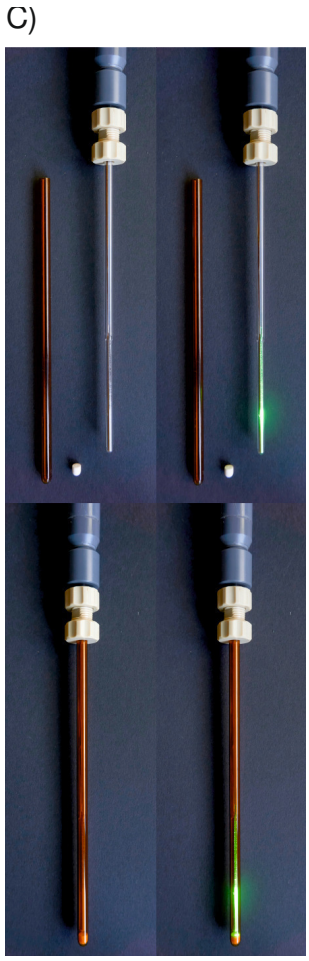

Figure 2. A) Schematic of UVNMR-illumination setup. B) Close-up of the illumination fiber and the reflection dip probe inside the NMR tube; C) Photos of the setup including the outer amberized NMR tube, PTFE reflector, screw cap, and coaxial insert with both optical fibers inside; (dis)assembled with/without light.

Owing to an outer diameter of the coaxial quartz glass insert of 3 mm and an inner diameter of 4 mm of the outer NMR tube, an active layer of 1 mm is given in the range of the NMR radio frequency (RF) coils (Figure 2B). To ensure homogeneity of the solution by diffusion, the distance between the tip of the insert and the PTFE reflector was set to approximately 1 mm (path length of approximately 2 mm). To adjust the path length, a customized screw cap was developed (Figure 2C, for details see the Supporting Information), which connects the NMR tube and the insert tightly, so even air-sensitive samples and (photo) reactions can be analyzed. The whole setup is portable, fully remote-controlled, and applicable to every conventional solution NMR spectrometer without any alteration. This allows for an extremely flexible application regarding the NMR setup (probe, field, temperature) adapted to the individual problems.

To enable combined, time-resolved UVNMR reaction profiles, an absolute time control of UV/Vis, NMR measurements, and illumination is required. Therefore, the NMR console was used as the central time control unit. It directly addresses the illumination device (LED transistor) and the UV/Vis spectrometer through TTL signals (Figure 2A), implemented as events in modified NMR pulse sequences (see Supporting Information). For a UV/Vis measurement, the UV/Vis spectrometer forwards the TTL signal of the NMR console to a D-Hal-light source to control its shutter, that is, the emitted light hits the sample exclusively during the UV/Vis-measurement.[15]

To demonstrate the power of our UVNMR-illumination setup combined *in situ* UV/Vis and NMR reaction profiles of a conPET process are presented. In this process, light (450 nm) transforms the photocatalyst N,N-bis(2,6-diisopropylphenyl)-perylene-3,4,9,10-bisdicarboximide (**PDI**) into the stable radical anion **PDI**$^{\bullet-}$ in presence of an electron donor **D** (in this case, NEt_3). A second photoexcitation of **PDI**$^{\bullet-}$ is proposed to allow for a reduction of aryl halides such as 4-bromo-benzaldehyde **Ald-Br** to the corresponding aryl **Ald** (Figure 1 and 3A/B and the Supporting Information).[8a] In this reaction, **PDI** shows extreme line broadening effects in the NMR spectra (see Figure 3C). Even prior to illumination, all signals of **PDI** are significantly broadened most probably owing to an exchange with an electron donor acceptor complex between NEt_3 and **PDI** with the typical distance-dependent line broadening of radicals.[3b] The protons $\mathbf{H_4}$ and $\mathbf{H_5}$ (Figure 3C, see the Supporting Information) attached to the central perylene core nearly vanished, $\mathbf{H_1}$ and $\mathbf{H_2}$ are broadened, and even proton $\mathbf{H_3}$ of the isopropyl groups on **PDI** are slightly affected.[16] In contrast, without illumination the UV/Vis spectra show only small absorption bands of **PDI**$^{\bullet-}$ (Figure 3D; Supporting Information). This hints that in specific cases, NMR spectroscopy might be very sensitive for the detection of electron donor-acceptor complexes. Immediately after turning on the light, the NMR proton

signals of the **PDI** core (**H_4**, **H_5**) vanish completely. The other NMR proton signals of **PDI** are only detectable for seconds or minutes. However, even in the case of detection within the first minutes, for example, of **H_3**, the severe line broadening prevents any reliable quantification of both diamagnetic photocatalyst and paramagnetic intermediate (Figure 3C).

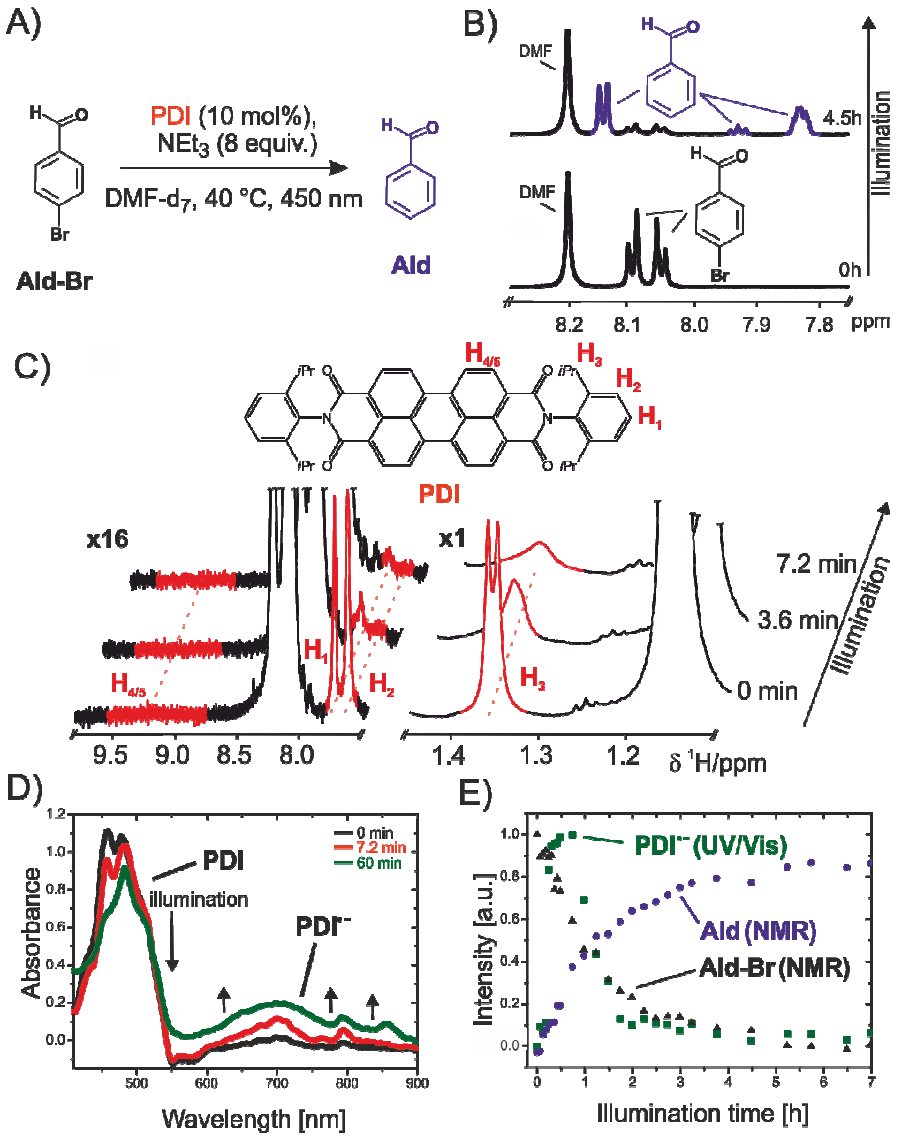

Figure 3. A) Photocatalytic reduction of 4-bromo-benzaldehyde **Ald-Br** to benzaldehyde **Ald** through a **PDI** catalyzed conPET process.[8a] B) ^{1}H spectra of the reaction mixture, before and after illumination (450 nm) showing **Ald-Br** and **Ald** at 313 K in [D_7] DMF. C) Line broadening and vanishing of the **PDI** proton signals (red) upon illumination because of exchange with **PDI$^{\bullet-}$**; D) conversion of **PDI** into **PDI$^{\bullet-}$** monitored by *in situ* UV/Vis spectroscopy. E) Combined NMR and UV/Vis reaction profiles allow for *in situ* kinetic information of both paramagnetic (**PDI$^{\bullet-}$**) and diamagnetic reactants (**Ald-Br**, **Ald**) in photocatalysis.

UV/Vis spectroscopy shows its power for the detection of stable radicals. After a few minutes of illumination at 450 nm, the absorption maxima of **PDI**$^{\bullet-}$ (698 and 794 nm)[8a] rise, while the absorbance of **PDI** (455 and 482 nm) steadily decreases (Figure 3D). Besides its advantages in eliminating all previously described common issues associated with reaction conditions in separated setups, this study also reveals a general application of this combined UVNMR-illumination setup. In case of UV/Vis detectable intermediates/reactants, a relative quantification over time by UV/Vis is feasible. Studies towards an absolute quantification are in progress.

Thus, the UV/Vis data provides important, time-resolved information about reactants invisible to NMR spectroscopy, enabling a semiquantitative reaction profile for the evolution of **PDI**$^{\bullet-}$. Complementary to the UV/Vis spectra, simultaneously recorded NMR spectra give full quantitative and structural insight into participating, diamagnetic reactants and reaction/decomposition products (Figure 3E).[17]

With this *in situ* combination of NMR and UV/Vis spectroscopy and illumination, complete reaction profiles of the whole progress of a reaction including paramagnetic and diamagnetic species can be obtained and important interactions as well as structural details can be investigated. This enables totally new possibilities to elucidate reaction mechanisms in photocatalysis. Further studies about this controversial mechanism are in progress.

Photoswitches are another promising field of applications for the *in situ* combination of NMR and UV/Vis spectroscopy and illumination. In our previous study about photoswitchable spiropyrans, deviations between the quantitative data of UV/Vis and NMR spectroscopy were found, demonstrating the importance of identical light intensities and reaction vessels in separated setups.[18] To demonstrate the advantages of our UVNMR-illumination setup with only one illumination device and a common reaction vessel, a spectroscopic analysis of a similar photoswitchable spiropyran is presented. In this case, the colorless 1′,3′-dihydro-1′,3′,3′-trimethyl-6-nitrospiro[2*H*-1-benzo-pyran-2,2′-(2*H*)-indole] **1** can be switched to its open, purple, zwitterionic state **2** (Figure 4A) by irradiation with UV light (365 nm) inside the NMR spectrometer at 300 K in [D_8]THF[11a] The *in situ* recorded UV/Vis spectrum (Figure 4B) shows new absorption maxima at 533 and 575 nm with continuous illumination. Complementarily, the NMR spectrum (Figure 4C) gives immediate information about the quantity of the opened spiropyran **2** (21% after 2 minutes). However, upon switching off the light, **2** vanishes within circa 24 s in the NMR spectrum ($\tau_{1/2}$ (300 K) = 17.4 s determined by UV/Vis spectroscopy), which

prevents a detailed structural study by NMR spectroscopy at 300 K (Figure 4D and the Supporting Information).

By cooling the sample inside the NMR spectrometer to 180 K, without changing any other parameter of the setup, the thermal back-reaction rate was reduced significantly (Figure 4E and the Supporting Information). This enables more time-consuming NMR experiments to investigate both species without degradation products (see Supporting Information).

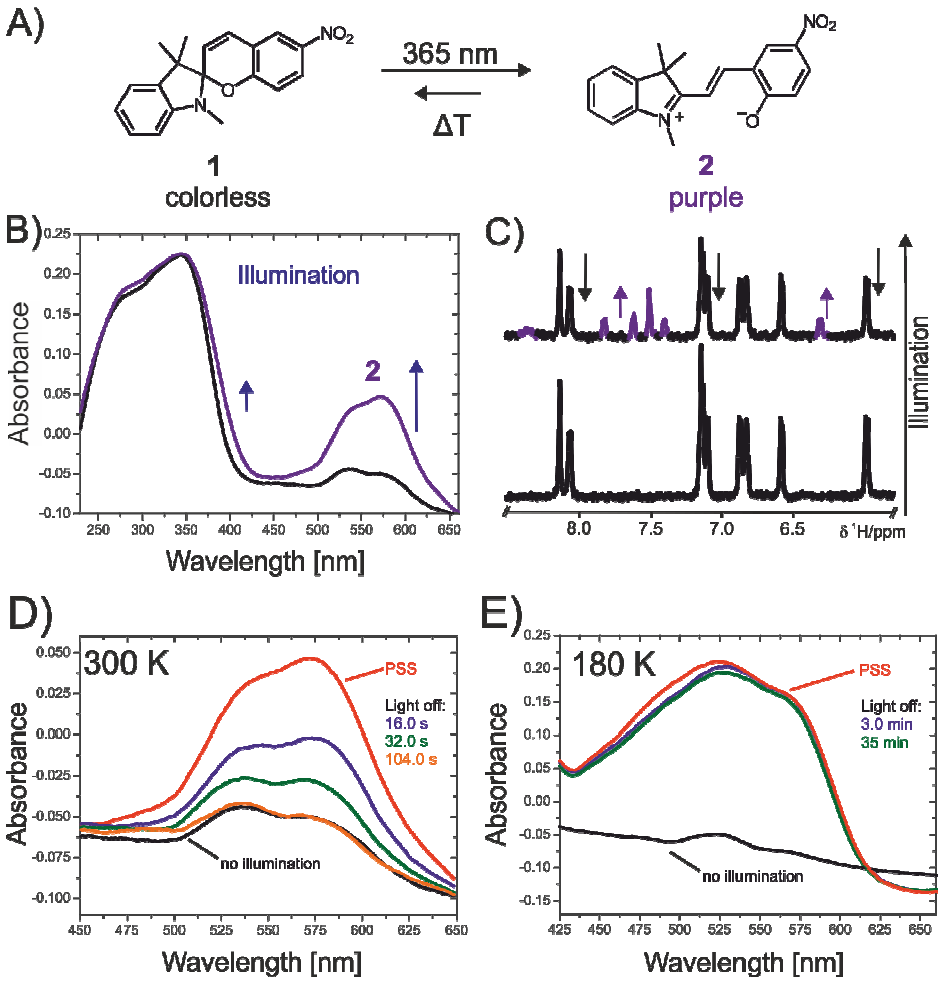

Figure 4. A) Equilibrium of spiropyran **1** and **2**. Upon excitation of **1** with a 365 nm LED, **1** switches into its open, colored form **2**. The photoswitch process can be detected by UV/Vis spectroscopy, while NMR spectroscopy unambiguously confirms the structure of the open form **2**. B) Absorption spectra under the influence of light (365 nm). C) Corresponding NMR spectra showing new signals of **2** after illumination at 300 K. D) UV/Vis spectra of the thermal back reaction of **2** to **1** at 300 K once the light is turned off. E) UV/Vis spectra of **2** at 180 K; the thermal back reaction is extremely slow, this enables a full investigation without the need of continuous illumination. PSS = photo stationary state.

Structural information about the preferred configuration and conformation can be essential to understand different binding properties of the isomers of photo switchable molecules, for example, in biochemical applications.[19] Furthermore, the time-dependent conversion of different isomers can be tracked online by NMR and/or UV/Vis spectroscopy to show the active species present during a reaction. In general the low temperature applicability of the setup enables temperature-dependent rate modulation and stabilization to detect unstable intermediates by NMR and UV/Vis spectroscopy. In addition, combinations of UVNMR with advanced NMR techniques like DOSY to investigate aggregates or complexes are feasible.

5.4 Conclusion

To summarize, in this study we present a fully automated triple combination of *in situ* high-resolution NMR and UV/Vis spectroscopy and illumination in a new optical fiber-based setup. By merging two very important methods in the field of mechanistic investigations, it is now possible to monitor and quantify paramagnetic and diamagnetic species simultaneously and in a time-resolved manner during a light-induced photochemical transformation by NMR and UV/Vis spectroscopy. Besides the elimination of all common issues related to the use of separated systems, like concentration and temperature, the setup circumvents all deviations in terms of light intensity, reaction vessel, convection, and diffusion. Its applicability in a wide temperature range opens the opportunity to modulate the reaction rate of ongoing reactions or switching cycles to stabilize transient intermediates or conformers. Overall, the combined triple setup including high-resolution NMR and UV/Vis spectroscopy and illumination with different wavelengths will allow for detailed mechanistic and structural investigations in various research fields.

5.5 References

(1) a) M. Majek, A. Jacobi von Wangelin, *Acc. Chem. Res.* **2016**, *49*, 2316–2327; b) I. Ghosh, L. Marzo, A. Das, R. Shaikh, B. König, *Acc. Chem. Res.* **2016**, *49*, 1566–1577; c) M. A. Garcia-Garibay, *J. Am. Chem. Soc.* **2012**, *134*, 8289–8292; d) J. M. R. Narayanam, C. R. J. Stephenson, *Chem. Soc. Rev.* **2011**, *40*, 102–113; e) K. Zeitler, *Angew. Chem. Int. Ed.* **2009**, *48*, 9785–9789; f) N. A. Romero, D. A. Nicewicz, *Chem. Rev.* **2016**, *116*, 10075–10166; g) B. König, *Eur. J. Org. Chem.* **2017**, *15*, 1979–1981.

(2) a) Y. Zhang, J. Kubicki, M. S. Platz, *J. Am. Chem. Soc.* **2009**, *131*, 13602–13603; b) U. Megerle, M. Wenninger, R.-J. Kutta, R. Lechner, B. König, B. Dick, E. Riedle, *Phys. Chem. Chem. Phys.* **2011**, *13*, 8869-8880, c) J. Wang, G. Burdzinski, J. Kubicki, M. S. Platz, *J. Am. Chem. Soc.* **2008**, *130*, 11195–11209; d) P. K. Verma, F. Koch, A. Steinbacher, P. Nuernberger, T. Brixner, *J. Am. Chem. Soc.* **2014**, *136*, 14981–14989; e) E. Riedle, M. K. Roos, S. Thallmair, C. F. Sailer, N. Krebs, B. P. Fingerhut, R. de Vivie-Riedle, *Chem. Phys. Lett.* **2017**, *683*, 128–134; f) J. Xue, H. L. Luk, S. V. Eswaran, C. M. Hadad, M. S. Platz, *J. Phys. Chem. A* **2012**, *116*, 5325–5336.

(3) a) H. Bartling, A. Eisenhofer, B. König, R. M. Gschwind, *J. Am. Chem. Soc.* **2016**, *138*, 11860–11871; b) C. Feldmeier, H. Bartling, K. Magerl, R. M. Gschwind, *Angew. Chem. Int. Ed.* **2015**, *54*, 1347–1351; c) M. V. Gomez, A. Juan, F. Jiménez-Márquez, A. de la Hoz, A. H. Velders, *Anal. Chem.* **2018**, *90*, 1542-1546; d) D. M. Schultz, F. Lévesque, D. A. DiRocco, M. Reibarkh, Y. Ji, L. A. Joyce, J.F. Dropinski, H. Sheng, B. D. Sherry, I. W. Davies, *Angew. Chem. Int. Ed.* **2017**, *56*, 15274-15278; e) N. Mallo, P. T. Brown, H. Iranmanesh, T. S. C. MacDonald, M. J. Teusner, J. B. Harper, G. E. Ball, J. E. Beves, *Chem. Commun.* **2016**, *52*, 13576–13579; f) J. Kind, L. Kaltschnee, M. Leyendecker, C. M. Thiele, *Chem. Commun.* **2016**, *52*, 12506–12509; g) E. Procházková, L. Čechová, J. Kind, Z. Janeba, C. M. Thiele, M. Dračínský, *Chem. Eur. J.* **2018**, *24*, 492–498; h) A. Bahamonde, P. Melchiorre, *J. Am. Chem. Soc.* **2016**, *138*, 8019–8030; i) A. Mills, C. O'Rourke, *J. Org. Chem.* **2015**, *80*, 10342–10345.

(4) a) A. Seegerer, J. Hioe, M. M. Hammer, F. Morana, P. J. W. Fuchs, R. M. Gschwind, *J. Am. Chem. Soc.* **2016**, *138*, 9864–9873; b) N. Sorgenfrei, J. Hioe, J. Greindl, K. Rothermel, F. Morana, N. Lokesh, R. M. Gschwind, *J. Am. Chem. Soc.* **2016**, *138*, 16345–16354; c) J. Greindl, J. Hioe, N. Sorgenfrei, F. Morana, R. M. Gschwind, *J. Am. Chem. Soc.* **2016**, *138*, 15965–15971.

(5) a) K. Chen, N. Berg, R. Gschwind, B. König, *J. Am. Chem. Soc.* **2017**, 51, 18444-18447; b) J. Dadová, S. Kümmel, C. Feldmeier, J. Cibulková, R. Pažout, J. Maixner, R. M. Gschwind, B. König, R. Cibulka, *Chem. Eur. J.* **2013**, *19*, 1066–1075; c) A. Eisenhofer, J. Hioe, R. M. Gschwind, B. König, *Eur. J. Org. Chem.* **2017**, *15*, 2194–2204.

(6) a) R. Kaptein, *J. Chem. Soc. D.* **1971**, 0, 732-733; b) M. Goez, in *Annu. Reports NMR Spectrosc.*, Elsevier Ltd., **2009**, pp. 77–147; c) M. Goez, in *Hyperpolarization Methods NMR Spectroscopy.*, Springer-Verlag Berlin Heidelberg **2012**, pp. 1–32; d) I. Kuprov, M. Goez, P. A. Abbott, P. J. Hore, *Rev. Sci. Instrum.* **2005**, *76*, 084103-1 – 084103-7.

(7) a) M. Enders, in *Model. Mol. Prop.* (Ed.: P. Comba), Wiley-VCH Verlag GmbH & Co. KGaA, Weinheim, Germany, **2011**, pp. 49–63; b) I. Bertini, C. Luchinat, G. Parigi, R. Pierattelli, *ChemBioChem* **2005**, *6*, 1536–1549; c) I. Bertini, C. Luchinat, G. Parigi, E. Ravera, *NMR of Paramagnetic Molecules : Applications to Metallobiomolecules and Models*, Elsevier B.V., **2017**; d) F. H. Köhler, in *Encycl. Magn. Reson.*, John Wiley & Sons, Ltd, Chichester, UK, **2011**; e) F. Rastrelli, A. Bagno, *Chem. Eur. J.* **2009**, *15*, 7990–8004.

(8) a) I. Ghosh, T. Ghosh, J. I. Bardagi, B. König, *Science* **2014**, *346*, 725–728; b) L. Zeng, T. Liu, C. He, D. Shi, F. Zhang, C. Duan, *J. Am. Chem. Soc.* **2016**, *138*, 3958–3961; c) I. Ghosh, B. König, *Angew. Chem. Int. Ed.* **2016**, *55*, 7676–7679; d) M. Neumeier, D. Sampedro, M. Majek, V. de la Pena O'Shea, A. Jacobi von Wangelin, R. Pérez-Ruiz, *Chem. Eur. J.* **2017**, *23*, 1–5.

(9) a) A. Graml, I. Ghosh, B. König, *J. Org. Chem.* **2017**, *82*, 3552–3560; b) M. Poznik, B. König, *React. Chem. Eng.* **2016**, *1*, 494–500.

(10) Recently a laser/EPR/low resolution NMR combination was introduced to investigate photo-induced DNP on the solvent, a potential combination of radicals, diamagnetic species and light in solution.; G. Liu, S.-H.- Liou, N. Enkin, I. Tkach, M. Bennati *Phys. Chem. Chem. Phys.* **2017**, *19*, 31823-31829.

(11) a) J. Piard, *J. Chem. Educ.* **2014**, *91*, 2105–2111; b) J.-P. Sauvage, *Angew. Chem. Int. Ed.* **2017**, *56*, 1–15; c) C. Cheng, J. F. Stoddart, *ChemPhysChem* **2016**, *17*, 1780–1793; d) B. L. Feringa, R. A. van Delden, N. Koumura, E. M. Geertsema, *Chem. Rev.* **2000**, *100*, 1789–1816.

(12) Combination of illumination and *in situ* UVNMR in the field of photoswitches was already described by Gaeva *et al*. However, detailed information about the setup is missing; E. B. Gaeva, V. Pimienta, S. Delbaere, A. V. Metelitsa, N. A. Voloshin, V. I. Minkin, G. Vermeersch, J. C. Micheau, *J. Photochem. Photobiol. A Chem.* **2007**, *191*, 114–121.

(13) a) P. M. Tolstoy, B. Koeppe, G. S. Denisov, H.-H. Limbach, *Angew. Chem. Int. Ed.* **2009**, *48*, 5745–5747; b) B. Koeppe, P. M. Tolstoy, H. H. Limbach, *J. Am. Chem. Soc.* **2011**, *133*, 7897–7908.

(14) C. Feldmeier, H. Bartling, E. Riedle, R. M. Gschwind, *J. Magn. Reson.* **2013**, *232*, 39–44.

(15) During the UV/Vis measurements the light of the illumination fiber is turned off by the NMR console (pulse program).

(16) The methine proton of the isopropyl group is under one of the DMF solvent signals and hence not further discussed.

(17) Owing to the charge-transfer complex formation even without light, which causessevere line broadening of all PDI signals in NMR spectra, a quantitative analysis could not be performed.

(18) C. Wolff, J. Kind, H. Schenderlein, H. Bartling, C. Feldmeier, R. M. Gschwind, M. Biesalski, C. M. Thiele, *Magn. Reson. Chem.* **2016**, *54*, 485–491.

(19) A. A. Beharry, G. A. Woolley, *Chem. Soc. Rev.* **2011**, *40*, 4422-4437.

5.6 Supporting Information

5.6.1 Setup

5.6.1.1 General Information

The setup presented in this publication was developed and optimized on a Bruker Avance III HD 600 (600.13 MHz) with a fluorine selective TBIF probe and Topspin 3.2. However this setup is applicable to any other modern NMR spectrometer with a 5 mm gradient probe head (as shown in section 5.6.1.3) and the related software. All components of the UVNMR-illumination device were commercially available if not otherwise indicated. Customized parts are labeled with the corresponding article number of the vendor. In the following sections the setup is shown in three parts: the electronic setup outside the NMR spectrometer, the spectroscopy setup inside the NMR spectrometer and the corresponding pulse sequences and settings for a fully automated acquisition.

5.6.1.2 Electronic Setup

The setup for simultaneous UV/Vis and NMR measurements under the influence of light from an external light source required a simple combination of mostly commercially available components (Figure S1). For the acquisition of NMR data an NMR spectrometer (here a Bruker Avance III HD 600; Bruker; Billerica, Massachusetts; USA) and a compatible NMR console (here: Avance III HD) is required. For fully automated measurements of UV/VIS and NMR spectra as shown in this publication two free Real-time Clock Pulse (RCP) outputs of the Intelligent Pulse Sequence Operator (IPSO) unit or the former Time Control Unit (TCU) are needed. These outputs can be found in all Bruker NMR consoles which are equipped with a TCU3 unit or newer versions of it. Unfortunately we do not have any information if the setup is also working fully automated with other NMR consoles since this setup was developed exclusively on Bruker machines and we did not have access to NMR consoles of different brands. However we do not see any problems to transfer the setup if the required RCP outputs are available. Manually triggered UVNMR experiments are possible with every setup.

The NMR console represents the central control unit of our device. Via the RCP outputs it is cable-connected to a commercially available UV/Vis spectrometer (Avaspec-ULS-2048-RS-USB2; Avantes; Apeldoorn, Netherlands) and an LED illumination device. This LED illumination device was already developed in our working group[1]. The corresponding highpower LEDs (365 nm and 450 nm) which were used in this publication were purchased by Lumitronix (Cree XT-E, royal blue, 500 mW, *68332*) and

Laser Components (LEUVA66X00RV00, 365 nm, 2.06 W). However any other commercially available LED can be used in this setup.

Due to the connection to the NMR console both components the LED illumination device as well as the UV/Vis spectrometer can be controlled fully automated by modified pulse programs via TTL signals [see section 5.6.1.4]. The UV/Vis spectrometer itself is further connected to a D-Hal-lamp (Avalight-DH-S-Bal; Avantes; Apeldoorn, Netherlands) by a customized Y-cable purchased by Avantes. Due to this connection between the UV/Vis spectrometer and the D-Hal-lamp the TTL signals from the NMR console can directly trigger an UV/Vis measurement and can open and close the internal shutter inside the D-Hal-lamp. This direct control of the shutter was an essential point in the development of our setup. If the shutter is opened outside the acquisition [ms] of an UV/Vis spectrum the light of the D-Hal-lamp (200-2500 nm) reaches unhampered the sample which can cause deviations in the results e.g. due to photodegradation by hard UV irradiation.

The NMR console and the UV/Vis spectrometer are furthermore connected to a PC with the corresponding software Bruker Topspin 3.2 (NMR) and Avasoft 8.6full (UV/VIS, Avantes; Apeldoorn, Netherlands). All measurements, UV/VIS as well as NMR are controlled by modified pulse programs in Topspin (see section 5.6.1.4).

To transfer the emitted light of the LED light source and the D-Hal-lamp into the sample inside the spectrometer and to read out the UV/Vis data with the UV/VIS spectrometer, all three components were connected to optical fibers which are guided into the NMR tube inside the NMR spectrometer (see following section).

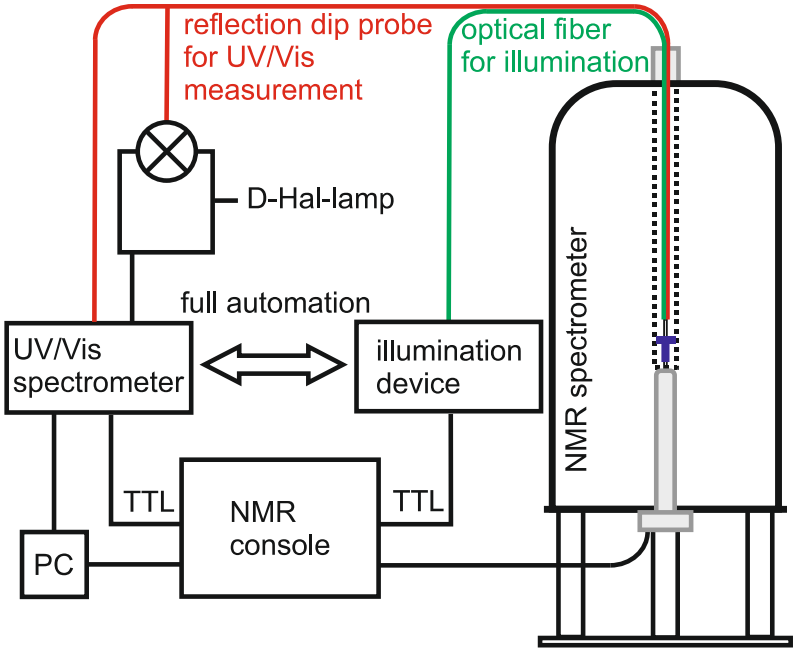

Figure S1. Schematic overview of all electronic and spectroscopic components of the UV/NMR-illumination setup including their wiring.

5.6.1.3 Spectroscopy Setup

For measuring UV/Vis and NMR spectra under the influence of LED light inside a NMR spectrometer it was necessary to design a new device which was placed inside a standard 5 mm NMR tube. To make the setup applicable for any conventional NMR user, it was essential to us that no alteration of the NMR spectrometer and/or the NMR probe was required as it was described in a former publication about UVNMR combinations.[2,3] Therefore a combination of different optical fibers was developed which was guided directly from the top of the NMR spectrometer into the NMR tube (Figure S1).

The LED light source (see section 5.6.1.2) is connected to a commercially available optical fiber with an outer diameter of 1000 µm (BFH48-1000high; Thorlabs). This illumination fiber is guided directly into the NMR sample (Figure S2A). To ensure a homogeneous illumination of the sample inside the NMR tube, the tip of the optical fiber was uncovered and roughened by sandblasting in the range of the NMR receiver coils. This setup for the illumination of NMR samples inside an NMR spectrometer was already described in an earlier publication of our working group.[1]

The D-Hal-lamp and the UV/Vis spectrometer are connected to a bundle of 7 optical fibers with an outer diameter of 100 µm each purchased by Avantes (FCR-7UV200). In the 230 mm long tip of this bundle the 7 optical fibers are arranged radial symmetrically (Figure S2B). The tip has outer diameter of 1000 µm.

The 6 outer fibers (Figure S2B, blue) are connected to the D-Hal-lamp, the central fiber (red) is connected to the UV/Vis spectrometer (changing the connection of the 6 outer fibers to the UV/Vis spectrometer instead to the D-Hal-lamp diminished the detected absorbance intensity). This “UV/Vis fiber” is also guided directly into the NMR tube inside the NMR spectrometer.

Here, the outer NMR tube is a standard thin wall tube with an outer diameter of 5 mm. To diminish the influence of light from the outside commercially available ambered tubes were used. To guide and to center the optical fibers (described above) inside the outer NMR tube a coaxial quartz glass insert (Norell NI5CCI-B-QTZ) with an outer diameter of 3 mm in the range of the stem was added. By nature natural quartz glass is transparent (90-95%) to light >210 nm which ensures the applicability of the setup even in the UV region.

On the bottom end of the tube a customized insert made of optical PTFE (RESTAN; www.image-engenieering.de) was put in place to reflect the light of the optical fibers which were connected to the D-Hal-lamp. The reflected light is afterwards detected by the central fiber (red) to give a UV/Vis spectrum of the solution inside the tube (Figure S2B).

Optical PTFE is a diffuse reflector and it is known to have a very high chemical and thermal resistance and can be shaped very easily. Furthermore the material is UV persistent and reflects more than 98% of incoming light in a range between 380-1700 nm. Due to its high thermal expansion coefficient it was necessary to test if the PTFE insert breaks the tube at higher temperatures. Therefore several “stress tests” with abrupt temperature changes were made. According to these tests our setup is at least applicable for a temperature range between 180-323 K. Outside this range no tests were made.

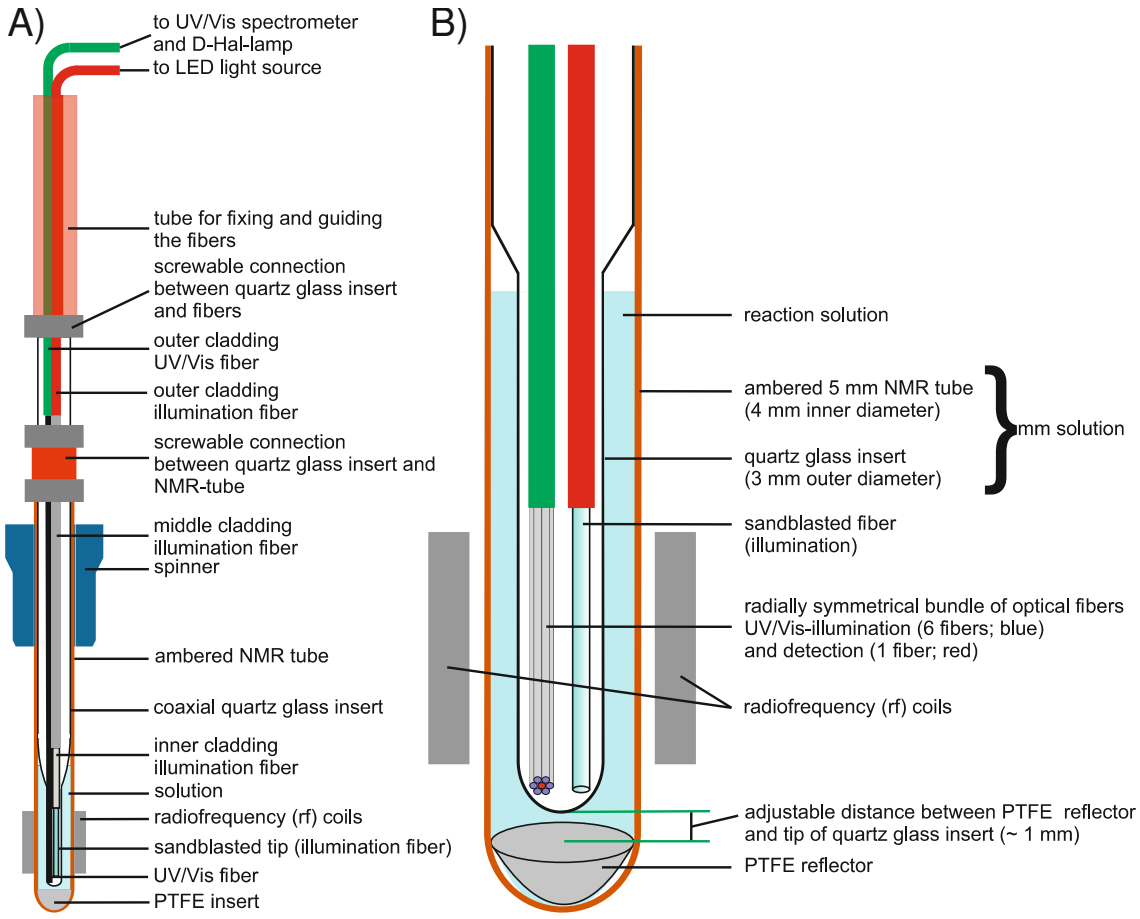

Figure S2. A) Depiction of all NMR tube related components B) Detailed setup of the UV/Vis related parameters.

To control the required pathlength for the UV/Vis measurements a new screw cap was developed (Figure S3). Depending on the concentration and the extinction coefficient according to the Lambert-Beer-law a particular distance between the PTFE reflector and the tip of the coaxial insert can be set to give an optimal UV/Vis spectrum. The screw cap is placed on the top of the outer ambered NMR tube and tightened by a customized union nut. Trough a 4 mm channel inside the screw cap the quartz glass insert can be introduced into the NMR tube and can be fixed at a particular height by a second union nut. Furthermore it is used to place the stem of the coaxial insert perfectly inside the range of the radiofrequency (rf) coils of the NMR spectrometer. This is essential to achieve a good shimming quality in the NMR experiments and to get good results.

For quantification, we highly recommend to use the NMR results due to slight deviations in the distance settings between blank and sample. However, during the reaction the distance stays constant enabling a relative quantification of ratios by UV/Vis.

Since photochemical reactions and compounds are often influenced by the presence of oxygen two O-rings were added to make the screw cap air tight. Due to this enhancement, reactions under inert conditions are now open for investigation (as shown in the recent PDI study in the manuscript). First tests showed an exclusion of air for at least 7 days.

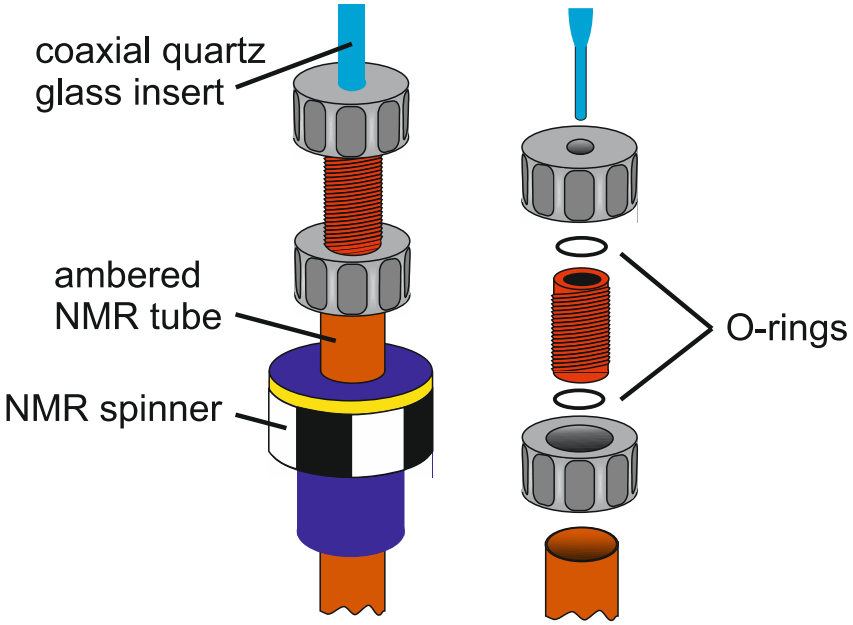

Figure S3. Detailed depiction of the airtight screw cap.

To link the optical fibers with the top end of the coaxial quartz glass insert a second screwable connector was developed. Similar to the airtight screw cap described before also here a union nut and an O-ring was used to connect the coaxial insert with a plastic tube in which both optical fibers were fastened. The tube is furthermore used to stabilize the whole setup and to inject it more easily into the NMR spectrometer.

5.6.1.4 Automation and Modification of Pulse Sequences

As described in section 5.6.1.2 an automated measurement of UV/Vis spectra and LED illumination is achieved by a direct connection of the UV/Vis spectrometer and the LED transistor to the NMR console (Bruker Avance III HD). They are cable (BNC) connected via two RCP outputs of the T-Controller located in the Intelligent Pulse Sequence Organizer (IPSO; here IPSO 19'') unit, which synchronizes all acquisition related processes.

However to run a combined UV/Vis and NMR experiment under the influence of the external LED light source which is exclusively controlled by the NMR console, modified NMR pulse sequences are required. In general the IPSO unit provides a variety of RCP outputs, whereas most of them have a preset function. The free RCP outputs can be programmed by the user adding special events to the standard pulse sequence. The outputs work on Transistor-transistor-logic (TTL) and are active low by default. By applying certain commands in the pulse program they can be switched from active low to inactive high and back.

Here, the free RCP outputs 28 and 29 were chosen to connect the LED light source and the UV/Vis spectrometer/D-Hal-lamp to the NMR console. According to the Bruker user manual, the following command syntaxes to control the devices were added to the pulse program.

d11 setnmr3^28 and **d11 setnmr3|28** turn the LED off and on

d11 setnmr3^29 and **d11 setnnmr3|29** close/open the shutter of the UV/Vis spectrometer and initiate a measurement

(The minimum switching time d11 is given at 25 ns. Note: d11 can also be replaced by a fixed value (e.g. 1s))

To control the UV/Vis spectrometer with these commands, it was necessary to enable the external trigger mode in the related UV/Vis spectrometer software (Avasoft 8.6full).

Figure S4 schematically shows the resulting pulse sequence of a combined UVNMR illumination experiment. Here, the UV/Vis measurement is conducted prior to the NMR measurement under LED illumination. First the LED is turned off, then the shutter inside the D-Hal-lamp opens and the UV/VIS spectrometer initiates a measurement. After the UV/Vis measurement is completed the shutter is closed and the LED is turned on again. Then the common acquisition cycle starts (here: 1D ^{1}H spectrum), resulting in one UV/Vis spectrum and one NMR spectrum for this experiment. The delay $d_{UV/Vis}$ is of special interest here. This delay represents the integration time of the UV/Vis measurement (see Avasoft) and is acquired from the manual measurement of the blank sample prior to the actual experiment and has to be adjusted for every new sample.

For every measurement with this UV/NMR-illumination-setup a blank measurement under the same conditions was made previously to set the parameters for the UV/Vis and NMR measurements.

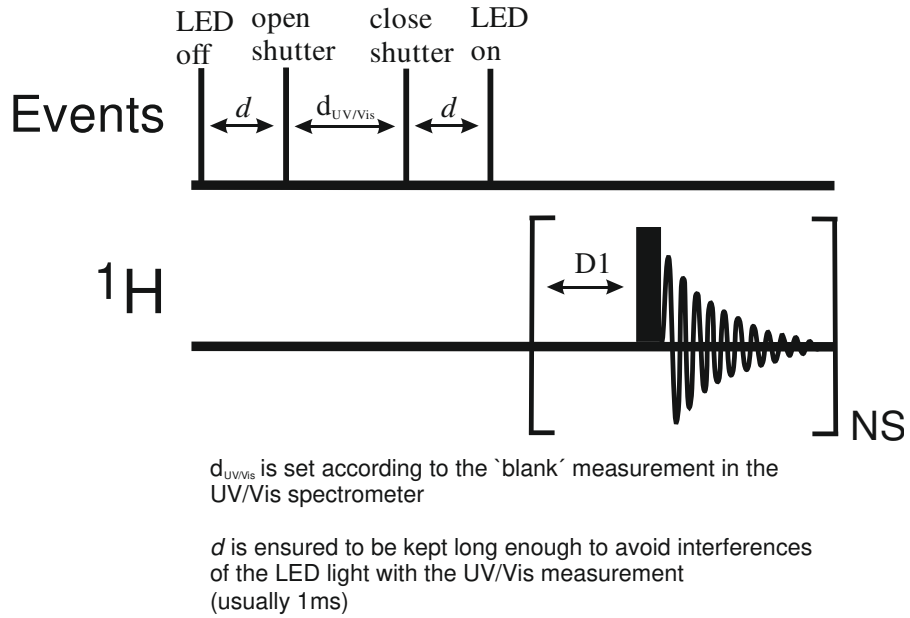

Figure S4. Modified pulse sequence of our combined UVNMR illumination experiment. A series of switching 5V TTL pulses of the T-Controller of the IPSO Unit directly control the UV/Vis spectrometer and the transistor of the illumination LED.

The corresponding pulse program to the pulse sequence shown in Figure S4 is:

```
;zg30_UV_light (based on zg30)
;avance-version (07/04/03)
;1D sequence
;using 30 degree flip angle
;performing one UV/Vis experiment before AQ cycle
;continous illumination during the whole experiment
;
;$CLASS=HighRes
;$DIM=1D
;$TYPE=
;$SUBTYPE=
;$COMMENT=

#include <Avance.incl>
```

```
"acqt0=-p1*0.66/3.1416"

1 ze
1m setnmr3^28 ;turn off illumination
d11 setnmr3|29 ;open shutter start UV/Vis experiment
1m setnmr3^29 ;close shutter
1m setnmr3|28 ;turn on illumination
2 30m
  d1
  p1*0.33 ph1
  go=2 ph31
d21
  30m mc #0 to 2 F0(zd)
exit

ph1=0 2 2 0 1 3 3 1
ph31=0 2 2 0 1 3 3 1

;pl1 : f1 channel - power level for pulse (default)
;p1 : f1 channel -  90 degree high power pulse
;d1 : relaxation delay; 1-5 * T1
;d11: set d11 according to the blank measurement in the UV/Vis spectrum
;d21: delay between experiments
;NS: 1 * n, total number of scans: NS * TD0

;$Id: zg30,v 1.9 2007/04/11 13:34:31 ber Exp $
```

;d11: set d11 according to the integration time of the blank measurement in the UV/Vis spectrum.

For most measurements the d11 was determined to be around 400 ms.

The delay of one millisecond (1 m) for the events (setnmr3^28; setnmr3^29; setnmr3|28) ensures that the light emission of the LED is definitely zero to avoid interferences with the UV/Vis measurement.[1]

In principle the command series for the UV/Vis measurement can be put anywhere in the pulse program e.g. before, after or during acquisition. Furthermore the command order can be changed at will if needed e.g. for experiments requiring light pulses instead of continuous illumination.

Since in our case the standby output level of the RCP used for the connection to the UV/Vis spectrometer and the D-Hal-lamp was high (~5 V) the shutter of the D-Hal-lamp was opened after every NMR experiment. To avoid the influence of the emitted light to the sample a customized TTL inverter between the NMR console and the UV/Vis spectrometer was added to set the standby TTL level low (~0 V).

5.6.1.5 Comparison of Reaction Rates – Conventional LED Illumination Setup vs New Combined LED UV/Vis Illumination Setup

To check for possible disadvantages of our new UVNMR-illumination setup we conducted a study about the illumination capabilities compared to our old illumination setup.[1] Figure S5 shows a schematic top view of our current illumination setup A) and our new UVNMR-illumination setup B) in the NMR tube. Our new systems have two major differences compared to our established illumination setup. First, instead of one fiber the glass insert is now filled with two fibers, the illumination fiber and the UV/Vis fiber. As the UV/Vis fiber is not transparent to light in horizontal axis this could lead to a ‘dark area’ (Figure S5B) in the sample which is not reached by the light emitted from the illumination fiber resulting in a hampered reaction rate. Secondly, two fibers require a bigger quartz glass insert (3 mm outer diameter), which in return reduces the layer thickness of the sample from 2 to 1 mm. This could lead to a faster reaction rate if the emitted light is not strong enough to thoroughly penetrate the whole sample in the old illumination setup. Either way, the differences of both setups are so pronounced when it comes to illumination that a comparison seems mandatory.

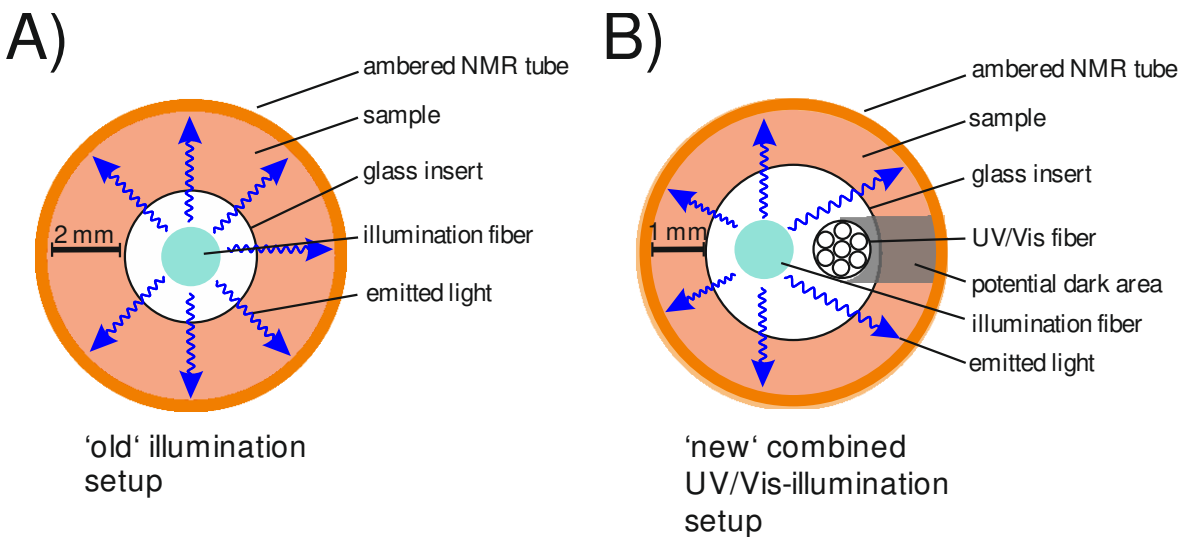

Figure S5. Schematic top view of the two LED illumination setups. A) Depiction of the old, conventional illumination setup with a layer thickness of 2 mm for the sample B) new combined UVNMR-illumination setup with a layer thickness of 1 mm for the sample. Due to the incorporation of the second UV/Vis fiber the issue of an unlit, dark area arises.

As a test reaction for the comparison of reaction rates the photocatalytic oxidation of 4-methylbenzyl alcohol (MBA) with riboflavin tetraacetate (RFTA) was chosen (Figure S6). This reaction was already thoroughly investigated in our working group and does not require the exclusion of oxygen.[4] Hence, a stock solution can be prepared for all samples which greatly improves the comparability of all measurements.

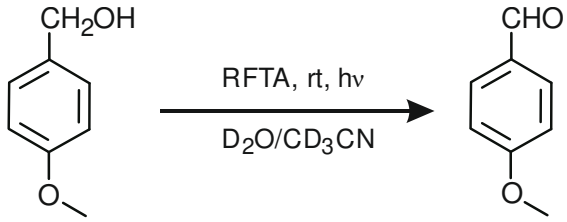

Figure S6. Photocatalytic oxidation of MBA is used as a test reaction for the comparison of reaction rates between the two illumination setups, shown in Figure S5.

Materials: The solvents D_2O and CD_3CN were purchased from Deutero GmbH and Sigma Aldrich. 4-Methoxybenzylalcohol was purchased from Sigma Aldrich and was used without further purification. The photocatalyst Riboflavin tetraacetate (RFTA) was synthesized according to the reported procedures.[4,5]

Sample preparation: The NMR samples were prepared in pairs as a 1 mL solution of D_2O/CD_3CN (1:1) containing 2 mM riboflavin tetraacetate (RFTA) and 20 mM 4-methoxybenzyl alcohol (MBA). The solution was then split and filled into two ambered NMR tubes, each containing 350 µL of the stock solution. Afterwards the tubes were connected to their illumination setup by inserting the respective glass insert (2 mm outer diameter for conventional; 3 mm outer diameter for the new quartz glass insert) and sealing everything airtight.

***In situ* NMR measurements:** NMR experiments were conducted on a Bruker Avance 500 spectrometer with a 5 mm QXI probe. The resulting NMR spectra were processed and evaluated with Bruker Topspin 3.2. The samples were illuminated by a Cree XT-E royal blue high power LED with a center wavelength of 450 nm and 500 mW optical output power (Lumitronix, Cree XT-E, *68332*). The light was guided directly into the sample with the help of an optical fiber as described previously.[1] After a first ^1H spectrum in the dark, all following spectra were recorded under continuous illumination. There was no need to record alternating illuminated and dark spectra since it was already shown that no signal is distorted by Photo-CIDNP effects in D_2O/CD_3CN. The kinetics were derived from the integrals of the ^1H aldehyde signal of 4-methoxybenzyl aldehyde (MBAld) since it does not overlap with other signals (Figure S7A). The integral of the ^1H MBAld signal was referenced to the aromatic protons of the starting material 4-methoxybenzyl alcohol (MBA).

Discussion: Figure S7A shows that MBAld is generated under continuous blue light illumination. The MBAld aldehyde signal does not overlap with any other signal and is hence suitable for integration. Figure S7B depicts the integral area of the MBAld aldehyde signal **1** under illumination over time for the two compared setups. Whereas the black kinetic corresponds to the conventional illumination setup containing only the illumination fiber and the smaller insert (2 mm) and the red kinetic belongs to the new setup incorporating the illumination and UV/Vis fiber in a bigger insert (3 mm). The reaction profiles clearly reveal that there is no significant difference between the two setups. One might even argue that the newer setup has a slightly higher reaction rate. This could be due to the smaller layer of thickness compared to the old setup (1 mm vs. 2 mm) which allows for a more potent illumination of the sample. But it could also be because of slight differences in the sandblasted fiber tips of the illumination fiber since every fiber tip is crafted individually. In summary, our new setup shows no significant variations in reaction rate compared to our old illumination setup, which implies that the 'dark area' (Figure S5B) caused by the UV/Vis fiber has no notable impact on the

reaction rate or at least is canceled out by fast diffusion or by the thinner layer of solution allowing for a better illumination.

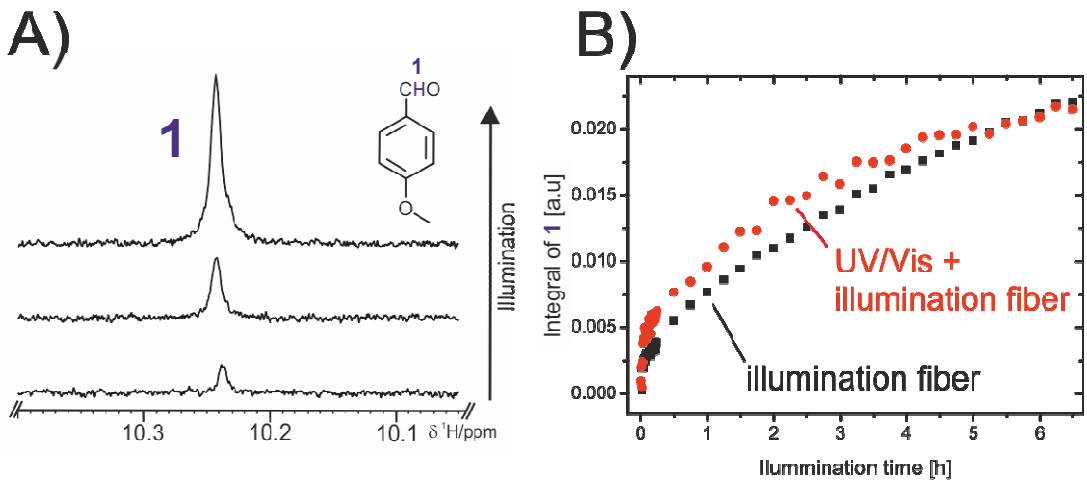

Figure S7. A) Photocatalytic generation of 4-methoxybenzyl aldehyde over time; the ^{1}H aldehyde signal 1 at 10.24 ppm poses a suitable signal for integration as it does not overlap with other signals B) Reaction profile of the ^{1}H aldehyde signal 1 at 10.24 ppm for the two illumination setups: Conventional illumination fiber (black) and UV/Vis fiber + illumination fiber (red).

5.6.2 Summary of conPET Processes and Investigations of the Photoreduction of Aryl Halides with PDI as Photocatalyst

5.6.2.1 Summary of conPET Processes

Recently, König *et al.* introduced the consecutive photoinduced electron transfer (conPET) process to achieve higher redox potentials.[6–12] Here aryl radicals can be obtained from aryl halides (**Q**) utilizing the excited states of stable radical anions (**Photocat**$^{\bullet-}$) (Figure S8). These stable radical anions are generated via a classical photoinduced electron transfer (PET) process with the help of a sacrificial electron donor (**D**; e.g. NEt_3, DIPEA). In conPET processes organic dyes (**Photocat.**; e.g. N,N-bis(2,6-diisopropylphenyl)-perylene-3,4,9,10-bisdicarboximide (PDI), Rhodamine-6G and 9,10-Dicyanoanthracene) are used as photocatalysts as they form stable colored radicals under inert atmosphere.[8–11] Upon a second photoexcitation these stable radicals (**Photocat**$^{\bullet-}$) are proposed to form a further excited state (**Photocat**$^{\bullet-*}$), which is able to transfer an electron to aryl halides resulting in an aryl radical precursor (**Q**$^{\bullet-}$). After fragmentation this precursor can be trapped by various additives to yield the desired product.[6–11]

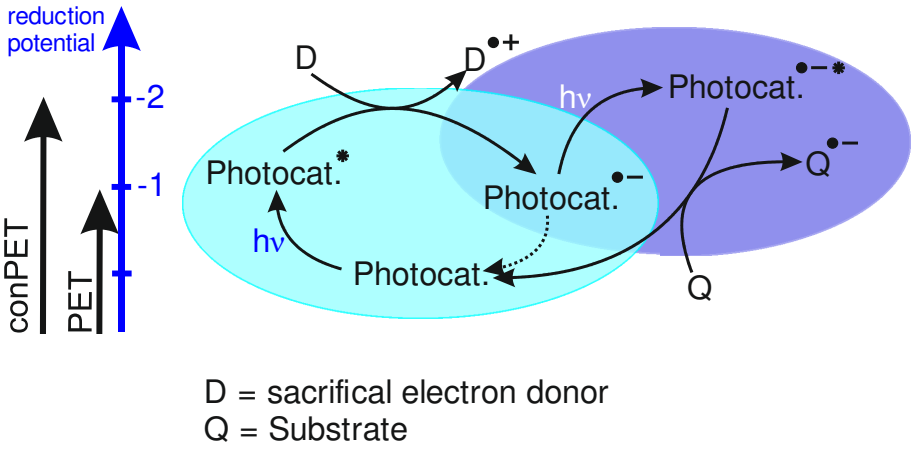

Figure S8. Schematic representation of a consecutive photoinduced electron transfer (conPET) process.

The first conPET process published in 2014 reported the photoreduction of aryl halides with blue light (455 nm) irradiation utilizing N,N-bis(2,6-diisopropylphenyl)-perylene-3,4,9,10-bisdicarboximide (PDI) as a photocatalyst.[8] The general reaction conditions are illustrated in Figure S9.

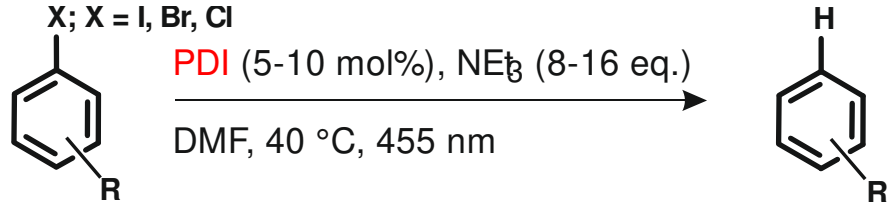

Figure S9. General conditions of the photoreduction of aryl halides via conPET.[8]

In the proposed and controversially discussed reaction mechanism (Figure S10), an initial photoexciation of **PDI** with blue light (455 nm) yields the excited **PDI***, which gets reductively quenched by the sacrificial electron donor NEt_3 to yield **PDI**$^{\bullet-}$ and **NEt$_3$**$^{\bullet+}$. The stable **PDI**$^{\bullet-}$ radical anion is proposed to be excited by a second photon (455 nm) to give **PDI**$^{\bullet-*}$. This photoexcited state is supposed to be able to reduce the given substrate (**Ald-Br**) resulting in an aryl radical precursor (**Ald-Br**$^{\bullet-}$**)** and ground state **PDI**. **Ald-Br**$^{\bullet-}$ then fragments into **Br**$^{-}$ and the neutral radical **Ald**$^{\bullet}$, which can abstract a proton from either **NEt$_3$**$^{\bullet+}$ or the solvent (e.g. DMF) to give the final product **Ald**.[8] If the proton was abstracted from **NEt$_3$** it will lead to a cationic imine species, which immediately reacts with water in solution to give diethylamine (**DEA**) and acetaldehyde.

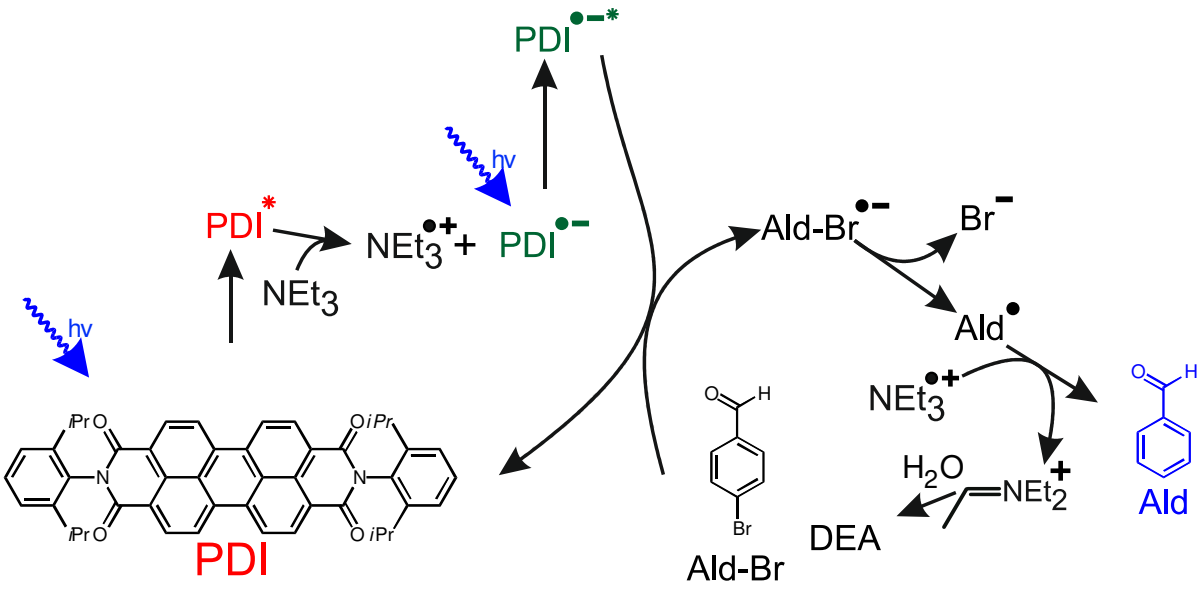

Figure S10. Catalytic mechanism of the first conPET process with PDI as proposed by König *et al.*[8]

5.6.2.2 Investigations of the Photoreduction of Aryl Halides with PDI as Photocatalyst

5.6.2.2.1 General Information

Materials:

The solvents DMSO-d_6 and DMF-d_7 were purchased from Deutero GmbH. Both solvents were dried over 4 Å molecular sieves and deoxygenated via Freeze-Pump-thaw prior to use. N,N'-Bis(2,6-diisopropylphenyl)-3,4,9,10-perylenetetracarboxylic-diimide (PDI) was purchased from TCI chemicals and used without further purification. 4-bromo-benzaldehyde (Ald-Br) and triethylamine (NEt_3) were purchased from Merck. NEt_3 was dried over 4 Å molecular sieves prior to use and 4-bromo-benzaldehyde (Ald-Br) was used without further purification.

Combined UVNMR-illumination reaction profiles

All measurements were conducted on a Bruker Avance III HD 600 (600.13 MHz) spectrometer with a fluorine selective TBIF probe in combination with our new UVNMR-illumination device described in section 5.6.1. The samples were illuminated by a Cree XT-E royal blue high power LED (Lumitronix, 450 nm; 500 mW, *68332*).

If not otherwise indicated, measurements were conducted at 313 K in 300 µL solutions of DMF-d_7 or DMSO-d_6 containing 1 mM (0.1 eq.) N,N-bis(2,6-diisopropylphenyl)-perylene-3,4,9,10-bisdicarboximide (PDI), 10 mM (1 eq.) 4-bromo-benzaldehyde (Ald-Br) and 80 mM (8 eq.) triethylamine (NEt_3).

Preparation blank:

Ald-Br and NEt_3 were dissolved in DMF-d_7 in an NMR tube under inert conditions. The quartz glass insert was added and the sample was sealed airtight with the customized screw cap (see setup).

Blank measurement:

The blank measurement was conducted prior to the combined reaction kinetic. The sample was injected into the NMR spectrometer to reach a temperature of 313 K. Then a blank UV/Vis spectrum was recorded. The resulting integration time given by the UV/Vis spectrometer determined the d11 delay in the NMR pulse program (section 5.6.1.4), which was necessary for later automation. An NMR spectrum was also taken as quality control, which ensured correct sample preparation.

Preparation sample:

Under argon atmosphere the required amount of PDI was added to the blank sample. The quartz glass insert was inserted and the sample was sealed with our customized screw cap. To dissolve the PDI completely the sample was sonicated.

Oxygen-test:

Prior to the kinetic investigations an oxygen-test sequence was conducted for every new sample to exclude the presence of oxygen. Therefore, the prepared sample was put into the NMR spectrometer to reach a temperature of 313 K. All **PDI** signals start to broaden once illumination starts. If oxygen is present in the reaction solution the **PDI** signals sharpen again once the light is turned off. This behavior can be exploited as a simple test to verify successful deoxygenation. Three single scan NMR spectra are measured in total. The first one before any illumination took place. The second one after an illumination time of 1.0 s and the third one two minutes after the illumination. As 1.0 s of illumination is already enough to induce the line broadening, the **PDI** signals are broader in spectrum two. If oxygen is present the **PDI** signals in spectrum three are sharp again, if deoxygenation was successful then spectrum two and three are identical.

Sample measurement:

For all NMR measurements the delay d11 in the pulse program was set to the required integration time determined in the blank UV/Vis measurement. The reaction profiles were generated by alternately recording non illuminated and illuminated ^{1}H NMR spectra. This ensured that no signal intensities were distorted by possible photo-CIDNP effects.[4] One UV/Vis spectrum was automatically recorded prior to every NMR measurement (dark and light). After a first spectrum without illumination a row of ^{1}H spectra was collected alternating between illuminated and unilluminated proton spectra. Only spectra without illumination were used to generate reaction profiles. The NMR kinetics are derived from the aromatic proton integrals of **Ald-Br** and **Ald** (Signal **3**, Figure S11) and referenced to the respective signal in the first spectrum without illumination. Assignments were made by evaluating standard sets of 1D and 2D NMR spectra. The chemical shifts were referenced to the solvent signals (DMF-d_7). The UV/Vis kinetics are derived from the absorption maximum of the radical anion of **PDI** at 798 nm (see manuscript). Its intensity is referenced semi-quantitatively to its own maximum absorbance (=1.0). Referencing the radical anion to the ground state **PDI** was not possible because of the donor-acceptor complex of PDI and NEt_3.

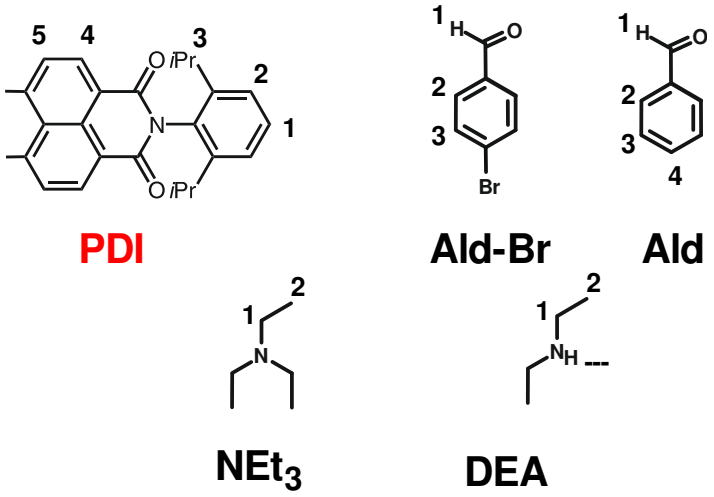

Figure S11. Numeration of PDI, Ald-Br, Ald, NEt_3 and DEA used for the assignment and further characterization.

5.6.2.2.2 Assignments of Starting Materials, Catalyst and Products

Assignments were made by evaluating standard sets of 1D and 2D NMR spectra.

Figure S12 shows the ^{1}H proton spectrum with an illustration of all reaction components before illumination under reaction conditions (PDI 1 mM, Ald-Br 10 mM, NEt_3 80 mM, deoxygenated in DMF-d_7 at 313 K) before illumination.

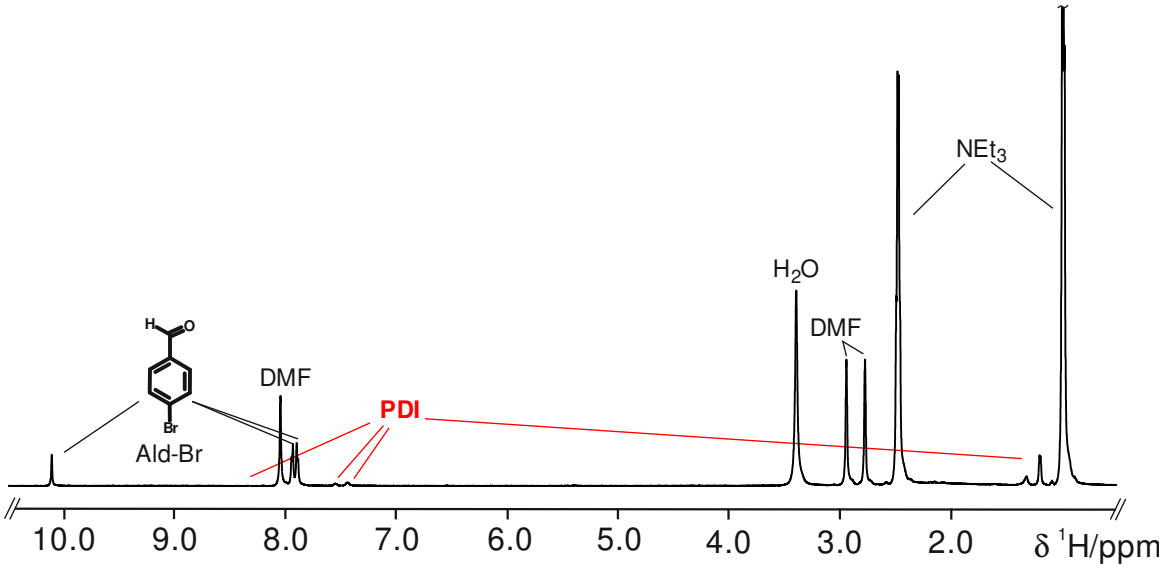

Figure S12. Full ^{1}H proton NMR spectrum of the reaction mixture at 313 K in DMF-d_7 before illumination. The reaction components PDI (1 mM), Ald-Br (10 mM) and TEA (80 mM) are illustrated.

Figure S13 depicts the assignments for the most prominent reaction components. As described in the manuscript all **PDI** signals are significantly broadened even prior to illumination with respect to their distance to the perylene core probably because of an acceptor-donor complex with **NEt_3.** .Especially the **PDI** proton signals **4** and **5** are broadened so much that they are only detectable as one broad signal just above the noise level (Figure S14). Hence the chemical shift for the **PDI** protons **4** and **5** can only be given in a chemical shift range from 9.7 to 8.6 ppm. The methine proton of the isopropyl group of **PDI** was not assignable as it is covered by the DMF signal at 2.92 ppm and is hence not discussed further. The remaining **PDI** proton signals could be readily assigned. The other reaction components (**Ald-Br**, **Ald**, **NEt_3** and **DEA**) also can be assigned in a straightforward manner. The amine proton of **DEA** is not assignable probably due to exchange line broadening with the residual water in solution. The reaction product **Ald** is partially deuterated (ratio 1:2 H/D), since the reaction is carried out in fully deuterated DMF which can also act as a proton source besides **NEt_3**.

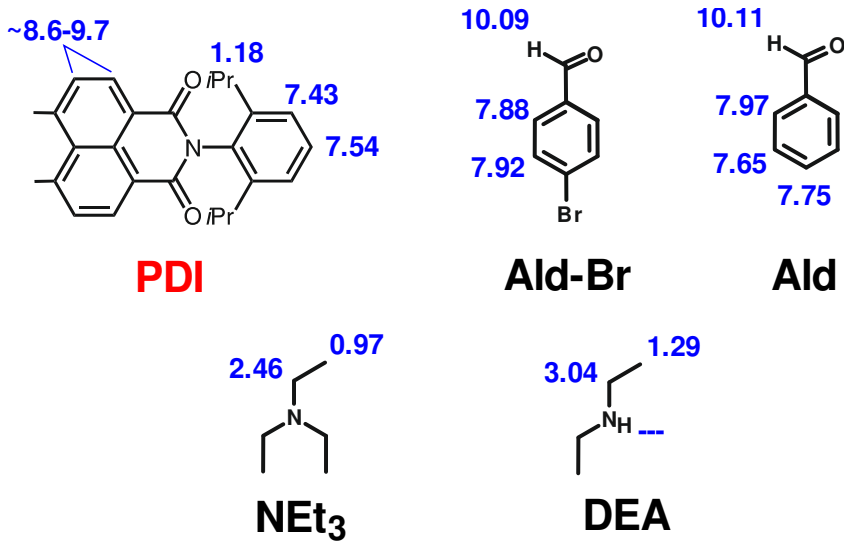

Figure S13. Assignment of PDI, Ald-Br, Ald, TEA and DEA in DMF-d_7. ^{1}H chemical shifts are highlighted blue and referenced to DMF (8.03 ppm). For the isopropyl groups only one chemical shift for the methyl groups is given because the methine proton is completely covered by the DMF solvent signal at 2.92 ppm.

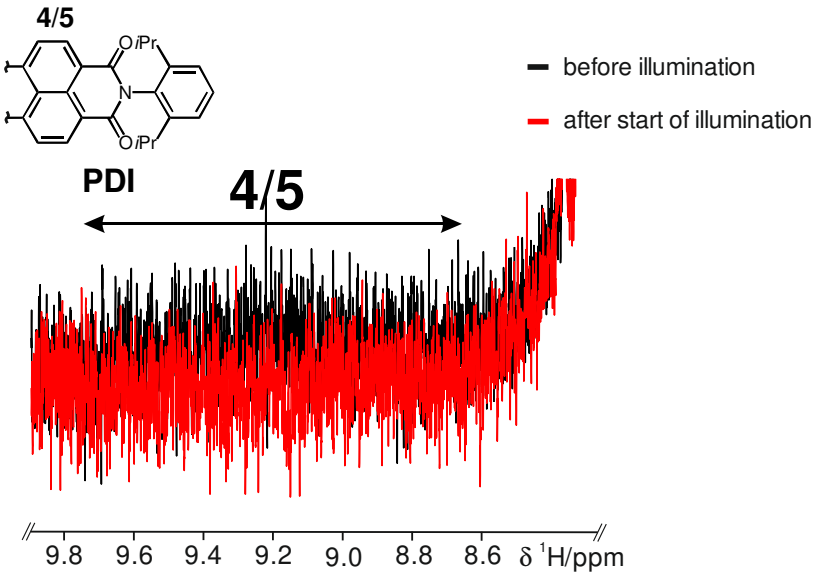

Figure S14. Excerpt of the ^{1}H proton spectrum region of the broadened PDI proton signals 4 and 5 prior to illumination (black) and after the light is turned on (red). The proton signals 4 and 5 appear as one broad signal just above the noise level and vanish immediately after the light is turned on.

5.6.3 Investigation of a Common Photoswitch

5.6.3.1 General Information

Materials:

The solvent THF-d_8 was purchased from Deutero GmbH. 1,3,3-Trimethylindlino-6'-nitrobenzopyrolospiran **1** was purchased from TCI chemicals and was used without further purification.

***In situ* UVNMR-illumination experiments:**

All measurements were conducted on a Bruker Avance III HD 600 (600.13 MHz) spectrometer with a fluorine selective TBIF probe in combination with our new UVNMR-illumination device described in section 5.6.1. The samples were illuminated by a high power UV LED (Laser Components, 365 nm, 2.06 W, LEUVA66X00RV00).

The samples described here, all contained a solution of 1 mM 1,3,3-trimethylindlino-6'-nitrobenzopyrolospiran **1** in 300 µL of THF-d_8.

Preparation blank:

To measure the required UV/Vis spectrum of a blank sample, 300 µL THF-d_8 were transferred into the NMR tube, the glass insert was inserted and the tube was sealed airtight with our customized screw cap.

Blank measurement:

The blank measurement was conducted prior to the kinetic investigations. The blank was put into the NMR spectrometer to reach a temperature of 300 K or 180 K respectively. Then a blank UV/Vis spectrum was recorded. The resulting integration time given by the UV/Vis spectrometer determined the d11 delay in the NMR pulse program (section 5.6.1.4), which was necessary for latter automation. An NMR spectrum was also taken as quality control, which ensured correct sample preparation.

Preparation sample:

The 1,3,3-trimethylindlino-6'-nitrobenzopyrolospiran **1** was added to the blank sample, the glass insert was inserted into the sample and the tube sealed airtight with our customized screw cap.

Sample measurement:

After a first proton spectrum without illumination, the photoswitching process of **1** to its open form **2** was observed by a row of ^{1}H NMR spectra under continuous illumination with 365 nm. One UV/Vis spectrum was automatically recorded prior to every NMR measurement (section 5.6.1.4). When the absorption maxima of the open species **2** reached a plateau at 300 K, the illumination was turned off and a row of ^{1}H NMR one scan spectra (one spectrum every 8 seconds with UV/Vis recordings) were recorded to follow the thermal back reaction to **1**. At 180 K a row of ^{1}H NMR spectra was taken every 20 min because of the drastically increased half-life $\tau_{1/2}$ of **2**. Quantification of the NMR signals was derived from the integrals of the methyl group (1) of **1** and the corresponding signal of **2**. Assignments were made by evaluating standard sets of 1D and 2D NMR spectra like ^{1}H, ^{1}H,^{1}H-COSY, ^{1}H,^{1}H-TOCSY, ^{1}H,^{1}H-NOESY, ^{1}H,^{13}C-HSQC, ^{1}H,^{13}C-HMBC. For the numeration see Figure S15. The chemical shifts were referenced to the solvent signals. The UV/Vis absorption maximum at 533 nm was taken for half life determination of **2**. Evaluation of the half life $\tau_{1/2}$ was done by the exponential fit function of Origin 8.

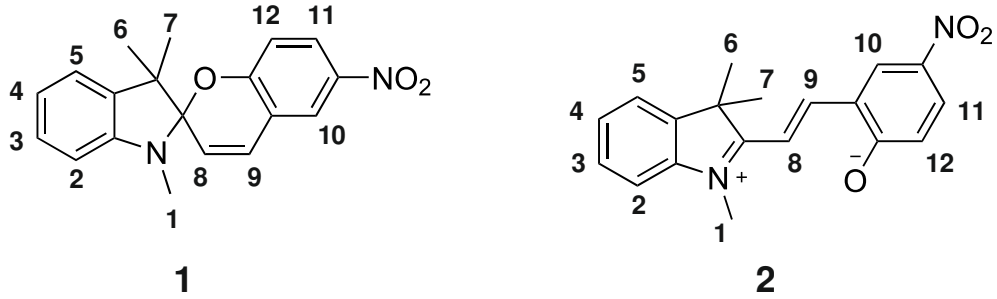

Figure S15. Numeration of 1,3,3-trimethylindlino-6'-nitrobenzopyrolospiran **1** and its open switched form **2** used for the assignment and further characterization.

5.6.3.2 Assignments of 1 and its Open Form 2

Assignments were made by evaluating standard sets of 1D and 2D NMR spectra (see Figure S16).

The open form **2** could not be assigned at 300 K as it started to photodegrade very fast (< 30 min) under continuous illumination with 365 nm preventing a full 2D NMR set. All other species (**1** at 300 K, **1** at 180 K and **2** at 180 K) could be assigned in a straightforward manner.

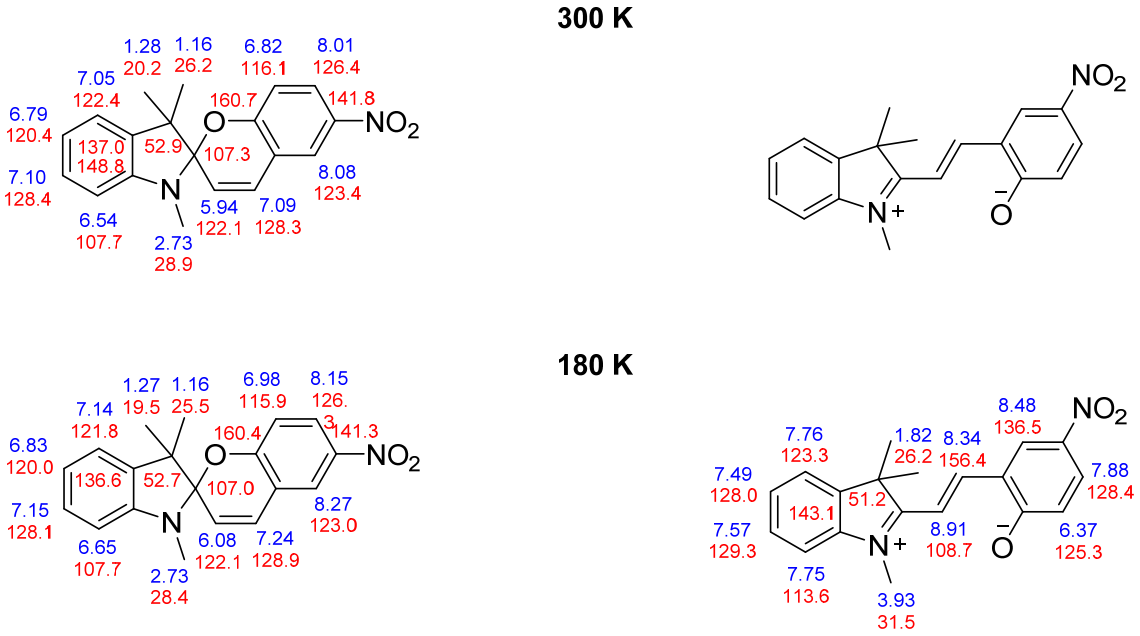

Figure S16. Assignment of **1** and its open form **2** in THF-d_8 at 300 K (top) and 180 K (bottom). ^{1}H chemical shifts are highlighted blue, ^{13}C chemical shifts are highlighted red. The assignment of the open form **2** at 300 K was not possible due to rapid degradation under continuous illumination with 365 nm.

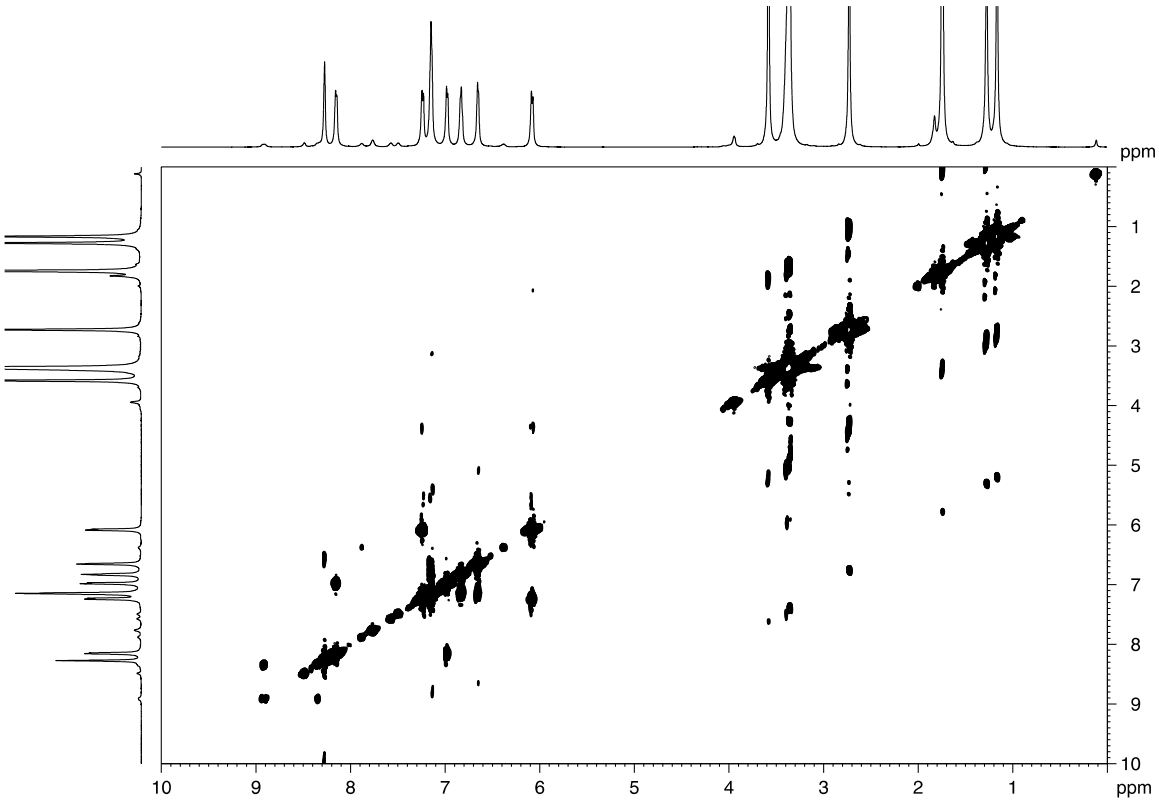

Figure S17. $^{1}H,^{1}H$-COSY of spiropyran **1** and its open form **2** in THF-d_8 at 180 K.

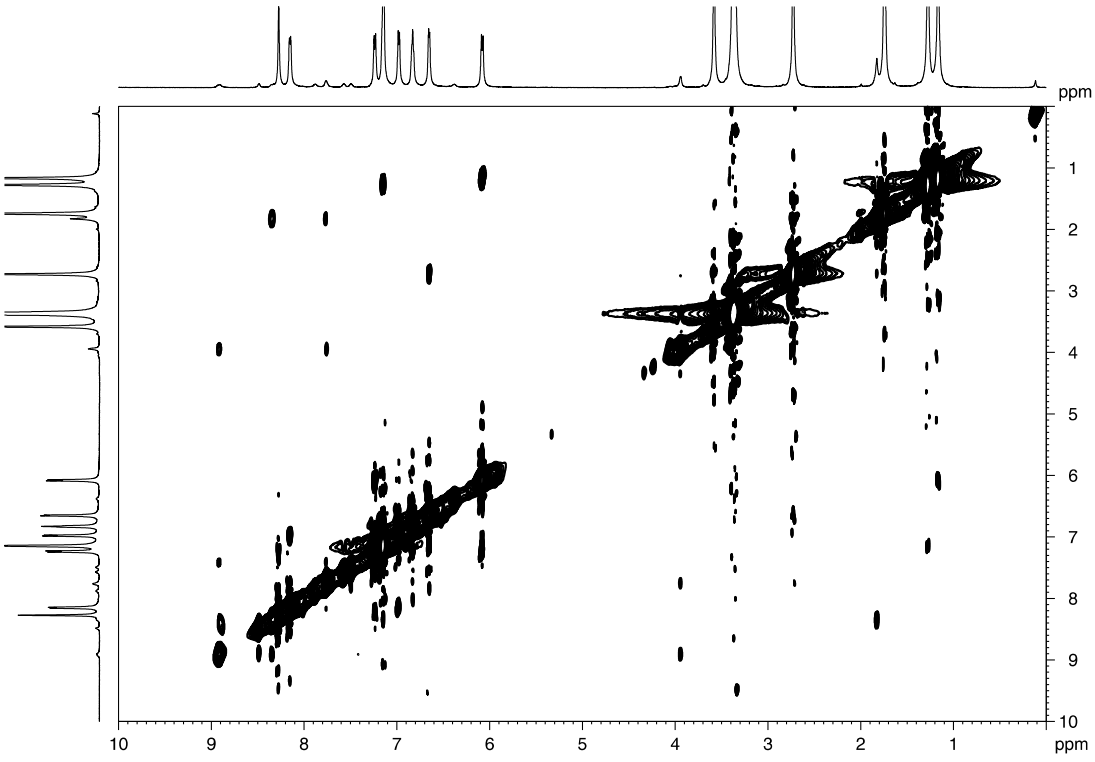

Figure S18. $^{1}H,^{1}H$-NOESY of spiropyran **1** and its open form **2** in THF-d_8 at 180 K. Mixing time 200 ms.

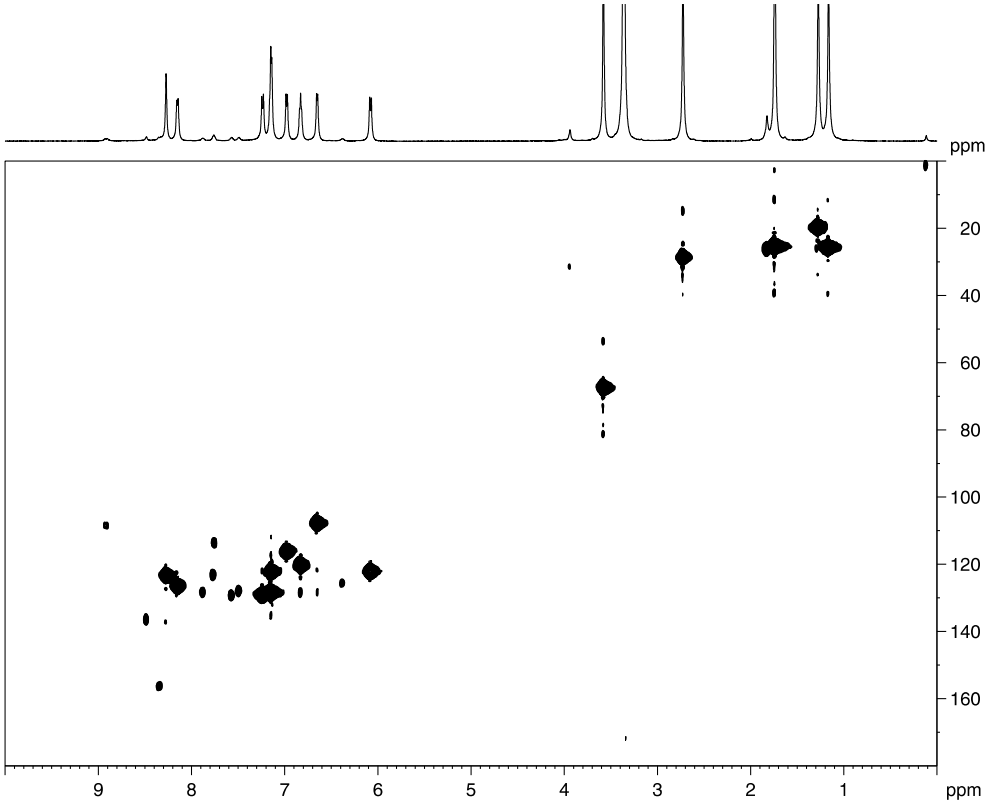

Figure S19. $^{1}H,^{13}C$-HSQC of spiropyran **1** and its open form **2** in THF-d_8 at 180 K.

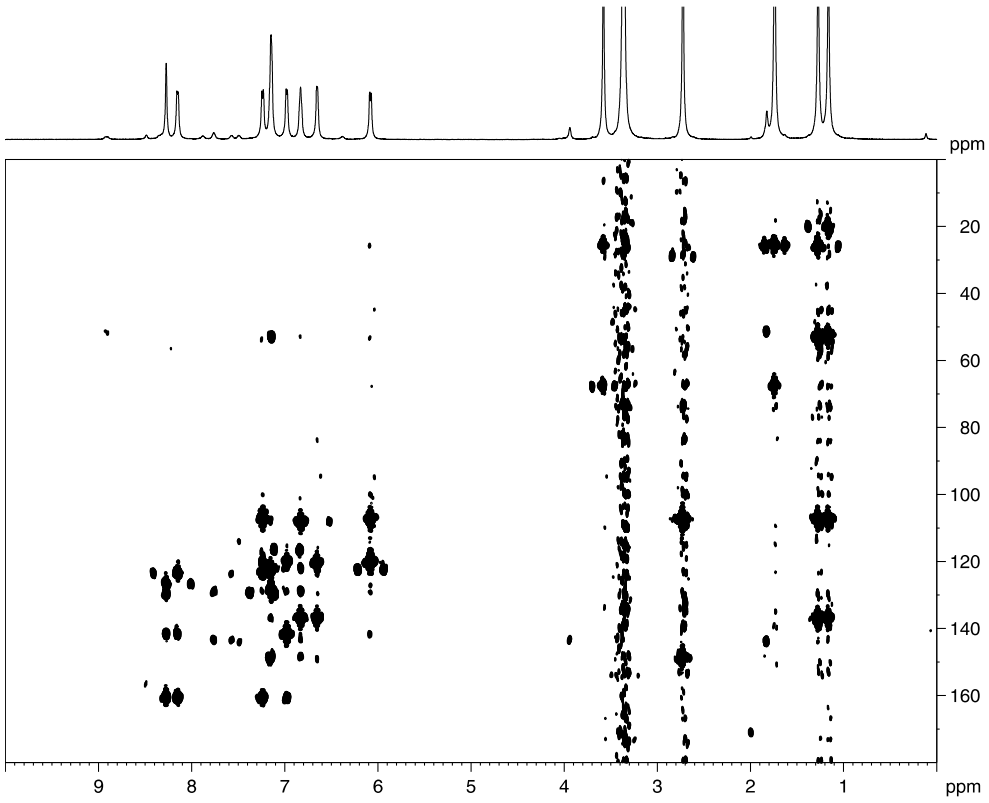

Figure S20. $^{1}H,^{13}C$-HMBC of spiropyran **1** and its open form **2** in THF-d_8 at 180 K.

5.6.3.3 NMR and UV/Vis Build Up and Decay Curves of 2

5.6.3.3.1 Isomerization Experiments at 300 K

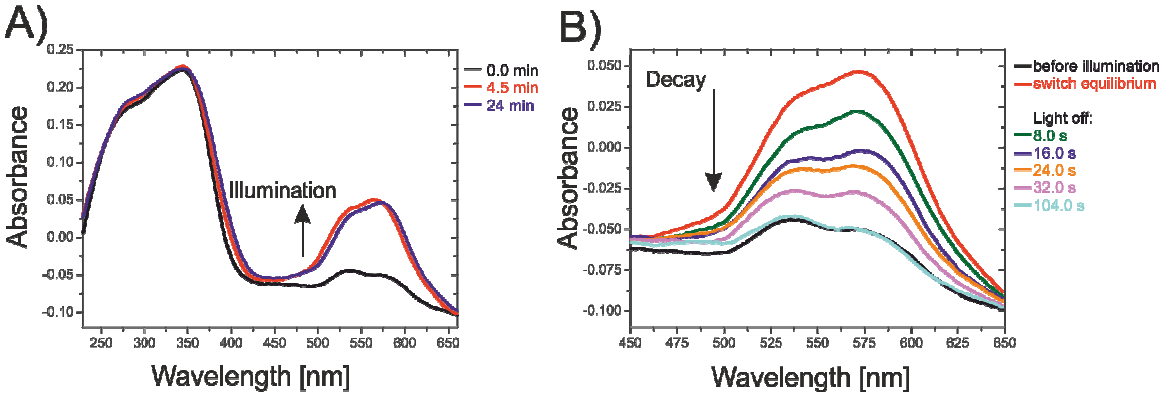

Figure S21. *In situ* recorded UV/Vis spectra of a solution of **1** in 300 µL THF-d_8 at 300 K A) buildup of the open form **2** under continuous illumination with 365 nm (increase of absorbance from 450-650 nm) B) excerpt of the UV/Vis spectrum from 450-650 nm showing the thermal back reaction of **2** to **1** once the light is turned off.

It is to be noted that the UV/Vis spectra recorded with the UVNMR-illumination setup sometimes show negative absorbances (as shown e.g. in S21). These negative absorbances are caused by slight deviations in the distance and/or positioning of the reflector and the dip probe between blank and actual measurement.

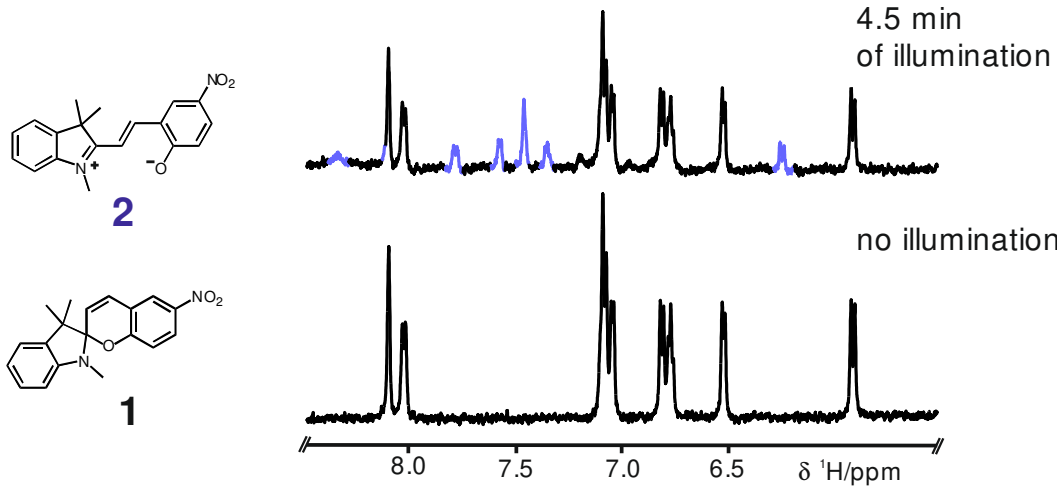

Figure S22. Excerpt of NMR spectra showing the photoswitch **1** in a solution of 300 µL THF-d_8 at 300 K prior to illumination (bottom) and the mixture of **1** and **2** once the photostationary state is reached (top) under illumination with 365 nm.

To evaluate the half-life $\tau_{1/2}$ of **2** in THF-d_8 at 300 K the light was turned off once the photostationary state was reached and one UV/Vis spectrum was taken every eight seconds. Afterwards the absorbance of the maximum at 533 nm (belonging to the open form **2**) was taken and plotted against the elapsed time (Figure S23). Those values were then fitted via exponential decay in Origin8 (ExpDec1). Using the equation shown in Figure S23 a half-life of 17.4 s was determined for **2** in THF-d_8 at 300 K.

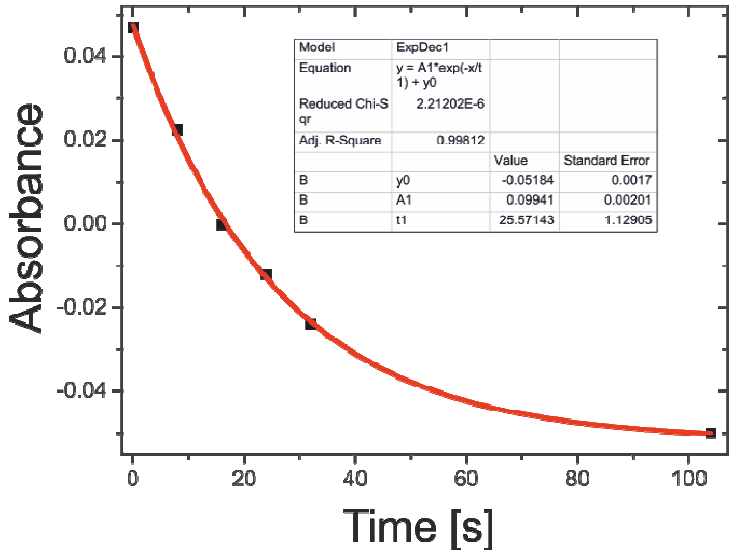

Figure S23. Plotted decay of the absorbance of **2**. After the photostationary state was reached the light was turned off to evaluate the half-life of **2** in THF-d_8 at 300 K. The absorbance values were taken from the maximum at 533 nm (see Figure S21B). Origin8 was used to fit the data via exponential decay (ExpDec1).

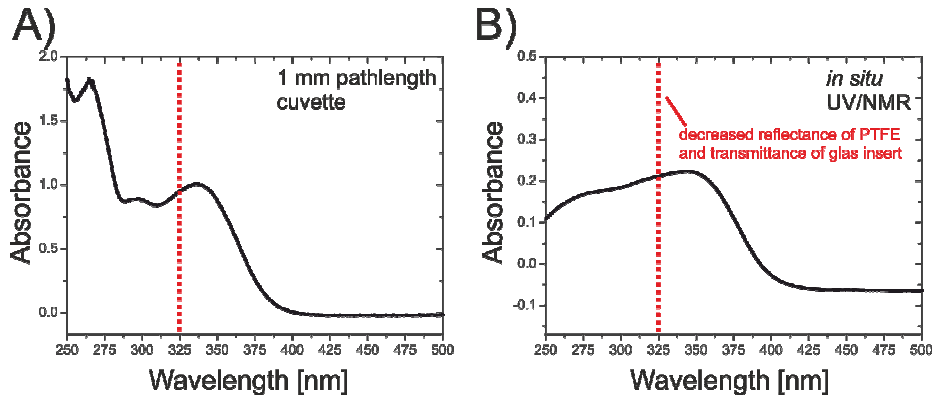

Figure S24. A) UV/Vis spectrum of **1** (1 mM) in THF in a 1 mm path length cuvette at ambient temperature. B) UV/Vis spectrum of **1** (1 mM) in THF with the in situ UVNMR-illumination device at 300 K. Until ~325 nm both spectra are comparable (respective absorbance maxima are 341 nm for A and 344 nm for B). Below 325 nm major differences can be observed between two methods probably because of the reduced reflectance of PTFE (from below 380 nm) and reduced transmittance of the glass insert at shorter wavelengths.

5.6.3.3.2 Isomerization Experiments at 180 K

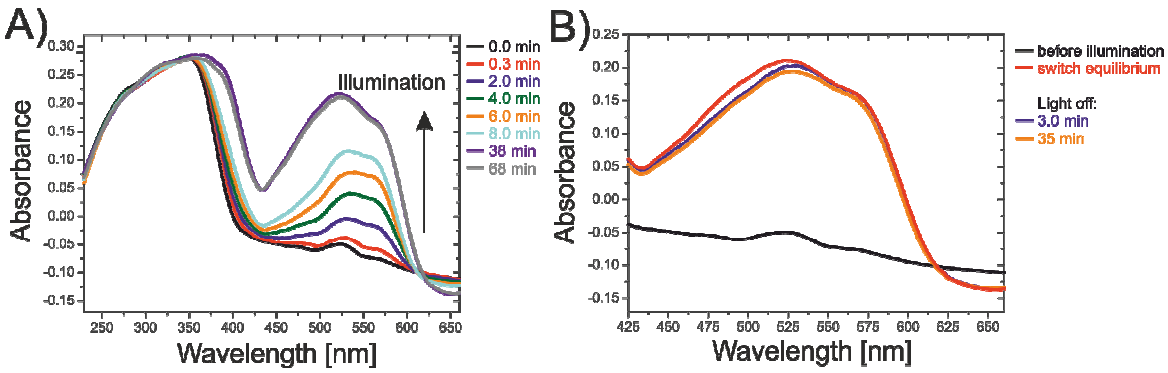

Figure S25. *In situ* recorded UV/Vis spectra of a solution of **1** in 300 µL THF-d_8 at 180 K A) buildup of the open form **2** under continuous illumination with 365 nm (increase of absorbance from 450-650 nm) B) excerpt of the UV/Vis spectrum from 425-655 nm showing that the thermal back reaction of **2** to **1** is prevented by the reduced temperature.

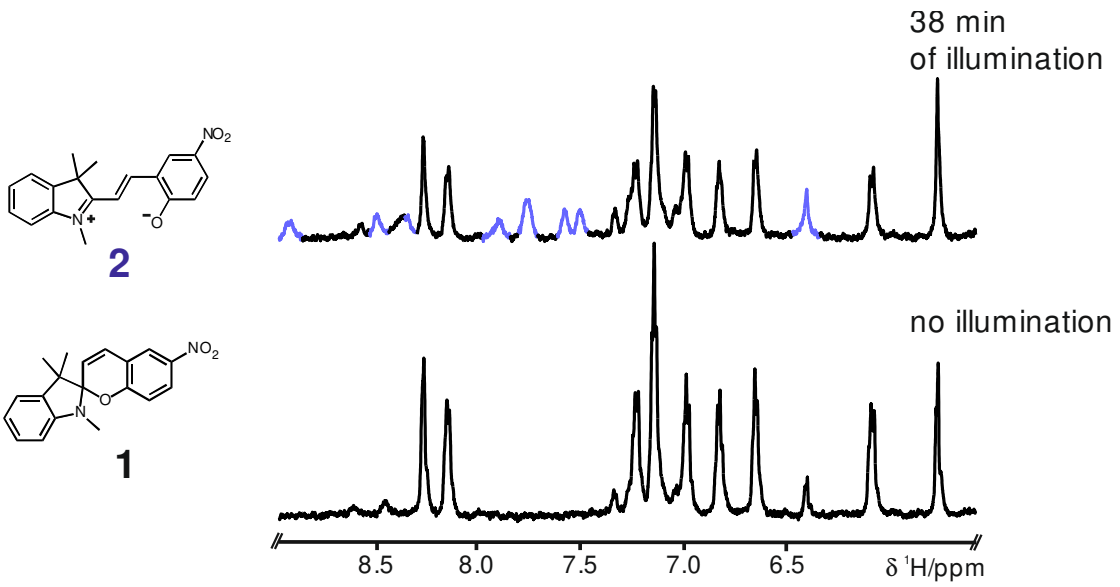

Figure S26. Excerpt of NMR spectra showing the photoswitch **1** in a solution of 300 µL THF-d_8 at 180 K prior to illumination (bottom) and the mixture of **1** and **2** once the photostationary state is reached (top) under illumination with 365 nm.

5.6.3.4 Photodegradation

It was observed that the photoswitch system of **1** and **2** is very prone to photodegradation at 365 nm. Both at 300 K and 180 K photodegradation starts after around 25-45 min preventing a study of the system under continuous illumination with 365 nm. Hence only **2** at 180 K could be structurally assigned unambiguously as the thermal back reaction could be prevented by the reduced temperature and so the light could be turned off without the decrease in intensity of signals of **2**. Figure S27 shows the photodegradation of **1** and **2** under continuous illumination with 365 nm in THF-d_8 at 180 K. The UV/Vis spectrum (Figure S27A) loses the characteristic absorbance of the open form **2** from 425-625 nm and even the dominant absorbance of **1** loses some absorbance at around 375 nm indicating that not only **2** but also **1** gets photodegraded under continuous irradiation. Figure 27B shows a row of NMR spectra corresponding to the UV/Vis spectra of Figure S27A. Here the strength of NMR spectroscopy is showing as it immediately confirms that not only the open form **2** but also the initial photoswitch **1** is completely degraded after overnight illumination with 365 nm.

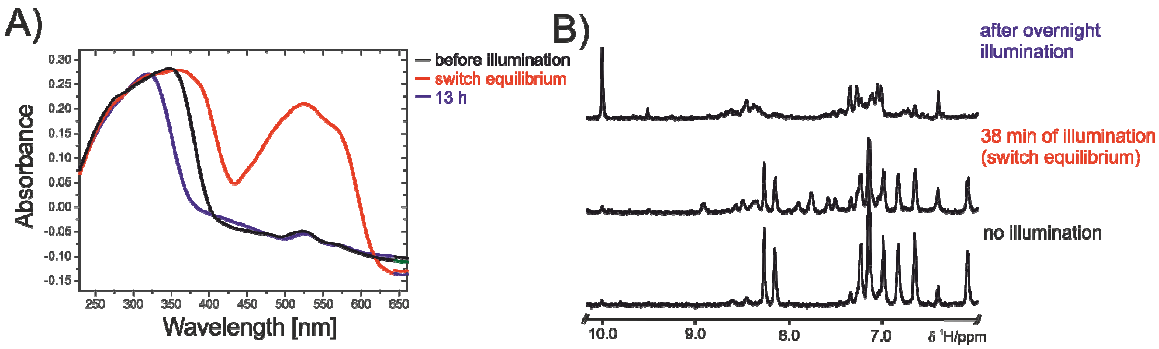

Figure S27. Degradation of the photoswitch **1** and its open form **2** under continuous illumination with 365 nm in THF-d_8 at 180 K. A) *in situ* recorded UV/Vis spectra show the combined absorbance of the photostationary state of **1** and **2** (red) is mostly gone after overnight illumination (blue) indicating photodegradation of **1** and **2**. B) row of NMR spectra corresponding to the UV/Vis spectra unambiguously confirm a full photodegradation of **1** and **2** under continuous illumination.

5.6.4 References

(1) C. Feldmeier, H. Bartling, E. Riedle, R. M. Gschwind, *J. Magn. Reson.* **2013**, *232*, 39–44.

(2) P. M. Tolstoy, B. Koeppe, G. S. Denisov, H.-H. Limbach, *Angew. Chemie Int. Ed.* **2009**, *48*, 5745–5747.

(3) B. Koeppe, P. M. Tolstoy, H. H. Limbach, *J. Am. Chem. Soc.* **2011**, *133*, 7897–7908.

(4) C. Feldmeier, H. Bartling, K. Magerl, R. M. Gschwind, *Angew. Chemie Int. Ed.* **2015**, *54*, 1347–1351.

(5) D. B. Mccormick, *J. Heterocycl. Chem.* **1970**, *7*, 447–450.

(6) A. Graml, I. Ghosh, B. König, *J. Org. Chem.* **2017**, *82*, 3552–3560.

(7) M. Poznik, B. König, *React. Chem. Eng.* **2016**, *1*, 494–500.

(8) I. Ghosh, T. Ghosh, J. I. Bardagi, B. Konig, *Science* **2014**, *346*, 725–728.

(9) M. Neumeier, D. Sampedro, M. Majek, V. de la Pena O'Shea, A. Jacobi von Wangelin, R. Pérez-Ruiz, *Chem. Eur. J.* **2017**, 1–5.

(10) I. Ghosh, B. König, *Angew. Chemie Int. Ed.* **2016**, *55*, 7676–7679.

(11) L. Zeng, T. Liu, C. He, D. Shi, F. Zhang, C. Duan, *J. Am. Chem. Soc.* **2016**, *138*, 3958–3961.

(12) B. König, *European J. Org. Chem.* **2017**, *2017*, 1979–1981.

6 Conclusion

In this thesis, the main focus of interest was the generation of an improved understanding about reaction mechanisms in modern organic chemistry by NMR spectroscopy. For the first time, several mechanistic questions in asymmetric aminocatalysis were answered by using a powerful combination of new tools and techniques (CEST, RDS-shift) with well-established NMR spectroscopic methods, like coupling constant analysis and 2D experiments. Additionally, to further push the boundaries of the field of reaction mechanism analysis, the application of the recently published DTS-hv method for the analysis of reaction pathways was transferred to the field of iminium ion catalysis and an innovative UVNMR-illumination setup was developed.

The power of NMR spectroscopy, enabling a quantitative and structural analysis of intermediates and reaction products were exploited in chapter 2 to investigate the remote-stereocontrol in dienamine catalysis. Dienamine catalysis represents a vinylogous version of enamine catalysis and enables the possibility to functionalize α,β-unsaturated aldehydes in their α or γ position via S_N type reactions. However, due to an increased distance between the shielding moiety of the catalyst and the active γ position of the dienamine key intermediate compared to enamine catalysis, the effectiveness of stereocontrol caused by Jørgensen-Hayashi type catalysts was questioned. Furthermore, the influence of the configuration of the diene subsystem within the dienamine intermediates on the enantiomeric excess was unclear, since the *Z/E* ratios of the double bond did not correlate with the *ee* values found in synthesis, if a shielding of one site by the catalyst moiety is given.

By detailed NMR spectroscopic investigations, a common structural preference including a *down* puckering of the pyrrolidine ring and a preferred *exo* conformation around the exocyclic C-C bond was found for all dienamine intermediates. Based on this structural analysis by NMR, which was corroborated by additional theoretical calculations, an effective shielding of the γ position in the case of large electrophiles was proven for Jørgensen-Hayashi catalyst derived dienamines. Therefore, according to the *ee* values found in synthesis and the observed *Z*/*E* ratios, a kinetic preference for the formation and conversion of the *E*,*s-trans*,*Z* over the *E*,*s-trans*,*E* isomer was assumed. To show this preference experimentally by NMR spectroscopy, a shift of the rate-determining step was induced by the modulation of the electrophile concentration by variations of the acidic

additive. Hence, the concentration of the *in situ* generated electrophile was reduced and the preferred conversion of the *E*,*s-trans*,*Z* isomer with the electrophile was made detectable within the NMR time scale. Additional computational investigations corroborated these findings and revealed this preference to be caused by CH-π interactions between the shielding moiety of the catalyst and the electrophile during the adduct formation. Depending on the catalyst, the strength of these interactions is changing, which was shown to influence the *ee* values of the product significantly. In summary, this study revealed the secret of a highly effective remote-stereocontrol in dienamine catalysis, being a delicate interplay of substrate, catalyst, and electrophile structure.

In chapter 3, the focus of the investigations was shifted to the field of enamine catalysis. Despite its huge success during the last two decades in synthesis, enabling various reactions and transformations, the formation process of enamine intermediates was still controversially discussed due to a missing experimental evidence for the iminium ion precursors for proline catalyzed reactions. By the implementation of the chemical exchange saturation transfer (CEST) technique, which is providing a higher sensitivity compared to standard NMR experiments, the previously missed iminium ion intermediate was now proven experimentally. These results pinpointed the proposed iminium pathway for the formation of enamines under our reaction conditions and corroborate former theoretical calculations. In general, the CEST technique was proven for the first time to be a powerful tool for the detection of elusive reaction intermediates below the detection limit of standard NMR spectroscopic measurements. Furthermore, it provides additional information about thermodynamics and kinetics of the intermediates in terms of populations and exchange rates, which can be of utmost importance for the analysis of reaction mechanisms. Therefore, it is regarded as a valuable tool for the detection of transient intermediates of ongoing reactions within various fields.

To further increase the number of tools and techniques for the investigations of reactions and to enlarge the scope of the field of reaction mechanism analysis itself, the application and the development of new mechanistic tools were also focused in chapters 4 and 5. Firstly, in chapter 4, the recently published decrypting transition states by light (DTS-hv) method was transferred into the field of iminium ion catalysis. It was shown, that the method can allow for a fast experimental access to the dominant reaction pathway of an asymmetric reaction of ketimines by light induced modulations of their double bonds. Therefore, the question arose, if the method is also transferable to a more complex system of iminium ion intermediates which feature two double bonds. A detailed theoretical approach describing the possibilities, chances, and limitations in iminium ion

catalysis was presented. Additionally, a preliminary study of a [3+3] annulation was conducted to positively prove the influence of light (365 nm) on an iminium ion catalyzed reaction. First NMR spectroscopic results to investigate the behavior of the iminium ions in presence of light (365 nm) and/or a nucleophile were presented. Notably, these investigations revealed the formation of an *E*,*Z* iminium ion isomer under irradiation (365 nm) at 300 K. So far, in the iminium ion catalysis community, a competition between the *E*,*E* and *E*,*Z* isomers is assumed to be responsible for the enantiomeric excess found in synthesis. However, if further evidence for the existence and the conversion of the *E*/*Z* isomers could be found also in absence of light, this assumption has to be reconsidered. Additional studies towards the detection and the influence of the *E*/*Z* isomers on the *ee* value of a reaction are in progress.

In the last chapter of this thesis, a combination of UV/Vis spectroscopy, NMR spectroscopy, and an *in situ* illumination device was presented as an innovative tool for the analysis of reaction mechanisms and transformations under the influence of light. The setup circumvents all common issues of separated setups like deviations in reaction conditions (concentration, temperature), light intensities, reaction vessels, convection, and diffusion. Furthermore, it is portable, independent of the magnetic field of the NMR spectrometer and can be used in a wide temperature range, which can be essential to investigate short lived isomers like it was demonstrated on the analysis of a photoswitchable spiropyran.

In general, for the analysis of chemical processes, it is often required to exploit the advantages of different methods and to combine their results to generate a full overview of all mechanistic features. Therefore, this new triple combination is highly suitable, since it uses the specific features of NMR and UV/Vis spectroscopy and allows for the simultaneous and time-resolved detection of diamagnetic and paramagnetic species under the influence of light. The potential of the UVNMR-illumination setup was demonstrated on a preliminary study of a light induced conPET process, enabling the first time acquisition of a combined UVNMR reaction profile of paramagnetic and diamagnetic species.

In summary, this thesis allowed for detailed insights into different reaction mechanisms by NMR spectroscopy and answered important questions in the broad field of asymmetric aminocatalysis. Furthermore, by the introduction of the CEST method for reaction mechanism analysis and the development of the UVNMR-illumination setup, it laid the foundation for further detailed mechanistic studies to improve the general understanding of reaction mechanisms in modern chemistry.

Eidesstattliche Erklärung

(1) Ich erkläre hiermit an Eides statt, dass ich die vorliegende Arbeit ohne unzulässige Hilfe Dritter und ohne Benutzung anderer als der angegebenen Hilfsmittel angefertigt habe; die aus anderen Quellen direkt oder indirekt übernommenen Daten und Konzepte sind unter Angabe des Literaturzitats gekennzeichnet

(2) Bei der Auswahl und Auswertung haben mir die zu Beginn des jeweiligen Kapitels aufgeführten Personen in der jeweils beschriebenen Weise unentgeltlich geholfen.

(3) Weitere Personen waren an der inhaltlich-materiellen Herstellung der vorliegenden Arbeit nicht beteiligt. Insbesondere habe ich hierfür nicht die entgeltliche Hilfe eines Promotionsberaters oder anderer Personen in Anspruch genommen. Niemand hat von mir weder unmittelbar noch mittelbar geldwerte Leistungen für Arbeiten erhalten, die im Zusammenhang mit dem Inhalt der vorgelegten Dissertation stehen.

(4) Die Arbeit wurde bisher weder im In- noch im Ausland in gleicher oder ähnlicher Form einer anderen Prüfungsbehörde vorgelegt.

Regensburg, den _____

Andreas Seegerer